OPEN ACCESS
IOP Publishing
Journal of Physics G: Nuclear and Particle Physics
J. Phys. G: Nucl. Part. Phys. **52** (2025) 050501 (128pp)
https://doi.org/10.1088/1361-6471/adb449

Major Report

Motivations for early high-profile FRIB experiments

B Alex Brown[1], Alexandra Gade[1], S Ragnar Stroberg[2], Jutta E Escher[3], Kevin Fossez[4], Pablo Giuliani[5,6], Calem R Hoffman[7], Witold Nazarewicz[1], Chien-Yeah Seng[5,8], Agnieszka Sorensen[1,9], Nicole Vassh[10], Daniel Bazin[1], Kyle W Brown[11], Mark A Caprio[2], Heather Crawford[12], Pawel Danielewicz[1], Christian Drischler[13], Ronald F Garcia Ruiz[14], Kyle Godbey[5], Robert Grzywacz[15], Linda Hlophe[3,5,16], Jeremy W Holt[17,18], Hiro Iwasaki[1], Dean Lee[1], Silvia M Lenzi[19], Sean Liddick[11], Rebeka Lubna[5], Augusto O Macchiavelli[20], Gabriel Martínez-Pinedo[21,22,23], Anna McCoy[5,24], Alexis Mercenne[25], Kei Minamisono[1], Belen Monteagudo[26], Petr Navratil[10], Ryan Ringgle[1], Grigor H Sargsyan[3,5], Hendrik Schatz[1], Mark-Christoph Spieker[4], Alexander Volya[4], Remco G T Zegers[1], Vladimir Zelevinsky[1] and Xilin Zhang[5]

[1] Department of Physics and Astronomy and the Facility for Rare Isotope Beams, Michigan State University, East Lansing, MI 48824-1321, United States of America
[2] Department of Physics and Astronomy, University of Notre Dame, Notre Dame, IN 46556-5670, United States of America
[3] Nuclear and Chemical Sciences Division, Lawrence Livermore National Laboratory, Livermore, CA 94551, United States of America
[4] Department of Physics, Florida State University, Tallahassee, FL 32306, United States of America
[5] Facility for Rare Isotope Beams, Michigan State University, East Lansing, MI 48824-1321, United States of America
[6] Department of Statistics and Probability, Michigan State University, East Lansing, MI 48824, United States of America
[7] Physics Division, Argonne National Laboratory, 9700 S. Cass Ave., Argonne, IL 60439, United States of America
[8] Department of Physics, University of Washington, Seattle, WA 98195-1560, United States of America
[9] Institute for Nuclear Theory, University of Washington, Seattle, WA 98195, United States of America
[10] TRIUMF, 4004 Wesbrook Mall, Vancouver, British Columbia V6T 2A3, Canada

[11] Department of Chemistry and the Facility for Rare Isotope Beams, Michigan State University, East Lansing, MI 48824-1321, United States of America
[12] Nuclear Science Division, Lawrence Berkeley National Laboratory, Berkeley, CA 94720, United States of America
[13] Department of Physics and Astronomy and Institute of Nuclear and Particle Physics, Ohio University, Athens, OH 45701, United States of America
[14] Massachusetts Institute of Technology, Cambridge, MA 02139, United States of America
[15] Department of Physics and Astronomy, University of Tennessee, Knoxville, TN 37996, United States of America
[16] Los Alamos National Laboratory, Los Alamos, New Mexico 87545, United States of America
[17] Cyclotron Institute, Texas A&M University, College Station, TX 77843, United States of America
[18] Department of Physics and Astronomy, Texas A&M University, College Station, TX 77843, United States of America
[19] Dipartimento di Fisica e Astronomia dell'Università and INFN, Sezione di Padova, I-35131 Padova, Italy
[20] Physics Division, Oak Ridge National Laboratory, Oak Ridge, TN 37831, United States of America
[21] GSI Helmholtzzentrum für Schwerionenforschung, Planckstraße 1, 64291 Darmstadt, Germany
[22] Institut fur Kernphysik (Theoriezentrum), Fachbereich Physik, Technische Universität Darmstadt, Schlossgartenstraße 2, 64289 Darmstadt, Germany
[23] Helmholtz Forschungsakademie Hessen fur FAIR, GSI Helmholtzzentrum für Schwerionenforschung, Planckstraße 1, 64291 Darmstadt, Germany
[24] Department of Physics, Washington University in Saint Louis, Saint Louis, MO 63130, United States of America
[25] Department of Physics and Astronomy, Louisiana State University, Baton Rouge, LA 70803, United States of America
[26] Department of Physics, Hope College, Holland, MI 49423-9000, United States of America

E-mail: brown@frib.msu.edu

Received 2 October 2024, revised 24 January 2025
Accepted for publication 10 February 2025
Published 6 May 2025

Abstract

This white paper is the result of a collaboration by many of those that attended a workshop at the facility for rare isotope beams (FRIB), organized by the FRIB Theory Alliance (FRIB-TA), on 'Theoretical Justifications and Motivations for Early High-Profile FRIB Experiments'. It covers a wide range of topics related to the science that will be explored at FRIB. After a brief introduction, the sections address: section 2: Overview of theoretical methods, section 3: Experimental capabilities, section 4: Structure, section 5: Near-

threshold Physics, section 6: Reaction mechanisms, section 7: Nuclear equations of state, section 8: Nuclear astrophysics, section 9: Fundamental symmetries, and section 10: Experimental design and uncertainty quantification.

Keywords: nuclear theory, nuclear structure, nuclear reactions, nuclear astrophysics, equation of state, fundamental symmeties, uncertainty quantification

1. Introduction

In 2008, the DOE Office of Science awarded a project to Michigan State University (MSU) to build the facility for rare isotope beams (FRIB) [1]. In May of 2022 there was a ribbon cutting ceremony for its completion, and the experimental program started. Since then, over 200 proposals have been submitted to the Program Advisory Committee (PAC). Those selected to run are chosen for their scientific impact and feasibility. The scientific impact of the proposals as well as the publication of the results relies on a strong collaboration of experiment with nuclear theory and astrophysical modeling. The published experimental results from FRIB already cover a broad range of topics, including the discovery of new isotopes [2], the measurements of a variety of nuclear observables obtained from decay spectroscopy [3–5] and reactions [6], and have reached the proton drip line for the precision mass spectrometry of a proton halo candidate [7], for example.

In May of 2023, an FRIB Theory Alliance (FRIB-TA) workshop was held at FRIB on 'Theoretical Justifications and Motivations for Early High-Profile FRIB Experiments'. This workshop brought together researchers with a broad range of interests in FRIB science.

The workshop started with a presentation on the capabilities for fast, stopped, and reaccelerated beams at FRIB. Opportunities for experiments over a wide range of the nuclear chart, out to the limits of nuclear stability [8], will be opened up as FRIB's capabilities are ramped up to the design values, including 400 kW of beam power [9]. The calculated beam intensities, assuming a beam power of 10 kW, are shown in figure 1. Proposals for the third Program Advisory Committee (PAC3) were submitted in October of 2024.

The feasibility of a proposal for an FRIB experiment is associated with the production of specific nuclei together with the instrumentation available. At the workshop, experimentalists gave talks on a wide range of instrumentation and types of observables that will be measured. Proposals are most often based on collaborations with theorists to articulate the connection between the measured observables and the scientific impact. At the FRIB-TA workshop, theorists gave talks on their present results and future plans. This was followed by discussions between theory and experiment to consider how the impact of the early FRIB experiments can be maximized by a close experiment-theory collaboration where results from both sides advance each other.

This white paper is the product of the collaboration of many who attended the FRIB-TA workshop. It covers a wide range of topics related to the science at FRIB. The sections are: section 2: Overview of modern theoretical methods, section 3: Experimental capabilities, section 4: Structure, section 5: Near-threshold Physics, section 6: Reaction mechanisms, section 7: Nuclear equations of state, section 8: Nuclear astrophysics, section 9: Fundamental symmetries, and section 10: Experimental design and uncertainty quantification, followed by a brief summary.

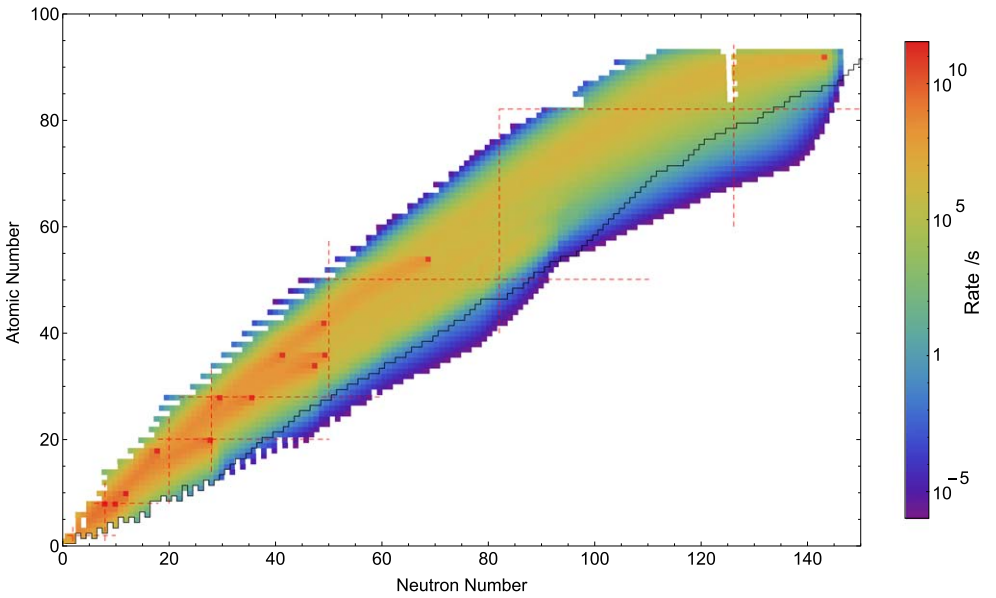

Figure 1. FRIB beam rates based on primary beam intensities of 10 kW for nuclei out to the proton and neutron drip lines predicted by calculations with the UNEDF1 energy-density-functional [10]. The thin black line on the neutron-rich side is the approximate boundary of known nuclei. The red squares are the primary beams produced by FRIB. These are fragmented to produce the other nuclei shown at the rates indicated on the right-hand side. The nuclei of interest for a given experiment are selected by the fragment separator. Figure courtesy of B.M. Sherrill (FRIB).

The author list starts with the workshop organizers, followed by the list of section leaders and then the list of contributors. Abbreviations used in the text are given Table I in Appendix C.

2. Overview of modern theoretical methods

The goal of low-energy nuclear structure theory is to build a unified microscopic framework in which nuclei, nuclear matter, and nuclear reactions can all be explained, described, and predicted. While this goal is ambitious, it is not beyond the realm of possibility. Hand in hand with breakthroughs in radioactive ion beam (RIB) experimentation, a rapid transition in nuclear modeling is taking place. Due to novel theoretical concepts, interdisciplinary collaborations, and high performance computing, nuclear theorists have been quite successful in cracking the nuclear many-body problem.

These are exciting times for theoretical nuclear structure research [11–14]. In the area of quantum chromodynamics (QCD), the underlying theory of strong interactions that governs the properties and dynamics of quarks and gluons that form baryons and mesons, significant progress is being made by computing properties of nuclear interactions, operators, and the lightest nuclei [15–18].

The nuclear many-body problem with protons and neutrons as degrees of freedom is an effective low-energy approximation to QCD. Nuclear effective field theory (EFT) has enabled theorists to construct high-quality two- and three-body inter-nucleon interactions consistent with the low-energy symmetries of QCD [19–22]. The low-energy coupling constants (LECs)

that incorporate unresolved short-distance (i.e. high-energy) physics, must be determined from experiment [23, 24] or eventually from QCD [23, 25].

Ab initio methods, i.e. systematically improvable *A*-body approaches based on inter-nucleon interactions [26], have seen dramatic progress over the past decade [27, 28]. Open-shell systems, excited states, heavy nuclei, and nuclear reactions are now within reach, and electroweak currents consistent with the strong interaction are available. Broadly, we can divide *Ab initio* many-body methods into quasi-exact solutions (no-core–shell model [29], quantum Monte Carlo [30], lattice effective field theory [31]), and more approximate but more widely applicable polynomial-scaling methods (coupled cluster [32], self-consistent Green's function [33], in-medium similarity renormalization group [34], many-body perturbation theory [35]). In an *Ab initio* framework, comparison to experimental data can reveal shortcomings either in the input (nuclear interaction, operators) or in the approximations made in the many-body solution. A proper understanding of both of these sources of error will then enable predictions with quantified uncertainties.

For light and medium-mass systems, configuration-interaction (CI) methods employing effective shell-model interactions optimized to various nuclear structure data offer detailed descriptions of nuclear excitations and decays [36–38]. In the area of weakly bound or unbound nuclear states, and reactions at near-threshold energies, modern continuum shell-model approaches unify nuclear bound states with resonances and scattering continuum within one consistent framework [39, 40].

For heavy complex nuclei the tool of choice is nuclear density functional theory (DFT) [41, 42]; the validated global energy density functionals often provide a level of accuracy typical of phenomenological approaches based on parameters locally optimized to experiment, and enable extrapolations into nuclear *terra incognita* [43]. The time-independent and time dependent extensions of DFT [44, 45] have provided quantitative descriptions of one of the toughest problems of nuclear structure: nuclear large amplitude collective motion, which includes such phenomena as shape coexistence, fission, and heavy-ion fusion [46–48].

These are exciting times also for nuclear reaction theory. For light nuclei, the combination of the no-core–shell model (NCSM) with the resonating group method (RGM) enables *Ab initio* descriptions of reactions with both nucleons and light composite projectiles. The method uses modern interactions rooted in chiral EFT, can include 3-nucleon forces and continuum effects, and has successfully predicted scattering, transfer, and capture reactions [49–52]. The use of symmetry-adapted bases provides a viable path to extend the approach to medium-mass nuclei [53, 54]. In addition, methods are being explored to extract nuclear scattering and reactions from computing eigen-energies of the nuclear systems in external traps [55–57], or from continuum states at complex energies [58, 59].

For medium-mass and heavy nuclei, we distinguish between direct and compound nuclear reactions. Traditional descriptions of direct reactions, such as the distorted-wave born approximation (DWBA) and adiabatic distorted wave approximation (ADWA) are increasingly combined with structure information from microscopic theories, in order to improve their predictive power [60–65]. Extensions of standard DWBA and eikonal approaches have been introduced to account for the dynamics between the transferred nucleon and the nucleus in descriptions of one-nucleon transfer and knockout reactions [66, 67]. The full coupled-channels (CC) approach accommodates multistep reaction mechanisms and the continuum-discretized coupled channels (CDCC) and Faddeev methods provide improved treatments of the breakup contributions [40, 68–70]. Extensions to include more complicated reaction mechanisms, such as core excitations and four-body channels, have been the focus of recent work [71–78].

Compound-nuclear reactions are treated in a phenomenological R-Matrix approach (for isolated resonances) or statistical Hauser–Feshbach (HF) theory (for overlapping resonances) [60, 79]. Efforts have been devoted to compiling recommendations for default inputs for HF calculations, which enable data evaluations as well as initial calculations for thousands of isotopes for astrophysics application [80, 81]. At the same time, significant progress has been in replacing the phenomenological models used in HF codes by microscopically-calculated quantities [81, 82].

From a theoretical point of view, short-lived exotic nuclei far from stability, studied at RIB facilities, offer a unique test of those aspects of the many-body theory that depend on the isospin degrees of freedom and the coupling to the continuum space. The challenge is to develop methods to reliably calculate and understand the properties of new physical systems, identify the impact of new observables on theoretical models, quantify correlations between predicted observables, and assess uncertainties of theoretical predictions. The use of advanced tools of uncertainty quantification and machine learning will help to speed up the cycle 'observation-theory-prediction-experiment' of the scientific method [83]. These new tools are expected to provide meaningful input for planned measurements at FRIB and will be used to interpret and use new nuclear and astrophysical information obtained at FRIB.

Using rare isotopes in heavy-ion collisions (HICs) produces dense nuclear matter within a large range of isospin asymmetry [84] and provides a connection to dense neutron-rich matter present in neutron stars and neutron star mergers [85–87]. In particular, comparisons of HIC observables to transport model simulations put constraints on the nuclear matter equation of state at densities well above the saturation density [88–93], currently inaccessible to *Ab initio* approaches [94]. Simulations are also used to identify promising observables [95–101], informing detector and experimental designs. An outstanding challenge in these studies is a quantitative understanding of model uncertainties [85, 102], addressed by investigations of different transport models in well-controlled simulation setups as well as through Bayesian analyses [92, 103, 104] and Bayesian model mixing [105]. The availability of high-performance computing has only recently made such studies feasible, providing a path to a comprehensive understanding of HIC dynamics [85].

New theoretical ideas in describing atomic nuclei, progress in RIB experimentation, the arrival of exascale computing platforms [14], and increased collaboration between nuclear theorists with their computer science and applied mathematics partners [10, 105]—all are paving the way for today's progress in theoretical nuclear structure studies. The important challenge for the field is to connect different many-body approaches, describing the nucleus at different resolution scales, in the regions of the nuclear landscape where they overlap. By bridging the gaps, one is aiming at developing one comprehensive picture of the atomic nucleus, from the single nucleon all the way to the superheavy species. This is an exciting prospect. On the journey to the comprehensive nuclear theory framework, important milestones will be marked by designer nuclei with characteristics adjusted to specific research needs [12, 106, 107]. Those rare isotopes are the key to answering questions in many areas of science and they will also provide society with numerous opportunities [108].

3. Experimental capabilities

3.1. Mass measurements

Expanding the reach of precision mass measurements at a level of $\delta m/m \approx 10^{-6}$–$10^{-8}$ [109] for rare isotopes to the most exotic regions of the nuclear chart is of utmost importance, enabling the direct observation of nuclear structure phenomena, such as (sub-)shell closures,

pairing effects, and the onset of deformation. FRIB is set to revolutionize precision mass measurements by opening a fresh territory within the nuclear chart, over 1300 isotopes with sufficient production rates and long enough half-lives with mass uncertainties greater than $50\,\mathrm{keV}/c^2$, thus, in collaboration with theory, paving the way for groundbreaking discoveries.

The two primary techniques employed in performing direct mass measurements of rare isotopes at FRIB are the TOF-Bρ technique [110, 111] and using Penning traps at the low-energy beam and ion trap facility (LEBIT) facility [112]. The TOF-Bρ technique uses the fast beams produced directly by FRIB and can perform measurements on rare isotopes with half lives down to 100's of nanoseconds with a mass precision down to $100\,\mathrm{keV}/c^2$.

3.2. Charge radii and nuclear moment measurements

In the last several decades, laser spectroscopy techniques have been extensively used to determine mean-square charge radius, R_{ch}, and moments of ground and isomeric states [113–120]. Especially, the bunched-beam collinear laser spectroscopy (CLS) has been almost exclusively used for charge radius measurements of long chains of radioactive isotopes and nuclei close to the nucleon drip lines. This is thanks to the bunched-beam CLS technique's high resolution due to the Doppler compression [121], and its high sensitivity due to the large background suppression by bunching the beam in fluorescence measurements [122–124] or by the virtual background free ion detection in resonant ionization measurements [125].

At FRIB, such CLS experiments are performed at the BEam COoling and LAser spectroscopy (BECOLA) facility [126, 127], which is designed to accept low-energy beams typically $30\,\mathrm{keV}/u$ from the gas stopping systems [128, 129], the offline batch mode ion source (BMIS) [130] for long-lived isotopes, and a dedicated local offline ion source [131] at BECOLA. Time-resolved laser resonant fluorescence and resonant ionization spectroscopy measurements with bunched beams [124, 125, 127] are performed for highly sensitive measurements of hyperfine spectra and their isotope shifts. A beam rate of as low as $\sim 10\,\mathrm{s}^{-1}$ has been achieved for ^{36}Ca ions [132] and ^{54}Ni atoms [133]. BECOLA has been extensively used to determine charge radius [132–137] and electromagnetic moments [138–140] of radioactive nuclei. The Resonance Ionization Spectroscopy Experiment (RISE) instrument was recently integrated into the BECOLA facility in collaboration with MIT to realize $\sim 1\,\mathrm{ion\,s}^{-1}$ sensitivity for laser spectroscopy. RISE has been commissioned with offline beams and hosted the first online experiment in 2024, aimed at determining the charge radii of *sd*-shell nuclei near the proton drip line. Similar to LEBIT, BECOLA is the only CLS facility worldwide making use of rare isotopes from projectile fragmentation, complementing capabilities at ISOL-type facilities [119].

The extraction of R_{ch} from the isotope shift depends on atomic factors that must be calculated [120, 141] or measured using the King plot [142] involving three or more isotopes whose R_{ch} are well determined through electron scattering and/or μ-capture measurements. The uncertainties involve two terms, one for the uncertainty of the hyperfine spectra, and the other related to the uncertainty of the atomic factors.

3.3. Charge-exchange reactions

Charge-exchange reactions can be used to extract Gamow–Teller strengths in the $\beta+$ and β^- directions, for reaction Q values that cannot be probed directly in β/EC decays. At NSCL, the (t, ^{3}He) reaction [143–150], used for extracting GT strengths from stable nuclei at the S800 spectrometer [151], has proven to be a versatile probe. For early operation at FRIB, tritium beam intensities that are more than 30 times higher can be achieved. At these intensities, detailed studies of Gamow–Teller strength distributions in the β^+ direction in heavier stable

nuclei can be investigated, which was previously very difficult. It will become possible to use the Summing NaI(Tl) gamma-ray detector (SuN) [152] in coincidence with the S800, and use the Oslo method for extracting level densities and γ-ray strength functions, similar to the β-Oslo method [153, 154], as described in section 8.2.

The isolation of $\Delta L = 0$ contributions from the measured differential cross sections as a function of excitation energy, and associated with the Gamow–Teller transition strength, is facilitated through a multipole decomposition analysis [155–157]. The Gamow–Teller transition strength is proportional to the $\Delta L = 0$ charge-exchange cross section at small momentum transfer ($q \approx 0$) [158, 159] The proportionality between strength and differential cross section is represented by the so-called unit cross section ($\hat{\sigma}$) [158]. The unit cross section is calibrated by using a pair of states for which the Gamow–Teller transition strength is known from β decay or electron capture [158]. If such calibrations are not available, phenomenological mass-dependent relations for $\hat{\sigma}$ are employed [160, 161].

Recently, the (d, ^{2}He) reaction in inverse kinematics was developed for probing GT strengths in the β^{+} direction on unstable nuclei [162], by using the active target time projection chamber (AT-TPC) [163] in combination of the S800 spectrometer [151]. At FRIB, it will be possible to probe GT strengths on neutron-rich nuclei that are important for astrophysics. The early science program will likely focus on light and medium-heavy systems, to gain experience with the injection of highly charged ions into the AT-TPC.

The (p, n) reaction in inverse kinematics for probing GT strengths in the β^{-} direction was developed some time ago. By combining the measurement of the heavy residual particle in the S800 [151] with the detection of the low-energy recoil neutron from the (p, n) reaction [164, 165] in the low-energy neutron detector array (LENDA), isotopes across the chart of nuclei can be studied. An attractive opportunity arises from the coincident study of the (p, n) reaction and the decay-in-flight by γ emission of the residual nucleus by using GRETINA [166]. Such measurements will be of impact for nuclear structure and decay studies, and enable the application of the charge-exchange Oslo method with unstable nuclei.

At FRIB, information about isovector giant resonances that are excited in unstable nuclei was obtained by using the above-mentioned (p, n) and (d,^{2}He) reactions in inverse kinematics, as previously used at NSCL and RIBF [162, 164, 167]. To reliably extract resonance parameters, the (p, n) reaction in inverse kinematics is the more likely candidate for early FRIB experiments due to the high luminosity that can be achieved even with modest beam intensities, see e.g. the extracted GT resonance strength distribution from a ^{132}Sn(p, n) experiment at RIBF [167].

Another opportunity for studying isovector giant resonances is by using rare-isotope beams as novel reaction probes for stable targets. By cleverly making use of rare-isotope beams, it is possible to isolate resonances that are otherwise very difficult to study. A good example is the (^{10}Be,^{10}B) reaction, in which a secondary ^{10}Be beam is used. The measurement of the γ decay in GRETINA from ^{10}B excited states provides separate $\Delta S = 0$, $\Delta T = 1$ and $\Delta S = 1$, $\Delta T = 1$ filters in one experiment. The ^{10}B detection in the S800 spectrometer is used to extract the excitation energy in the target nucleus. This probe was first used successfully to extract information about the isovector giant monopole resonance (IVGMR) in ^{28}Al by using the ^{28}Si(^{10}Be,^{10}B*(IAS)) reaction [168], where IAS refers to the ^{10} isobaric analog state of the ^{10}Be ground state. With the much higher beam intensities available at FRIB, studies of heavy nuclei will be possible. The (^{10}C,^{10}B) reaction can be used to investigate the β^{-} direction [169, 170], based on the same principle.

Ultimately, the high rigidity spectrometer (HRS) [171] at FRIB will be a game changer for charge-exchange experiments in inverse kinematics. Until the HRS is available, improvements to the detector systems used in combination with the S800 spectrometer will enhance

experiments. Increased solid-angle coverage in the transition from GRETINA to GRETA and adding the ability to perform pulse-shape discrimination in LENDA to remove γ background in (p, n) experiments are important enhancements.

3.4. In-beam gamma-ray spectroscopy

In-beam γ-ray spectroscopy is a work-horse capability for rare-isotope beam facilities across the globe. In-beam spectroscopy enables studies of both nuclear structure and reactions from stability to the most exotic nuclear systems, leveraging techniques from direct reactions to Coulomb excitation to compound nuclear reactions to explore a broad range of nuclear properties. At FRIB, in-beam γ-ray spectroscopy is enabled by a number of advanced detector systems.

The segmented germanium array (SeGA) is an array of 18 single-crystal HPGe crystals each segmented with 32 outer surface contacts [172]. While limited in solid-angle coverage and thus efficiency, SeGA offers flexibility for varied installation configurations including close-packed geometries surrounding a target or configurations at larger distances with varied angles, allowing optimization of any given experiment. The segmentation of the SeGA crystals allows good Doppler correction for in-beam spectroscopy, reducing the finite opening angle of the detectors. SeGA is a versatile detection system which will continue to play an important role at FRIB in the next years.

For experiments which require high detection efficiency and can tolerate lower energy resolution (of order 10% FWHM at 1 MeV), the scintillator array CAESAR (CAESium iodide ARray) is another important tool [173]. CAESAR offers an efficiency of approximately 40% at 1 MeV with 192 CsI(Na) scintillation crystals in a close-packed array with very high solid angle coverage. For exotic light systems, where the level density is low and experiments may only expect to populate a handful of excited states, CAESAR provides a powerful capability to push to very low production rates.

Finally, the gamma-ray energy tracking array (GRETA) [174] will be completed in 2026 with a full complement of 120 large-volume HPGe detectors housed in 30 Quad modules and covering approximately 80% of the solid angle around a target position. GRETA takes advantage of the 36-fold segmentation of each HPGe crystal, combined with digital signal processing and advanced computational capabilities to reconstruct the position of each γ-ray Compton scatter or photoelectric interaction. With interaction positions reconstructed with several mm accuracy, γ-ray tracking algorithms can cluster these together and identify the most likely scattering sequences, thus allowing rejection of background events which either did not originate at the target position or did not deposit their full energy. GRETA will provide a world-unique capability at FRIB, with high-resolution ($\sim$0.2% FWHM), high efficiency ($\geqslant$30% at 1.3 MeV) spectroscopic capability with excellent peak-to-total ($\geqslant$50% at 1.3 MeV) for experiments with fast and with re-accelerated beams. Combined with advanced targets and a broad range of auxiliary devices, GRETA will be a key device for a large part of the FRIB science program.

3.5. Charged-particle, beta and gamma decays

The FRIB Decay Station Initiator (FDSi) is the initial stage of the FRIB Decay Station (FDS) [175] for early FRIB experiments. It is an efficient, granular, and modular multi-detector system designed under a common infrastructure. The FDSi brings multiple complementary detection modes together in a framework capable of performing decay spectroscopy with multiple radiation types over a range of beam production rates spanning ten orders of magnitude.

At the core of the FDSi is a system for stopping incoming radioactive ions and detecting their subsequent charged-particle decay emissions. Stopping systems include inorganic scintillators [176] or large area segmented silicon detectors. The choice between the two detector options depends on the needs of the experimental investigation. Additional detector arrays surround the central implantation detector to monitor delayed radiation in the form of photons and/or neutrons. Again, the specific configuration is adjustable to match the science goals of each experiment. The FDSi can be instrumented with either a 2π or 4π array of HPGe Clover detectors combined with LaBr/CeBr scintillators for precision timing measurements. Neutron detection is accomplished with the NEXTi/VANDLE [177] neutron time-of-flight detection system. Thermal neutron detection is also possible with ^{3}He gaseous counters.

Measuring the strength function following beta-decay can be accomplished using a total absorption spectrometer. As part of the FDSi the Modular Total Absorption Spectrometer can be used. MTAS is a one-ton volume of NaI scintillator detectors segmented parallel to the beam axis. Separate from the FDSi, the Summing NaI (SuN) total absorption spectrometer is also available [152]. SuN is a 16 inch right cylinder of NaI segmented in eight separate detectors segmented perpendicular to the beam axis. Both MTAS [5] and SuN [178] have been used with fast fragment beam to extract the strength distribution of exotic isotopes.

The early science program of the FDSi will predominately focus on the structure of exotic nuclear systems in medium-mass nuclei using a system with 2π of HPGe Clover detectors combined with 2π of time-of-flight neutron detection [3, 4] before proceeding to heavier systems. The development of the FDS will occur concurrently with the operation of the FDSi.

3.6. Neutron emission

The experimental study of neutron-unbound systems near and beyond the neutron drip line is generally based on invariant-mass spectroscopy, as the direct measurement of the core+xn system is not possible due to its extremely short lifetime. Invariant-mass measurements allow for the reconstruction of the relative energy spectrum from the energy and momenta of the coincident decay particles (charged fragment, neutrons, and γs). A key strength of this approach lies in the ability to probe correlations between decay particles, including neutrons. This makes invariant-mass spectroscopy a valuable tool to study exotic phenomena such as neutron halos or multi-neutron decays.

At FRIB, the standard Sweeper-MoNA setup is dedicated to invariant-mass studies. The separation of the charged fragments from the neutrons is provided by the 5.3 Tm dipole Sweeper magnet placed at 30° from the beam axis. The particle identification (PID) of the fragment of interest is then determined from energy loss (Z selection), position tracking, and time-of-flight (A selection) measurements using a suite of charged particle detectors positioned at the focal plane of the magnet. The neutron is detected by the MoNA-LISA position-sensitive neutron detector [179], placed at about 8 meters from the target. The momentum of the neutron is reconstructed from the hit position and the time-of-flight information between the MoNA-LISA array and a plastic scintillator positioned upstream of the target. In addition, the γ detector CAESAR [173] can be used to identify decays to excited bound states in the charged fragment.

One of the main advantages of the kinematic complete measurement is the study of the correlations of the decay particles, including the correlations between the decay neutrons. An important limiting factor is, however, the neutron detection efficiency and resolution. Given that a neutron only loses a part of its energy in a single interaction, the same neutron can be therefore detected multiple times in the array, a phenomenon known as cross-talk. The current MoNA-LISA efficiency for single neutron detection is approximately 70%. Yet, the

efficiency drops significantly for multi-neutron events, primarily due to challenges in identifying and rejecting cross-talk events.

The dominating factor for the overall resolution of the reconstructed relative energy in the MoNA-Sweeper setup is the position resolution of the neutron detector. In order to overcome the constraints of the current design, the MoNA collaboration is actively developing a next-generation neutron detector. This new design aims to significantly enhance the precision in determining the vertex of neutron interactions by replacing the Photomultiplier Tubes with Silicon Photomultiplier arrays as readout technology. The new neutron detector aims at significantly improving neutron position resolution by using a different technique, namely direct light detection, compared to other traditional neutron detectors that rely on time-difference measurements. While the over-all detection efficiency will be reduced, the enhanced resolution will make up for this, resulting in higher quality data. This new detector system will be used in combination with existing higher-efficiency detectors such as MoNA-LISA.

3.7. Heavy-ion collisions

Heavy-ion collision experiments at FRIB will proceed in distinct phases, reflecting the availability of detector technology and beams.

The first experiments at FRIB will rely on arrays of charged-particle and neutron detectors. The construction of a nearly-4π array of thin, fast plastic scintillators to infer the plane of the reaction is underway at MSU. This new detector will be added to the high resolution array (HiRA) [180] and upgraded large area neutron array (LANA) [181]. HiRA is a small array of Si–Si-CsI(Tl) telescopes for detecting protons and other light, charged particles. Two versions of HiRA exist with 4 and 10 cm CsI(Tl) crystals, capable of stopping 115 and 200 MeV protons, respectively. The LANA neutron walls are comprised of liquid scintillator bars for measuring neutron energies by time-of-flight. These walls utilize pulse-shape discrimination to separate neutrons from gamma-rays, and have a thin, fast-plastic scintillator wall in front to veto charged particles. These detector arrays will be utilized to measure neutron-to-proton ratios, directed and elliptic flow, and other observables sensitive to the nuclear equation of state.

The next phase of heavy-ion collision experiments at FRIB will focus more on ratios of charged pions, similarly to the SπRIT experiment at RIKEN [182, 183]. These experiments will require the development of a new time projection chamber (TPC). The most straightforward development path in this case is to construct a TPC similar to the Active-Target Time Projection Chamber and SOLARIS solenoid magnet [163] to run with 200 MeV/nucleon beams. A major task here will be the construction of an inner field cage with the goal of reducing the space charge effects, arising from the column of positive ions that builds up in the beam region from the ionized gas. Likely, a higher-density pad plane will also be required to manage the relatively high charged-particle multiplicities in heavy-ion collisions. The modified time projection chamber can be used to measure both flow as well as the pion ratios.

The final phase of development currently planned for heavy-ion collision experiments at FRIB will utilize the HRS [171] and the upgrade of available beam energies to 400 MeV/nucleon with FRIB400. These experiments will require the development of a TPC that will fit into the gap of the first dipole magnet of the HRS. The planned, usable gap of the HRS dipole is 15 cm smaller than that of the SAMURAI magnet at RIKEN, which means that the SπRIT TPC cannot be utilized in this case without major modifications to the design, including designing the field cage, readout, and other detector components anew. Therefore, it will be likely more efficient to construct an entirely new detector. While there is an overlap between

the science enabled by the HRS TPC and the solenoid TPC, described in the previous paragraph, the HRS TPC will have a higher efficiency for pion identification and will allow for coincident neutron detection.

3.8. Re-accelerated rare-isotope beams

A unique capability at FRIB is the possibility to post-accelerate rare-isotope beams produced via fragmentation. This scheme enables the production of high-quality beams at lower energies than the typical fragmentation regime, regardless of the chemistry of the selected ions. The main scientific goals of this capability involve the use of reactions to explore the properties of radioactive nuclei from structural, astrophysical and reaction point of views.

In its present status the ReA linear accelerator is capable to accelerate charged radioactive ions at energies ranging from 0.3 to 10 MeV/nucleon with emittance qualities typical of primary beams. An upgrade to higher energies is planned to augment the energy reach to about 20 MeV/nucleon [184], depending on the mass-to-charge ratio. The instruments making use of these beams are the solenoidal spectrometer apparatus for reaction studies (SOLARIS) [185–187], the separator for capture reactions (SECAR) [188], and the JANUS setup [189]. In addition, general purpose beam lines are available to accommodate other instruments.

SOLARIS is a dual mode solenoidal spectrometer that can be used either with a Silicon array detection setup similar to the HELIOS spectrometer [190], the ISOLDE solenoidal spectrometer (ISS) [191, 192], or with the AT-TPC [163]. The main purpose of this instrument is to gain access to the structure of radioactive isotopes via simple, one-step and momentum-matched reactions in inverse kinematics. The silicon array mode is suitable for beam intensities of 10^4 pps and above, and provides excellent missing mass resolution approaching 100 keV and a large solid angle coverage. SOLARIS provides arrays both backward and forward relative to the target location, hence covering multiple reaction channels simultaneously. The AT-TPC mode extends the reach to use similar reactions at very low intensities, down to 100 pps. This is possible thanks to the 2–3 orders of magnitude gains provided by the large thickness and solid angle coverage of the AT-TPC, without degradation of the energy and angular resolutions. In addition, the AT-TPC can be used with the high quality beams of ReA to measure excitation functions in a very efficient manner, simply by using the energy loss of the beam traveling through the gas and the recorded vertex location of each reaction. This opens the door to resonance scattering experiments on radioactive nuclei. Another capability of the AT-TPC is the possibility to detect and measure the particle decay of unbound resonances and reconstruct their excitation spectrum using invariant mass methods. This is particularly interesting for the study of threshold resonances.

The SECAR separator is primarily dedicated to the study of (p, γ) and (α, γ) capture reactions in inverse kinematics on radioactive nuclei at low energy, directly related to the study of hydrogen and helium burning in explosive stellar environments. It is equipped with a windowless target system and is designed with acceptances large enough to transmit the heavy recoils without significant loss. The primary beam rejection design goal of this instrument is 10^{-13}, with an additional 10^{-4} rejection provided by the focal plane detection system. This extremely high rejection should allow the measurement of resonance strength down to 1 μeV.

The JANUS setup [189] is dedicated to the measurement of barrier-energy Coulomb excitation induced by a high-Z target on rare-isotope beams. In the low-energy domain provided by ReA, multiple excitations occur and reach higher excited states, characterizing their degree of collectivity from the deduction of $B(E2)$ transition strengths and quadrupole

moments. The setup is composed of a set of annular silicon strip detectors that detect scattered beam particles and target recoils, while their Doppler-shifted γ-ray decays are detected by the surrounding SeGA [172]. Once completed, the GRETA array [174] can be used for Coulomb excitation studies as well, greatly enhancing the sensitivity for the γ-ray detection.

4. Structure

Experiments at FRIB will provide unprecedented access to properties of neutron-rich nuclei out to the neutron dripline. Connections between theory and experiment have been discussed in recent reviews [193–196]. The following sections discuss open theoretical questions in nuclear structure and how they relate to the variety of experimental data.

In the study of nuclear structure, the goal is to understand the properties of nuclei by identifying the relevant degrees of freedom, and by connecting these properties to the underlying interaction between nucleons. The relevant degrees of freedom could be collective modes like clustering, superfluidity, vibrations and deformations; they could be related to a set of active orbitals defined by shell gaps; or they could be related to the proximity of the continuum. The main new information provided by FRIB will relate to how these features are intertwined and modified in very neutron-rich nuclei, and how these various degrees of freedom interplay with the continuum. Historically, the various degrees of freedom have been understood phenomenologically, e.g. by putting in a single-particle spin–orbit potential 'by hand'; however these features must arise from the underlying nuclear forces. Studying neutron-rich systems will help to lift the degeneracy of various explanations of how this occurs. For example, from an *Ab initio* standpoint, the one-body spin–orbit potential gets contributions from both two-body and three-body interactions. Due to the Pauli principle, the three-neutron force is well understood, hence, changes in the effective spin–orbit potential as neutrons are added can illuminate its microscopic origin.

First, we examine the evolution of shell structure with examples from several regions of the nuclear chart. Following this, there are separate sections on collectivity, isospin symmetry, spin-isospin response, and nuclear pairing. Notations and abbreviations for the shell-model orbitals and commonly used truncations (model spaces) are described in the Appendix.

4.1. Evolution of shell structure

In nuclear physics, 'shell structure' refers to the independent-particle picture in which nucleons move in an effective mean-field potential and groups of degenerate or quasi-degenerate single-particle orbitals are separated by energy gaps. The number of nucleons required to fill all orbitals below one of these gaps is called a 'magic number'. Many of the regularities of nuclear data can be qualitatively understood in terms of these magic numbers. In addition, quantitative CI calculations make use of magic numbers to define the model space to be used for a given region of the nuclear chart. For example, the $0d_{5/2}$, $1s_{1/2}$, $0d_{3/2}$ orbitals define the *sd* model space as a starting point for calculations of the properties of nuclei between the magic numbers 8 and 20. The textbook magic numbers 2, 8, 20, 28, 50, 82, and 126 apply to nuclei in the valley of stability. Moving away from stability, the mean field changes and shell gaps disappear or appear in new places, generating new magic numbers. This phenomenon is called shell evolution, and it has been argued that the primary drivers of shell evolution are the monopole component of the tensor force [193, 197] and continuum effects [198, 199]. FRIB is especially well-suited to explore the latter.

Shell structure is not a directly observable property; it is a framework in which to interpret and understand experimental data. Consequently, various nuclear properties should be

considered in order to develop a coherent picture of evolving shell structure. Important signals of a shell gap include a relatively high energy of the first excited 2^+ state (for even–even nuclei); a relatively small electric quadrupole transition strength $B(E2; 2^+ \rightarrow 0^+)$; a gap in the effective single-particle energies (ESPE); and relatively large jumps in differential quantities derived from binding energies and radii.

The ESPE are the single-particle energies obtained from the differences between the calculated energy of a pure closed-shell configuration for A nucleons and the energies of pure single-particle states in nuclei with $A \pm 1$. These ESPE are derived from the CI Hamiltonian with a given model space and cannot be observed in experiment. For open-shell (mixed) CI configurations one can obtain theoretical centroid SPE energies for nucleus A using the energy differences of states for a given (n, ℓ, j) in nuclei with $A \pm 1$ relative to A weighted by their spectroscopic factors [200, 201]. If the mixed configuration is dominated by the closed-shell configuration, the ESPE and centroid SPE are the same within a few hundred keV.

In single-nucleon transfer reactions one observes cross sections from nucleus A to states with (ℓ, j) in the nuclei $A \pm 1$. To compare with CI calculations one requires reaction theory to extract spectroscopic factors from cross sections. One must make assumptions about the radial part of the overlap function associated with each of the (ℓ, j) states. These spectroscopic factors can then be used to compare to calculations and to obtain centroid SPE [201]. Figure 2 shows the energies of 2_1^+ states in the region $N, Z \lesssim 50$. It is evident that the $N = 20$ magic number disappears below $Z = 14$. This region has been called an 'island of inversion' [202]. Most nuclei with proton and neutron numbers between 8 and 20 have ground and low-lying states that are described by configurations within the *sd* model space. All of these nuclei also have excited 'intruder' states that are described by configurations involving the excitation of nucleons from *p* into *sd* or *sd* into *fp* orbitals. For nuclei inside the island of inversion, this order is inverted (the intruder configuration is the ground state). Other islands of inversion have been identified in the regions around $N = 8$ for $Z < 5$, $N = 28$ below ^{48}Ca, and $N = 40$ below ^{68}Ni [203]. Based on CI calculations, a 5th island of inversion is predicted below ^{78}Ni [204]. In general, whether a nucleus is inside the island of inversion depends on the competition between shell structure and correlation energy [205]. The connection to shape-coexistence has been recently reviewed in [206]. All of these islands of inversion lie in neutron-rich regions of nuclei that will be studied at FRIB.

Another experimental signature of magic numbers is given by the double difference in the binding energies (BE) defined by

$$D(q) = (-1)^q[2\ \mathrm{BE}(q) - \mathrm{BE}(q+1) + \mathrm{BE}(q-1)], \tag{1}$$

for isotopes ($q = N$ with Z held fixed) or isotones ($q = Z$ with N held fixed). The example of $D(N)$ for the calcium isotopes is shown in figure 3, revealing peaks at various (sub)shell closures. The corresponding shell-model orbitals are indicated at the bottom of figure 3. The row of '?' beyond $N = 36$ indicates one of the regions of nuclei to be explored by FRIB. One will learn how pairing depends on the neutron excess, whether or not ^{60}Ca is a doubly-magic nucleus, and to what extent the nuclear landscape extends beyond ^{60}Ca.

Likewise, the changes in nuclear charge radii contain important experimental signatures of shell structure. As an example, the charge radii of the calcium isotopes are shown in figure 3, displaying several important features. In particular, there is an obvious odd–even oscillation which has been variously attributed to pairing effects [208] and to quadrupole deformation [207, 209]. In addition, there are changes in the slope of the charge radii at $N = 20$ and $N = 28$ that are associated with the change in the nominally filled neutron valence orbitals in the sequence $0d_{3/2}$, $0f_{7/2}$ and $1p_{3/2}$. These slope changes in the evolution of charge radii, which appear in all isotopes at the magic numbers, provide a challenging test for nuclear structure

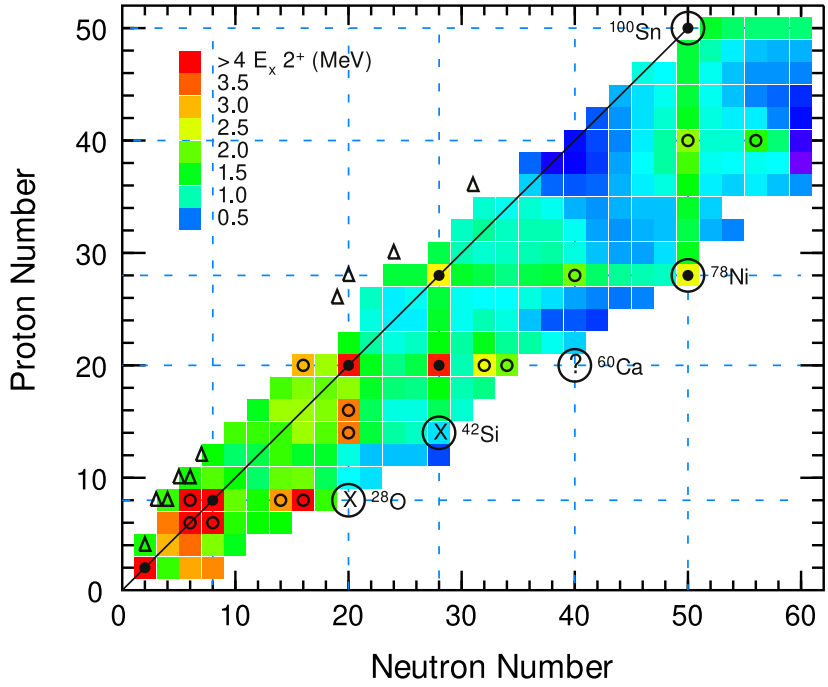

Figure 2. Even-even isotopes in the lower region of the nuclear chart. The colors indicate the energy of the first 2^+ state. The filled black circles show the doubly-magic nuclei associated with the magic numbers 8, 20, 28 and 50. The small open circles show the doubly-magic nuclei associated with the *j*-filled numbers 14, 16, 32, 34 and 40. The large open circles indicate the nuclei near the driplines that are the focus of this section. Two open circles with crosses indicate that these nuclei are observed to be in islands of inversion. The open circle with '?' for ^{60}Ca indicates that its properties are not yet known. The triangles are those nuclei observed to decay by two-proton emission. Adapted from [207]. Reproduced from [195]. CC BY 4.0.

models. Experimental data for the charge and matter radii for the heavier calcium isotopes will provide information on the neutron skin with its linkage to the nuclear equation of state.

On the theory side, shell evolution can be visualized by calculating ESPE as a function of N or Z. Neutron ESPE around $N = 20$ and $N = 40$ as a function of proton number are shown in figure 4. Representative CI results are obtained with the FSU [210, 211] and jj44a [212] Hamiltonians for $N = 20$, 40, respectively. These are compared with the results from a representative energy-density functional using the Skx interaction [213]. The difference in the $N = 20$ gap predicted by FSU and Skx can be traced partly to the strong tensor component of the FSU interaction, which has the effect of repelling the $0d_{3/2}$ and $0f_{7/2}$ ESPE [193]. Moving from ^{34}Si to ^{28}O, the $1p_{3/2}$ ESPE bends over and moves into the continuum (the vertical line), which generally tends to reduce the energy of low-ℓ orbits. The combination of tensor and continuum effects reduce the $N = 20$ gap for nuclei from about 6 MeV in ^{34}Si to about 3 MeV in ^{28}O, resulting in the island of inversion below ^{34}Si. A similar story plays out at $N = 40$, shown on the right panel of figure 4, but there are interesting differences related to the different ℓ values involved. Comparing $0g_{9/2}$ with $0f_{7/2}$, the smaller gap at $N = Z = 40$ relative to $N = Z = 20$ results in a deformed ^{80}Zr ground state compared to a spherical ^{40}Ca ground state (^{40}Ca has low-lying deformed excited states). The $0g_{9/2} - 1d_{5/2}$ ESPE gap is

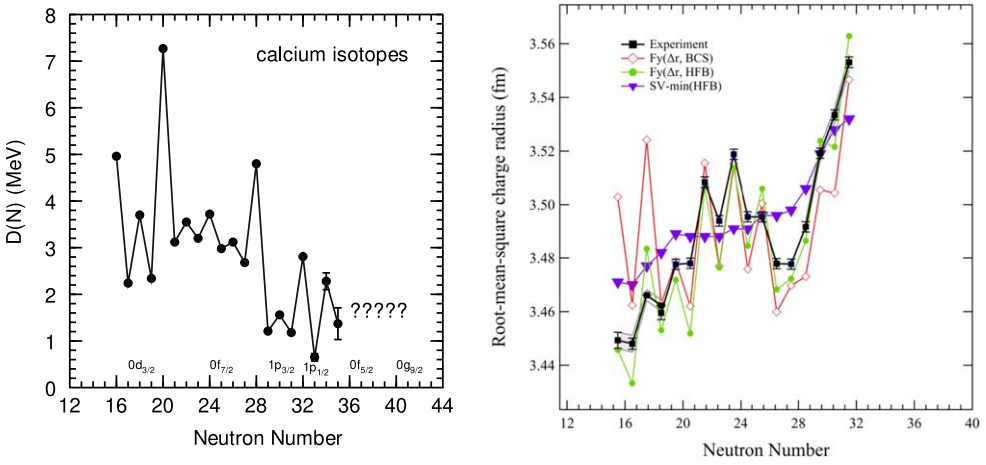

Figure 3. Left: experimental $D(N)$ for $Z = 20$ given by equation (1). The black dots with error bars are the experimental data. The orbitals that are being filled are shown (adapted from [207]). Adapted from [132], with permission from Springer Nature. Right: experimental rms charge radii for the calcium isotopes, compared to theoretical calculations [132]. Reprinted (figure) with permission from [207], Copyright (2022) by the American Physical Society.

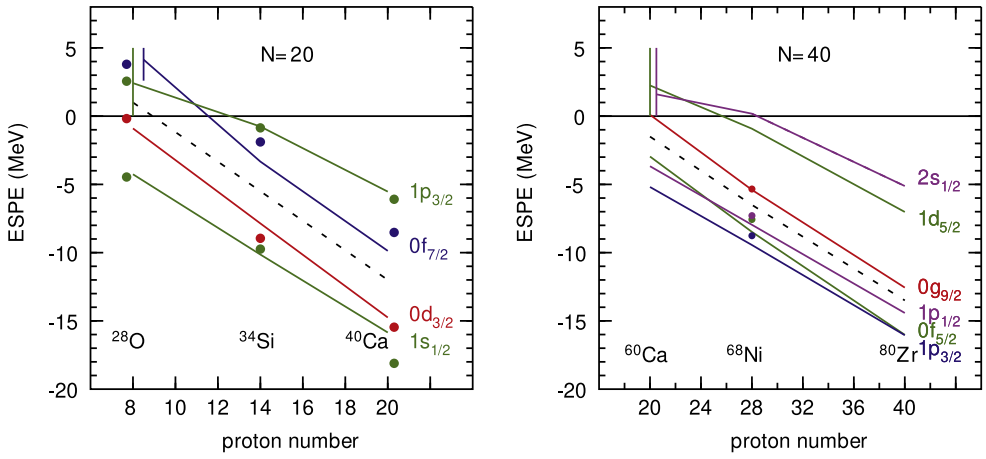

Figure 4. Left: $N = 20$ neutron effective single-particle energies as a function of proton number, computed with the Skx functional [213] (solid lines) and the FSU shell-model interaction [210, 211] (filled circles). The neutron orbitals below the dashed line are filled. The vertical lines at $N = 8$ indicate orbitals in the continuum. Right: same, but for $N = 40$, using Skx (lines) and the jj44a Hamiltonian [212] (circles).

larger than that for $0f_{7/2} - 1p_{3/2}$, which is why ^{100}Sn is a better doubly-closed-shell nucleus than ^{56}Ni. Despite this relatively large gap, CI calculations need to explicitly include the $1d_{5/2}$ in the model space to obtain the large proton–neutron deformation energy in the region of ^{80}Zr and in the $N = 40$ island of inversion below ^{68}Ni. Continuing toward ^{60}Ca, the low-ℓ $2s_{1/2}$ and $1d_{5/2}$ orbits enter the continuum, closing the $N = 50$ gap. For ^{60}Ca, these Skyrme ESPE are very different from those obtained with the LNPS Hamiltonian [214] where the $0g_{9/2} - 1d_{5/2}$ gap is close to zero (see figure 1 in [214]).

The calculations shown in figure 4 do not explicitly contain continuum components, but the ESPE implicitly contain effects of the continuum because the interactions are fit to data. In the regions around ^{42}Si, ^{60}Ca, and ^{78}Ni, the experimental data required to constrain empirical Hamiltonians (or EDFs) is limited. This will be filled in by new FRIB experiments. Single-particle models of nucleons in a finite potential well can be used as a qualitative guide to energies and neutron decay widths, but ultimately, *Ab initio* Hamiltonians must be constructed in a basis that explicitly contains the continuum. section 5 of this whitepaper is devoted to the physics of the single-particle and many-body states in the continuum.

Experimentally, shell structure can also be illuminated by reactions probing the single-particle structure of nuclei. Such reactions include light-particle reactions such as (d, p), performed in inverse kinematics at FRIB, and knockout reactions at fragmentation-beam energies [215, 216]. The cross sections for these reactions can be used to infer spectroscopic factors and experimental ESPEs, though some challenges remain in the interpretation of these reactions (see section 6).

Below, we highlight several 'outpost' nuclei, indicated by circles in figure 2. These nuclei involve relatively simple configurations that can be connected with experiments and used to assess the theoretical models. Some specific questions of interest for each of these regions are also discussed.

4.1.1. The region around ^{28}O: neutron clustering. Due to the closed proton shell, the dominant correlations in the neutron-rich oxygen isotopes are among the neutrons. ^{28}O lies beyond the neutron dripline, and has recently been observed to decay by emission of four neutrons with a total energy of 0.46(5) MeV [217]. The phenomenological interpretation is that the the dominant configuration for the ^{28}O ground state has two neutrons excited from the *sd* to the *fp* shell, placing it in the $N = 20$ island of inversion.

The charge rms radii, $R_{\rm ch}$, for oxygen and fluorine isotopes have been calculated with *Ab initio* [218] and relativistic mean-field theory [219], among others. However, experimental data on the ground-state $R_{\rm ch}$ and electromagnetic moments for these isotopes are not yet available. Laser spectroscopy measurements for oxygen and fluorine isotopes are planned to be performed at the BECOLA facility at FRIB. The obtained data will be critical for an understanding of structure and continuum effects around ^{24}O and to benchmark theory in a continuum-imapcted region of nuclei most accessible to *Ab initio* type calculations.

4.1.2. The region around ^{42}Si: quadrupole plus continuum. The nucleus ^{42}Si lies in the chain of the *jj* magic nuclei ^{132}Sn and ^{78}Ni, but the ESPE gaps at $Z = 14$ and $N = 28$ are not large enough to provide magicity. As with the $N = 20$ island of inversion, both proton and neutron gaps are small, so quadrupole correlations become important. There are rapid shape changes in these nuclei [220]; CI calculations predict a positive 2^+ ^{42}Si quadrupole moment, indicative of a prolate shape [195], and a negative 2^+ quadrupole moment for ^{40}Mg.

Due to the lack of experimental information, the empirical Hamiltonians for the region of ^{42}Si are not well established. For the two most widely used Hamiltonians, SDPF-MU [221] and SDPF-U-Si [222], the predictions for excited states above the 2^+ in ^{42}Si are very different [223, 224]. In the region of ^{42}Si near the neutron dripline, the ESPE for the $1p_{3/2}$ and $1p_{1/2}$ orbitals will be influenced by the proximity to the continuum, which is also important for describing two-neutron halos around $N = 28$ [225].

The first published FRIB experiment established new β-decay lifetimes for the nuclei in the region around $N = 28$ toward the neutron dripline [3]. The results were in reasonable agreement with calculations [226] based on the SDPF-MU [221] Hamiltonian. These β decays involve first-forbidden β transitions to low-lying states and Gamow–Teller transitions

to excited states that cross the $Z = 20$ shell gap starting around 3 MeV in excitation (see figure 3 in [226]). The second FRIB experiment with the FDSi studied the detailed γ and neutron decay spectra of ^{45}Cl to establish the β branching to states up to 8 MeV in ^{45}Ar [5]. Compared to theoretical results with the SDPF-MU Hamiltonian, it was found that the $Z = 20$ shell gap needed to be reduced by about 1 MeV to describe the β-decay strength function. This type of interplay between experiment and theory will be important for future FRIB experiments and advances in the modeling of nuclei.

4.1.3. The region around ^{60}Ca: pairing in the continuum. Like ^{28}O, the nucleus ^{60}Ca has a nominally closed-shell proton configuration, and so the dominant collective mode should be pairing. One difference from ^{28}O is that, primarily due to the mean-field spin–orbit potential, the $N = 40$ gap is weaker to begin with and there is a higher density of states near the Fermi surface. This could lead to a strong interplay between collective pairing and continuum effects (see section 4.5 below).

The nucleus ^{60}Ca has been observed to be stable against neutron decay in its ground state [227], but the properties required to determine whether or not $N = 40$ is a magic number for ^{60}Ca are not yet known. In the region of ^{60}Ca, there are many theoretical extrapolations and predictions for the location of the neutron dripline [228–231] and the properties of excited states of nuclei in the region of ^{60}Ca [214, 232–238]. The ESPE gap between the $0f_{5/2}$ and $0g_{9/2}$ orbitals is the most important unknown quantity. Lenzi *et al* [214] have used the LNPS Hamiltonian to extrapolate the neutron ESPE from $Z = 28$ down to $Z = 20$. Their $0f_{5/2} - 0g_{9/2}$ ESPE gap for ^{60}Ca is close to zero (see figure 1 in [214]) with the implication that ^{60}Ca will not exhibit $N = 40$ doubly-magic features. The recent calculations of Li for the $N = 40$ and $N = 50$ islands of inversion [239] result in ^{60}Ca and ^{68}Ni having similar doubly-magic properties.

The excitation energy of 2^+ states in ^{56,58}Ca have recently been reported [238]. If ^{60}Ca had a closed shell for $N = 40$, one would expect the 2^+ states of ^{56,58}Ca, coming from the relatively isolated $(0f_{5/2})^n$ configurations, to have about the same excitation energy [237]. The measured energies [238] fall from 1456(12) keV in ^{56}Ca to 1115(34) keV in ^{58}Ca. It was concluded [238] that this was caused by a small $0f_{5/2} - 0g_{9/2}$ ESPE gap. The γ-ray transition for ^{58}Ca only has about four counts above the background in the spectrum (figure 1 in [238]) and the experimental evidence for this 2^+ state needs to be strengthened. ^{61,62,63}Ti are observed [240] to lie in the $N = 40$ island of inversion below ^{68}Ni. A $9/2^+$ isomeric state has been reported in ^{63}Ti [240]. One needs much more experimental spectroscopic information related to the $0f_{5/2}$, $0g_{9/2}$ and $1d_{5/2}$ orbitals for $N > 36$ near ^{60}Ca to develop a clearer picture of the structure in this region of rapid shell evolution.

4.1.4. The region around ^{78}Ni: A 5th island of inversion? The doubly-magic properties of ^{78}Ni have been established by the observation of the 2^+ state at 2.60 MeV [241]. Energy spacings of proton ESPE have been deduced from the γ-ray decays of low-lying states in ^{79}Cu [242]. Based on the excited-state energy systematics for $Z = 29$, one expects the ground state of ^{79}Cuto have $J^\pi = 5/2^-$ with an excited state of $J^\pi = 3/2^-$ at 0.66 MeV. This establishes the approximate spacing between the $0f_{5/2}$ and $1p_{3/2}$ proton ESPE. The second excited state observed at 1.51 MeV would then be expected to have $J^\pi = 1/2^-$ and be related to the ESPE for the $1p_{1/2}$ orbital. The information related to absolute ESPE for these states and other ESPE around ^{78}Ni require mass measurements for ^{77,78,79}Ni, ^{79}Cu and ^{77}Co. Below ^{78}Ni, CI calculations predict ^{76}Fe to be the start of a 5th island of inversion with the breaking of the $N = 50$ magic number below $Z = 28$ [204]. The structure physics involves configurations built on $2p$–$2h$ (and higher) neutron excitations across $N = 50$. This configuration is predicted

to start as an excited state band below 3 MeV ^{78}Ni, and then is lowered in energy to become deformed ground-state bands (with $\beta \approx 0.3$) in nuclei below ^{78}Ni. Measurements of the radii, electric quadrupole moment, and magnetic dipole moments of isotopes in the neighborhood of ^{78}Ni will provide important guidance to understand the structure of this region [243, 244]. The $N = 50$ gap depends upon the neutron single-particle energies for $0g_{7/2}$, $1d_{5/2}$ and $2s_{1/2}$ which are connected to energies of low-lying states in ^{79}Ni.

As discussed in section 8, the magic number $N = 82$ for isotopes below ^{132}Sn is responsible for the binding-energy discontinuity at $N = 82$ which leads to the *r*-process abundance peak for $A \approx 130$. How does the structure physics leading to the 5th island of inversion for $N = 50$ influence the models and predictions for the structure of nuclei below ^{132}Sn? The $2p$–$2h$ excitation across $N = 82$ will lead to deformed excited states (isomers) and influence the binding-energy trend across $N = 82$.

4.1.5. The region around ^{100}Sn: The end of the $N = Z$ line. At the top end of the $N = Z$ line, the exploration of nuclei around ^{100}Sn will provide many opportunities for connections between theory and experiment. Quantitative ESPE need to be established from masses and spectra of ^{99,100,101}Sn, ^{99}In and ^{101}Sb. The nucleus ^{100}Sn also provides a unique opportunity to study Gamow–Teller β decay. The observed transition probability B(GT) is about a factor of four smaller than the closed-shell prediction. Details of theoretical results compared to experiment for this decay are discussed in section 9 on Fundamental Symmetries. For other nuclei in this region, the large Q_β values enable the study of Gamow–Teller strength up to and beyond the proton separation energy with total-absorption spectroscopy (TAS), presenting an interesting challenge for nuclear theory. More details are presented in section 4.4.1. As described below in section 4.5, the region of the heaviest $N = Z$ nucleus will probe the evolution of isoscalar pairing approaching the continuum.

Below ^{100}Sn, the nucleus of ^{80}Zr [245] turns out to be substantially more bound and lighter than expected from systematic trends of nuclear masses, suggesting ^{80}Zr to have a deformed double shell closure. The isotopes ^{90,96}Zr are near spherical with a very rapid onset of strong deformation beyond ^{96}Zr within the isotopic chain [246, 247]. Measurement of the charge radii for the Zr isotopes, combined with theoretical models, will help clarify the rapidly changing structural evolution taking place in these isotopes. For the odd-mass Zr isotopes the nuclear spin, magnetic dipole, and electric quadrupole moments can also be determined from the hyperfine structure via laser spectroscopy. These nuclear moments will provide an excellent testing ground for nuclear models [248, 249].

4.2. Collectivity

4.2.1. Collective degrees of freedom and connections to microscopic theory. Collectivity gives rise to simple patterns in the spectra and decay modes reflecting the emergence of new degrees of freedom related to the coherent motion of many nucleons. FRIB experiments in conjunction with theory have the potential to offer new insight into a wide range of questions associated with collectivity, especially in nuclei with extreme proton–neutron imbalance. How do deformation, shape coexistence [250], clusterization [251], and pairing [251] influence nuclear structure and observables? What are the dominant collective excitation modes giving rise to the low-lying structure? How is the structure of halo states influenced by collective correlations? What are the relevant approximate symmetries arising in the many-body system, e.g. Sp(3, *R*) [252–255], SU(3) [256, 257], and SU(4) [258], and how do they help us to understand the relevant degrees of freedom?

Ab initio theory in combination with experiment can help to identify the relevant degrees of freedom for collective structures. This, in turn, can lead to a microscopically motivated simple picture that accurately describes collective structure. While descriptions of collective structure were traditionally the domain of phenomenological models, *Ab initio* approaches are placing nuclear structure theory on a predictive footing and give insight into how collective phenomena emerge. Signatures of collective phenomena, including deformation [253, 255], rotation [259–265] and clustering [49, 251, 266–274], emerge in *Ab initio* predictions. However, computational challenges limit the ability of *Ab initio* calculations to resolve certain aspects of collective correlations, notably the overall scale of quadrupole correlations. Furthermore, structure can be highly sensitive to details of the choice of internucleon interaction (section 2), while electromagnetic (and weak interaction) observables are also sensitive to in-medium effects arising from the fact that the nucleus does not consist of point particles [275, 276]. Therefore it is critical to have experimental validation to give us confidence in the collective picture emerging from *Ab initio* theory.

Traditional signatures of collective behavior [277] provide a first point of contact between theory and experiment. These include binding energies, 2^+ excitation energies, $E2$ transitions, and quadrupole moments. FRIB experiments can provide access to regions of the nuclear chart near, e.g. islands of inversion and near proton and neutron driplines, where new collective degrees of freedom appear in the low-lying spectrum. FRIB experiments can also provide measurements of relevant observables across larger swaths of the nuclear chart, thereby enabling a systematic study of the evolution of these observables along isotopic chains, to more rigorously test theoretical predictions. Notably, laser-spectroscopy experiments at BECOLA-FRIB will enable precision measurements of nuclear electromagnetic properties such as charge radii, nuclear quadrupole moments, and nuclear dipole magnetic moments [120]. Recent experimental developments, such as the resonance ionization spectroscopy experiment (RISE) at BECOLA, will enable these measurements across the nuclear chart. For light nuclei, e.g. in the *pf* shell, measurements can be achieved from the proton dripline to the neutron dripline. In such light nuclei, where radii do not simply follow the global empirical formula [132, 278], both the radius and quadrupole moment must be taken into consideration in determining the nuclear deformation.

However, these basic observables are not sufficient to test the more detailed picture arising in *Ab initio* calculations, e.g. rotational bands, proton–neutron triaxiality [279], shape coexistence [280], and halo structure. Further spectroscopic information on excited states and transitions is crucial. Even where *Ab initio* methods cannot presently resolve the overall scale of the binding energy or $E2$ strengths, correlations among calculated observables [281, 282] permit robust predictions of relative properties (e.g. excitation energies and $E2$ ratios) [283–285] to be tested against experiment. In particular, data on electromagnetic transitions are sparse in the light nuclei where many of the *Ab initio* approaches are most applicable. For $E2$ transition strengths, Coulex experiments are critical, as lifetimes are often dominated by $M1$ decay. These measurements will require reaccelerated beams. Because of the importance of proton–neutron asymmetry in exotic light nuclei, neutron quadrupole matrix elements provide an important probe of the collective structure complementary to the electromagnetic measurements. Ratios of neutron and proton matrix elements (M_n/M_p) [286] can be obtained by combining Coulomb excitation with inelastic scattering experiments [287]. Recent developments in precision laser spectroscopy experiments with radioactive molecules [288, 289] have the potential to enable access to yet-to-be-explored electroweak nuclear properties across isotopic chains [290]. These experiments promise to yield information on the weak charge distribution within the nucleus from which information of the quadrupole

distribution of the neutrons could be extracted [290]. FRIB, in combination with the ongoing isotope harvesting program [108], will provide various opportunities for these studies.

4.2.2. Octupole excitations. Electric octupole, $E3$, excitations are observed throughout the nuclear chart [291]. However, significantly enhanced $B(E3)$ strengths are only expected in regions of the nuclear chart where the Fermi surface lies between spherical single-particle levels differing by $\Delta j = \Delta l = 3$, i.e. at proton and neutron numbers of approximately 34, 56, 88, and 136 [292, 293]. Possibly only a handful out of these nuclei with enhanced $B(E3)$ strengths are statically octupole deformed in their ground states [294]. A sudden increase of the $B(E3; 3^- \rightarrow 0_1^+)$ strength to 30 W.u. and more was recently discussed around the $A = 72$ prolate-oblate shape transitional point [295], i.e. on the neutron-deficient side of the nuclear chart where $Z \approx N \approx 34$. A clear theoretical interpretation of the $B(E3)$ strength increase is missing. Systematic studies of such effects in the corresponding neutron-rich isotopes are also missing so far. Experimentally, many of the nuclei in the $A = 68$ mass region and $A = 90$ mass region, where ^{96}Zr [296] is located, would already be accessible at FRIB with 20 kW beam power. Their octupole collectivity could be determined using, e.g. inelastic proton scattering in inverse kinematics with fast beams. Theoretically, octupole deformation has often been studied at the mean-field level [297–299]. From a shell-model perspective, one needs to understand the interplay between the *sd* shell, *fp* shell and the *sdg* orbitals in generating enhanced $B(E3)$ strengths in the $A = 68$ and $A = 90$ mass regions.

4.2.3. Pygmy dipole resonance. Properties of the giant dipole resonance (GDR) excited by isovector ($\Delta T = 1$) probes for excited states with $J^\pi = 1^-$ are well established for stable nuclei and are understood as the collective out-of-phase oscillation of all protons against all neutrons. In the shell model, these are coherent mixtures of $1\hbar\omega$ $1p$–$1h$ states with collective energies pushed up above $1\hbar\omega$. In neutron-rich nuclei, the smaller isoscalar and isovector dipole strength observed below the GDR is called the pygmy dipole resonance (PDR). It has traditionally been interpreted as a collective oscillation of the neutron skin against the core, though this interpretation has been questioned [300]. Understanding the PDR in terms of $1p$–$1h$ and collective contributions remains a theoretical challenge [300–304].

The isovector part of the PDR can influence neutron-capture rates when calculated with statistical HF approaches [154, 305–307]. To provide more robust predictions for γ-ray strength functions of rare isotopes involved in nucleosynthesis processes [308–311], continued experimental and theoretical studies of the structure of the PDR are essential. Early FRIB experiments will be able to indirectly measure the γ-ray strength function and access its possible influence on (n, γ) reactions by using experimental approaches such as the β-Oslo method [153, 154] or $(d, p\gamma)$ surrogate reactions [312]. (d, p) one-neutron transfer reactions have already been used to explore the neutron $1p$–$1h$ structure of the PDR in more detail for ^{208}Pb [313], ^{120}Sn [314], and ^{62}Ni [315]. At FRIB, these types of experiments can be carried out in inverse kinematics at ReA using, for example, SOLARIS [186, 316]. Beyond-mean-field approaches are needed to understand such data and the structure of the PDR [300, 317, 318]. The science case for direct studies of the complete electric dipole strength of rare isotopes with the energy upgrade of FRIB, FRIB400, has been presented [84].

4.3. Isospin symmetry

Isospin is an approximate symmetry of the nuclear force which can be traced back to the light masses of the up and down quarks as compared to typical QCD scales [319, 320]. Isospin is also broken by the electromagnetic interaction. Naively, because the Coulomb force is

understood and significantly weaker than the strong nuclear force, isospin-breaking corrections should be trivial to calculate. However, the interplay of correlations with Coulomb and other isospin-breaking forces leads to non-trivial effects in nuclei which remain a challenge for theory. In particular, it is difficult to unambiguously disentangle the effects due to isospin-breaking strong interactions from those due to Coulomb combined with isospin-conserving strong interactions. Beyond its intrinsic interest, a proper understanding of how isospin-breaking forces manifest in nuclei is an important component of the theoretical corrections for superallowed β decays, described in section 9.1.

Powerful probes of isospin breaking effects in nuclei are the masses within an isobaric multiplet, labeled by isospin T. In the limit of isospin symmetry, the $2T + 1$ constituents of the multiplet would have identical masses (or equivalently, identical binding energies). Isospin-breaking interactions lead to a shift of these masses, given in first-order perturbation theory by the isobaric multiplet mass equation (IMME): $BE(T_z) = a + bT_z + cT_z^2$, where $T_z = (N - Z)/2$, and a, b, c are parameters unconstrained by isospin symmetry. Higher-order terms like dT_z^3 and eT_z^4 can arise from second-order effects or many-body forces. Experimental results for these coefficients have been compiled [321]. CI calculations of these terms can be linked to the underlying Coulomb and isospin-dependent interactions [322–325], while, so far, *Ab initio* calculations have had difficulties predicting the IMME coefficients [326]. Charge radii of the $T = \pm T_z$ members of the multiplet that can be measured at FRIB provide a further constraint to help disentangle the contributions of the various sources of isospin symmetry breaking (see also section 9.1).

In addition to the IMME, valuable information on isospin-symmetry breaking in nuclei can be obtained from the study of excitation energy differences of analog states in mirror nuclei (Mirror energy differences), MED(J, T) = BE(J, T, $T_z = +T$) − BE(J, T, $T_z = -T$), and isobaric triplets (Triplet Energy Differences), TED(J, T) = 2BE(J, T, $T_z = 0$) − BE(J, T, $T_z = +T$) − BE(J, T, $T_z = -T$), as well as from the measurement of transition probabilities between analog states in these nuclei. From the theoretical side, approaches based on the interacting shell model have been shown to reproduce the MED and TED with good accuracy, provided an isospin-breaking term is added to the effective isospin-conserving nuclear interaction once Coulomb effects have been taken into account [327, 328]. While a single correction term seems to hold for the MEDs measured so far, its origin has not yet been fully understood. Tests are needed very far from stability. Large MEDs have been obtained between isobaric states of non-natural parity due to the different energy gaps for protons and neutrons caused mainly by the electromagnetic spin–orbit interaction [329, 330]. Moreover, the development of accurate effective interactions that involve more than one major shell are needed to describe non-natural-parity MEDs.

On the experimental side, these studies become quite demanding for the most proton-rich members of isobaric multiplets because of their low production cross sections toward the proton dripline and challenges in beam purity. Using proton-rich rare-isotope beams from FRIB, these studies can be extended to the proton dripline. The high-resolution, high-efficiency GRETA γ-ray spectrometer will enable extending the MED and TED studies and probe the validity of our understanding of isospin symmetry breaking at largest values of isospin.

The investigation of MEDs has also put into evidence the role of the continuum (see also section 5); specifically, the role of the larger radius of low-l orbits with respect to the other orbits in a major shell [331, 332] in the evolution of the MED as a function of the spin or excitation energy. More recently, MED studies in the *sd* shell indicate that, when fractionally occupied, the radius of the $s_{1/2}$ orbital is about 1.7 fm larger than the d orbitals. This difference suddenly decreases, to about 0.6 fm, when occupied by at least one nucleon [333]. A

similar behavior is observed between the *p* and the *f* orbitals in the *fp* shell [334, 335]. The measurement of the charge radii and isotope shifts in different regions of the nuclear chart, and in particular in the proton-rich side, together with an extension of MEDs into the upper *pf* shell, will be essential to understand this phenomenon.

4.4. Spin-isospin response

For a given initial state one can study final states reached by processes associated with one-body operators characterized by their orbital ΔL, spin ΔS, and isospin ΔT tensor structure, that have $\Delta T_z = -1,\ 0,\ +1$. There are experiments at FRIB focused on charge-exchange processes $\Delta T_z = -1,\ +1$ associated with β decay and charge-exchange reactions. Simple examples are Fermi β decay with $(\Delta L,\ \Delta S,\ \Delta T) = (0,\ 0,\ 1)$, and Gamow–Teller transitions with $(\Delta L,\ \Delta S,\ \Delta T = (0,\ 1,\ 1)$ induced by β decay and charge-exchange reactions such as $(t,\ ^3\mathrm{He})$ $(E_{\mathrm{beam}} \gtrsim 100\,\mathrm{MeV}/u)$. Experimental methods and instrumentation used for these is discussed in section 3. The purpose is to study properties of individual low-lying final states, and to assess strength functions over a large excitation-energy range of final states [145, 148, 150]. Experiments at FRIB will study the β decay of very neutron-rich nuclei, and charge exchange on targets away from stability via inverse kinematics.

Exploration of the spin-isospin response of nuclei offers a unique view at the single-particle degree of freedom as well as bulk properties of the nuclear medium. Characterizations of the allowed Gamow–Teller spin-isospin response of nuclei uniquely probe the validity of nuclear structure models up to high excitation energy. In hydrodynamical models of the nucleus, isovector giant resonances are interpreted as density oscillations of the neutron versus the proton fluid and continue to provide information on macroscopic nuclear properties associated with isovector fields.

4.4.1. Beta decay. FRIB beams will provide an unprecedented opportunity to access very neutron-rich nuclei with large β-decay energy windows. Possible at the lowest beam rates, one can obtain essential information on the half-lives and the decay properties of very neutron-rich nuclei that can be used to probe theoretical models at the extremes. The spin and parity selection rules inherent to β decay enable a characterization of the structure of low-lying states in the decay daughter, often complementing the structure information obtained from in-beam γ-ray spectroscopy. The studies of β decay near neutron-rich magic nuclei, such as ^{54}Ca, ^{60}Ca, ^{78}Ni, and ^{132}Sn [336], are particularly important in this regard to benchmark the dominant configurations of the respective model spaces defined by the magic nuclei.

When the β Q value is larger than the neutron separation energy of the daughter nucleus, neutron unbound states will be populated. Calculations for the γ-particle decay competition for these states requires configurations in the continuum [337]. The neutron emission hindrance has been linked to the mismatch of the wavefunctions between the precursor and decay daughter [338]. The other aspect of β-delayed neutron spectroscopy is that it enables selective studies of neutron unbound states and provides information about the location and widths of nuclear resonances in nuclei far from stability. This kind of effort is expected to mainly focus on low-Z nuclei where the expected widths of tens of keV [339] are measurable with current experimental techniques. Here the goal is to connect data and theoretical models, including continuum coupling effects [337], which will reveal themselves through modifications of widths and excitation energies. Neutron-rich nuclei can have multi-neutron emission [340]. Interesting questions as to the simultaneous or sequential character of β-delayed multi-neutron emission remained unanswered in the first attempt of a correlation measurement [341] and pose an interesting challenge for experiment and theory in the future.

When combined with neutron detection and total absorption methods, the detailed spectroscopy of β decays will provide access to a broad spectrum of excited states in very proton–neutron asymmetric systems. The same experimental methods employed in deformed regions will help establish how the strength distribution evolves with deformation in very neutron-rich systems [342]. New-generation experiments with polarized β-delayed emitters can produce spin-resolved strength distributions. The decay studies performed on island-of-inversion nuclei will provide another set of constraints for nuclear models that set out to describe such quantities at the intersection of statistical and discrete descriptions of nuclear physics. Non-statistical aspects of neutron emitting states are discussed in section 6.3.

Neutron emission probabilities and β decay half-lives are important for modeling the *r*-process path (see section 8.2). For applications to nuclear astrophysics, experiments will only provide some information on a limited number of nuclei. All other information needed relies on calculations provided by nuclear theory. Beta decay for lighter nuclei mainly involves Gamow–Teller type transitions. But for heavier nuclei, one must include first-forbidden type transitions. One must assese the renormalization (quenching) needed for these operators in neutron-rich nuclei either [276] empirically or with the explicit addition of two-body currents. The latter was also found to be essential for improving the predictions of nuclear magnetic moments [343].

Theoretical calculations provide detailed information on the β strength distributions to final states from which neutron-decay probabilities can be obtained. Experimental data related to these final-state distributions and neutron decay modes will be obtained with total-energy γ absorption spectrometers such as the summing NaI detector (SUN) and the modular total absorption spectrometer (MTAS) that is part of the FDSi section 3.5.

One of the early FDSi experiments at FRIB reported a rapid increase in the β-decay strength distribution above the neutron separation energy in ^{45}Ar in the decay of ^{45}Cl, interpreted to be caused by the transitioning of neutrons into protons excited across the $Z = 20$ shell gap [5]. This demonstrates the potential of integrated quantities such as strength functions to probe the proton single particle degree in neutron-rich nuclei. Advancing decay spectroscopy in general, the full FDS is aspired by the community (see section [175]).

4.4.2. Charge-exchange reactions. Charge-exchange reactions at intermediate beam energies ($E_{\mathrm{beam}} \gtrsim 100\,\mathrm{MeV}/u$) provide excellent ways to probe the isovector response of nuclei [143–150]. Charge-exchange reactions can be used to extract weak-interaction strengths that cannot be obtained from β decay. Even though the charge-exchange reaction is mediated via the strong nuclear force, it can be used to extract information about allowed weak transitions associated with the transfer of zero angular momentum ($\Delta L = 0$), with the transfer of spin ($\Delta S = 1$, Gamow–Teller type) or without the transfer of spin ($\Delta S = 0$, Fermi type) (see the experimental methods in section 3)

Charge-exchange reactions provide a unique experimental method to obtain Gamow–Teller strengths in the β^+/EC direction in neutron-rich nuclei. From a structure viewpoint this part of the Gamow–Teller strength is blocked by the filled orbitals in the neutron excess. Thus, any strength observed provides a test for theoretical models of correlations among the neutrons. These theoretical models provide EC rates needed for astrophysical applications (see section 8).

There is significant interest to study isovector giant resonances, which, in a macroscopic picture, are out-of-phase density oscillations of the neutron and proton matter inside the nucleus. The characteristics of these isovector giant resonances provide information about bulk properties of nuclei and the nuclear equation of state that is complementary to that obtained from isoscalar resonances [344] and helpful for extrapolating to systems with small

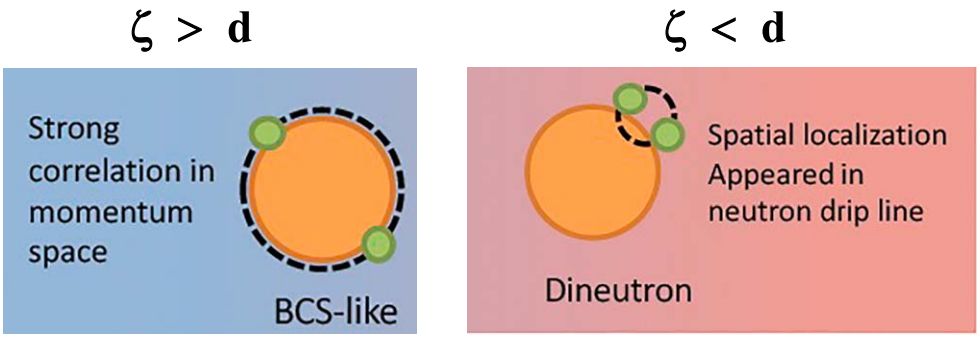

Figure 5. Schematic illustration of the expected change in behavior between Cooper pairs and di-neutrons is indicated. Reprinted (figure) with permission from [354], Copyright (2006) by the American Physical Society.

or large neutron-to-proton ratios [167, 345]. Microscopically, isovector giant resonances are described as collective one-particle-one-hole ($1p$–$1h$) excitations in combination with the transfer of isospin. A systematic study of the excitation energies and collectivity of isovector giant resonances can be directly compared to *Ab initio* [162, 165], configuration-interaction [145, 149, 346], and density-functional [148, 150, 347] models to shed light on remaining ambiguities in the isovector part of the nucleon–nucleon effective interactions [347, 348].

4.5. Pairing effects

In 1958, Bohr, Mottelson and Pines [349] suggested a pairing mechanism in the atomic nucleus analogous to that observed in superconductors [350]. Since the publication of that seminal paper, a wealth of experimental data have been accumulated, supporting the important role played by neutron–neutron and proton-proton 'Cooper pairs' in modifying many nuclear properties such as deformation, moments of inertia, alignments, etc [351–353]. Driven by advances in experimental techniques, the development of sensitive and highly efficient instruments and the availability of rare-isotope beams, the pairing correlations can now be studied in exotic nuclei out to and beyond the neutron dripline. Of particular interest is the role of neutron–neutron pairing in neutron-rich isotopes, where the effects of weak binding and continuum coupling are important. Illustrative results for nuclear matter [354] show that the correlation length, ζ, of an *nn* pair and their separation distance, d, depend on the nuclear matter density. At normal density $\zeta > d$, typical of Cooper pairs. At lower densities that could be relevant in the surface of weakly bound nuclei, $\zeta < d$, and a localization of di-neutrons appears, signaling a possible Bardeen–Cooper–Schrieffer (BCS) pairing to Bose–Einstein condensation (BEC) crossover transition as schematically shown in figure 5.

An indicator for weak binding effects could be considered from the following general arguments. The neutron separation energy is given by $S_n \approx \lambda + \Delta$, with λ the Fermi level and Δ the pairing gap. Near the valley of stability, the quasi-particle binding is dominated by the mean field and $S_n \approx \lambda$. As we increase the number of neutrons, approaching the drip line, $\lambda \rightarrow 0$ and $S_n \approx \Delta$, i.e. correlations dominate. Thus, it is natural to expect that the transition between the two regimes will start to take place when $S_n \approx \Delta$.

Two-neutron transfer reactions have provided a unique tool to understand neutron pairing correlations in nuclei [355–357]. In formal analogy with the case of quadrupole shape fluctuations [357, 358], where an important measure of collective effects is provided by the reduced transition probabilities (i.e. $B(E2)$'s), one can associate a similar role to the transition

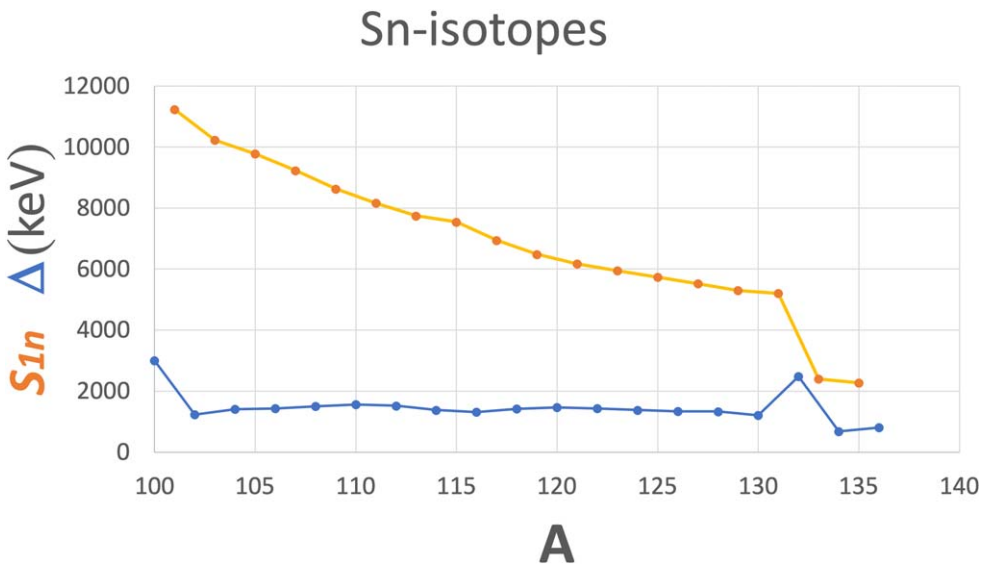

Figure 6. Comparison of one neutron separation energy, S_{1n} and pairing gap, Δ, for the tin isotopic chain.

operators $\langle f|a^{\dagger}a^{\dagger}|i\rangle$ and $\langle f|aa|i\rangle$ in the two-particle transfer mechanism between the initial $|i\rangle$ and final $|f\rangle$ states.

The criteria discussed above can also be related to the asymptotic behavior of the Cooper pairs $\rightarrow e^{-Kr}$. For strongly bound nuclei, $K \approx 2\kappa = 2\sqrt{2mS_{1n}}/\hbar$, the tail of the particle density. For weakly bound nuclei, $K < 2\kappa$ and the pair condensate extends further outside the surface. While a reaction such as (^{18}O,^{16}O) might be of interest, it seems clear that (t, p) reactions will continue to play a crucial role to study pairing correlations in neutron rich nuclei since they are particularly suited to directly probe the $2n$ pair density.

The Sn isotopes are the classic example of superfluidity in atomic nuclei and their ground states are well described as a BCS neutron condensate. Following from the criteria introduced earlier, in figure 6 the S_{1n} and Δ are compared across the isotopic chain, showing an indication that just above the $N = 82$ shell closure weak binding effects may start to influence the low-lying pairing properties of ^{134}Sn and heavier isotopes.

In fact, theoretical calculations based on Skyrme–Hartree–Fock mean field and continuum RPA predict a significant increase in the neutron pair-transfer strength to low-lying excited 0^+ pairing vibrational states. For very neutron-rich Sn nuclei with $A > 140$, a large increase in the pairing gap is expected, which results in an increased ground state to ground state pair-transfer strength [359, 360]. This behavior is attributed to the loosely bound $2p_{1/2}$ and $2p_{3/2}$ orbitals, extending far beyond the nuclear surface. Currently, it is not possible to study Sn nuclei with $A > 140$, but the region where strong transitions to pairing vibrational states are predicted, just above ^{132}Sn, will be within reach at FRIB once it reaches full power and even more so with the envisioned 400 MeV/u energy upgrade. Having this in mind, it is worth considering some other cases that would be of much interest to study. An inspection of the condition $S_{1n} \approx \Delta$ suggests that weak-binding effects might start to show beyond ^{56}Ca and ^{78}Ni.

Crucial theoretical input for these studies will be systematic state-of-the art calculations of two-neutron transfer strength for a given isotopic chain including the effects of weak binding

and continuum coupling. These will guide the experimental program by suggesting the best cases to study and provide input to the reaction codes needed to calculate the reaction cross sections measured in the experiment.

The odd–even staggering in BE(Z, N) is linked to the pairing interactions in nuclei. Theoretically, the pairing is determined directly from the neutron–neutron $J = 0$, $T = 1$ interaction within the valence space, and indirectly from the proton–neutron interaction between neutrons in the valence space and protons in the core. Thus, BE for neutron-rich nuclei will provide new insight into the role of these two mechanisms.

A very interesting region in the Segrè chart is the one around the $N = Z$ line. Here, protons and neutrons occupy the same single-particle orbitals and, therefore, their interaction is maximized. These nuclei open the possibility of studying different fundamental properties of the nuclear interaction as for example, the proton–neutron pairing, that presents two different isospin channels, isoscalar $T = 0$ and isovector $T = 1$. While the latter is present also in the proton-proton and neutron–neutron well-known isovector pairing interaction, the former is exclusive of the proton–neutron interaction and the $T = 0$ pairing should manifest mainly in $N = Z$ nuclei [361, 362].

The BE of nuclei around $Z = N$ can be used to deduce $T = 0$ proton–neutron pairing energies, often denoted as V_{np}. The V_{np} extracted for nuclei up to ^{74}Rb have placed an essential constraint on microscopic models, and have led to the construction of models with SU(4) symmetry [363]. High-precision mass measurement for nuclei above ^{78}Rb will provide the information needed to address the question of how V_{np} evolves [363, 364] from the strongly deformed ^{80}Zr [245] nucleus to the doubly-magic ^{100}Sn nucleus.

5. Continuum physics

Continuum physics is the study of how the structure of quantum systems and the nearby presence of the continuum of scattering states and decay channels affect each other. Systems in which continuum couplings are important are called open quantum systems. In low-energy nuclear physics, continuum physics naturally lies at the intersection between structure and reaction theory, which are historically concerned with how nucleons self-organize into bound states (section 4), and how nuclei interact over time in scattering processes (section 6), respectively. Continuum physics is thus important to understand properties of nuclei that: (i) are excited near or beyond a given particle emission threshold, or (ii) have a large N/Z imbalance and lie near or beyond the edges of nuclear stability.

The phenomenology of continuum physics is broad and encompasses halo and universal s-wave physics (sections 5.3, 5.4), decay and notably exotic decay modes (section 5.2), continuum-mediated phenomena such as superradiance (section 5.1), as well as complex physics involving an interplay between continuum couplings and standard emergent phenomena such as pairing, deformation, or clustering (section 5.3). Some of the most pressing open problems in the description of nuclei as open quantum systems are, for instance, understanding the origin of near-threshold clustering, developing accurate and scalable theoretical methods to describe many-body resonances and broad resonances, and unifying nuclear structure and reactions in an approach where all decay channels are open. Progress on any of these problems will help move forward nuclear astrophysics (section 8) and better constrain nuclear forces in new extreme conditions.

In the coming decades, FRIB will dramatically push forward the exploration of the drip lines and lead to the discovery of thousands of new isotopes. Continuum physics will thus be critical for the success of the FRIB mission. Below, we first provide a more detailed account

of near-threshold physics, and then selected cases of recent developments and studies that illustrate the status of the field.

5.1. Near-threshold physics

The study of exotic nuclei provides an unparalleled opportunity to explore the physics of open quantum many-body systems [199]. Quantum systems near thresholds exhibit a rich array of features, reflecting the coupling between discrete and continuum spaces. In particular, halo phenomena and the associated threshold discontinuities have been recognized for a long time [365–371], but only recently have their direct manifestations been observed in experiments. Single-particle states with low Coulomb and centrifugal barriers are particularly affected by the continuum threshold resulting, for instance, in discontinuities in various observables reflecting structural modifications of states such as spectroscopic factors [39, 372, 373], and in a modification of single-particle energies [374–376]. The theoretical treatment of threshold phenomena is difficult. Even for bound systems typical basis expansion techniques become impractical near thresholds, and alternative methods for including continuum couplings must be considered [50, 367, 377, 378].

Above the threshold, for states embedded in the continuum, additional coupling via the continuum emerges. Interactions between overlapping resonances leads to collectivization and distribution of decay widths [373]. The phenomenon of superradiance [379] in which overlapping resonances naturally segregate into, on the one hand superradiant states strongly coupled to the continuum and, on the other hand, trapped or decoupled resonances, is an interesting phenomenon to investigate in future experiments. The complete understanding of resonances and their widths will require understanding the time dependence of formation and decay, background and non-resonant components. Aspects of non-Breit–Wigner spectral functions and non-exponential decay are explored in [380].

The well-known near-threshold alpha clustering phenomenon [381] is another excellent arena for exploring the effects of continuum couplings. Numerous broad alpha resonances have been experimentally observed, and there are indications of the isospin symmetry being broken due to superradiant alignment [382]. The conservation of probability and the associated unitarity of the scattering matrix [372, 379] are responsible for non-resonant near-threshold features such as threshold cusps [371]. An examination of the experimental and theoretical implications and perspectives on clustering effects in exotic nuclei near threshold energies, resulting from a recent FRIB Topical Program on ‘Few-Body Clusters in Exotic Nuclei and Their Role in FRIB Experiments’, provides additional clues on how to study these effects [383]

A remarkable example showing the full complexity of the near-threshold physics is the case of β-delayed proton decay of ^{11}Be [384]. The excessive decay rate observed for the beta-delayed proton decay in ^{11}Be [385] prompted speculations on the nature of the decay including exotic processes beyond the standard model [386, 387]. The $1/2^+$ ground state of ^{11}Be nucleus is by itself a remarkable example of a one-neutron s-wave halo state bound by only 0.5 MeV just below the expected p-wave state. The sequential decay process occurs via a proton resonance in ^{11}B [388, 389] conveniently located near the threshold and thus strongly enhancing proton decay instead of alpha decay, despite the latter channel being nearly 3.0 MeV above the $\alpha + {}^7$Li threshold [386, 390, 391]. The proximity of the proton resonance to the neutron decay threshold is also noteworthy. Near-threshold resonances strongly coupled to their corresponding channels are expected to play an important role in astrophysical processes.

Theoretical advancements in time-dependent techniques [392, 393] have opened up new possibilities for studying unstable nuclei and exploring open quantum systems more broadly. The dynamics of decay provides valuable insights on the interplay between internal dynamics and decay processes, and more specifically on the formation of the decaying state, exponential decay, and post-exponential processes driven by non-resonant components. In decays involving a three-body final state, where energy, momentum, and angular momentum conservation laws are insufficient to fully constrain the dynamics, correlations between observables may offer experimental methods for tracking the evolution of the wave function. See, for instance, [380].

5.2. Two-nucleon emission

Due to the presence of the Coulomb barrier having a confining effect on the proton density, the one- and two-proton ($2p$) drip lines lie relatively close to the valley of β-stability. As a result, relatively long-lived, proton-unstable nuclei can exist beyond the drip line [394, 395]. The vast territory of proton-unstable nuclides contains rich and unique information on nuclear structure and dynamics in the presence of the low-lying proton continuum.

The phenomenon of ground state $2p$ radioactivity has generated much excitement as the experimental data on lifetimes and correlations between emitted protons provide us with unique structural information. Direct $2p$ decays have been found in a handful of even-Z isotopes, in which single-proton decay is energetically blocked. Currently, $2p$ radioactivity has been detected in: ^{19}Mg, ^{45}Fe, ^{48}Ni, ^{54}Zn, and ^{67}Kr. In addition, several broad resonances associated with prompt 2p decay were reported in, e.g. ^{6}Be [396] and ^{11,12}O [397–400].

In [401], the position of the two-proton drip line has been determined with the help of a Bayesian model averaging technique by using several global mass models. The most promising new candidates for the two-proton radioactivity searches at FRIB, with the predicted lifetimes between 10^{-7} and 10^{-1} s turned out to be: ^{30}Ar, ^{34}Ca, ^{39}Ti, ^{42}Cr, ^{58}Ge, ^{62}Se, ^{66}Kr, ^{70}Sr, ^{74}Zr, ^{78}Mo, ^{82}Ru, ^{86}Pd, ^{90}Cd, and ^{103}Te. In some heavy nuclei, such as ^{103}Te and ^{145}Hf, a competition between alpha and two-proton decay is expected.

For decaying proton pairs, long-range final-state Coulomb interaction is essential. Consequently, to study the mechanism of 2p decay, theoretical models must fully control the behavior of the decaying system at large distances and long propagation times. Recently, a realistic time-dependent framework has been developed [393] providing precise solutions with correct three-body asymptotics. This study demonstrated that the energy and angular correlations in the Jacobi-Y angle between emitted nucleons strongly depend on the initial-state structure. Hence, the inter-nucleon correlations provide invaluable information on the dinucleon structure in the initial state. An illustrative example of time-dependent calculations of two-nucleon decay is shown on figure 7 for the exotic isotopes of oxygen. Such results indicate that the anticipated high resolution data from FRIB on energy and angular nucleon–nucleon correlations will provide unique insights into the structure of proton and neutron pairs in rare isotopes.

5.3. Experiments near the neutron dripline between N = 20 and N = 28

The nuclear region suitable for early investigation at FRIB includes neutron-rich nuclei spanning across the neutron magic numbers $N = 20$ and $N = 28$, see figure 8. In this region, the dominance of low-angular momentum components in the ground-state wave functions is becoming apparent [375, 403]. One can investigate the interplay among the evolution of the single-particle structure, deformation, effects due to weak binding and continuum, which may

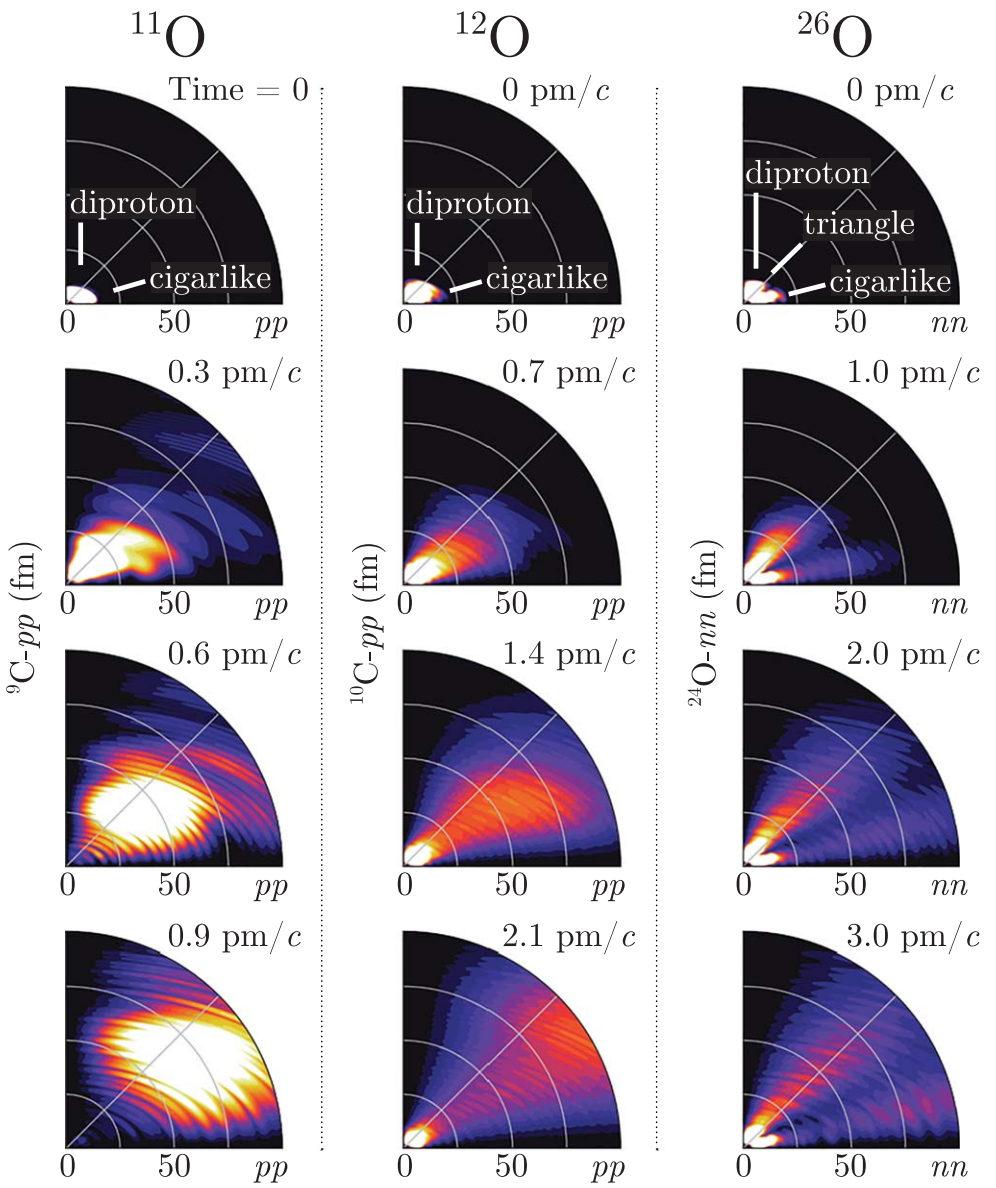

Figure 7. The density distributions of two-nucleon decays from the ground states of ^{11,12}O (2p emitters) and ^{26}O ($2n$ emitter) isotopes for four different time slices. From [402]. Reproduced from [402]. © IOP Publishing Ltd. All rights reserved.

lead to unexpected emergent phenomena. The interpretation of data will rely on collaborations with theory (discussed in the next section) that takes into account such rich aspects.

The interplay between emergent phenomena and near-threshold physics presents new interesting ways to study nuclear structure. Halo states, characterized by weak binding and a spatially extended wave function of valence nucleons, are illustrative. Experimental signatures for the halo formation in light dripline nuclei have been obtained from studies of the ground-state properties through measurements on masses, charge and matter radii, and

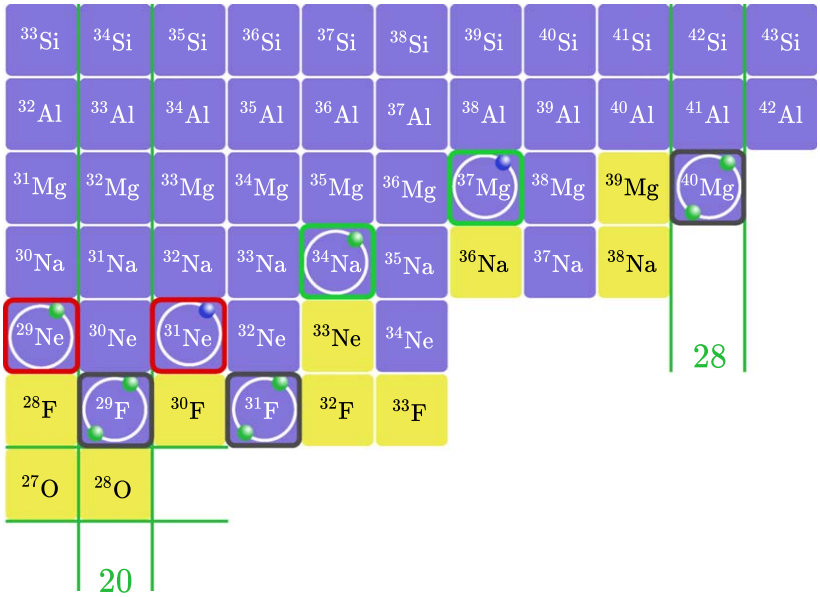

Figure 8. Subset of the chart of nuclides ranging from the neutron-rich O ($Z = 8$) to the Si ($Z = 14$) isotopes. The red, gray, and green squares denote known *p*-wave neutron halo ground-state systems, anticipated ground-state halo nuclei, and single-neutron *p*-wave halo ground-state systems that will be the focus of early FRIB experimental work, respectively. The yellow squares indicate particle-unbound systems.

spectroscopic information. However, effects of weak binding on their excitation properties remain largely unexplored [404]. Therefore, important open questions remain with respect to the existence of various soft or decoupled excitation modes [405], the role of core excitations and deformation in halo formation and its properties, and the influence of the spatially extended wave functions on collective modes such as rotations and vibrations. A detailed understanding of nuclear structure properties of halo nuclei or near-threshold states in general is also important to predict new halo candidates in heavier mass regions at and beyond $N = 50$ where mechanisms for the halo formation are expected to be diverse [84, 403, 406].

In general, the formation of halos is favored in weakly-bound states with typical neutron separation energies $S_n < 1$ MeV and a low centrifugal barrier ($\ell = 0, 1$). Therefore, the location of the neutron orbitals $0f_{7/2}$ and $1p_{3/2}$ in the $N = 20$–28 region is critical. The near degeneracy of these orbitals leads to deformation driven via the Elliott–Jahn–Teller effect, which tends to lower the *p*-wave over the *f*-wave states. Halo aspects have been experimentally observed in (^{29}F [407], ^{29}Ne [408], ^{31}Ne [409], ^{37}Mg [410]) and more are predicted by theory: ^{34}Na as a one-neutron halo, ^{31}F and ^{40}Mg as two-neutron halos. An overview of observed and predicted *p*-wave halo nuclei in the region of interest is presented in figure 8.

These nuclei will be explored at FRIB with a variety of experimental techniques. β decay properties are among first to be studied as in the FRIB Day-One experiment of Crawford *et al* [3]. One- and two-proton removal are used to populate more neutron-rich nuclei. For bound states, one can carry out excited-state lifetime measurements [411] aimed at transition strengths and collective modes. Invariant-mass spectroscopy based on neutron decay followed by the detection of γ-ray decays provides binding and excited-state energies for unbound

systems. Inelastic scattering on targets such as the (d, d') or (p, p') provides selectivity in the population and characterization of collective states.

For Coulomb breakup reactions, the amplitude and shape of the $\mathrm{d}B(E1)/\mathrm{d}E_{\mathrm{rel}}$ distribution is sensitive to the state configuration (spectroscopic factors, ℓ value), the neutron separation energy, and perhaps deformation. The expected integrated cross sections and $B(E1)$ strength are exceptionally large in halo nuclei as a result of the dominance of the electric dipole strength at low excitation energies (soft $E1$ excitation). An increase in the $\mathrm{d}B(E1)/\mathrm{d}E_{\mathrm{rel}}$ distribution at small E_{rel} values will be indicative of a halo character related to p-wave contributions. See [412, 413].

One particular region of interest is the F ($Z = 9$) isotopic chain where a two-neutron halo structure has recently been suggested in ^{29}F [407]. FRIB experiments out to ^{33}F will provide key pieces of new empirical information pertaining to the competition between continuum effects, deformation, and coherent correlations, and other central or many-body effects, on ground and excited states [414–416]. Of particular interest is the role played by the occupancy of the $\nu 1p_{3/2}$ orbital.

The ground state of ^{40}Mg presents an intriguing case where an interplay between weak binding and collectivity might explain the curious low-lying structure observed. The first spectroscopy studies of ^{40}Mg [417, 418], carried out at RIKEN/RIBF, revealed some intriguing differences between the observed γ-ray spectrum and those of the neighboring ^{36,38}Mg isotopes. The transition energies deviate from the smooth trend seen in lighter isotopes and cannot be reproduced by state-of-the-art shell-model calculations that have been very successful in this region. Thus, one might be tempted to speculate that this could be due to the effects of weak binding. In fact, ^{40}Mg lies close to the neutron dripline and is a potential candidate for a halo nucleus with two neutrons occupying the $p_{3/2}$ orbital [419–421], Of particular interest are the effects of the continuum on nuclear rotational motion, that have been studied in [414, 422] in the framework of the particle-plus-core problem using a non-adiabatic coupled-channel formalism. The subtle interplay between deformation, shell structure, and continuum coupling can result in a variety of excitations in an unbound nucleus just outside the neutron dripline, as predicted for the low-energy structure of ^{39}Mg.

In a recent work [404], the coupling of a two-neutron halo to a core was studied in a phenomenological approach. From the known properties of ^{38,40}Mg, possible particle-core coupling schemes and their impact on the low-lying excitation spectrum were presented. It is natural to expect that effects of weak binding on excited states will show when the energy scales of the two degrees of freedom become comparable:

$$E_{\mathrm{core}}(2^+) \approx E_{2n}(2^+). \tag{2}$$

The picture that emerges is one where the low-lying 2^+ excitations in ^{40}Mg result from a strong competition of the core and the $2n$ subsystems. While this scenario seems appealing, it is clear that further experimental and theoretical works will be required to fully elucidate the structure of ^{40}Mg.

It will be important to push the early FRIB β decay experiments in this mass region [3] out to ^{40}Mg and beyond. Beta decay of halo nuclei has recently been reviewed in [423]. The large available Q_β value means that a large fraction of the decays will proceed via delayed one- and two-neutron emissions. How is the final state distribution affected by the two-neutron halo structure?

5.4. Ab initio calculations in light nuclei and FRIB physics

The *Ab initio* framework plays an important role in the FRIB scientific mission by providing a feedback between models of nuclear forces and observations. However, while the reach of *Ab initio* calculations has increased dramatically in the past few decades [27], there remains many challenges to provide reliable predictions in the medium-mass region and beyond, notably due to uncertain constraints in some sectors of nuclear forces [378]. Light nuclei ($A \leqslant 16$) offer interesting opportunities to test our understanding of nuclear forces within the *Ab initio* framework, not only because systematic quasi-exact calculations appear computationally feasible, but also due to the presence of near-threshold phenomena and their interplays with emergent features such as clustering or deformation, on which nuclear forces have seldomly been tested.

Many light nuclei have been studied that are particle unbound in their ground state, and all of them have unbound excited states. Neutron-halo states, where the last few neutrons have a large ground-state spatial extension can be found in ^{6,8}He, ^{8}B, ^{11}Li, and ^{11}Be. Bound states are characterized by their spin-parity J^{π} and energy position E, unbound states can manifest themselves as decaying resonances defined by their width Γ, inversely related to their lifetime $\tau = \hbar/\Gamma$. There are also $\ell = 0$ antibound states or virtual resonances affecting the low-energy scattering cross section.

The description of these inherently time-dependent states starting from high-precision nuclear forces thus requires a unified approach to nuclear structure and reactions. Extending *Ab initio* methods to weakly bound and unbound systems thus presents a considerable challenge. Some of the state-of-the-art works in this region include for instance the Faddeev–Yakubovsky calculations with the uniform complex-scaling method [424], the NCSM and its extensions (NCSM-RGM and NCSMC) based on the resonating group method [49, 50, 425, 426], and the Gamow density matrix renormalization group (G-DMRG) method [427, 428] and the no-core Gamow shell model (NCGSM) [39, 428, 429] based on the Berggren basis [430, 431].

Providing stronger constraints on nuclear forces using near-threshold phenomena will hopefully improve *Ab initio* predictions in regions of interest for FRIB, and perhaps offer valuable insight into the the many-body dynamic of near-threshold states and their interplays with emergent features, which in turn will help better understand the formation of the drip lines [43, 228], notably around islands of inversion.

As an illustrative example, the NCSMC approach has been applied to investigate near threshold resonances in several systems. The ^{3}H(d, n)^{4}He and ^{3}He(d, p)^{4}He reactions are leading processes in the primordial formation of the very light elements (mass number, $A \leqslant 7$), affecting the predictions of Big Bang Nuleosynthesis (BBN) for light nucleus abundances [432]. With its low activation energy and high yield, ^{3}H(d, n)^{4}He is also the easiest reaction to achieve on Earth, and is pursued by research facilities directed toward developing fusion power by either magnetic (e.g. ITER) or inertial (e.g. NIF) confinement. At low energies, the fusion reaction rate in ^{3}H(d, n)^{4}He is significantly enhanced by the $3/2^{+}$ resonance appearing just about 50 keV above the DT threshold; compared to 210 keV for the mirror resonance in the ^{3}He(d, p)^{4}He reaction. Using a chiral NN+3N interaction, the NCSMC calculations [51, 433] were able to reproduce the $3/2^{+}$ resonance in the ^{3}H(d, n)^{4}He channel quite well, revealing its s-wave nature. The outgoing d-wave $n - {}^{4}$He channel is characterized by a strongly varying diagonal phase shift that does not reach 90°. The NCSMC calculations were also able to predict the enhancement of the fusion cross section when the reacting nuclei are polarized [51]. It should be noted that this resonance is responsible for the

production of 99% of ^{4}He in BBN with the remaining 1% of primordial ^{4}He coming from the ^{3}He(d, p)^{4}He reaction [434, 435].

The NCSMC was also used to investigate resonances in ^{7}Li and ^{7}Be [436, 437]. In [437], a subthreshold s-wave $1/2^+$ resonance just above the threshold of ^{6}He+p was reported. For technical reasons, the calculations had been performed by considering the $^3\mathrm{H} + {}^4\mathrm{He}$, ^{6}Li+$n$, and ^{6}He+$p$ mass partitions separately without taking into account their coupling. Apparently the same s-wave $1/2^+$ subthreshold resonance was observed in the ^{6}Li+n mass partition just below the $^6\mathrm{Li}(J^\pi = 0^+, T = 1)+n$ threshold. In a separate ongoing investigation, a broader $1/2^+$ resonance seem to play a role in the $^3\mathrm{H} + {}^4\mathrm{He}$ scattering at $\sim$7 MeV. An experimental search for the predicted $1/2^+$ resonance above the ^{6}He+p has been performed without success [438] although an isospin anti-analog $(3/2^-, 1/2)$ resonance just above the $(3/2^-, 3/2)$ state also predicted in [437] was found. It is likely that the discussed $1/2^+$ resonance exist between the ^{6}Li+n and ^{6}He+p thresholds in ^{7}Li and a more realistic prediction of its position and width requires proper coupling of all the mass partitions. Calculations in this direction are under way.

Recently the NCSMC capability was extended to calculate Fermi and Gamow–Teller β-decays with the final state bound or in the continuum [391]. Motivated by the TRIUMF experiment [388], calculations were performed for the ^{11}Be β-decay with the proton emission. Focusing on the $1/2^+$ final states, a resonances in ^{11}B have been identified with a substantial Gamow–Teller strength. By applying a phenomenological adjustment (dubbed NCSMC-pheno) of the *Ab initio* calculation, the resonance was shifted to the position observed in the experiment [388]. The NCSMC-pheno predicted width of the resonance matched closely the experimentally found width [391]. The calculated Gamow–Teller branching ratio was about an order of magnitude smaller than that reported in the TRIUMF experiment, although still two orders of magnitude higher than non-resonant value [384]. It should be noted that the chiral NN+3N interaction used in [391] reproduced the parity inversion in the ^{11}Be ground state as well as in the isospin-analog $(1/2^\pm, 3/2)$ resonances in ^{11}B.

The parity inversion in ^{11}Be and its extended halo ground state was investigated within NCSMC in [378]. It was found that only a chiral Hamiltonian with a non-local 3N interaction reproduces the inversion. We note that a non-local chiral 3N interaction was utilized in [391]. A near-threshold enhancement of the $E1$ strength in the photo-dissociation of ^{11}Be was investigated in [378] with obtained strength in agreement with experiment. The calculations confirm the non-resonant nature of this enhancement. The ground-state asymptotic normalization coefficient (ANC) predicted in these calculations have been later confirmed in phenomenological calculations investigating the breakup of ^{11}Be and ^{10}Be(d, p)^{11}Be transfer reaction [439, 440].

In a related unpublished study, the s-wave halo $1/2^+$ ground state and the d-wave extended excited $5/2^+$ state of ^{15}C have been investigated utilizing the NCSMC with the ^{14}C+n continuum channels. The calculated ANCs, $C_{1/2^+} = 1.282\ \mathrm{fm}^{-1/2}$ and $C_{5/2^+} = 0.048\ \mathrm{fm}^{-1/2}$, have been later validated in the experimental data analysis in [441].

6. Reaction mechanisms

Describing the dynamics of interacting many-body systems produced at radioactive beam facilities provides unique challenges and broad opportunities. Integrating structure and reaction theory into a unified framework forms the basis for microscopic descriptions of interacting nuclei and provides critical links to observables. FRIB experiments will play an important role in testing current reaction theories on nuclei that have so far been out of reach.

This will highlight areas in need of improvement and increase the reliability of the nuclear reaction inputs used in applications. Accurate reaction calculations are needed for applications: reaction cross sections are important ingredients for multi-physics simulations used in the areas of astrophysics, national security, medicine, and nuclear energy. In addition, a robust understanding of reaction mechanisms aids in planning and interpreting the experiments that are used to probe structure aspects of nuclei.

A significant challenge for nuclear reaction theories is the integration of reliable structure information in the calculations. To quantitatively describe and predict nuclear reaction outcomes, both the structure information and the reaction mechanisms included in the theory have to be accurate. In the past decade, efforts have focused on treating structure and reactions on the same footing in *Ab initio* approaches, which have primarily been applied to light nuclei, and to integrate more advanced structure descriptions into both direct and statistical reaction theories, which are used for medium-mass and heavy nuclei. FRIB experiments will have the opportunity to provide data for chains of isotopes, to study the impact of the evolution of shell structure and collectivity on reaction observables, and to probe changes in the relative importance of the reaction mechanisms as one moves away from stability to nuclei with lower level densities and less binding.

6.1. Ab initio approaches to reactions

An important goal of nuclear theory is to predict both static and dynamic properties of nuclei in a consistent framework. Remarkable progress has been made in recent years in the development of many-body approaches from first principles to scattering and nuclear reactions (see [40, 49, 82] for reviews). Truly microscopic approaches take into account nucleon degrees of freedom along with their correlations within and between the reaction fragments. Coupled with realistic inter-nucleon interactions, these approaches provide *Ab initio* predictions of reaction observables, including phase shifts and reaction and scattering cross sections.

For light nuclei, the combination of the NCSM with the RGM, currently applicable for reactions with both nucleons and light composite projectiles, treats nuclear structure and reactions on equal footing and has successfully predicted scattering, transfer, and capture reactions [49–51, 442].

The use of symmetry-adapted (SA) bases, within the SA-NCSM [255, 443], provides a viable path to extend the NCSM/RGM approach to describe reactions with medium-mass nuclei [53, 54]. The SA-NCSM can accommodate larger model spaces and reach heavier nuclei than traditional NCSM methods, including ^{20}Ne [255], ^{21}Mg [444], ^{22}Mg [445], ^{28}Mg [446], ^{32}Ne and ^{48}Ti [447]. These larger model spaces make it possible to predict collective observables, such as $E2$ transition strengths and quadrupole moments, without effective charges, as well as α-decay partial widths and ANCs [271, 445, 448]. Measurements of these quantities serve as stringent tests of the predictive power of these *Ab initio* approaches, which aim at describing both structural nuclear properties and reaction outcomes, and help identify potential weaknesses in the theory.

RGM-based methods will provide theoretical support for planned and upcoming FRIB experiments for neutron-rich isotopes, especially for understanding deformation and the role of intruder states in the proximity of the drip line (e.g. for He, C, Ne, Mg, and Ca isotopes). Comparisons between predictions and FRIB data will also be critical for understanding the impact of these phenomena on reaction outcomes. Collective correlations have been shown to play a key role in measurements of nuclei across the nuclear chart, and experiments are now starting to explore such properties for exotic nuclei, see, e.g. [449–451]. Charged-particle inelastic scattering is particularly sensitive to collective effects and can—with some additional

development—be performed in inverse kinematics. FRIB scattering measurements will not only shed light on the evolution of collectivity away from stability; they will also test to what extent our present theoretical approaches capture the relevant correlations [53, 54, 383, 452].

Nuclear lattice simulations provide a very different, but complementary, approach to computing *Ab initio* nuclear structure and reactions using chiral effective field theory [453]. Recent progress has allowed calculations to be performed using high-fidelity chiral interactions to produce accurate predictions for the properties of light and medium-mass nuclei [454] and measure A-body correlations between nucleons to probe intrinsic shapes, deformation, and clustering [272, 455]. Efforts are now in progress to develop efficient algorithms to compute the energies and decay widths of nuclear resonances. Of particular interest are the properties of neutron-rich nuclei. This includes both excited states of bound nuclei as well as unbound nuclei past the dripline such as ^{28}O [217] that decay into multi-neutron channels. There is much interest in understanding continuum scattering features for such multi-neutron systems [456–458].

In addition, two other methods are being explored to extract nuclear scattering, reactions, and response functions from spatially localized wave functions: (1) eigenenergies of the nuclear systems in external traps [55–57], or (2) continuum states at complex energies [58, 59]. Because these methods use localized wave functions, they could potentially take advantage of the recent progress of *Ab initio* structure methods in computing continuum state observables in the nuclear chart wherever the structure methods are feasible, thus expanding the applicability of *Ab initio* continuum calculations. In addition, for both methods, fast emulations for the input parameters are being developed, which will enable uncertainty quantification of the continuum predictions and allow for more meaningful comparisons with experiments. The anticipated FRIB detections of new drip-line nuclei, either shallow bound or resonant states, and their binding energy and/or width measurements, can provide valuable benchmarks for these methods and the nucleon interaction theories on which these methods are based. These continuum methods can then provide inputs for other physics areas, such as capture reaction cross-sections for nuclear astrophysics and neutrino-nucleus scattering cross-sections for neutrino oscillation measurements.

6.2. Direct reactions: transfers, inelastic scattering, breakup, and knockout

Direct reactions change few degrees of freedom in the reaction partners and serve as excellent probes of nuclear structure. Of interest are both individual single-particle and collective degrees of freedom. Particle transfer reactions are useful for determining the former, and inelastic scattering is used to probe the latter. Scattering experiments can also be used to study resonant states in light exotic nuclei. Both transfer reactions and inelastic scattering have been used extensively to study properties of stable nuclei—and both reaction types can be used to explore exotic nuclei in inverse-kinematics experiments. In confronting experimental observables, theory needs to improve the underlying structure description that is assumed in the reaction model, e.g. moving from simplistic collective or single-particle models to more sophisticated structure models. It also needs to account for reaction mechanisms that have been studied, but that are not regularly included when describing experimental observables, e.g. including two-step reactions, couplings to excited states in deformed nuclei, breakup contributions, etc. This will be relevant not only to better extract the structure properties of exotic nuclei from FRIB reaction experiments; it will also shed light on the reaction mechanisms at work.

An important goal of nuclear theory is to obtain accurate descriptions of the nuclear reaction dynamics, while taking into account the underlying nuclear structure. While *Ab initio*

descriptions of direct nuclear reactions have seen great advances for light systems, a broader application across the nuclear chart, for a wide range of beam energies, is presently not feasible. However, in many cases the complicated many-body problem can be reduced to a few-body problem. For elastic and inelastic scattering, single and multichannel optical potentials are typically used to solve an effective two-body Schrödinger equation. For single-particle transfer reactions, one considers an effective three-body problem whose exact solution can be obtained using Faddeev methods [459]. The approach can be generalized to two-particle transfer processes leading to a four-body scattering problem that is described within the Faddeev–AGS equations in momentum space [460] and Faddeev–Yakubovsky equations in coordinate space [461]. The numerical cost associated with the exact few-body methods has led to various approximate techniques that have validity within specific kinematic conditions. Commonly utilized techniques include the DWBA, the adiabatic distorted-wave approximation ADWA, the CDCC, and variants thereof [40, 60, 68–70, 76–78].

Complementing these developments are efforts to use structure information from microscopic theories in reaction calculations. One-body overlap functions from the Green's function Monte Carlo and variational Monte Carlo methods are used in descriptions of transfer and knockout reactions [61, 62] and transition densities from the (quasiparticle) random phase approximation enter calculations of inelastic scattering and reaction cross sections [63–65, 462].

To better understand the interplay of nuclear structure effects and reaction mechanisms, multiple types of reaction data are needed. Elastic and inelastic scattering, in particular angular distributions, provide stringent checks of the optical model and structure models used. Inelastic scattering data can be used to study the effect of couplings between ground and excited states, as well as re-arrangement effects (due to density differences between the ground and excited states) on the scattering observables [65]. Experimental efforts that study a chain of isotopes, or at least multiple nuclei with large isospin differences, will be particularly valuable, as they can shed light on the evolution of nuclear properties with neutron excess and/or as a function of deformation. Exclusive and inclusive cross sections are needed to better understand the relative importance of elastic and inelastic breakup mechanisms, as well as complete and incomplete fusion in transfer reactions [66, 383, 463–472].

A combination of elastic scattering and breakup measurements can potentially provide information on the structure of one-neutron halo nuclei. This is true if the prediction of the recoil excitation and breakup (REB) model holds, which finds that the elastic scattering pattern of one-neutron halo nuclei from a heavier target is very similar to the angular pattern obtained when the halo nucleus breaks up into its core and halo neutron [473]. Within the REB model, the ratio of the angular distributions for elastic scattering and breakup is only a function of the projectile nuclear wave function and can thus provide sensitive information on the halo structure of the projectile. This ratio method has been studied theoretically for both one-neutron and one-proton halo nuclei [474–476]. Given the potential impact of this approach, it is important to experimentally test the predictions of the underlying reaction model. In particular, it would be valuable to confirm that this new reaction observable is independent of the reaction process and to establish under which experimental conditions this independence holds.

The status of the theoretical treatment of nucleon knockout reactions, heavy-ion as well as proton-induced, was reviewed recently in great detail [477]. The broad conclusions are that (i) no consistency is achieved yet between different ways of modeling (p, $2p$) and (p, pn) reactions and that (ii) the reduction factor dependence as function of the asymmetry ΔS at the Fermi surface reported for Be- and C-induced knockout reactions has not been found to manifest itself in the handful of quasi-free knockout and transfer reactions at the extremes of

ΔS published so far [477, 478]. The asymmetry $\Delta = |S_n - S_p|$ for proton removal and $\Delta = -|S_n - S_p|$ for neutron removal and is defined in terms of proton (S_n) and neutron (S_p) separation energies, For Be- and C-induced knockout, novel approaches are being developed to explore inclusion of processes that hinder core survival when a minority nucleon is removed and the majority nucleon separation energy is low [67, 470]. First valuable attempts to quantify the uncertainty in knockout reactions evaluate a single aspect, such as optical model potentials that carry their own sizable uncertainty [479], but do not yet interrogate, as a whole, something akin to the consistent formalism used over decades to analyze knockout data [480, 481]. For example, as shown in [481], the geometry of the bound-state potential is crucial and aspects such as the optical model potentials should not be viewed in isolation. In general, the use of direct reactions for the extraction of absolute spectroscopic factors[27] remains difficult due to uncertainties in reactions models which, at present, are not on the same footing with the nuclear structure calculations that provided needed input—this is not different for knockout reactions and remains a challenge and opportunity for nuclear theory that could advance the field tremendously. Quasi-free knockout of the (p, $2p$) or (p, pn) type becomes only competitive at FRIB after the energy upgrade to FRIB400 [84] so that the nucleons in the exit channel have at least 200 MeV of energy. This energy regime for the exit-channel proton or neutron inside the nucleus starts to minimize distortions encountered in the energy-dependent nucleon–nucleon (NN) cross sections that are typically input to models used to describe quasi-free knockout reactions [84, 477].

6.3. Statistical descriptions of compound-nuclear reactions

Nuclear astrophysics and other applications require cross sections for compound-nuclear reactions, in particular for neutron-induced reactions [482–484]. Application needs drive many measurements and nuclear reaction data evaluations [485, 486], which culminate in evaluated data being broadly made available in databases at the NNDC, IAEA, and other data centers around the globe. To a large extent, the reaction evaluations rely on reaction descriptions that contain phenomenological components and thus require nuclear data for parameter adjustments. For reactions on isotopes that have not been measured, or for unknown reaction channels, the calculations often have to rely on regional, or even global, systematics. Experiments that can provide constraints on the models used have potentially very high impact, not only because a specific reaction involving a particular nucleus will be better known, but also because the measurements can affect the regional systematics developed and the results can be propagated through simulations relevant to an application. Moreover, experiments that probe the limits of validity of the reaction descriptions can provide impetus and guidance for developing the next generation of reaction theories.

Compound-nuclear reactions are traditionally treated in a phenomenological R-matrix approach (for isolated resonances) or statistical HF theory (for overlapping resonances) [60, 79–81, 487, 488]. Practical HF calculations require optical-model potentials and nuclear-structure information in form of level densities and gamma-ray strength functions, plus fission barriers where decay by fission has to be considered. Spins and parities of low-lying nuclear levels, and their decay branchings, are needed as well.

Optical-model potentials, which are crucial for both direct and statistical nuclear reaction calculations, have been the focus of recent research that seeks to ground the potentials in

[27] Spectroscopic factors, while not directly observable, provide a useful measure for how well a state calculated in a many-body framework (e.g. the shell model) or observed in a transfer or knockout reaction can be described as a simple single-particle or single-hole configuration relative to a (ground) state in the neighboring nucleus. For a more detailed discussion, the reader is referred to sections 2 and 3.4.1 of [477].

microscopic calculations, to extend our knowledge of these potentials to unstable targets, and to quantify associated uncertainties. Some aspects are discussed in the next subsection and a more in-depth review of recent optical-model developments is given in [82].

Phenomenological level density models and gamma-ray strength functions have become much more accurate in the last decade, and significant progress has been made in obtaining these quantities from microscopic approaches. Both shell model and DFT-based approaches have been employed to predict level densities [489–496]. While Hartree–Fock(–Boguliubov) methods, combined with a combinatorial approach, can be used across the isotopic chart, correlations due to many-particle many-hole configurations and/or rotational excitations, which do affect the level densities, have to be accounted for through (adjustable) correction factors [497]. Very recent work has laid out a path to go beyond the mean-field approximation by exploiting boson-expansion methods [498]. Approaches based on the shell model, on the other hand, are limited by the model space sizes and interactions that are available to shell-model calculations and therefore are typically restricted to light and medium-mass nuclei, or heavier nuclei near closed shells. The shell model Monte Carlo (SMMC) method addresses the challenge of the model space size by reformulating the shell model in the framework of auxiliary field Monte Carlo [499–501]. Where suitable interactions are available, SMMC can provide microscopic predictions of nuclear properties across a wide range of nuclear systems, extending from medium-sized to rare earth nuclei [502–504]. Shell-model approaches do include correlations beyond those contained in mean-field models, and innovative methods for efficiently calculating moments and smart model-space truncations [493–495, 505], coupled with high-performance computers, are pushing the existing boundaries.

Microscopic calculations of gamma-ray strength functions are challenging, as theory needs to cover a wide range of transition energies, several multipole-parity combinations ($E1$, $M1$, $E2$, etc), and contain the collective correlations that shape the strength functions. This is difficult for the shell model—again for reasons related to model-space size and availability of suitable interactions (in particular for cross-shell excitations). DFT-based methods, in particular the QRPA, have been used to calculate strength functions for a large number of nuclei [506–508]. Since these calculations construct the strength function from excitations built on the ground state, they cannot provide reliable predictions for the low-energy portion of the strength function. Work is underway to push the limits of the shell model [505] and to account for additional correlations in the DFT-based approaches [509–511]. Such theory extensions are expected to yield predictions of phenomena such as pygmy resonances, toroidal resonances, and the shape of the low-energy tail of the gamma-ray strength functions ('low-energy enhancement' [512]). Since these features cannot be directly observed in experiments, it is important to integrate the structure into (direct) reaction descriptions and plan experiments that are sensitive to the predictions. Shedding light on these features is not only interesting from a nuclear structure perspective, it is also important for developing more reliable statistical reaction calculations of neutron capture cross sections.

Experimental quantities, such the average spacings between s-wave and p-wave neutron resonances at the neutron separation energy (D_0 and D_1, respectively), and the average radiative width ($\langle\Gamma_\gamma\rangle$), are known to provide strong constraints for level density models and calculated gamma-ray strength functions, but these quantities are not available for unstable isotopes. Early work showed some promise in getting information on resonance properties from beta-delayed neutron emission [513, 514]. However, many questions remain. In particular, it is an open question whether beta-decay populates states in the daughter nucleus that damp into a compound nucleus (which then decays statistically via gamma or neutron emission) or produces states that decay via direct or semi-direct decay mechanisms

[515–520]. In the former case, one may infer constraints on level densities and strength functions from observing the beta-delayed neutron and/or gamma emission.

Similarly, if beta decay, with subsequent neutron emission, proceeds through the compound nucleus stage, one can decouple the nuclear structure effects from the neutron emission, which is a precondition for using HF codes to describe β–n processes [521]. Recently, however, evidence for non-statistical neutron emission was discovered, and the concept of doorway states was used to explain the data [519, 520]. Mounting evidence [522, 523] shows that the neutron emitting states in medium and heavy nuclei are very narrow. For all of these situations, a better microscopic description is needed for the description of β-delayed neutron emission. FRIB will provide ample access to β-delayed neutron emitters in different regions of the nuclear chart, offering up various bound and unbound single-particle configurations in various Q-value windows.

Multiple indirect methods have been introduced to obtain information on level densities and gamma-ray strength functions [154, 524–526]. One challenge for experiments aiming to obtain information on level densities and gamma-ray strength functions is that the observables reflect convolutions of these quantities. It is therefore important to explore multiple experimental approaches which can complement each other. One should also consider forward modeling of the reaction (using theory inputs where needed) and the experimental set-up, with uncertainty propagation, in order to identify how specific aspects of the level densities and gamma-ray strength functions are reflected in the observables of a planned measurement. For level densities, experiments that can shed light on the impact of deformation and shell closures, the role of correlations, and the dependence on neutron excess would be particularly valuable. Typical approximations for level density models, such as their dependence on spin and parity, need to be further investigated. For gamma-ray strength functions, one needs to better understand the microscopic origin of the observable features of the strength function including the behavior at low gamma energies, the role of deformation and collectivity, and the dependence of these properties on neutron excess.

The use of the HF statistical reaction description is only justified when the fusion of the projectile with the target nucleus produces a compound nucleus in an energy regime of strongly-overlapping resonances. For light (*sd*-shell and below) nuclei and nuclei near the dripline, characterized by low level densities, it is not a priori justified to use the HF description. Nuclear data evaluators routinely connect R-matrix descriptions at very low projectile energies with HF descriptions at higher energies, using experimental data as guide for the evaluations [527, 528]. No information is available to guide calculations for very neutron-rich nuclei near the dripline. In addition, at low level densities one expects contributions from direct and semi-direct reactions [529–535]. Experimental guidance and reaction theory developments are needed, e.g. for providing neutron capture rates for astrophysical simulations.

6.4. Surrogate reactions and reaction mechanisms

In the absence of theoretical predictions for the major ingredients to HF calculations (optical model potentials, level densities, gamma-ray strength functions), it is important to obtain constraints for cross section calculations. The surrogate reaction method provides such constraints for compound nucleus (CN) reactions through a combination of theory and experiment. The CN designation does not simply refer to a composite system made of two nuclei—it indicates that the reaction partners fuse and produce a system in statistical equilibrium. This system remembers the conserved energy, angular momentum, and parity, but otherwise forgets how it was produced. In the second stage of the reaction, the CN decays—

by a combination of fission, gamma emission, and particle evaporation. Many reactions of interest to nuclear astrophysics and societal application are CN reactions.

The surrogate reaction method uses a direct reaction—typically charged-particle scattering or a transfer reaction—to produce a CN (more precisely, it produces a doorway state that evolves into a CN). The subsequent decay of the nucleus is observed, and a quantity that is characteristic of the exit channel of interest (e.g. a fission fragment or a γ-ray characteristic of a reaction product) is measured in coincidence with the outgoing surrogate-reaction particle. By combining a theoretical description of the direct-reaction mechanism used to produce the CN with modeling the decay, and comparing with the coincidence measurement, one can extract constraints on the CN decay models. This then allows one to produce a data-constrained calculation of the desired CN reaction. The method has been reviewed in [524], a pedagogical introduction into the underlying ideas was given in [526], and more recent developments for (d, p) reactions have been discussed in [66].

Proof-of-principle applications to ^{90}Zr(n, γ), ^{95}Mo(n, γ), utilizing (p, d) and (d, p) reactions, and the determination of ^{87}Y(n, γ) for the unstable ^{87}Y isotope have demonstrated the application to neutron-capture reactions [312, 536]. Inelastic alpha particle scattering was utilized to simultaneously determine neutron-induced fission and radiative capture cross sections for ^{239}Pu [537]. More recent work has focused on obtaining (n, γ), (n, n'), and (n, $2n$) reactions from inelastic scattering with protons and light ions [538, 539] and on measurements in inverse-kinematics. Also considered are (n, p) reactions [540]. Fission reactions, which were the focus of the earliest surrogate reaction measurements, are being revisited [541, 542], including in inverse-kinematics experiments [543].

The theoretical description of the reaction that produces the doorway state is non-trivial, as the excitation energies of the system produced are in the range of a few MeV to 20–30 MeV, two-step reaction mechanisms have been found to contribute, and the role of width fluctuations needs to be considered in some cases [466, 536, 539, 544–546]. Modeling of the CN decay, to connect with the experimental observable, benefits from knowledge of the structure of the decaying nucleus. Finally, a better understanding of the evolution from a doorway state to a CN is desirable.

In addition to investigating the reaction mechanisms in more detail, it is important to expand, improve, and test the experimental techniques to be used with radioactive beams: Experimental conditions may make it more difficult to obtain and utilize the decay observables that have been used in the past, cover a more limited range of excitation energies in the compound nucleus, have different background challenges, and/or have lower count statistics. Validating the method by comparing the results from two different surrogate reaction mechanisms, e.g. (d, p) and inelastic scattering, against each other and against other approaches (indirect measurements or predictive theory) will be valuable. Theoretical and experimental work that sheds light on these aspects will not only enable the broader applicability of the surrogate reaction method; it will also provide new insights into the interplay of direct and compound reaction mechanisms.

6.5. Optical-model potentials for reaction calculations

Optical-model potentials (OMPs) describe the effective interaction between a target nucleus and a projectile. They are essential ingredients in analyses of direct reactions, such as elastic and inelastic scattering, transfers, breakup and knockout reactions, as well as for the description of compound nuclear reactions. The imaginary part of the OMP reproduces the loss of flux from the elastic scattering channel due to all other processes that are not explicitly accounted for in the calculation. The importance of such potentials and various techniques for

obtaining OMPs are discussed in a recent review [82]. The role of (dispersive) optical-model potentials for constraining the equation of state (EOS) and for providing input to transport model simulations are discussed in section 7.4.

Phenomenological nucleon–nucleus optical models that have been adjusted to reproduce a large collection of nuclear data, such as the Koning–Delaroche (KD) and Chapel–Hill (CH) OMPs, have been tremendously successful in reproducing not only the data they have been trained on, but also newer measurements [547, 548], especially if uncertainties are incorporated in the study [549]. The extensive collection of data on stable isotopes that was used for determining these models is unlikely to find a counterpart for unstable nuclei. Thus it becomes important to (a) pursue approaches that can utilize theoretical predictions of nuclei and nuclear matter, (b) identify experimental observables that constrain various components of the optical potentials needed, and (c) strive to collect additional data for OMP training and testing whenever it is feasible in FRIB experiments. Of particular interest are elastic scattering cross sections, charge-exchange reactions, and ratios of cross sections measured on different isotopes along an isotopic or isotonic chain. Bound-state properties can also be used to constrain and test dispersive optical models [82, 550].

Recent theoretical approaches have employed realistic inter-nucleon interactions, typically derived within chiral effective field theory, without the need to fit interaction parameters in the nuclear medium. These models have evolved from earlier theoretical frameworks, such as the one introduced by Feshbach, which led to the Green's function formulation [551–553] and the successful dispersive optical model, as well as the pioneering work by Watson [554, 555], leading to the spectator expansion of the multiple scattering theory [556]. Notably successful recent applications include *Ab initio* nucleon–nucleus potentials for elastic scattering of closed-shell nuclei at low projectile energies ($\leqslant$20 MeV per nucleon) based on the Green's function technique with the coupled-cluster method [557, 558], the SA-NCSM [559], and the self-consistent Green's function method [560]. In these approaches a precise experimental threshold can be a vital input for achieving faster convergence and decreasing the uncertainty on the calculated reaction observables. Figure 9(a) shows an example of such a calculations for ^{4}He + n. Additionally, *Ab initio* approaches have been employed for light targets in the intermediate-energy regime ($\geqslant$65 MeV per nucleon) using the spectator expansion of the multiple scattering theory in conjunction with the *Ab initio* no-core–shell model [40, 561, 562]. Furthermore, optical potentials have been derived from two- and three-nucleon chiral forces in nuclear matter [563]. These potentials provide cross sections for elastic proton or neutron scattering and can be used as input for modeling (d, p) and (d, n) reactions [564].

It is possible to integrate microscopic nuclear structure information into the construction of OMPs by using the Feshbach formulation [570]. This approach links the OMP to the underlying nucleon–nucleon interaction and allows one to build a nonlocal dispersive potential, where the nonlocality arises from the nonlocal nature of the underlying nucleon–nucleon interactions [571]. The general form of the OMP in Feshbach formulation is given by $V_{\rm OP} = U_0 + V_{\rm pol}$, where U_0 is a static energy independent mean field potential, while $V_{\rm pol}$ is an energy dependent non-local term constructed using the underlying structure of the many-body system.

Using these ingredients in the Feshbach formulation, it becomes possible to construct OMPs based solely on microscopic nuclear structure predicted by theory. An example is discussed in [569], where an OMP for n + ^{24}Mg was constructed from intrinsic states provided by shell-model calculations. The resulting neutron scattering predictions are in good agreement with the experimental scattering data, as shown in figure 9(b). Approaches like this can provide a viable path for extending OMPs to very exotic nuclei, where measurements will

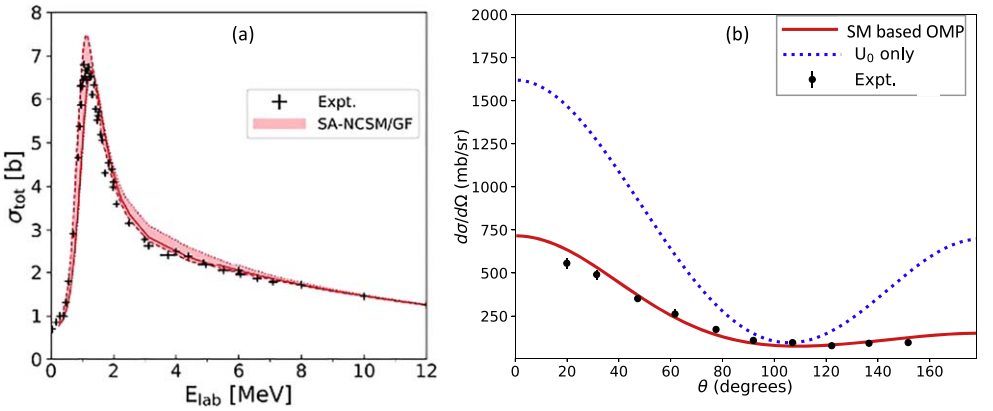

Figure 9. (a) Total cross section for $n + {}^{4}$He versus the neutron kinetic energy in the laboratory frame calculated using the *Ab initio* SA-NCSM with Green's function technique, see [559]. The light red band shows the spread from calculations within a range of HO frequencies $\hbar\Omega = 12$–20 MeV. Reprinted figure, with permission from [Burrows *et al* Phys. Rev. C 109, 014616 (2024)]. Copyright (2024) by the American Physical Society. Experimental data is from [565–567]. (b) Differential cross section for neutron elastic scattering off ^{24}Mg at 1.9 MeV bombarding energy. The solid red curve corresponds to predictions using the OMP constructed with around 600 intrinsic states from shell model calculations. The blue dotted line corresponds to calculations with the real Woods–Saxon potential only. Results with the full potential are in excellent agreement with experimental data from [568], indicated by black circles. For details, see [569]. Reprinted (figure) with permission from [559], Copyright (2024) by the American Physical Society.

remain scarce, but important for validating the predictions. To use this approach to construct optical-model potentials for exotic nuclei, data is needed to develop and test shell-model interactions for nuclei in the region of interest, and to test the predictions of the newly-constructed potentials, e.g. through comparisons to differential proton elastic scattering data for selected nuclei.

6.6. Fission

Nuclear fission, the process by which a heavy nucleus splits into two or more smaller nuclei along with the release of energy, has been a cornerstone of nuclear physics since its discovery. Recent advancements and a heightened understanding of its intricacies have spurred renewed interest in the field, highlighting its significance in both basic and applied nuclear science. Applications spanning the energy sciences, medical isotope production, and stockpile stewardship have the fission process as a central reaction channel and require high quality nuclear experimental and theoretical data. In nuclear astrophysics, a comprehensive understanding of fission is vital to pin down the endpoint of *r*-process nucleosynthesis and to understand the outgoing fragments' masses and energetics in fission recycling [572, 573]. This same understanding of the fission decay can also inform our knowledge on the structure and stability of superheavy elements and is at the heart of any analysis of superheavy searches [574, 575].

In recent years, advances in theory and computation have permitted more comprehensive microscopic studies of nuclear fission (see [576–578] for recent reviews). This includes advances in the fidelity of the many-body methods as well as improved analysis techniques to

perform systematic studies for a range of isotopes and fission modes [579]. While microscopic global studies are still a major computational challenge, continued methods development [580] and the adoption of machine learning into the pipeline [581, 582] promises to ease the burden of integrating microscopic approaches into *r*-process simulations. The enormous progress in leadership class computing systems has enabled unprecedented fidelity in the simulation of the real-time dynamics of fissioning systems, though it remains incredibly challenging to properly quantify the uncertainties in a Bayesian manner. Even more challenging is the inclusion of fission observables in the calibration of microscopic models [583], though such data promises to be very information-rich. Observables that would be strong tests for theory include charge and mass yields, total kinetic energies, and their correlations.

One method of producing isotopes of interest is via near-barrier fusion reactions with exotic projectiles. Relatively high rates of reaccelerated beams in the tin and calcium region in particular will allow for systematic studies on entrance channel effects in heavy-ion fusion. Microscopic methods have been successful in describing these reactions in recent years, though current state-of-the-art many-body methods suitable for large scale calculations are known to be under-constrained by experimental data [584] or otherwise deficient [585]. At FRIB one promising region for early experiments of fusion-fission reactions is in the vicinity of mercury and platinum. This region has several nuclei that exhibit interesting asymmetric fission modes [586–589], making them good candidates to investigate the impact of shell effects as one sweeps along the isotopic chains. The same is true of heavier elements, though higher excitation energies and competing reaction channels such as quasifission may complicate direct fission studies. While this does pose a challenge, the onset of quasifission provides an opportunity to test time-dependent theoretical simulations of the reaction dynamics at play in near-barrier heavy-ion reactions. Recent theoretical studies have noted the similarities in fragment yields and deformed shell effects between fission and quasifission [584, 590, 591], a phenomenon that can be probed by exploring different entrance channels leading to the same compound at the same excitation energy. One of the first approved experiments at FRIB will tackle this with beams of ^{48,49}Ca on ^{174,173}Yb making ^{222}Th. Due to the varying shell effects and transfer dynamics [592] in these systems, some combinations of target and projectile will lead to substantially longer-lived pseudo-compound quasifission fragments. If the build-up of particle-number fluctuations increases as suggested in [593], this implies that the quasifission mass yields should be broader for more asymmetric entrance channels. This will also inform similar time-dependent studies of multinucleon transfer reactions where the fragment mass widths predicted by theory need stringent tests [594] as well as the strong correlation between proton and neutron transfer noted in some studies [595].

7. Equation of state

Investigations of the EOS play an essential role in nuclear physics by pursuing the understanding of bulk properties of nuclear matter and by providing a crucial input for studies of collisions of heavy nuclei, cold neutron stars and neutron star mergers, and core-collapse supernovae. Since the EOS can be both meaningfully constrained by comparisons of phenomenological approaches with data [86, 88, 92, 93, 182, 183, 596–599] as well as calculated from, e.g. *Ab initio* approaches [600–603], it can provide important benchmarks for EFTs of nuclear interactions. Furthermore, constraints on the EOS can provide a unique handle on the dependence of elementary interactions on the surrounding medium [88, 604–606], including nonperturbative regions currently inaccessible to *Ab initio* approaches (e.g. at densities over

twice that of the saturation density of symmetric nuclear matter $n_{\rm sat}$ and at high temperatures attained in neutron star mergers [607, 608] and energetic heavy-ion collisions [85, 609]).

The EOS can be written as a sum of isospin-symmetric and isospin-asymmetric contributions. In terms of the energy per particle E, one often uses the expansion around $\delta = 0$,

$$E(n, \delta) = E(n, 0) + S(n)\delta^2 + \mathcal{O}(\delta^4), \tag{3}$$

where n is the baryon density, $S(n)$ (sometimes also denoted as $E_{\rm sym}$) is known as the symmetry energy, δ is the isospin asymmetry parameter defined as $\delta = (n_N - n_P)/(n_N + n_P)$, where n_N and n_P are the neutron and proton densities, respectively, and $\mathcal{O}(\delta^4)$ indicates higher-order terms which are often neglected (for a discussion of these terms, see, e.g. [610]). In the above equation, the first term represents the energy per particle of symmetric nuclear matter, while the remaining terms account for the additional contribution occurring when $\delta \neq 0$. Both the symmetric and the asymmetric contributions are often further expanded about the saturation density of symmetric nuclear matter $n_{\rm sat}$, where the properties of nuclear matter have been extensively studied. Thus, one can write

$$E(n, 0) = E_0 + \frac{1}{2!}K_0\left(\frac{n - n_{\rm sat}}{3n_{\rm sat}}\right)^2 + \frac{1}{3!}Q_0\left(\frac{n - n_{\rm sat}}{3n_{\rm sat}}\right)^3 + \ldots, \tag{4}$$

where E_0 is the binding energy of symmetric nuclear matter at the saturation density, $n = n_{\rm sat}$, and $K_0 \equiv \left(9n^2\frac{d^2E}{dn^2}\right)_{n=n_{\rm sat}}$ is the incompressibility of symmetric nuclear matter at $n = n_{\rm sat}$. Similarly, the symmetry energy can also be expanded as

$$S(n) = S_0 + L_{\rm sym}\left(\frac{n - n_{\rm sat}}{3n_{\rm sat}}\right) + \frac{1}{2!}K_{\rm sym}\left(\frac{n - n_{\rm sat}}{3n_{\rm sat}}\right)^2 + \ldots, \tag{5}$$

where S_0 is the symmetry energy at $n = n_{\rm sat}$ and $L_{\rm sym}$ (sometimes also simply denoted as L) is the slope of the symmetry energy at $n = n_{\rm sat}$.

While there exist fairly well-established constraints on the EOS for conditions similar to those characteristic of normal nuclear matter (where E_0, K_0, and S_0 are relatively tightly constrained [93, 344, 611, 612]), its behavior away from $n_{\rm sat}$ and for systems with large asymmetry in the isospin content remains poorly known [85]. It is, therefore, the subject of numerous theoretical and experimental efforts worldwide. Currently available and planned experiments at FRIB include studies of the giant monopole resonance in neutron-rich isotopes, nucleon elastic and inelastic scattering on medium-mass and heavy isotopes, and central reactions of heavy nuclei. These experiments will probe the EOS over the widest accessible range of isospin asymmetry, both around saturation and up to densities $n \approx 1.5n_{\rm sat}$ [85], allowing for robust connections with the physics of neutron stars and their mergers. With the proposed FRIB400 upgrade of the available beam energies, it will become possible to study both the isospin- and the density-dependence of the EOS up to $n \approx 2n_{\rm sat}$ [84, 85].

7.1. Microscopic calculations of the EOS within chiral EFT

In the FRIB and multi-messenger astronomy era, the density regime $n \approx (1\text{–}2)n_{\rm sat}$, which can be probed by nuclear theory, nuclear experiments, and neutron star observations, provides a 'golden window' of opportunities for dense matter research [613]. Chiral EFT, combined with algorithmic and computational advances in many-body theory (see section 2), has made tremendous progress in describing nuclear matter at low densities, $n \lesssim 2n_{\rm sat}$, with quantified theoretical uncertainties; see, e.g. [85, 603, 614] for extensive review articles.

Theoretical uncertainties in chiral EFT calculations increase rapidly for densities above $n \approx n_{\rm sat}$. Robust statistical comparisons of nuclear theory predictions with empirical constraints in this regime will enable rigorous benchmarks of chiral interactions [615, 616] and model selection between competing EFT implementations, leading to the construction of improved microscopic EOS models. To this end, advances in chiral EFT are needed to improve its predictive power in the 'golden window' and to resolve issues [231, 617–620] related to, e.g. regulator artifacts, modified power counting, and differing predictions in medium-mass to heavy nuclei. In particular, improving chiral three-nucleon forces for next-generation *Ab initio* predictions [231, 621, 622] of neutron-rich nuclei, now increasingly available in experiments, including those at FRIB, will be crucial for confronting theoretical results with nuclear data. An example of such a cross-cutting research direction is predicting and measuring mirror nuclei [623, 624] as well as neutron-rich nuclei expected to have large neutron skins [84], such as ^{86}Ni. Predictions for the structure and evolution of neutron stars based on the same nuclear interactions can then be confronted with astrophysical observations, covering physics across more than 18 orders of magnitude. These advances will elucidate key questions in *Ab initio* many-body theory, including: (i) Where does chiral EFT break down, and what is the underlying mechanism?; (ii) How should chiral two- and few-body forces be organized (i.e. the power counting) in a medium?; and (iii) What are the phases of neutron star matter at $n \gtrsim n_{\rm sat}$?

7.2. Isospin dependence of the EOS

Enhancing our understanding of the dependence of the current EOS models on isospin asymmetry, including studies of nonquadratic and nonanalytic terms in the isospin expansion of the EOS [610, 625], will be an important task in the FRIB era. To this end, new experimental constraints on low-energy EOS parameters, such as the nuclear symmetry energy at $n_{\rm sat}$ and nuclear incompressibility, are necessary. As an example, for densities around $n_{\rm sat}$ the approved FRIB experiment 'The Isoscalar Giant Monopole Resonance in ^{132}Sn: Implications on the Nuclear Incompressibility' (21056) will shed light on the isospin expansion of the incompressibility of bulk nuclear matter $K = K_0 + K_\tau \delta^2$, where K_τ represents the deviation of the incompressibility of bulk nuclear matter away from the symmetric limit ($\delta = 0$) up to the second order in δ (note that $K_\tau \neq K_{\rm sym}$ because the nuclear saturation density depends on δ and $\delta \neq 0$, see [626, 627]).

As previously discussed, the isospin-dependence of the EOS, which also depends on density, is not well-constrained at $n \gtrsim n_{\rm sat}$. This can be seen in the left panel of figure 10, in which theoretical predictions for the symmetry energy (i.e. the contribution to the energy per particle due to the isospin asymmetry) are shown as a function of the baryon density up to $n \approx 2n_{\rm sat}$. Although different EFT predictions agree with one another within uncertainties (shown as bands), these uncertainties tend to be significant in the 'golden window'. The uncertainties are further magnified when constructing, e.g. the neutron star EOS through physics-guided extrapolations toward high densities present at the centers of heavy neutron stars (see, e.g. [628]). The left panel of figure 10 also shows a selection of experimental constraints on the symmetry energy, depicted as symbols with error bars. More precise experimental constraints on the symmetry energy, e.g. from extractions of neutron skins and measurements of isospin-dependent observables in collisions of heavy neutron-rich nuclei, will provide valuable guidance for microscopic models of the EOS for astrophysical simulations. Here, DFT [41, 42] is critical for determining these low-density EOS parameters from nuclear experiments. However, as PREX–II [629] and CREX [630] emphasized,

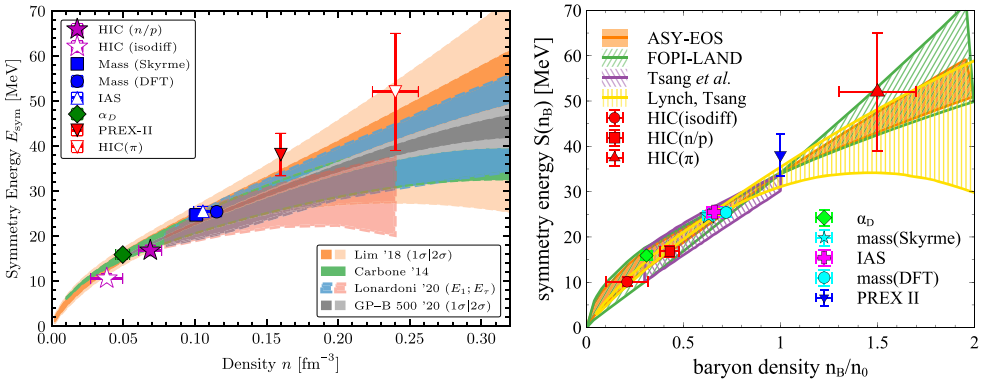

Figure 10. Left: symmetry energy as a function of the baryon density as predicted by several chiral EFT calculations (bands). Various experimental constraints are depicted by symbols with error bars. Theoretical uncertainties are significant and increase rapidly in the density regime $n \approx (1–2)n_{sat}$. Figure modified from [603]. Reproduced from [603]. CC BY 4.0. Right: selected constraints on the symmetry energy obtained, among others, from comparisons of experimental data to results of transport simulations of heavy-ion collisions (bands labeled as 'ASY-EOS', 'FOPI-LAND', and 'Tsang *et al*' and symbols labeled as 'HIC(isodiff)', 'HIC(n/p)', and 'HIC(π)'). Figure modified from [85]. Reprinted from [85], Copyright (2024), with permission from Elsevier.

extrapolations to the neutron-rich regime of current DFT models need improvements, for which microscopic EOS calculations of neutron-rich matter may provide guidance.

EFT calculations of pure neutron matter are particularly relevant here because, in this case, chiral three-nucleon forces are simplified and have no unknown parameters through next-to-next-to-next-to-leading order (N^{3}LO) [631, 632]. This results in a good agreement between different many-body approaches and overall relatively small uncertainties at $n \lesssim n_{sat}$. At densities away from n_{sat}, experimental constraints on the symmetry energy can be obtained from studies of central heavy-ion reactions, which we elaborate on in the next subsection.

Differences in the rms charge radii of mirror nuclei are also sensitive to the symmetry energy, in particular to the slope parameter L_{sym} [633, 634]. The size of the difference depends on the product DL_{sym}, where $D = |N - Z|$ is the difference between the number of neutrons and the number of protons in a nucleus. Several cases have already been measured: ^{36}Ca–^{36}S ($D = 4$) [635], ^{54}Ni–^{54}Fe ($D = 2$) [133], and ^{32}Ar–^{32}Si ($D = 4$) [636], with results for L_{sym} consistent with those extracted from the neutron skin of ^{48}Ca and from the analysis of the gravitational waveform of the binary neutron star merger GW170817 [637]. These L_{sym} determinations are model dependent [207, 624], and more data are required to assess and reduce the model dependence. FRIB will provide access to the proton-rich nucleus ^{52}Ni in the mirror pair ^{52}Ni–^{52}Cr ($D = 4$), and both nuclei in the mirror pair ^{22}Si–^{22}O ($D = 6$). Ultimately, the mirror pair ^{48}Ca–^{48}Ni is of great interest due to its large $D = 8$ and the connection to the neutron skin of ^{48}Ca. However, current estimates suggest that the production rate of ^{48}Ni, even with FRIB operating at full beam power, will remain too low for laser spectroscopy in the near future.

7.3. EOS and in-medium properties of nuclear matter from heavy-ion collisions

Heavy-ion collisions (also referred to as central heavy-ion reactions) at beam energies from a few tens of MeV/nucleon to several GeV/nucleon in the fixed-target frame probe the broadest range of baryon densities (from a few tenths of to a few times the saturation density)

and temperatures (from a few MeV to well above one hundred) available in terrestrial laboratories [85]. In particular, the near-term and future heavy-ion collision experiments at FRIB, given its world-leading range of accessible proton- and neutron-rich heavy isotopes, are uniquely posed to probe the symmetry energy component of the EOS at densities up to $2n_{\rm sat}$ [84, 85].

At the same time, heavy-ion collision experiments can only measure final momentum-space distributions of particles, and any properties of matter created in the collisions must be inferred from their influence on the evolution of the collision. Moreover, systems created in central heavy-ion reactions are short-lived and out-of-equilibrium for significant portions of their evolution. Consequently, conclusions on the properties of nuclear matter based on experiments colliding heavy nuclei require comparisons to results of simulations obtained within the framework of transport models.

Using transport theory to infer features of the colliding systems is a challenging endeavor. This is because in order to provide a robust description of observables, the simulations need to describe all stages of the reaction, from the initial nuclei to fragments reaching the detectors, while taking into account the interplay between numerous details of the underlying physics which vary in prominence over time. The complex problem of benchmarking the simulations benefits from the availability of broad and accurate experimental data. This can be primarily achieved through experimental designs in which 4π detectors register as much information as possible on reaction events (primarily about charged products of the reaction, as neutral particle measurements continue to prove difficult, albeit not impossible). The resulting abundant data sets contain information on particles emitted over broad kinematic ranges and, therefore, carrying insights on various physics elements driving the dynamics of the collisions. Oftentimes, such comprehensive heavy-ion collision data are analyzed over several years, if not decades, with subsequent analyses yielding answers to questions that were not originally considered when the experiment was staged. It follows that the best approach to heavy-ion collision measurements is to measure as many of the collision products as possible (i.e. to use comprehensive detectors), irrespective of the particular observable pursued within a given experimental campaign.

Numerous studies [88, 91, 97–99, 638–640] identify heavy-ion observables particularly sensitive to the nuclear matter EOS. As an example, the right panel of figure 10 shows selected constraints on the symmetry energy, including constraints from heavy-ion collisions obtained using proton and neutron anisotropic collective flows [641], isospin diffusion [596, 642], ratios of neutron to proton spectra [642, 643], neutron to charged fragments ratios [644], and ratios of pion spectra [182, 183]. However, the complexity of heavy-ion reactions also means that a given observable is affected not only by multiple different reaction stages, but also by various properties of the colliding systems. Consequently, no single observable tests *exclusively* the EOS. The impact of the EOS on a given EOS observable, such as anisotropic collective flows or subthreshold meson yields, often competes with that of, e.g. the momentum dependence of particle mean fields [645, 646] or details of subthreshold particle production [182, 647]. This challenge to determine and quantify the influence of particular physics inputs on chosen observables has to be addressed by theorists and experimentalists alike, aided by recent developments in statistical approaches and artificial intelligence methods, thus enabling more stringent constraints.

Notably, the above challenge presents a unique opportunity to shed light on in-medium properties of nuclear matter and address multiple outstanding problems in nuclear physics, including the momentum-dependence of the nuclear EOS at densities away from the saturation density, in-medium hadron cross-sections, off-shell dynamics, subthreshold particle production, and cluster production mechanisms. This opportunity must be met with a

concerted program to further develop theoretical foundations of various elements of transport theory and phenomenological solutions used in simulations. On the experimental side, the isospin-dependence of many processes that constitute an input to transport models will be thoroughly studied in upcoming experiments at FRIB, creating an opportunity for collaborations across different subfields. Similarly, the fact that *Ab initio* calculations are beginning to be carried out at finite temperatures [648, 649] can also become highly important for interpretations of experimental heavy-ion data by providing more relevant reference studies. Indeed, the extrapolation from a non-equilibrium system created in a heavy-ion collision to the nearest equilibrium state at a given density and temperature is expected to be more reliable than a similar extrapolation to such a state at the same density and zero temperature.

Below, we briefly overview several key properties of nuclear matter that significantly influence interpretations of heavy-ion collision data. We note that a robust description of heavy-ion collisions in the FRIB energy regime calls for including *all* of these aspects. For a complementary discussion of these and other inputs to simulations of heavy-ion collisions, see [85].

7.3.1. Momentum dependence of nucleon interactions. The momentum dependence of nuclear potentials emerges from elementary *NN* interactions (which are predominantly attractive at low *NN* energies but turn into predominantly repulsive at higher energies) and from exchange terms [605, 650]. The momentum dependence of mean fields in cold matter at and below the saturation density can be tested in elastic scattering of nucleons off nuclei. However, in heavy-ion collisions, the momentum dependence is probed over different densities and in hot rather than cold matter. Fortunately, while studying the EOS effects without the influence of the momentum dependence effects is impossible, the opposite is true. The EOS effects subside in collisions of lighter heavy-ion systems and at higher impact parameters. At the same time, the influence of momentum dependence is enhanced at high transverse momenta. These factors allow one to calibrate the momentum dependence (as a function of density and isospin imbalance) before attempting to extract the EOS from data. Moreover, microscopic many-body calculations of nucleonic potentials as a function of density, momentum, and neutron-proton imbalance (and recently even temperature [648, 649]) make the momentum dependence at different nucleonic densities a subject of interest in its own right. Furthermore, these calculations can aid the modeling of the collisions by narrowing the ranges of interaction parameter values that need to be confronted with data.

FRIB, naturally, offers a greater variation of the isospin composition of collided nuclei than has been available at other facilities to date. At early stages of the collisions, the relative isospin imbalance in high-density matter primarily reflects that of the original nuclei. The different response of isospin positive and negative particles to the asymmetric component of the EOS influences their dynamics during the collision and is ultimately reflected in final-state observables, such as, e.g. charged pion ratios [97, 182, 183]. Thus, comparisons of simulations with observables measured in FRIB experiments bear the promise to simultaneously constrain, e.g. both the density and the momentum dependence of the asymmetric contribution to the EOS, which would be equivalent to constraining the symmetry energy parameters and the effective mass splitting between neutrons and protons [182, 647]. Here, careful evaluations of physics assumptions and simulation frameworks are crucial to meaningful extractions of the properties of nuclear matter; multiple such efforts have already been started [102, 651].

7.3.2. Influence of a medium on particle cross-sections. The inputs to transport simulations also include cross-sections for elementary collisions. Following Occam's Razor principle,

early transport calculations adopted cross-sections obtained from measurements of elementary processes. However, these typically led to excessive nucleon stopping as compared to measurements from central heavy-ion collisions, resulting in a mismatch between the simulations and the data already on the level of simple rapidity distributions [652, 653]. Moreover, reduced in-medium cross-sections (i.e. cross-sections smaller than those in free space) not only seemed to be needed by phenomenology, but they also emerged from microscopic calculations [652, 654–658]. As a result, parametrizations for the in-medium cross-section reductions were developed and employed in collision simulations covering broad ranges of incident energy and masses of colliding systems [659–661]. However, the consensus on the level of cross-section reduction was shaken by recent measurements by the SπRIT Collaboration of Sn + Sn systems at 270 MeV/nucleon [662]. To reproduce rapidity distributions for central collisions as measured by the SπRIT experiment, virtually all transport codes [102] need larger in-medium cross sections than in the case of other data in this general energy region [663–665]. Among the possible explanations for this puzzle, one can consider the fact that other experiments in this energy regime used either lighter or heavier ion species (possibly introducing systematic differences) or that the centrality selection was less stringent. Still, the issue must be clarified from both the theoretical and the experimental sides. FRIB will operate in the energy regime in question and can contribute more significant variations in the isospin composition of the colliding systems at a given mass than other accelerators. Notably, the isospin dependence of in-medium cross sections remains poorly understood [658, 666, 667].

7.3.3. Development of off-shell properties and subthreshold production. Subthreshold production (that is particle creation below nominal energy thresholds) in different isospin channels can be a sensitive tool for testing the symmetry energy around $2n_{\rm sat}$ [84, 668]. During a heavy-ion collision, nucleons and other hadrons in the dense region of the system undergo frequent collisions with each other. In particular, these interactions effectively decrease a particle's lifetime in a given state, leading to an increased particle width. Similarly, particle widths can change in the medium due to a modification of the decay channels, stemming from altered energy thresholds in the medium. In both cases, significant widths imply that additional elementary interactions can take place off-shell while still satisfying energy conservation, facilitating subthreshold particle production [669–671]. The subthreshold particle production will, in general, be characterized by different thresholds for different isospin states.

The strong sensitivity of near-threshold pion yields to relatively modest in-medium particle energy variations can be demonstrated even by transport calculations without genuine in-medium width enhancements [647]. However, a full exploitation of subthreshold production as a tool for constraining the symmetry energy calls for using off-shell transport to reach meaningful conclusions from comparisons to data. While off-shell transport approaches with positive definite distribution functions (amenable to Monte Carlo sampling) exist [650, 672–676], they have been sparsely used for simulations of lower-energy heavy-ion collisions.

7.3.4. Nuclear clusters and correlations. While nuclear clusters emerge as independent degrees of freedom at densities below the saturation [251, 272, 677–679], their formation in heavy-ion collisions is generally initiated at higher densities (at most only modestly below saturation) since several nucleons need to appear in the same phase-space region for the formation to occur [680, 681]. Moreover, depending on the kinematic region where given collision products are considered (e.g. midrapidity versus forward rapidity), often the density

region where the cluster formation occurs can only emerge through decompression from high-density matter. Since the relative neutron-proton imbalance characterizing the high-compression stage is retained throughout the nearly-adiabatic expansion [682, 683], the dependence of cluster yields on the isospin composition in selected kinematic regions becomes a probe of the symmetry energy at densities above the saturation density and, more generally, of isovector characteristics at those densities.

In order to fully utilize observables related to nuclear clusters and extract the isospin properties of nuclear matter, models of cluster production need further development. Currently invoked production mechanisms [684] can be typically divided into cluster-finding algorithms based on coalescence, that is with criteria based on the proximity of particles in the coordinate and momentum space (sometimes also including criteria related to the binding energy of a cluster [685]), and into models where nuclear clusters are introduced as independent degrees of freedom that can be produced in elementary scatterings [686, 687] (which in principle can accommodate the modification of cluster properties due to the surrounding medium). Both categories of approaches have their shortcomings. Coalescence-based algorithms, typically applied toward the end of a heavy-ion collision evolution, do not account for the influence of nuclear clusters on the collision dynamics. Approaches treating clusters as independent entities usually consider only the lightest clusters (often just deuterons) due to challenges in including the increasing number of relevant production channels for heavier clusters. Furthermore, on the theoretical level, cluster formation is related to intermediate-range correlations and strong quantum effects which extend beyond the classical mean-field picture utilized in transport. Therefore, the problem of cluster formation in heavy-ion collisions touches on fundamental properties of nuclear matter, and successful phenomenological descriptions have the potential to shed light on particular mechanisms involved.

Notably, similar fundamental questions are apparent in nuclear short-range correlations (SRCs) that can be measured in, e.g. nucleon knock-out experiments [688–691]. Through phenomenological descriptions based on inclusion of high-momentum tails in the initial nucleon distribution or considerations of three- and many-body collisions, SRCs have been likewise shown to appreciably influence heavy-ion collision dynamics [671, 692–694]. Moreover, SRCs are also shown to be strongly dependent on the isospin composition of the surrounding medium [695, 696]. Consequently, theoretical descriptions of heavy-ion collisions at FRIB and FRIB400 might substantially benefit from utilizing models accounting for effects due to SRCs. Moreover, such investigations hold the promise to complement the current and planned programs investigating SRCs at the Jefferson Lab and the future Electron-Ion Collider by studying the dynamical evolution of SRCs in dense isospin-asymmetric nuclear matter. Here, sensitive observables may include both pion yields [671] and bulk observables [694]. Such studies can also further advance the understanding of the role of tensor forces [696, 697] at high densities and the development of off-shell transport models.

7.4. Optical potentials

As discussed previously in section 6.5, nucleon–nucleus optical potentials are a crucial input for nuclear reaction studies involving target nuclei beyond the lightest isotopes. The optical potential can be directly related [698] to the nucleon self-energy, which plays a key role in theoretical investigations of the EOS. Here, one starts with the momentum- and energy-dependent nucleon single-particle propagator $G(q, \varepsilon)$ in nuclear matter, which is related to the irreducible self-energy $\Sigma(q, \varepsilon)$ through the Dyson equation $G(q, \varepsilon) = G_0(q, \varepsilon) + G_0(q, \varepsilon)\Sigma(q, \varepsilon)G(q, \varepsilon)$, where q and ε

are the single-particle momentum and energy, respectively. The nucleon self-energy at positive energies is identified with the optical potential [698], which can then be inferred from elastic and inelastic scattering experiments. For isospin-asymmetric target nuclei, one empirically observes in the optical potentials for proton and neutron projectiles a splitting of the Lane form [699]: $U_{n,p}(E) = U_0(E) \pm U_I(E)\delta_{np}$, where $\delta_{np} = (N - Z)/(N + Z)$ is the isospin asymmetry parameter expressed in terms of the number of neutrons N and protons Z, $U_I(E)$ is called the isovector optical potential, and the $+$ $(-)$ sign applies in the case of neutrons (protons). Quasi-elastic charge-exchange reactions (p, n) are especially sensitive to $U_I(E)$ [699]. This has been exploited in [700] to refine the isovector radius and diffuseness parameters of nucleon–nucleus optical potentials and study correlations between these geometry parameters and the symmetry energy slope parameter L.

The optical potential at positive energies is related to the nuclear shell model potential at negative energies through a dispersion integral connecting the real and imaginary components of the self-energy, see, e.g. [550, 701]. Therefore, with a sufficient amount of bound-state and scattering data, dispersive optical potentials can provide unique insights into nuclear structure and its connections to the EOS. For instance, in [702] the neutron-skin thicknesses Δr_{np} of ^{16,18}O, ^{40,48}Ca, ^{58,64}Ni, ^{112,124}Sn, and ^{208}Pb were obtained from a dispersive optical model analysis that included data from elastic scattering angular distributions, total cross sections, reaction cross sections, and level properties. In particular, the obtained value of $\Delta r_{np}(^{208}\text{Pb}) = 0.12$–$0.25$ fm is consistent with models [599] predicting moderate values of $L = 30$–90 MeV, as well as the broad constraints coming from the PREX-II experiment [629] that found $\Delta r_{np}(^{208}\text{Pb}) = 0.283 \pm 0.071$ fm and $L = (106 \pm 37)$ MeV [703].

From the Hugenholtz–Van Hove theorem [704], the single-particle energy at the Fermi surface is directly related to the energy per particle $\bar{E}(k_f)$ of the medium through

$$\frac{k_f^2}{2M_N} + \Sigma(k_f, \varepsilon(k_f)) = \bar{E}(k_f) + \frac{k_f}{3}\frac{\partial \bar{E}(k_f)}{\partial k_f}, \tag{6}$$

where k_f is the Fermi momentum and M_N is the nucleon mass. This relationship has been used [705] to derive an explicit relationship between the symmetry energy at saturation S_0, the slope parameter L, and the optical potential. Using the global set of nucleon–nucleus optical potentials available at the time, [705] found $S_0 = 31.3 \pm 4.5$ MeV and $L = 52.7 \pm 22.5$ MeV. More generally, the self-energy defines the spectral function

$$A(q, \varepsilon) = \frac{-2\,\mathrm{Im}\Sigma}{(\varepsilon - \frac{q^2}{2M} + \mathrm{Re}\Sigma)^2 + (\mathrm{Im}\Sigma)^2}, \tag{7}$$

which can be integrated over the single-particle energy and momentum to obtain the bulk energy per particle through the Galitskii–Migdal–Koltun sum rule [706, 707]. This technique is commonly used in self-consistent Green's function theory to obtain the EOS of nuclear matter at zero and finite temperature [708, 709]. In the future, consistent microscopic modeling [710, 711] of the EOS and optical potentials based on the same underlying nuclear forces will provide an opportunity to establish correlations between the empirical parameters of the EOS and optical potentials.

Finally, proton and neutron optical potentials (self-energies) are an essential input for transport model simulations of medium-energy heavy-ion collisions [85], which provide an additional experimental means of probing the (hot) dense matter EOS. In the past, phenomenological single-particle potentials have typically been used in transport simulation studies. However, more recently microscopic predictions from chiral EFT have been used to

constrain single-particle potentials and study their impact on heavy-ion collision observables [712, 713].

7.5. Upcoming and proposed experiments at FRIB

The experimental approach to studying the nuclear EOS away from saturation density at FRIB is split into several phases, reflecting the availability of beams and equipment (see section 3.7). The first heavy-ion collision experiment at FRIB, 'Measuring the isospin dependence of the nucleon effective mass at supersaturation density' (23058), has been approved in PAC2. That experiment will focus on constraining the momentum dependence of the nuclear potential around (1–1.5)n_{sat} through measurements of spectral ratios of neutrons and protons as well as directed and elliptic flow in ^{56,70}Ni + ^{58,64}Ni reactions at projectile energies of 175 MeV/nucleon. While the sensitivity of the spectral ratio to the momentum dependence of the symmetry energy drops off with increasing density [643], flow remains a sensitive observable for the symmetry energy up to 1 GeV/nucleon [714]. The mid-mass, 200 MeV/nucleon beams available in the first few years at FRIB will probe a density window in which both of these observables can yield information about the symmetry energy. This is especially advantageous as model uncertainties from transport calculations will likely be different between the two observables. The obtained results can be combined with previous experimental constraints at low density (both from prior heavy-ion collision experiments at NSCL [103] as well as with independent constraints from optical models [715]), while at high density the reference is provided by the current state-of-the-art results from the SπRIT campaign at RIKEN [182, 183], studying Sn + Sn reactions at beam energies of 270 MeV/nucleon.

In later phases, the experiments will shift to focus on the flow and yield ratios of charged pions. These pion measurements will initially concentrate on reactions at lower energies than those studied at RIKEN. This will allow for the study of sub-threshold pion production, which is an important input to transport model calculations of the pion ratio [716]. Subsequently, the increased intensities and larger isospin asymmetry of the FRIB400 beams will allow for unprecedented studies of the nuclear EOS using spectral ratios of charged pions. In particular, the increased beam energy will lead to higher overall yields of charged pions. This will allow for studies with lower beam intensities, which are expected in the case of beams of rare isotopes with high isospin asymmetry.

8. Nuclear astrophysics

8.1. Motivation and needs for progress in nuclear astrophysics

2022 not only marked the first ever FRIB experiment, but also coincided with the 65th anniversary of the work that established the first comprehensive theory of nucleosynthesis laying the foundation of the modern field of nuclear astrophysics [717]. It was evident from even the early days that studies of the origin of the elements are intimately tied to understanding the properties and reactions of both, stable and unstable nuclei (see also [718]). Therefore laboratory measurements have been central to driving progress in nuclear astrophysics from the beginning.

With FRIB now online, hundreds of species yet to be probed in terrestrial environments can become available to experiments. This is particularly timely since in the last few years observation has begun a revolution of its own, with the first gravitational waves from binary neutron star mergers detected [719]. Now, we have seen the light emitted from the first multi-

messenger neutron star merger event (GW170817) [720, 721], which pointed to the presence of lanthanide elements, implying mergers to be a site of heavy element production. Such observational abilities will only be enhanced by future gravitational wave dectectors. For example, Cosmic Explorer [722, 723] and the Einstein Telescope [724] could present the opportunity to observe many more binary mergers than LIGO. Additionally, GW170817 and its associated kilonova optical transient being observed across the electromagnetic spectrum by over 70 observing teams well-demonstrates the incredible ability of the observational community to perform highly detailed follow-up of events that have been localized by early detection via various messengers such as gravitational waves, gamma-rays, optical transient surveys, or neutrinos. In addition to this new access to multi-messenger events, our bank of metal-poor star observations (which can be tied more directly to individual events due to their being enriched by fewer events than our Sun [725]) is set to grow as well. Observational campaigns such as the R-Process Alliance [726] will present a new wealth of abundance data that we must decipher and integrate into global analyses with other observables.

Studies have shown conclusively that interpretation of observables requires nucleosynthesis calculations which account for the uncertainties in the nuclear physics properties of relevant species (e.g. [727]). This applies to all nucleosynthesis observables such as Solar and stellar abundances [717, 728], meteorites [729, 730], light curves [731–734], and MeV gamma emission [735]. This intimate connection between observables and nuclear physics properties presents the opportunity for not only nuclear physics to inform astrophysics, but vice versa as well [736]. For instance, questions remain on the ultimate reach of the rapid neutron capture process (*r*-process) in neutron star mergers but should late time heating of the environment from fission or alpha decay take place, this could show itself in the light curve [737, 738]. This would not only conclusively point to the production of actinides at this site, but would constrain the fission barriers and branching ratios in the actinide regions [573, 739], requiring them to be such that production of late time long-lived fission species is possible. Ultimately, it is fundamental to be able to connect astrophysical simulations that describe the properties and dynamics of the ejected material [740] with radiative transfer modeling of the kilonova spectra [741] to be able to determine which specific elements are produced and under which conditions. Similar efforts are critical to understand observables of core collapse and thermonuclear supernovae, novae, and x-ray bursts.

Therefore the need for a back and forth between theoretical studies of nucleosynthesis and nuclear physics experiments is clear, with the FRIB era now providing new exciting prospects to tackle several of the fundamental questions in nuclear astrophysics (e.g. [572, 742]). In order to study astrophysical processes, reaction network inputs are needed based on realistic astrophysical simulations [743, 744], as well as experimental information to constrain the relevant astrophysical reactions. The nuclear data needs of reaction networks vary among astrophysical scenarios, and even individual model efforts. As far as unstable nuclei are concerned, networks typically require capture rates (neutron capture, proton capture, and alpha capture rates being particularly crucial), other charged particle and neutron induced rates such as (α, n), (α, p), (n, p), (p, α), beta-decay rates with branching ratios for the emission of protons or neutrons, continuum electron capture rates, and fission. In neutron stars, heavy ion fusion rates with unstable nuclei may also play a role. Masses serve as both a direct network input in the form of separation energies as well as a required input to model theoretical capture and decay rates where measured rate values are unavailable. Additionally, the need for nuclear data is not isolated to solely the nucleosynthesis network. For example, post-processing of network outputs with additional pieces of nuclear data, such as the energy liberated in individual decays in the different products: electrons, gammas, alpha-particles,…, is required to make predictions for electromagnetic signals from astrophysical events. This in

addition requires knowledge of the atomic processes that determine the spectra formation at the photospheric and nebular phases [745, 746]. Recent studies have also shown that considering isomers can affect the overall decay of synthesized species at late times and impact the light curve [747–749]. The wealth of nuclear physics information needed highlights that nuclear astrophysics will be an FRIB customer for many years to come. Despite the fact that many important investigations will require longer timescales due to the large number of measurements and the required synchroneous advances in multiple fields, there are fundamental questions that can start to be systematically addressed in the near term. We detail below some of the motivations and needs for some specific nearer term and longer timescale investigations.

8.2. Nucleosynthesis on the neutron-rich side of stability

8.2.1. Investigations to constrain nuclear theory approaches and extrapolations. Investigating the astrophysical production of the elements inevitably leads to a need to study neutron capture reactions since reaching the heaviest species is only possible through neutron capture nucleosynthesis. The astrophysical *s*-, *r*-, and *i* processes (slow, rapid, and intermediate respectively) all proceed via a series of neutron captures to make heavier isotopes and beta-decays to reach the next highest element number. It is via this dance between neutron capture and beta-decay that elements all the way up to the actinides can be made in astrophysical environments. Thus global models for neutron capture, beta-decay, and fission are crucial nucleosynthesis inputs, so we discuss these specially here.

For neutron captures, very little experimental information exists beyond the stable species where the *s* process operates. Additionally, the increasing complex structure of exotic species in the neutron-rich regions presents a challenge to reaction theory models, which leads to nucleosynthesis studies being dependent on HF models (previously discussed in section 6.3). HF utilizes the assumption that the reaction forms an intermediate compound nucleus that can be treated mostly independently of the initial state, as well as a statistical averaging to make use of a level density since modeling all level transitions and resonances in heavy systems can become unfeasible. Although HF methods are known to have issues at closed shells and toward driplines where statistical averaging is no longer appropriate due to the level structure, currently there are very few studies of alternative methods to calculate neutron capture rates globally [527].

The impact of optical-model uncertainties on calculated capture rates remains to be rigorously studied. This is particularly challenging for target nuclei far from stability. New global optical models need to be developed, which requires microscopic predictions, experimental data, or a combination of both. Similarly, more work is required to obtain realistic gamma strength function (gSF) and level density (LD) models for unstable isotopes. Studies have found that the gSF and LD models used in HF calculations can produce capture rates that differ by several factors to an order of magnitude or more, and these uncertainties propagate to the predictions for astrophysical abundances [750]. For more details on the present status of HF calculations, see section 6.3.

Given the uncertainty in the calculated capture cross sections resulting from insufficiently-known level densities and gamma-ray strength functions, indirect methods will continue to play an important role for determining neutron capture rates. It is via indirect approaches, such as the surrogate reactions method or Oslo-type measurements (first discussed in section 3.3), that FRIB can make both immediate and long-term progress toward informing neutron capture in neutron-rich regions. The Oslo and beta-Oslo methods utilize charged-particle (transfer or scattering) reactions and beta-delayed gamma-emission

measurements, respectively, to obtain information on the gamma-decay of the compound nucleus of interest to the neutron-capture reaction. The experiments yield quantities that are a convolution of the LD and gSF; methods have been developed to extract both quantities and provide them for HF calculations; for a review, see [154].

The surrogate reaction method was originally developed to determine neutron-induced fission; for a review, see [524]. In recent years, theory developments have made it possible to apply the method also to neutron-capture reactions [66, 524, 526]. Multiple applications have demonstrated that the method provides meaningful experimental constraints for cross sections calculations of neutron capture on isotopes near stability [312, 536, 537]. The approach does not rely on auxiliary quantities like s-wave resonance spacings (D_0) or average radiative widths ($\langle\Gamma_\gamma\rangle$), which are not available for unstable target isotopes, thus making it a promising method for exotic, neutron-rich or proton-rich, nuclei. To obtain reaction rates relevant to astrophysical processes that involve isotopes well outside the valley of stability, it is necessary to further develop and validate the method beyond the range of current applications. Both inelastic scattering and (d, p) transfer reactions are good candidates to reach a large number of exotic isotopes. New developments are underway to explore these opportunities. For more details, see the discussion in section 6.4 and the references given there. In general, it is important to test the assumptions underlying indirect measurements and validate the resulting cross sections against additional measurements or theoretical predictions. This will not only provide more reliable cross sections, but it will also yield insights into the underlying reaction mechanisms.

Global models for beta-decay are of equal importance to those for capture rates. Here, more experimental information to benchmark models is available, but decisively disappears for many neutron-rich lanthanides, $N = 126$ nuclei, and beyond. Additionally, the few relatively recent global beta-decay models have shown a significant difference between model predictions for rates near and beyond $N = 126$, and have found that first-forbidden transitions play an important role here [751, 752]. Nucleosynthesis studies have shown that the beta-decay model adopted can decisively change predictions for abundances and light curves (e.g. [733, 753–755]). Global beta-decay models typically make use of methods such as QRPA as well as HF in order to predict beta-delayed neutron emission probabilities [756], but as is the case with neutron capture, how appropriate it is to apply approaches like HF should be an important focus of longer term FRIB investigations.

Fission in the neutron-rich regions is the ultimate unknown territory. With much of our experimental information quarantined to proton-rich actinides, on the neutron-rich side experiments have mostly probed species of relevance to reactor physics such as ^{239}Pu, ^{235}U, and ^{238}U. Although such species are indeed produced in neutron-rich neutron capture nucleosynthesis such as the *r* process (for instance ^{235}U and ^{238}U are present in stars and our Sun), fissioning species impacting nucleosynthesis calculations are predicted to be in regions that are much, much more neutron-rich [739, 755, 757]. There are few models available which predict barrier heights globally for neutron-rich actinides, however already this limited set demonstrates a diversity of possible behavior. For instance, fission rates calculated using the barrier heights of the Finite Range Liquid Drop Model (FRLDM) model produce an *r* process that terminates near $A \sim 295$ (around $Z, N \sim 94, 200$, a few neutrons past the $N = 184$ shell closure), whereas nucleosynthesis applications of rates using the HFB-14 fission barriers are capable of synthesizing nuclei much higher in the chart with an $A > 300$ [739]. Note that nucleosynthesis calculations reaching the neutron-rich actinides are very sensitive to the physics around $N = 184$, which at the moment is purely a theoretically predicted shell closure, so searching for experimental hints of shell closures past $N = 126$ in the future could directly impact nucleosynthesis studies of actinide production.

Overall, fission can impact nucleosynthesis observables both by actively participating during the synthesis, introducing fission cycling into the dynamics and affecting the final abundances, and by impacting the electromagnetic afterglow (such as light curves and gamma rays) of the material present. Late-time fission effects on the electromagnetic emission depend on longer-lived fissioning species that lie closer to where current measurements have taken place, and so this will be discussed in the long-lived actinide section below as being potentially approachable by FRIB in upcoming years. However the fission cycling that influences abundances occurs at much earlier times when the nuclear flow lies in the very neutron-rich regions near $Z = 94$, $N = 184$. Studies have shown that when the synthesis reaches this deep into the actinides, the fission yields trends (i.e. how yields change along an isotopic chain) and fission barriers (which affect the nuclear flow) crucially impact the abundances around the second *r*-process peak at $A \sim 130$ [573, 739, 758]. Furthermore depending on whether the fission deposition is dominantly symmetric or asymmetric, fission can also contribute significantly to the light precious metals region around $A \sim 110$ [759] as well as the lanthanide region around $A \sim 150$ [760]. Unfortunately, the fissioning nuclei which have been found to impact *r*-process abundances lie well beyond the reaches of any current or planned experiments [573, 739, 758]. Nevertheless, in the long-term future FRIB could potentially still provide some guidance to fission modelers by working to systematically extend the reach of probed nuclei in the neutron-rich actinides. Measurements of barrier heights, fission yields, and decay branchings could provide constraints for extrapolations and benchmarks for theoretical calculations. Additionally, the outcome of neutron-rich nucleosynthesis in the actinide region is determined by several fission processes (e.g. neutron-induced, beta-delayed and spontaneous fission) and alpha decays which could all play a role in setting the nucleosynthesis abundances. For all the fission processes it is important to investigate both rates and yields since both are dependent on the fission kinematics. Despite the challenges of probing the neutron-rich actinide region, it is important for experiments to push into this desolate frontier since it is connected to some of the biggest questions in nuclear astrophysics such as the ultimate nucleosynthesis reach of nature (i.e. how heavy of species can be synthesized) as well as whether or not the superheavy elements can be produced in astrophysical environments [761–763].

8.2.2. Connecting FRIB to the synthesis of elements beyond tellurium and up to the actinides. We first discuss the main *r* process, which synthesizes elements beyond ∼Te all the way to the heaviest elements found in nature, though it may also be co-produced with some of the lighter elements. Astrophysical sites of the *r* process eject material at a variety of neutron-richness, temperatures, and densities which can host nucleosynthesis. Figure 11 demonstrates the *r*-process path (most abundance species at a given proton number) for two distinct types of ejecta that both produce a main *r* process, one being a hot, low entropy, low density condition of moderate neutron-richness ($Y_e = p/(n + p) = 0.2$ and another being a cold, low entropy, high density tidal tail condition which is extremely neutron-rich ($Y_e = 0.01$). The figure shows the paths at the moment of 'freeze-out', that is when the neutron-to-seed ratio goes to 1 and the path begins to move back toward stability. During this stage late-time neutron captures as well as beta-decays shape the final abundances, and also influence any fission fragments that have been deposited around or after freeze-out. As can be seen from comparing the location of the paths to the thin black line representing currently probed species, the *r*-process paths traverse over the presently unexplored territory outside the black line on their way to stability. Over the course of this journey, their abundances are altered from the bottom plot to that shown in the top. Therefore numerous opportunities to inform the evolution of the main *r* process are possible for FRIB, from measurements of

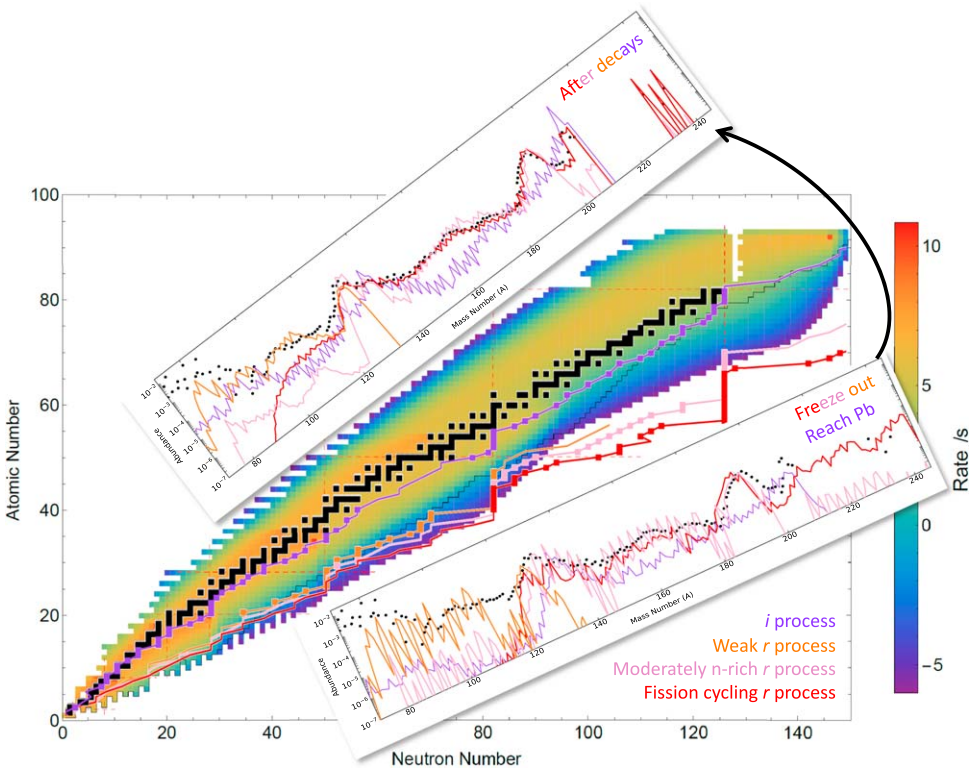

Figure 11. The FRIB production rates compared to the 'paths' (most abundance species at a given proton number) for a 'weak' *r* process (orange), moderately neutron-rich *r* process (pink) and a fission cycling *r* process (red). The snapshot is taken at the moment of 'freeze-out' for each *r*-process case, and the abundances at this time are shown in the bottom plot as compared to the Solar *r*-process residuals from [764]. Also shown is the path of an *i*-process calculation (purple) at the moment that the path significantly populates lead species. The final abundances following the decay of the nuclei to stable species is shown in the top plot. For the *r*-process cases, the path is shown as a line when the abundance is more than 10^{-11} and as boxes connected by a line if the abundance exceeds 10^{-5}. For the *i*-process case the abundance limits for the line only, boxes plus line is 10^{-15}, 10^{-9} respectively. Note the significant number of species whose properties shape the final abundances which are presently unprobed (outside of the thin black line as in figure 1) but can be reached by FRIB.

nuclei near $N = 82$, to the lanthanide (a.k.a. rare-Earth) species, as wells as near $N = 126$ and beyond. We discuss each of these areas specifically here as well as the science questions that can be approached via dedicated studies of each region.

Nuclei near N = *82*. The Solar isotopic abundance pattern (see figure 11) is clearly influenced by nuclear structure with 'peaks' of especially high abundance seen in the presence of magic numbers and enhanced stability, as is the case with the second *r*-process abundance peak at $A \sim 130$. This enhancement in the abundances is known to come from a so-called 'pile-up' at neutron shell closure $N = 82$, where the *r* process must wait to beta-decay before capture can proceed beyond $N = 82$ into the lanthanide region. Additionally processes with conditions that do not permit significant capture into the lanthanides, such as a so-called 'weak' *r* process (see figure 11), can also reach $N = 82$ nuclei. Therefore this peak in the Solar

abundance distribution could be a convolution of multiple ejecta components from a single type of event or could in fact be shaped by different types of events. Disentangling these possibilities requires pinning down the predicted shape of this peak in the presence of different conditions. For instance if fissioning nuclei are produced and their fission yields are assumed to be symmetric, then their daughter products will deposit near $A \sim 130$, influencing second peak abundances [765]. If instead the deposition is mostly asymmetric (e.g. [766, 767]), the $N = 82$ peak can be depleted relative to Solar in favor of enhancements in the abundances of lanthanides and light precious metals like silver [759]. Therefore the shape of the $A \sim 130$ peak connected to $N = 82$ hints at not only the involvement of different astrophysical sites but could also point to what specific types of conditions may be present at a given site.

Thus, around $N = 82$ is an interesting area to further pin down masses, beta-decay rates, and neutron emission probabilities (P_n values) due to their influence on the population of key species. For instance the ^{129}I abundance is connected the physics near $N = 82$, which is of interest since the $^{129}\mathrm{I}/^{247}\mathrm{Cm}$ abundance ratio in meteorites has been shown to be capable of peering directly into the conditions of the last *r*-process event that enriched our Solar System since this ratio does not change as a function of time due to the similar half-lives of these radioisotopes [729]. Species near $N = 82$ are also neutron-rich fission products, which can produce heat and gamma rays during the nucleosynthesis, affecting electromagnetic signals from events like mergers and their remnants [733]. Thus pinning down nuclear structure at and near $N = 82$ is tied to key astrophysical observables.

How nuclear structure evolves as one approaches the dripline is not only of interest for fundamental dripline studies, but also of relevance for nucleosynthesis predictions. For instance, astrophysical conditions with particularly high neutron densities can find the synthesis to occur very near the dripline (see for example the fission cycling *r*-process path in figure 11). The first ever FRIB experiment explored isotopes approaching the neutron dripline near $N = 28$ [3], which well demonstrates the special role FRIB can play in illuminating dripline physics in the neutron-rich regions. Note that the *r*-process paths of all *r*-process example cases in figure 11 show pile-up to occur at $N = 82$ outside the black line of previously probed nuclei. Thus pressing $N = 82$ measurements down toward the $N = 82$ dripline would take full advantage of the wealth of neutron-rich species FRIB is capable of making for the first time and would be of great interest to nuclear astrophysics.

Lanthanide nuclei. Neutron-rich lanthanide species (with $Z = 57$–71, also called rare-earth nuclei) share a fortuitous overlap with the FRIB production reach. Measurements in this region have been extended and made more precise in recent years, for example at the Canadian Penning Trap (CPT) at CARIBU at Argonne [768], Jyväskylä [769], and RIKEN [770]. Therefore, excellent benchmarks exist for future FRIB experiments to capitalize on when looking to further such explorations toward currently unprobed species. Thus this area provides a wealth of discovery opportunities while also capitalizing on more recent efforts.

Rare-earth nuclei are also connected to long standing questions of heavy element production as well as new observational capabilities. For instance, the Solar isotopic pattern hints of an enhanced stability of neutron-rich lanthanide species due to a peak found near $A \sim 164$ which is not connected to a closed shell [760, 771]. Since nuclear masses reflect underlying structure, here mass measurements are especially important. Mass measurements will also propagate into the nucleosynthesis predictions through separation energies determining neutron capture and photodissociation rates, as well as beta-decay half-lives and P_n value predictions. In particular, the properties of $Z = 58$–62 nuclei with neutron numbers $N \sim 104$–110 have been found to be especially connected to whether simulations can reproduce the rare-earth peak [772]. Given the overlapping FRIB reach in this area, the

prospect of resolving the longstanding question of rare-earth peak origins within the next decade is promising.

Another important open question in heavy element nucleosynthesis is the origin of the so-called 'robustness' or 'universality' of lanthanide abundances in the abundance patterns of metal-poor stars rich in *r*-process elements. That is, here metal-poor stars have shown a remarkable consistency with each other as well as the Solar abundance pattern, when it is common for studies to find the abundance pattern to be sensitive to the astrophysical conditions present at the nucleosynthesis site [764, 773]. Could this be hinting that the astrophysical site of *r*-process production that enriched our Sun is the same as the source that enriched these stars? Does this mean that the *r* process occurs in a similar way throughout the Galaxy? Or does this hint that there are nuclear physics processes at play such as fission cycling that could wash away any initial differences in the astrophysical conditions? To address these questions, an understanding of the properties of neutron-rich lanthanides (such as masses, beta-decay rates, and P_n values) is crucial in order to pin down how rare-earth abundances are finalized during the *r* process.

Other key investigations over the last few years also bolster the community's interest in the lanthanides, such as modeling kilonova light curves from neutron star mergers as well as a budding interest in the *i* process. Although the *i* process was first proposed decades ago [774], it has gained traction in recent years through indications that some metal-poor star patterns are best fit by something with a neutron density between that of an *s* process and *r* process [775, 776]. Additionally, recent hydrodynamic simulations of rapidly accreting white dwarfs and certain types of AGB stars have shown the neutron densities needed for an *i* process to be possible in these environments [777, 778]. This process has been predicted to take place only a few neutrons away from stability where neutron capture timescales can exceed those for beta-decay (see figure 11). Thus studies have found that the *i* process is most sensitive to neutron capture rates and would greatly benefit from constraints on these models [779] (from either surrogate measurements or methods such as Beta-Olso informing the strength functions and level densities that enter neutron capture predictions). The lanthanides are a particularly interesting region to study from an *i*-process perspective, with elemental abundance ratios in stars such as [Ba/Eu] being used to differentiate *i*-process enrichment from *s* process and *r* process [780]. As noted above another important aspect of the need to improve lanthanide abundance predictions lies in the sensitivity of kilonovae to the overall lanthanide mass fraction present in the ejecta. The high atomic opacities of lanthanide species give them the ability to push the light curve to longer timescales and toward the infrared, thereby providing the opportunity for conclusive identification of such species in the ejecta (as was the case with the first ever observed neutron star merger GW170817). New insights into mergers from the kilonova of this event are still being discussed and future gravitational wave detection prospects further present an urgency to refine our predictions of the evolution of spectral features of kilonova [781] so that more conclusive statements can be gleaned about the amount of mass ejected [734], the geometry of the ejecta [782, 783], and the value of the Hubble constant [784].

Nuclei near N = *126*. The solar abundance distribution also shows a peak at $A \sim 195$ associated with nucleosynthesis undergoing pile-up at $N = 126$. Studying this peak is directly connected to illuminating the production of platinum and gold as their stable isotopes can be found at $A = 195$–196, 198 and $A = 197$ respectively. Here FRIB has the ability to inform modeling of reaction rates, beta-decays and masses greatly since at the present there are no measurements past ^{206}Hg ($Z = 80$) on the $N = 126$ isotonic chain. Even though the FRIB reach will be unable to explore the dripline at $N = 126$, pushing measurements down this chain toward the dripline is crucial for an understanding of the strength of this shell closure.

Current mass models predict very different strengths of this shell closure (i.e. how big of a drop there is in the one neutron separation energy at $N = 126$) which leads to different predictions for how long species are held up here before the synthesis can proceed to the actinides. Thus the $N = 126$ shell closure has been referred to as the 'gateway to the actinides' and studies have shown that predicting the abundances of long lived-actinides such as ^{232}Th and ^{235,238}U are sensitive to the mass trends [728, 785, 786] and to beta-decay rates [758] around $N = 126$. Additionally, for some nuclear structure models the ability to approach the heaviest regions of the nuclear chart may only be currently possible at or near closed shells like $N = 126$ given the simpler valance structure here compared to that needed to be considered in the deformed rare-earths. Therefore this area offers a nice overlap between astrophysical interest and approachability by both nuclear structure theory and experiment.

In addition to the influence that the masses have on the nuclear flow at $N = 126$ (e.g. [787, 788]), beta-decay rates around this closed shell have been shown to also greatly affect abundance predictions. Global rate calculations have found that including first-forbidden transitions changes predictions significantly [751, 752] which can lead to faster rates to the right versus left of $N = 126$. Therefore studying beta-decay strength functions and rates around $N = 126$ is impactful for global structure models and astrophysics. Currently, the nuclear physics uncertainties in the region stymie the ability to conclusively link unique features of the associated $A \sim 195$ abundance peak, such as its overall width, with particular types of astrophysical conditions. For instance, it had previously been discussed that potentially neutron star mergers could not be the source of Solar System enrichment due to the narrow third peak predicted when these very neutron-rich environments see significant late time neutron capture. However studies later showed that using different beta-decay treatments can change the third peak abundance predictions toward something more in line with the Solar width [789]. Another interesting link between third peak abundances and astrophysical conditions lies in considering 'slow' versus 'fast' ejecta components, since studies have shown that fast (i.e. rapidly expanding) ejecta can be tied to a shift in the third peak toward higher mass numbers [731, 790–794]. In addition to clear connections between $N = 126$ and the astrophysical environment, unlike $N = 82$ and rare-earth regions, there are no potential contributions from fission deposition here, making $N = 126$ abundances less convoluted than other parts of the pattern. Therefore measurements which put $N = 126$ structure on firmer footing are directly connected to diagnosing whether or not abundance predictions for a particular astrophysical environment align with observations.

Long-lived actinides. Information on actinide species (found beyond $N = 126$ and ^{208}Pb) has been disproportionately mapped out in neutron-deficient regions over neutron-rich regions. For instance, although it is an important channel during the decay of heavy *r*-process species, beta-delayed fission has never been experimentally observed on the neutron-rich side, so confirmation alone would be important progress. Thus exploratory missions to push the boundaries on neutron-rich actinide measurements would take incredibly important steps of great benefit to those modeling neutron-rich actinide properties. This is also a regime that could shed light on nuclear structure given the speckled branching ratios between beta-decay, alpha-decay, and spontaneous fission seen here. Additionally, several species in this region are known to have anomalously long half-lives on the order of days, years, or longer which can have important consequences for observations of electromagnetic signals from astrophysical events such as mergers (light curves are sensitive to decays that take place on the order of the expansion timescale).

For instance it has been discussed since the early days of nuclear astrophysics that ^{254}Cf with its ~60 day spontaneous fission half-life could greatly affect kilonovae [717] due to its high Q-value introducing heat into the system, as well as the high thermalization efficiency of

fission fragments [731]. Note however that the effect ^{254}Cf could have specifically on kilonovae has only been discussed in the last few years following GW170817 [737, 738]. ^{254}Cf serves as an excellent example of the key pieces of nuclear data lying just outside current measurements since its direct beta-feeder ^{254}Bk, which provides the only pathway to populate ^{254}Cf, has unknown branching ratios. Thus, should ^{254}Bk be found to undergo alpha-decay 100% of the time, the long-standing question of ^{254}Cf's potential impact of light curves could be definitively answered. It is not just long-lived ^{254}Cf that makes neutron-rich actinide branching ratios important to probe. Since neutron-rich actinides are largely unprobed territory there lies the opportunity to find others like ^{254}Cf. For instance, studies have found a few neutron-rich rutherfordium isotopes with theoretical spontaneous fission half-lives on the order of days to also be able to impact light curves greatly and allow for identification of superheavy elements in the ejecta [733, 795]. Additionally, studies of MeV gamma-ray emission from real-time *r*-process events have found gammas with energies $>$3.5 MeV to be unique to fission since neutron-rich species that have high enough Q-values to emit gamma rays in this energy range have already undergone beta-decay [735]. Thus an observation of gamma-rays at energies $>$3.5 MeV requires emission of either prompt gammas from the fission itself or delayed gammas from the beta-decay of the associated neutron-rich fission daughters [735]. Further probing the gamma spectrum from neutron-rich fission species would directly inform such studies and potentially change the expected contribution of prompt fission gammas relative to those from beta-decays. Note that the prospects of observing real-time MeV gamma rays from a merger are limited to either galactic events or events in nearby galaxies such as those within the Local Group (e.g. the large magellanic cloud (LMC)), and further face the challenge of the relative rarity of merger events (estimates range from $\sim$20 to $\sim$400 mergers every Myr in the Milky Way, which is $\sim$100–1000 times less frequent than core-collapse supernovae) [796]. Nevertheless, since gamma spectral features provide a type of fingerprint for specific isotopes, they present the important prospect of detailed information on the ejecta composition [797, 798]. Additionally, gamma-ray observations offer unique opportunities to identify the remnants of the Milky Way's last neutron star mergers [798, 799].

Spontaneous fission is not the only process of interest since alpha particles have also been shown to efficiently thermalize in merger ejecta thus long-lived alpha-decays can play a dominant role in late-time kilonova heating when there are no species undergoing spontaneous fission to compete with [731, 739, 800]. Alpha-decays on the order of hours, days, or years can also lead to distinct MeV gamma ray emission from mergers, as is highlighted by the recently introduced prospect of utilizing the 2.6 MeV gamma-ray line of ^{208}Tl as a beacon of *in situ* neutron capture nucleosynthesis [796]. Although the role it can serve to identify the isotopic composition in astrophysical environments has only recently been highlighted, this particular emission line of ^{208}Tl is well-known in numerous other fields of science, including clinical imagining studies utilizing ^{224}Ra [801], geological surveys estimating thorium concentrations [802, 803], nuclear safeguard measures looking for highly enriched ^{232}U [804], and as a well-established background and calibration point for experiments [805, 806]. The ^{208}Tl emission line could be visible during the electromagnetic follow-up of a neutron star merger event, or could be observed locally from an AGB star or rapidly accreting white dwarf actively synthesizing the heaviest elements, and would correspond to an unambiguous signature of the production of ^{208}Pb and thus elements lighter than lead such as gold could be conclusively stated to be present. The ^{208}Tl 2.6 MeV gamma-ray line shows itself on observable timescales due to the alpha decays feeding this species on the order of hours (^{212}Bi), days (^{224}Ra) and years (^{228}Ra). Since the observable timescales of kilonovae and MeV gamma emission align with the decay timescales of long-lived actinides,

pushing the boundaries of known half-lives and branching ratios in the neutron-rich actinides has clear and direct connections to deciphering the electromagnetic emission from multi-messenger events. Thus should developments at FRIB permit studies of this area, this region offers high impact overlap between measurement opportunities and nucleosynthesis needs.

8.2.3. Connecting FRIB to the synthesis of elements between iron and tellurium. In astrophysical environments such as neutron star mergers and collapsars there is the possibility to form a disk around the central remnant (e.g. [807, 808]) and the ejecta from this disk can have conditions which support *r*-process nucleosynthesis. Although previous studies suggested disk material to be more processed and thus generally less neutron-rich than that which is dynamically ejected earlier during the merger [792, 809], more recent studies which run their hydrodynamic simulations out to longer times (>1 s) have changed this picture [740, 810–812]. Thus both merger dynamical ejecta and post-merger accretion disks are comprised of a distribution of ejecta types (e.g. [813, 814]), correspondingly producing a wide range of elements all the way from the *r*-process first peak at $A \sim 80$ to beyond the third peak at $A \sim 195$. This is achieved via the total ejecta hosting a range of neutron-richness Y_e, as well as a variance in the manner that the temperature and density evolves. We refer to the components of the ejecta with synthesis taking place between $N = 50$ and $N = 82$, and forming elements with mass numbers between $A \sim 80$ and $A \sim 130$ such as strontium and silver, as undergoing a 'weak' *r* process (shown in figure 11). For weak *r* processes in both mergers and supernovae, (α, n) reactions can also play an important role [815]. The prediction of both weak and main *r*-process production in mergers is supported by the observations surrounding GW170817, where first a lanthanide-free blue component (such as a weak *r* process) was first observed followed by a red component containing lanthanide elements [720, 721], and further bolstered by the identification of Sr in the absorption spectrum [816].

Thus, in the weak *r*-process regime between $N = 50$ and $N = 82$, there are opportunities to impact *r*-process studies through measurements of masses, beta-delayed neutron emission probabilities P_n, and (α, n) reactions. Additionally, surrogate measurements to inform neutron capture have begun to penetrate the neutron-rich regions in the $N = 50$–82 regime relevant for *i*-process abundance predictions [817]. Such measurements would not only inform *i*-process predictions, but serve to constrain and inform the neutron capture models relevant for the *r* process by providing systematics that can be applied further along the isotopic chain. Studying the Solar System composition of elements from Sr to Sn is therefore dependent on pinning down the nuclear physics properties of relevance for weak *r* process as well as weak *i* process so that their relative contributions can be teased out. Additionally, how these compare to contributions from supernovae (e.g. [818–820]) and other events capable of forming elements between iron and tellurium can then be better addressed.

An additional recent development that makes this region of interest is the prospect of identifying the signature of fission fragment deposition here. Recent works have demonstrated that asymmetric fission taking place late during the *r* process can inject neutron-rich daughter products which stabilize the abundances of light precious metals such as silver and palladium relative to the lanthanides [759]. This introduces a new type of 'universality' of lanthanide abundances relative to light precious metals which can be verified through comparison with trends in stellar abundance ratios [759, 821]. Thus constraining the nuclear properties along the decay path of fission daughter products would help to constrain whether fission deposition signatures have been hiding in metal poor stars, which would connect FRIB to approved future observations with the Hubble Space Telescope aimed at measuring the currently scarce cadmium ($Z = 48$) abundances of relevance to this question.

Weak processes and in particular (anti)neutrino absorption reactions play a fundamental role in determining the proton-to-nucleon ratio both in core-collapse supernovae and neutron-star mergers. Those reactions are expected to operate on nucleons as nuclei typically form once the neutrino fluxes have substantially decreases as the ejecta moves away from the neutrino source. However, it is interesting to consider what will happen if neutrino fluxes remain large once nuclei are formed. Under these conditions, and assuming moderate neutron-rich ejecta, a kind of *r* process may operate where the increase in element number is due to charged-current neutrino reactions instead of beta-decays. This process has been named νr process [822] and is expected to contribute to the production of neutron deficient nuclei, the so-called p-nuclei, particularly ^{92,94}Mo and ^{96,98}Ru. Compared with other alternative scenarios like the νp process, it has the advantage that can produce the long lived ^{92}Nb that has been observed in the early solar system. At the moment, it is unclear the astrophysical scenario in which the νr process may operate. Most likely it involves magnetically driven outflows like those found in magneto-rotational supernovae or collapsars. From the nuclear physics side, it requires neutrino-nucleus cross sections for nuclei to both sides of the stability valley. They require knowledge of both Gamow–Teller and forbidden strength distributions that can be determined by charge-exchange reactions (e.g. [149]).

8.3. Nucleosynthesis on the proton-rich side of stability

8.3.1. FRIB Experiments addressing stellar nucleosynthesis. Stellar nucleosynthesis produces the majority of elements in nature, and proceeds mostly along the valley of stability through reactions on stable nuclei. This is a consequence of the long burning timescales that allow ample time for the majority of rare isotopes produced in a nuclear reaction to decay back to stability before the next nuclear reaction occurs. However, during the explosive burning of oxygen and silicon during a core collapse supernovae marking the endpoint of the stellar nucleosynthesis sequence for massive stars, timescales are much shorter and reactions on rare isotopes become important. This stellar burning stage is important to explain the origin of isotopes and elements in the Si–V range, and also contributes, together with thermonuclear supernovae, to the iron peak elements (e.g. [823]). In addition, explosive silicon and oxygen burning is responsible for the synthesis of a broad range of γ-ray emitters that are sufficiently long-lived to be ejected by the supernovae to be observable with space or balloon based gamma-ray observatories [824–826]. The production of the longest-lived gamma-ray emitters are also important to explain supernova light curves, meteoritic signatures of early solar system radioactivity (e.g. ^{53}Mn), isotopic signatures in pre-solar grains (e.g. ^{44}Ti) or the composition of cosmic rays (e.g. ^{44}Ti, ^{49}V, ^{51}Cr, ^{55}Fe, ^{57}Co, and ^{59}Ni) (see [825] and references therein).

During explosive oxygen and silicon burning, the stable $N = Z$ products of previous stellar burning, predominantly ^{16}O, ^{20}Ne, ^{32}S, and ^{28}Si, are rapidly driven toward nuclear statistical equilibrium by a wide range of fusion reactions as well as α, p, and n induced reactions. As weak interactions are not in equilibrium, the neutron to proton ratio remains roughly equal and nucleosynthesis proceeds mainly along the $N = Z$ line toward the iron region, thus involving neutron deficient rare isotopes. However, the region of nucleosynthesis is broad, and in a few cases, driven by captures of neutrons released in the nuclear reactions, extends a few mass units out on the neutron rich side, e.g. to ^{43}K, ^{47}Sc, or ^{59}Fe.

In principle, equilibrium nucleosynthesis is expected to be relatively independent of detailed nuclear reaction rates. However, as temperatures are dropping during nucleosynthesis, equilibrium breaks up into an increasing number of equilibrium clusters connected through slow reactions that are critical for determining the final nucleosynthesis outcome. The

important reactions for the synthesis of isotopes of interest have been identified in sensitivity studies [825, 827–829] and include a large number of α, p, and n induced reactions on stable and radioactive targets up to Ni. It will be feasible at FRIB to produce reaccelerated beam for many of the radioactive cases of interest, as the relevant nucleosynthesis temperatures are relatively high (typically 1–3 GK but in some cases reaching up to 5–6 GK) resulting in relatively larger cross sections, and as the target nuclei are relatively close to stability facilitating beam production. Proton and α-induced reactions could then be readily measured directly with the SECAR recoil separator, the JENSA gas jet target, the AT-TPC active target time projection chamber, or the MUSIC multi-sampling ionization chamber detector (see discussion of experimental set-ups in section 3).

For (n, p) and (n, α) reactions, probing the reverse reaction may provide valuable constraints. It will be important to carry out a parallel effort at stable beam and neutron beam facilities to determine or constrain the reactions on stable targets. Only a comprehensive program will ultimately advance our understanding of supernova physics and the origin of the elements.

8.3.2. FRIB experiments addressing the p process. The p process is a classical nucleosynthesis process defined as being responsible for the synthesis of the rare neutron deficient stable isotopes between ^{74}Se and ^{196}Hg that cannot be produced by neutron capture processes, the so called p-nuclei. Nowadays a γ process is thought to be responsible for the synthesis of the p-nuclei [830]. In the γ process an initial distribution of heavy seed nuclei, for example produced by a previous s process in a previous generation of stars, is exposed to sudden heating that induces (γ, n) photodisintegration reactions that drive the composition to neutron deficient unstable isotopes. The composition is further modified by subsequent (γ, p) and (γ, α) reactions, as well as the inverse capture reactions capturing the released particles. Proposed sites are the explosive O/Ne burning in core collapse supernovae, or the outer layers of thermonuclear supernovae.

A long-standing challenge has been the synthesis of the p-nuclei ^{92,94}Mo and ^{96,98}Ru that are particularly abundant in the solar system, and cannot be produced with sufficient abundance in standard γ-process scenarios. Accurate nuclear physics is needed to test various proposed model solutions to this puzzle, and to ultimately use p-process nucleosynthesis to probe the physics of core collapse supernova shock fronts, the physics of thermonuclear supernovae, and the physics of the supernova progenitor stars that potentially impacted the distribution of heavy seed nuclei for the γ process. The most important reactions have been identified in sensitivity studies [831–833] and include a mixture of reactions on stable and unstable neutron deficient nuclei in the $A = 71$ to $A = 196$ mass range. While the reactions on stable nuclei have been measured in many cases, information on the reactions on unstable nuclei is extremely limited, with first limited experiments only being performed very recently [834]. There is an opportunity to address this lack of data at FRIB. In particular the important branchings between (γ, n) and (γ, p) or (γ, α) are mostly located a few mass units away from stability and can be probed by measuring directly the inverse (p, γ) and (α, γ) reactions. As level densities tend to be high, important information can already be obtained with limited early FRIB beam intensities by measuring excitation functions at the upper end or above the Gamow-window. Such measurements can already provide constraints for statistical model inputs, especially the relatively uncertain α-optical potential. Experiments can be carried out using gamma detection arrays such as SuN [835], which can be combined with SECAR for increased sensitivity.

8.3.3. FRIB experiments addressing the νp rocess. Neutrino-driven outflows as part of core-collapse supernova ejecta have long been discussed as site for heavy element nucleosynthesis, especially for the *r* process. There has been a tremendous progress in simulations of core-collapse supernovae allowing for fully self-consistent three-dimensional explosions. These calculations seem to indicate that strong neutrino fluxes irradiating the innermost supernova ejecta drive the composition mostly to proton-rich conditions, though small pockets of neutron rich regions may still produce a weak *r* process. Under such proton-rich conditions the νp process is expected to operate. It is a sequence of proton captures and (n, p) reactions producing neutron-deficient nuclei like ^{92,94}Mo and ^{96,98}Ru. Proton capture reactions operate closer to the stability than for the *rp* process and may be more amenable to a statistical treatment. (n, p) reactions are particularly important and several key reactions have been identified [836]. (n, p) reactions on unstable targets can be constrained at FRIB by directly measuring the inverse (p, n) reaction in inverse kinematics by using reaccelerated beams with for example the SECAR recoil separator in conjunction with a neutron detection array. Proton capture rates on unstable nuclei can be measured using the same techniques discussed for the *p* process.

8.3.4. FRIB experiments addressing the rp process in x-ray bursts. X-ray bursts are thermonuclear explosions on the surface of neutron stars that accrete matter from a binary companion. In systems where the accreted material is hydrogen rich, and where the CNO cycle does not burn all the hydrogen prior to the ignition of the burst, bursts are powered by the rapid proton capture process (*rp* process). The *rp* process synthesizes heavy elements up to $A \approx 110$ via a proton captures and beta-decays proceeding on the proton rich side of the valley of stability [837–839]. The possible contribution of the rp-process to galactic nucleosynthesis is an open question. While models predict the ejection of some material during a burst [840, 841] the historical frequency of events is likely insufficient for a significant contribution. However, accurate predictions of the nucleosynthesis are needed to predict possible spectral signatures of the ejected material that could be searched for with future x-ray observatories, and to predict the composition of the neutron star crust that is determined by the majority of burst ashes that remains on the neutron star [842]. The latter is essential for modeling crust processes and neutron star cooling observables in transiently accreting systems (section 8.4).

Furthermore, due to the slow beta-decays in the reaction sequence, the *rp* process is relatively slow and significantly extends and shapes the burst light curve. With accurate nuclear physics, burst light curve observations in systems with stable bursting behavior, where multiple bursts can be averaged to obtain a precise light curve, can be compared with models to extract the surface red shift, which provides a constraint on the mass-radius relationship of the neutron star and the nuclear equation of state [843].

The important nuclear reactions that affect observables in x-ray bursts have been identified in sensitivity studies [843, 844] and involve mostly unstable, neutron deficient target nuclei. In the vast majority of cases, reaction rates have not been measured directly. With reaccelerated beams at FRIB direct measurements of (p, γ) reactions will be possible with the SECAR recoil separator once beam intensities reach 10^6 pps or more. (α, p) reactions can already be probed at somewhat lower beam intensities using either the JENSA gas jet target [845], the AT-TPC active target time projection chamber [846], or the MUSIC multi-sampling ionization chamber [847]. As many of the important reactions are relatively far from stability, level densities are low and reaction rates tend to be dominated by single, isolated, narrow resonances. In these cases, indirect experimental approaches can already dramatically reduce reaction rate uncertainties. These include beta-delayed particle emission, for example

with the GADGET active target system [848], and (d, n) transfer reactions using the GRETINA gamma detection array with the LENDA neutron-detection array [849]. Both techniques are particularly well suited for early FRIB experiments, the former because of the relatively low beam intensity requirements, and the latter due to the fact that the experiments can be performed with fast beams avoiding the beam losses from stopping and reaccelerating. (d, n) transfer reactions can also be measured with the SOLARIS spectrometer taking advantage of reaccelerated beams from ReA6 for measurements at lower energies. The future ISLA spectrometer will also open up opportunities for such indirect reaction measurements.

8.4. Accreted neutron star crusts

Transiently accreting neutron stars offer an observational window into the physics of the neutron star crust [842]. During an accreting outburst, the crust is heated by various types of thermonuclear x-ray bursts on the surface, as well as by nuclear reactions throughout the outer and inner crust, induced by the continuously increasing local pressure due to the ongoing accretion. During the subsequent quiescent phase that can last in quasi persistent transients for years, the cooling of the crust can be observed through repeated x-ray observations of the decreasing surface temperature. Such cooling curves provide insights into the structure of the crust, neutron superfluidity, nuclear pasta, and the nature of the neutron star core. The nuclear reactions may also induce density jumps that may lead to gravitational wave emission as the neutron star is rapidly spinning [850]. Interpretation of these observables requires accurate nuclear physics of nuclei up to mass 110 from stability to the neutron drip line. While the majority of these nuclei are expected to be within reach at FRIB in the future (including the FRIB400 upgrade), early experiments can already extend the boundary of known masses, electron captures, and beta-decay transition strengths of importance for heating and cooling of the crust through neutrino losses. The FDSi FRIB decay station initiator will be able to measure ground state to ground state beta-decay transition strengths by measuring beta-delayed neutrons and gamma rays via the MTAS or SuN total absorption spectrometers [178]. LEBIT Penning trap mass measurements and time-of-flight mass measurements can extend knowledge of the mass surface significantly, including the critical ^{40}Mg region. New machine learning techniques, for example using Bayesian mass model averaging, are being developed to extend the impact of new measurements to short distance extrapolations [230, 851].

Charge exchange measurements on neutron rich nuclei in the EC/$\beta+$ direction provide unique experimental information on the Gamow–Teller strength in this direction [149]. Experiments can be carried out on selected nuclei that can be used to evaluate theoretical models that are be used for the entire ranges of nuclei required for astrophysical modeling. Collaboration with theory is needed to help choose the optimal targets. The (d, ^{2}He) reaction in inverse kinematics with the AT-TPC active target time projection chamber has recently been developed as a tool [162].

9. Fundamental symmetries

Despite its great success, the Standard Model (SM) of particle physics falls short to explain many important observed phenomena in cosmology, such as dark energy, dark matter, the baryon asymmetry of the Universe and the neutrino mass, which calls for the search of physics beyond the Standard Model (BSM). The test of various fundamental symmetries of the SM, such as C, P, T-symmetry, lepton and baryon number conservation, existence of Lorentz-invariant currents beyond the 'vector minus axial' ($V - A$) structure and the flavor-universality in weak interactions, constitutes a major component in the search of BSM

physics at the 'precision frontier', with the hope to unveil small differences between experimental results and SM predictions. Famous examples of such experiments include neutrinoless double beta decay ($0\nu\beta\beta$), searches for permanent electric dipole moments (EDMs), parity-violating electron scattering (PVES), muon $g-2$, and precision beta decays. Their importance is well articulated, for example, in the 'Fundamental Symmetries, Neutrons, and Neutrinos' (FSNN) whitepaper for the 2023 Nuclear Science Advisory Committee (NSAC) long range plan [852].

Many such experiments are carried out in hadron/nuclear systems. Apart from requirements of experimental precision, a proper understanding of the relevant hadronic or nuclear physics is necessary to (1) disentangle the SM background from possible BSM signals, and (2) properly translate the experimental bounds to constraints on BSM parameters. This is extremely challenging due to the large QCD uncertainties. Fortunately, the rapid development of lattice QCD, effective field theory and nuclear *Ab initio* methods in recent years have made first-principles calculations with fully-controlled theory uncertainties possible. At the same time, a data-driven analysis based on dispersion relations allows us to relate the required hadron/nuclear theory inputs to experimental observables. In this section we discuss examples of such developments in both theory and experiment that lead to new breakthroughs at the precision frontier and open new research opportunities relevant to FRIB.

9.1. Nuclear beta decays and CKM unitarity

Low-energy processes mediated by the charged-current weak interaction provide promising ways to test the SM and search for new physics. Within the SM, the strength of the charged current reactions is determined by elements of the Cabibbo–Kobayashi–Maskawa (CKM) matrix [853, 854]. Decays of pions, neutrons, nuclei, kaons, taus, and hyperons allow one to determine two CKM matrix elements, namely, V_{ud} and V_{us}, respectively. The SM predicts that these parameters respect the so-called unitarity relation, $|V_{ud}|^2 + |V_{us}|^2 + |V_{ub}|^2 = 1$, where V_{ub} is so small that it can be neglected at the current level of precision. In recent years, there has been a resurgence of interest in the precise determination of these matrix elements due to the emergence of a number of intriguing tensions at the 3σ level. Mutually-inconsistent results are observed in the determination of V_{ud} from neutron and nuclear beta decays, and V_{us} from leptonic and semileptonic kaon decays, and a global fitting also suggests a $\sim 3\sigma$ deficit in the unitarity relation (see figure 12) known as the 'Cabibbo-angle anomaly', which provides a tantalizing hint for the existence of BSM physics (see, e.g. [855] and references therein).

For a precise determination of V_{ud} useful to test the unitarity relation, a 0.01% precision is needed for both experiment and theory for nuclear beta decays. We will discuss how FRIB can play an important role, to provide both the direct experimental inputs (such as the decay half-lives), and the indirect ones necessary to narrow down the SM theory errors.

9.1.1. Tree-level nuclear structure effects and relations to nuclear charge radii. Superallowed $0^+ \to 0^+$ beta decays of $T = 1$ nuclei provide currently the best determination of V_{ud} because it is a pure Fermi transition of which theory uncertainties are under better control [855]. The direct experimental measurables are the so-called ft-values, where t is the partial half-life and f is the statistical rate function that depends on $Q_{\rm EC}$, the mass difference between the initial and final atomic nuclei.

An important tree-level nuclear matrix element in the superallowed nuclear beta decay is the weak transition form factor. At zero momentum transfer, it gives the well-known Fermi matrix element $M_{\rm F}$; at finite momentum transfer it probes the actual distribution of the active nucleons eligible for charged weak transitions, which we denote as $\rho_{\rm cw}$. Both quantities are

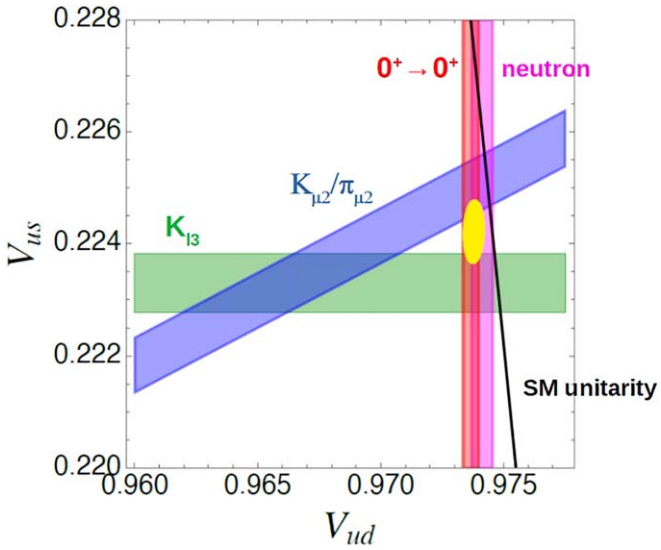

Figure 12. The CKM matrix elements V_{ud} and V_{us} measured from different charged weak decay processes: Superallowed nuclear beta decays ($0^+ \rightarrow 0^+$), neutron beta decay, semiletonic kaon decay ($K_{\ell 3}$) and leptonic kaon/pion decays ($K_{\mu 2}/\pi_{\mu 2}$). Figure reproduced from [855] with permission. Reproduced from [855]. CC BY 4.0.

crucial in the precise determination of the beta decay rate, but both are plagued with nuclear theory uncertainties. First, for superallowed beta decays, we have $M_{\rm F} \rightarrow M_{\rm F}^0 = \sqrt{2}$ in the isospin limit; but isospin-symmetry-breaking (ISB) interactions, predominantly the Coulomb repulsion between protons, introduces a correction $M_{\rm F}^2 = (M_{\rm F}^0)^2(1 - \delta_{\rm C})$. In the past 6 decades [856] the quantity $\delta_{\rm C}$ was computed in various nuclear models, but the results show no sign of convergence (see, e.g. [857] and references therein). Second, the charged weak distribution $\rho_{\rm cw}$ enters the statistical rate function f which, in many existing reviews, was assumed to be very precisely determined. However, the current understanding of this distribution is based on traditional shell model calculations [858], of which theory uncertainties are not properly quantified.

Recent studies show that these quantities can be obtained, in a largely model-independent way, from experimental measurements of nuclear charge distributions which can be performed at, say, the BECOLA facility at FRIB (see, e.g. section 3.2). First, for superallowed beta decays of $T = 1$ nuclei, isospin symmetry relates $\rho_{\rm cw}$ to the charge distributions of the nuclei within the same isotriplet [859]; the latter can be inferred from the nuclear charge radii. At the same time, the isospin-mixing effects that generate $\delta_{\rm C}$ are the same as those inducing ISB corrections to nuclear charge radii, so by precise measurements of the latter one can also probe the relevant nuclear matrix elements responsible for $\delta_{\rm C}$ [860, 861]. Examples of isotopes whose radii are relevant inputs and accessible at FRIB are ^{14}O, ^{26}Si, ^{42}Ti and ^{50}Fe.

9.1.2. Radiative corrections and Ab initio calculations. To extract V_{ud} from the measured Fermi superallowed nuclear beta decay ft values, one needs to apply two nuclear structure dependent corrections. The first is the ISB correction $\delta_{\rm C}$ discussed in the previous subsection, and the second is the $\delta_{\rm NS}$ correction that corresponds to the modification of the single-nucleon axial γW-box diagram (see figure 13) due to nuclear structure effects. These corrections are

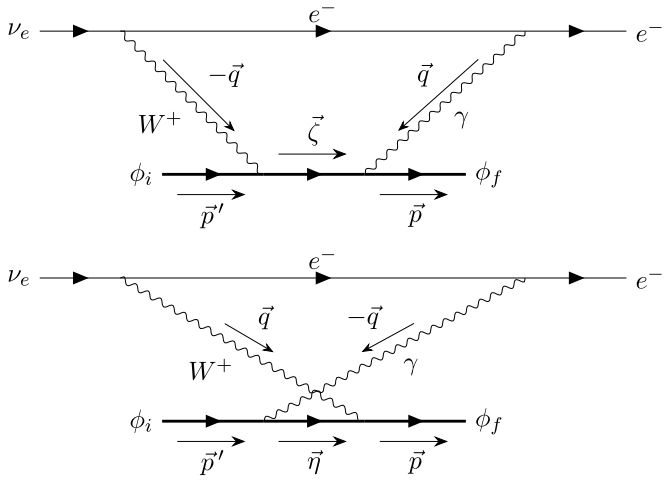

Figure 13. Diagrammatic description of the γW-box, with top and bottom corresponding to time-reversed processes.

known with a rather large uncertainty especially the latter one. In fact, the current uncertainty in V_{ud} extracted from Fermi transitions is dominated by theory.

With advances in *Ab initio* nuclear theory, it now becomes feasible to calculate these corrections from first principles and with a quantifiable theoretical error. For the *p*- and light *sd*-shell nuclei, the quasi-exact NCSM [29] and its extension the NCSM with continuum (NCSMC) [49, 425, 862] methods are applicable. Chiral two- and three-nucleon interactions serve as the input for these calculations.

The NCSM was applied to calculate the δ_C correction for the $^{10}C \rightarrow {}^{10}B$ Fermi transition in the past [863]. It was found that this correction is very slowly converging with the size of the NCSM harmonic-oscillator (HO) basis due to the sensitivity of the correction to nuclear radii and to the admixture of the 1-particle-1-hole states in the 0^+ ground- and the isospin analog final states by the Coulomb interaction. These issues should be resolved within the NCSMC that describes both bound and unbound states in atomic nuclei in a unified way and provides proper wave function tails for the bound states. By applying the recently developed formalism for calculating beta decay transitions within the NCSMC [391], the δ_C correction for the $^{10}C \rightarrow {}^{10}B$ Fermi transition are in progress.

The formalism for the calculation of the nuclear structure correction δ_{NS} has been developed in [864]. On the nuclear many-body side, one needs to evaluate matrix elements of operators consisting of a sequence of an energy-dependent and momentum-transfer-dependent electroweak current, the many-body nuclear propagator (Green's function), and an electroweak current again (see the diagrams in figure 13) between the initial and final states, e.g. the 0^+ ground state of ^{10}C and the final $J^P(T) = 0^+(1)$ excited state of ^{10}B. The computation of the many-body Green's function poses a challenge as it in principle involves the summation of an infinite number of intermediate eigenstates. However, it turns out that the calculation of the Green's function can be facilitated by the application of the continued fraction Lanczos algorithm [865, 866] that has been implemented and applied within the NCSM formalism before, e.g. for calculations of anapole and electric dipole moments [867, 868]. Ongoing δ_{NS} calculations suggest that the convergence with the NCSM basis size is satisfactory, unlike in the δ_C case, and there is no need to apply the much more involved NCSMC approach. Still, the δ_{NS} calculations are quite challenging due to the momentum and

energy transfer dependence of the electroweak operators, and integrations involving poles and residua. The first complete *Ab initio* calculation [869] agrees well with phenomenological calculations used so far in the V_{ud} evaluations [870], but with a significantly-reduced theory uncertainty which indicates the power of the new methodology.

While we presently focus on calculations for the $^{10}C \rightarrow {}^{10}B$ Fermi decay, the NCSM and NCSMC formalism would be immediately applicable to the $^{14}O \rightarrow {}^{14}N$ decay, and with some development to the $^{18}Ne \rightarrow {}^{18}F$ and $^{22}Mg \rightarrow {}^{22}Na$ decays as well. Beyond contributing to V_{ud} extraction, studying the $^{10}C \rightarrow {}^{10}B$ itself is already quite interesting as it provides the most stringent bounds on scalar currents, and any deviation from the SM expectation would be strongly indicative of new physics.

With the *Ab initio* results for the nuclear structure corrections within reach, we call for new measurements of the $^{10}C \rightarrow {}^{10}B$ Fermi decay to reduce the experimental uncertainties in particular of the beta decay branching ratio.

9.2. Tensor and scalar currents in electroweak interaction

The 'vector-minus-axial vector' ($V - A$) structure of the charged-current electroweak interaction in SM has been established thanks to detailed measurements of angular correlations in nuclear beta decay. In addition to the tests of CKM unitarity, beta decay efforts are at the front line in searches for evidence of additional Lorentz-invariant scalar (S) and tensor (T) interactions that arise in SM extensions. In the recent years, experimental developments coupled with state-of-the-art nuclear-theory calculations have resulted in a new generation of beta decay studies that continue to achieve unprecedented precision (see [852] for a more comprehensive review). In particular, atom-traps and ion-traps have been used to accumulate and suspend samples of beta-decaying isotopes in vacuum, allowing for the measurements of the low-energy nuclear recoils, from which the neutrino momentum can be deduced. Experiments have reached increasingly precise results for the beta-neutrino angular correlations in ^{8}Li [871, 872] and ^{8}B [873–875]. Atom traps have been used to determine this correlation in ^{6}He [876] and to polarize ^{37}K atoms to measure the beta asymmetry [877, 878]. These experiments have achieved very high precision ($\sim$0.3%), placing stringent limits on the possible existence of tensor interactions and right-handed currents. There are well-defined paths to further improve this precision. In particular, with the help of *Ab initio* calculations of beta decay observables, several independent studies have provided precision input for the interpretation of beta decays in ^{6}He [879, 880] and ^{8}Li [282], which greatly improves the previous state-of-the-art results.

9.3. Two-body axial vector currents

Unlike the vector current, the weak axial current is not conserved in strong interactions, leading to non-negligible two-body currents which play a significant role in the quenching of GT decay rates [276, 881, 882]. An appealing feature of chiral effective field theory is that it provides a framework for systematically constructing electroweak currents which are consistent with the nuclear force.

While this is a SM process, it also factors into searches for new physics. For example, it has been an open question for decades whether the GT component of the $0\nu\beta\beta$ transition operator should use a quenched axial coupling constant g_A [883]. The same axial current enters into the calculation of structure factors for direct detection of dark matter under the weakly interacting massive particle (WIMP) hypothesis [884, 885], and the γW-box correction for superallowed Fermi decays [886] (see section 9.1.2).

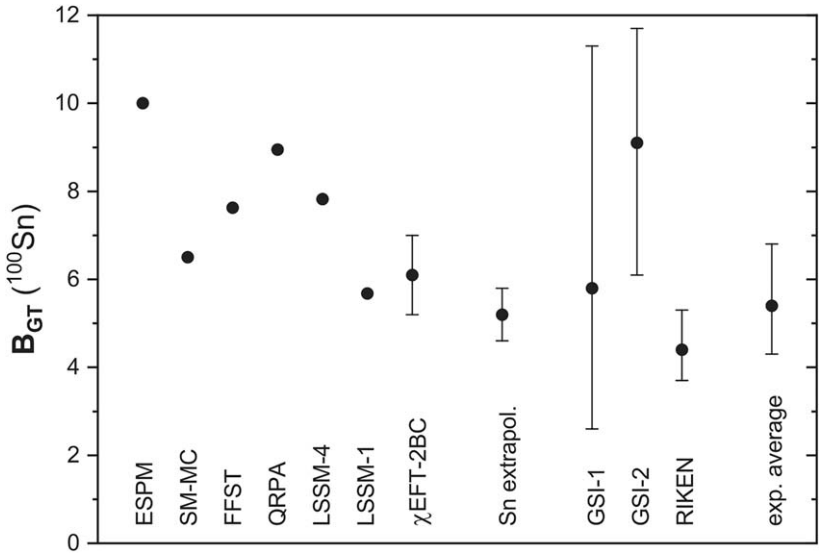

Figure 14. Reduced GT transition probability B(GT) for the decay of ^{100}Sn. The points labeled GSI-1, GSI-2 and RIKEN are experimental, while the other points are theory. Note that the ESPM point has been multiplied by a quenching factor 0.75^2. Taken from [889]. Reprinted (figure) with permission from [889], Copyright (2019) by the American Physical Society.

It is therefore of great interest to validate chiral EFT's systematic approach to the weak axial current. Arguably, the cleanest test of the approach is not the few-nucleon system, but ^{100}Sn. This is because the presence of many particles enhances the effect of two-body currents to ∼30% compared with the ∼2% effect seen in the decay of ^{3}H [887, 888]. In addition, the doubly-magic nature of ^{100}Sn leads to the transition being dominated by a single configuration, so that the many-body calculation does not need to handle fine cancellations among equal-sized terms.

Currently, a significant limiting factor in utilizing the decay of ^{100}Sn is the large experimental uncertainty, as illustrated in figure 14, from [889]. Another measurement with similar precision to the RIKEN result would help clarify the situation.

9.4. Heavy element isotopes for tests of P and T violation

One of the major outstanding puzzles in physics is the predominance of matter over antimatter in the Universe. Explaining this asymmetry requires, among other things, violation of symmetry under CP, equivalent to T violation. While the Standard Model does contain sources of CP violation, these are insufficient to explain the observed baryon density, indicating the need for new physics beyond the Standard Model. Many new physics scenarios would manifest as a permanent EDM of the electron, nucleons, or nuclei [890], which can be searched for experimentally with very high precision. An especially promising system for searching for EDMs is in nuclei with static octupole deformation, which leads to parity doubling and consequentially a dramatically enhanced EDM. Recently it has been proposed that further significant enhancement in sensitivity could be obtained with radioactive molecules [290]. Consequently, the light actinides and especially Ra and Rn have attracted a lot of interest in recent years because their odd-A isotopes could be octupole deformed [288, 891–898].

A recent collaboration between FRIB, Harvard, and MIT has been formed to develop an experimental apparatus for searches for CP violation with radium-containing molecules, such as RaF and RaOH. Precision measurements of these systems are expected to provide insights into the *P*, *T*-violating nuclear Schiff moment of ^{225}Ra. Nuclear theory will play an essential role in connecting Schiff moment measurements with the underlying sources of CP violation.

Recent Coulomb-excitation (CoulEx) experiments established that $^{222-226}$Ra are very likely statically octupole deformed in their ground states, while the even–even Rn isotopes are not [899–901]. Direct measurements of the relevant experimental observables in the odd-*A* isotopes which would be used in EDM searches are still missing, leading to large theoretical uncertainties for the expected enhancement [902]. These properties can be measured with laser spectroscopy on ions and molecules, with an early focus on thorium isotopes. FRIB has developed ^{232}Th^{+}, ^{232}ThO^{+} and ^{232}ThF^{+} beams from the offline BMIS, which will be used for preparatory studies for experiments on short-lived Th isotopes.

In addition to ground-state properties, sub-barrier Coulomb excitation with secondary beams of these odd-*A* isotopes will become possible at FRIB. Especially the expected beam rate for ^{229}Pa at 20 kW power [903] would make such an experiment possible once the secondary beam is developed and GRETA [174] is available at ReA. ^{229}Pa could possibly have the closest-lying parity doublet [904], though the experimental situation is still unclear [905]. Anticipated early-FRIB beam rates for ^{225}Ra are not sufficient to perform detailed γ-ray spectroscopy experiments after Coulomb excitation for which typically 10^5 particles per second (pps) are needed. CoulEx experiments could also test the predicted enhancement of the $B(E3; 3_1^- \rightarrow 0_1^+)$ strength in U and Th isotopes with mass $A \approx 224$–228 [293, 906], which might prove even more octupole collective than $^{222-226}$Ra. Once the secondary beams are developed, these experiments would already be possible at 20 kW power. Either GRETA [907] with a Silicon detector array or CHICO2 [908] for particle detection, or the JANUS setup [189] could be used at ReA.

The results from these experiments together with nuclear models for pear-like nuclei will be essential for the extraction of new physics. Understanding the nuclear structure of these elements is also important to benchmark theories to extend studies to even heavier elements [909, 910].

Molecules can serve as highly sensitive probes for measuring hadronic P-violation, offering enhancements of over eleven orders of magnitude compared to atomic experiments [911]. Recent developments in the field are expected to be implemented at FRIB in the coming decade [912]. Advances in nuclear theory will be crucial for linking future precision studies of electroweak nuclear properties, such as anapole moments [867], with tests of the SM and constraints on new physics.

10. Experimental design and uncertainty quantification

All the topics we have explored cover immense ground in nuclear physics and closely related areas. We now close with a discussion on the role that scientific computing and computational statistics will play in tying everything together to foster the experiment-theory cycle for FRIB science. This cycle is represented schematically in figure 15.

Previous work on experimental design within nuclear physics has usually focused on developing a cost function to be optimized with respect to experimental choices, including the target selection. These approaches have tackled, for example, the selection of momentum transfer measurements for parity violating electron scattering experiments [913, 914], the optimization of the angle and energy settings in proton Compton scattering [915], and the selection isotopes candidates for mass measurements at FRIB [916]. The specific nuclear physics domain, as well as

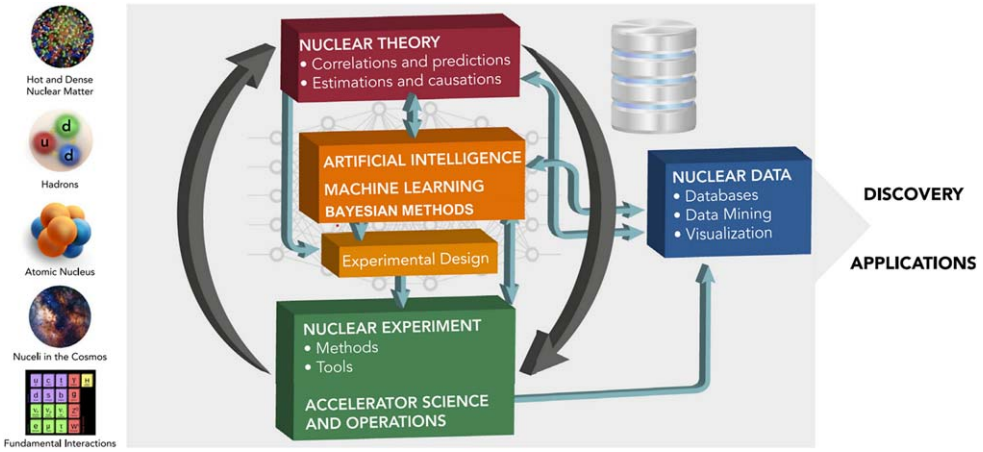

Figure 15. Schematic representation of the theory-experiment cycle in nuclear physics, enabled by Bayesian statistics and advanced scientific computing methods (Adapted from *'Colloquium: Machine learning in nuclear physics (2022)'* [83]). Reprinted (figure) with permission from [83], Copyright (2022) by the American Physical Society.

the details of the different experimental setup vary in a wide spectrum across these and other similar efforts, but in all of them a constant unifying theme is the focus on uncertainties, both from experimental and theoretical origin. Bayesian statistics provides an ideal probabilistic framework to draw conclusions from data in the context of these uncertainties. One main pillar of this framework lies in the explicit and clear statements of all assumptions about the various sources of uncertainties and their interactions. By making these assumptions transparent, the framework naturally lends itself to constant evaluation and refinement of the constructed statistical model. A second, equally important, pillar of Bayesian statistics resides in the philosophy of iteratively updating knowledge using new data. This iterative approach integrates expert knowledge and previous relevant data with new observations to refine our understanding as new information becomes available. This process is defined through Bayes' theorem [105, 917]:

$$P(\boldsymbol{\alpha}|\boldsymbol{D}) = \frac{P(\boldsymbol{D}|\boldsymbol{\alpha})P(\boldsymbol{\alpha})}{P(\boldsymbol{D})}. \tag{8}$$

The *posterior* distribution $P(\boldsymbol{\alpha}|\boldsymbol{D})$ contains the new information on the model parameters $\boldsymbol{\alpha}$, or anything else we are interested in, conditional on the new data $\boldsymbol{D}$. The model could be any of the theoretical frameworks described before, for example DFT [918] or optical potentials [581], or even data-driven approaches such as neural networks [919], Gaussian processes [920], or dynamic mode decomposition [921]. The model parameters $\boldsymbol{\alpha}$ could be those describing interaction strengths or nuclear potential sizes, for example, or hyperparameters controlling the data-driven model. The posterior distribution is built by the combination of the *likelihood* $P(\boldsymbol{D}|\boldsymbol{\alpha})$, which characterizes the process in which the observed data $\boldsymbol{D}$ could correspond to a given parameter configuration $\boldsymbol{\alpha}$, together with the prior $P(\boldsymbol{\alpha})$, which contains all the previous information, as well as expert knowledge, on the model parameters $\boldsymbol{\alpha}$. The *evidence* $P(\boldsymbol{D})$ serves to quantify how well the current overall framework, combining both the theoretical physical model and the statistical description of the uncertainties, accounts for the data $\boldsymbol{D}$. See figure 17 below as an example of a 2D representation of a Bayesian posterior distribution for the parameters of a relativistic mean field model [922].

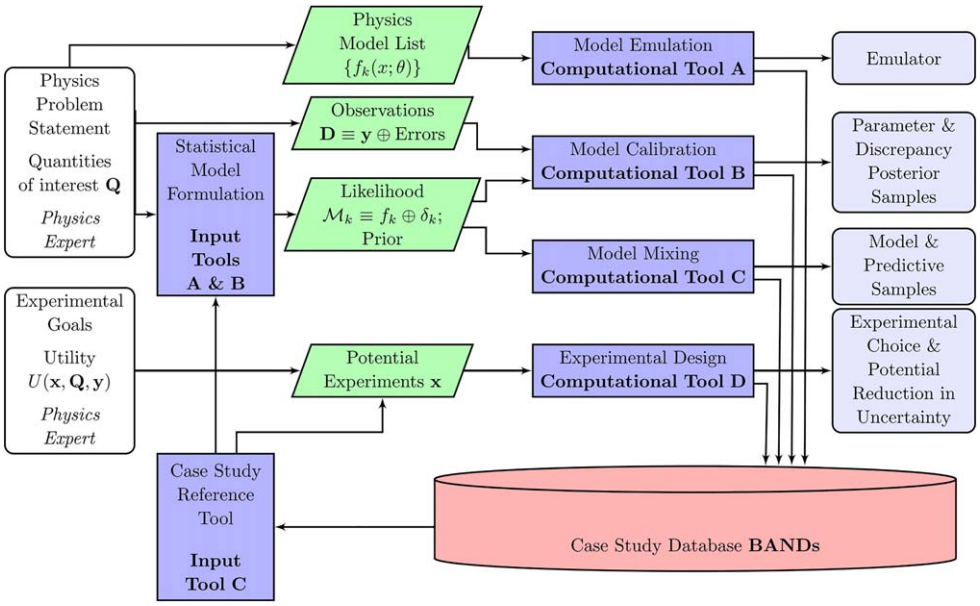

Figure 16. Flowchart of the various tools that are part of the BAND framework [923] (Reproduced from *'Get on the BAND Wagon: a Bayesian framework for quantifying model uncertainties in nuclear dynamics'* [105]). Reproduced from [105]. © IOP Publishing Ltd. All rights reserved.

The process of constructing an adequate prior and likelihood form for a given situation can be a non-trivial statistical task, while the actual exploration and evaluation of the posterior distribution can be computationally challenging. The theory community has recognized [925, 926] and supported a wide spectrum of efforts in these directions, including recurring meetings and workshops such as the Information and Statistics in Nuclear Experiment and Theory series [927], the TALENT school on 'Learning from Data: Bayesian Methods and Machine Learning' [928], and the FRIB-TA Summer School 2023 on Uncertainty Quantification and Emulator Development [929], the creation of collaborations focused on Bayesian methods such as BAND [930] and BUQEYE [931] and computational advancements such as NUCLEI [932], as well as explicit descriptions on the importance of these methods in the 2023 Long Range Plan for Nuclear Science [933]. Figure 16 illustrates the efforts pursued by the BAND collaboration to create useful software for the community in various aspects directly related to this section's discussion.

The calibration and quantification of uncertainties of theoretical models through equation (8) is often done by Markov Chain Monte Carlo methods [917], requiring hundreds, thousands, or even millions of evaluations of the model itself. To mitigate the computational burden that such task entails, a great effort has been done in recent years to develop and implement emulators [918, 922, 934–965], which are algorithms or models that can mimic full theory calculations at a much faster pace with a negligible loss in accuracy. This is usually achieved by either finding and exploiting low-dimensional latent structures to build a reduced order model [922], or by finding alternative maps between inputs and outputs through universal approximants such as Gaussian processes [918] or neural networks [582]. The construction of these emulators requires an appreciable computational cost up-front, but once deployed they allow nuclear theory to reach new calculational frontiers, with the inclusion of uncertainties.

It is worth noting that these ideas and techniques are not unique to nuclear physics, and recent decades have seen tremendous developments across many other science disciplines and engineering [966–968], especially with the rise and rapid development of machine learning [83, 921]. Even outside of the context of model calibration, surrogate models or emulators provide a more efficient way to perform large scale systematic studies or for exploring previously calibrated models for more expensive computational workloads [584]. They can also be used to access, via extrapolations, new computations that are otherwise infeasible. Some examples include computing the properties of quantum systems with Monte Carlo sign problems using parameter extrapolation [935] and the properties of quantum states for different finite spatial volumes [948] and as functions of energy in the complex plane [58] (see section 6.1). Alternatively, some of these methods can be used to directly create data-driven physical models [921, 969–971], giving access to new paths for capitalizing on the available data through the power of machine learning. Further investments in developing and adapting these technologies for nuclear physics will be crucial in the immediate theory-experiment cycle, especially if they can also benefit the actual experimental data acquisition and control (see for example [972] and [973]). Of particular importance will be the creation of user-focused open software tailored to the nuclear physics community as well as education and training activities [929, 942, 958–960].

Once various theoretical models have been calibrated and their uncertainties have been quantified, whenever possible, methods such as Bayesian Model Averaging [974] and Bayesian Model Mixing [975] can help combine their predictions into a more precise and reliable overarching model within the Bayesian framework (see [105] for a detailed explanation of both methods within a nuclear physics context). These approaches compute the uncertainties associated with averaging or mixing models and help in identifying measured observables that are challenging to be reproduced by the collective of models (see, e.g. [245]). This helps to focus future community-wide experimental and theoretical efforts for resolving the discrepancies. In the absence of measured data to compare with, such approaches can help in identifying regions of interest for targeting future experiments where the variability of the collective wisdom of models is maximal [230]. Model extrapolations to uncharted territory is often aided by other machine learning and statistical tools [581, 919, 920, 976, 977]. Similar to the development of emulators, Bayesian model averaging and mixing methods have received increasing attention by the nuclear physics community in recent years [43, 230, 245, 401, 978–984], as well as the creation of user-focused software [985, 986].

As new experimental data becomes available, the calibration and uncertainty quantification of models should be updated as quickly as possible. Without a swift update process, the combined theoretical knowledge will lag behind and will not be able to efficiently contribute to the theory-experiment cycle, leading to sub-optimal decisions and reducing the impact of new experimental campaigns. To address this issue, recent efforts have started for the construction of pipelines for the continuous calibration of theoretical models, exploiting modern machine learning tools for the sampling and storing of posterior distributions [924], as well as leveraging cloud computing infrastructures for the calculation, storage, and distribution, of data [196, 987]. Figure 17 shows the Bayesian posterior parameter distribution from the calibration of a relativistic mean field model [922] learned through the normalizing flow-neural network framework described in [924]. Once the neural network is trained, it can be shared, deployed, and sampled from easily. Once new data becomes available, it can be used as a prior starting point for creating a new posterior, truly embracing the Bayesian philosophy of continuously updating knowledge.

The construction of an online central resource for the storage and continuous update of these theoretical model calibrations and predictions, as well as other resources and tools such

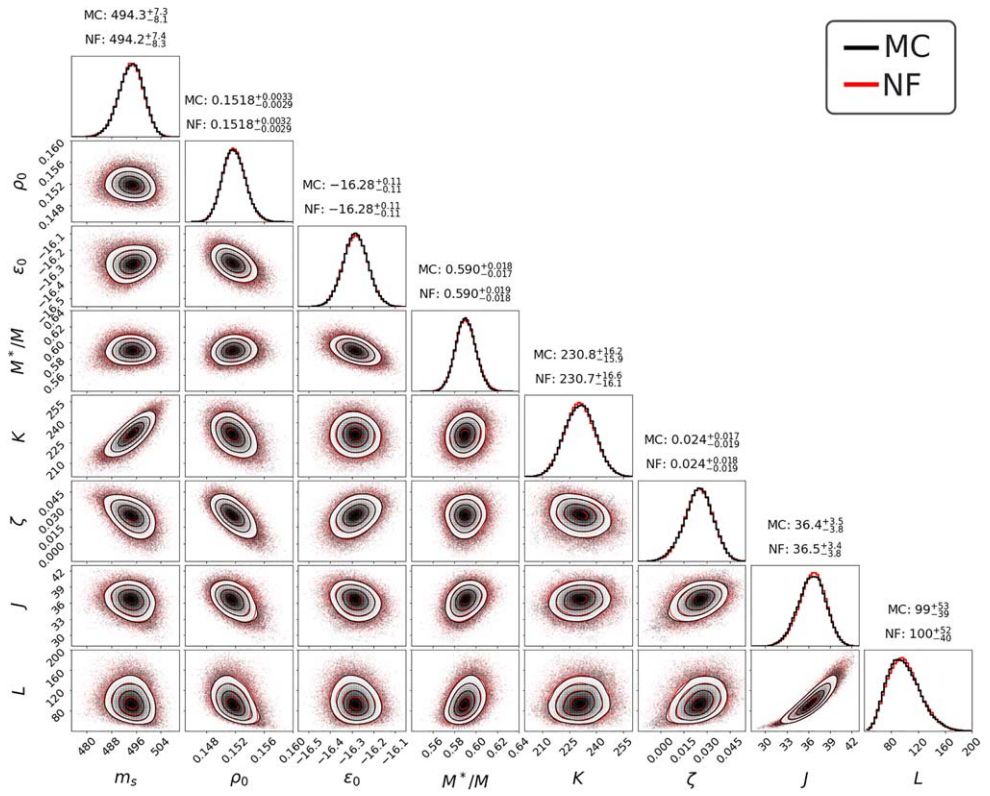

Figure 17. Comparison between the samples obtained by Markov Chain Monte Carlo (black) and Normalizing Flows (red) for the relativistic mean field Bayesian calibration obtained in [922]. The theoretical model has a total of 8 parameters that were calibrated to the masses and charge radii of 10 nuclei. The normalizing flow samples reproduce all the features of the corner plot of the original data, overlapping well enough to make it hard to distinguish between them. (Reproduced from [924]). Reproduced from [924]. CC BY 4.0.

as the developed model emulators and updated experimental conditions, will play a critical role in community efforts. Facilitating interconnection through workshops and easy-to-use platforms [988], embracing the open source philosophy and leveraging cloud computing infrastructures, will help lower the entry barrier for researchers across a wide institutional spectrum, scientific backgrounds, and career stages. This allows many people to add their efforts to the task of sustaining an efficient and effective theory-experiment cycle in FRIB science. These efforts will help to broaden participation in the scientific community in this new era of discovery.

11. Summary

During the last decades, the nuclear theory community sketched a rough road map for a predictive theory of nuclei. Today, low-energy nuclear theory research has substantially matured due to new information on exotic nuclei from exotic beam facilities, novel theoretical methods resulting in quantified predictions, and high-performance computing speeding up the experiment-theory cycle. The important challenge for the field is to bridge different many-

body approaches, describing the nucleus at different resolution scales, in the regions of the nuclear landscape where they overlap.

A goal of research at FRIB is to understand the properties of nuclei by identifying the relevant degrees of freedom, and by connecting these properties to the underlying interaction between nucleons. The relevant degrees of freedom can be collective modes like clustering, superfluidity, vibrations and deformation; they can be related to a set of active nucleon orbitals defined by shell gaps; or they may be related to the proximity of the particle continuum near the driplines. The main new information provided by FRIB will relate to how these features are intertwined and modified in nuclei near the fringes of the nuclear chart, and how these various degrees of freedom interplay with the continuum. In section 4, we used several specific regions of nuclei of importance for the evolution of nuclear structure to illustrate how neutron clustering may impact nuclear properties in ^{28}O, the interplay of quadrupole correlations and the neutron continuum in the region around ^{42}Si, the impact of pairing in the continuum on the neutron-rich end of the Ca isotopic chain, shell evolution leading to a 5th island of inversion around ^{78}Ni, and the proximity of self-conjugate, doubly-magic ^{100}Sn near the proton dripline. While these are specific examples, it is clear that the very concepts and interplays outlined there will repeat as new territory becomes available on the nuclear chart during FRIB's capabiliy ramp-up. Then we singled out aspects of collective degrees of freedom, isospin symmetry, the spin-isospin response of nuclei, and pairing effects.

Near-threshold physics is poised to play an important role in the FRIB scientific program, first and foremost in the exploration of the drip lines, but also in understanding the structure of low-lying resonances of astrophysical interest involving, for instance, clustering. In addition, near-threshold physics strongly impacts properties of many light nuclei, which remain the ideal testing ground for nuclear forces using quasi-exact *Ab initio* approaches.

Several priorities related to near-threshold physics were identified to advance the FRIB scientific mission. One of the main challenges that both theorists and experimentalists will have to face in the exploration of the drip lines is the existence of interplays between standard emergent phenomena such as deformation, clustering, pairing, or collective motion, and near-threshold phenomena. In that regard, and considering FRIB technical capabilities, the region around the $N = 20$ island of inversion near the neutron drip line, where deformation is known to emerge, presents a unique opportunity. Specifically, the study of p-wave halo states in this region, in which p waves are intruder states, could provide valuable insight on how weak-binding affects deformation and rotational motion. Similarly, neutron-rich fluorine isotopes recently appeared as an ideal place to study the effect of the intrusion of a low-lying unbound p wave on nuclear structure in this region. Obtaining a detailed spectroscopy of $^{28-31}$F should be prioritized as well as it may provide important clues as to how far the drip line extends up to $N = 28$. At $N = 28$, the isotope ^{40}Mg, which may or may not have a two-neutron halo ground state, continues to elude our current understanding of the region. Beta-decay studies in this region should be prioritized as well. All these studies will provide stringent tests for nuclear models and help in understanding interplays involving near-threshold phenomena. At a theory level, continuum couplings need to be better accounted for both in effective and *Ab initio* approaches to deal with multi-nucleon resonances and clustered states.

In a broader context, the FRIB scientific program should also seize opportunities to study exotic phenomena such as two-proton decay or near-threshold clustering, which provide unique windows on nuclear correlations and few-body dynamics in nuclei. Finally, while not the primary focus of FRIB, light nuclei must continue to be studied both theoretically and experimentally to improve the quality of first-principle calculations in regions of interest of FRIB and provides insight into complex near-threshold emergent phenomena.

FRIB will bring unprecedented opportunities for exploring bulk behavior of nuclear matter, including carrying out comprehensive studies of the nuclear matter EOS and its dependence on both density and isospin content. Experimental campaigns centered on constraining the EOS will lead to a better understanding of properties of heavy nuclei as well as elucidate the evolution and composition of astronomical objects characterized by extreme densities (such as supernovae, neutron stars, and merging binary neutron star systems) and provide robust constraints for *Ab initio* nuclear theory. At and below the saturation density of symmetric nuclear matter, experimental opportunities to probe the effects of isospin on the EOS include measurements of giant monopole resonances, electric dipole polarizabilities, and scattering data for proton- and neutron-rich nuclei. Both well below and well above the saturation density, relativistic collisions of heavy nuclei (also referred to as central heavy-ion reactions) provide unparalleled opportunities to constrain the isospin-dependence of the EOS. Importantly, extraction of the EOS from measurements relies on comparisons of experimental data to model predictions. A particular challenge in constraining the isospin dependence of the EOS with experimental measurements lies in the fact that, compared to, e.g. neutron stars, the isospin excess in experimentally-available nuclei is relatively small and the effects due to isospin are subtle. Here, FRIB's unique capability to provide high-statistics beams of proton- and neutron-rich heavy nuclei will push the boundaries of accessible values of the isospin imbalance as well as lead to exceptional experimental precision. The proposed FRIB400 upgrade will further dramatically increase the yields of nuclei with large isospin asymmetry, allowing for measuring properties of extreme neutron-rich nuclei, such as neutron skins, as well as for studies of dense nuclear matter up to twice saturation density, critical for multi-messenger astrophysics. On the theoretical side, this opportunity must be matched by development of comprehensive models characterized by high accuracy. Measurements constraining the EOS at and above the saturation density will lead to rigorous tests of *Ab initio* approaches such as chiral Effective Field Theory (see sections 7.1 and 7.2). Observables measured in energetic heavy-ion collisions will not only enable studies of the isospin dependence of the EOS, but also of the momentum dependence of single-particle potentials, the dependence of particle cross sections on density, subthreshold particle production, and nuclear clusters and correlations; here, robust inferences are contingent on reliable inclusion of relevant physical processes in transport model simulations of heavy-ion collisions (see section 7.3). Explorations of the influence of isospin imbalance on nucleon elastic and inelastic scattering on medium-mass and heavy isotopes will lead to tight constraints on optical potentials and, more generally, nucleon self-energies, directly related to the EOS (see section 7.4). With some of the relevant FRIB experimental programs underway (see section 7.5), this is an exciting time for developing strong theoretical foundations for future interpretations of observables related to the EOS.

Nuclear astrophysics studies aim to illuminate the ultimate origin of the elements we observe in nature. From the early days of the field, studies have been centered around the intimate connection between nuclear physics properties and astrophysical observables (such as Solar and stellar element abundances) and thus have always had theory, experiment, and observation recognized to be of equal importance. Given that astrophysical environments produce exotic, unstable nuclei far from stability and beyond currently explored territory, FRIB experiments have the opportunity to shed light on key nuclear properties affecting the formation of elements. The information that FRIB can provide is of relevance to nucleosynthesis studies on both the neutron-rich and proton-rich side of stability, and would aid to understand x-ray bursts, accreting neutron stars, core-collapse supernovae, and neutron star mergers to name a few astrophysical sites. Thus opportunities for FRIB to revolutionize our understanding of element synthesis exist across the nuclear chart. Particularly exciting is the

huge range of new isotopes FRIB will be able to produce of relevance for the rapid neutron capture process (*r* process) which is believed to be responsible for making the heaviest naturally occurring nuclei. Such experimental efforts are quite timely given recent leaps forward in the observational community's abilities in 'multi-messenger science' via collecting numerous distinct observations from an astrophysical event (such as light curves, gamma rays, neutrinos, and gravitational waves). Such multi-messenger information combined with experimental constraints on nuclear properties is the holy grail of nuclear astrophysics, serving to inform models of astrophysical environments and the synthesis they are capable of. In this paper we discuss the various needs for nuclear astrophysics studies, including advancements of global models for nuclear masses, decays (e.g. beta and alpha decays), reactions (e.g. neutron and proton capture), and fission. We also highlight how probing specific regions of the nuclear chart and specific isotopes can help to address some of the most fundamental questions in the field of nuclear astrophysics.

FRIB also offers many opportunities for precision tests of the SM predictions and probe new physics at low energies; the latter, among other things, is needed to address the various unexplained observations in cosmology. As an example, precise measurements of nuclear beta decay lifetimes and correlations (such as $\overrightarrow{p_e} \cdot \overrightarrow{p_\nu}$) allow us to test the CKM matrix unitarity and to constrain exotic electroweak interactions such as scalar and tensor currents; we have seen a tremendous progress in the development of *Ab initio* methods to compute tree- and loop-level nuclear matrix elements in the decay processes. Furthermore, FRIB experiments provides invaluable inputs to pin down important nuclear effects in beta decays, for instance the measurements of nuclear charge radii help to determine the weak decay form factor and isospin-breaking corrections, and the measurement of GT decay rates help to valide chiral EFT's treatment of the weak axial current. Finally, future FRIB experiments on nuclear deformations and excitations will greatly propel the search for permanent EDMs that may provide sources of CP violation to explain the matter-antimatter asymmetry.

In the experimental design and uncertainty quantification section we explore the key role that scientific computing and Bayesian statistics play in the theory-experiment cycle for FRIB science. Within this context, we discuss the use of emulators for speeding up the necessary expensive computations, methods such as Bayesian Model Mixing for combining the predictions of different theoretical models, and the construction of cloud computing-based pipelines for the continuous calibration of these models as new data becomes available. We close the discussion by highlighting that these technologies not only can help in the design of future experiments at FRIB, but can also lower the barrier for new generations to join the scientific efforts, creating a more diverse and inclusive scientific community in this new era of discovery.

Acknowledgments

D.B., A.G., H.I., S.L., and R.L.: Supported by the U.S. Department of Energy, Office of Science, Office of Nuclear Physics award DE-SC0023633 (FRIB).

K.M. and R.R.: Supported by NSF Grant PHY-2111185.

B.A.B.; Supported from NSF Grant PHY-2110365.

K.W.B.: Supported by the National Science Foundation under Grant No. PHY-2309923.

M.A.C.: Supported by the U.S. Department of Energy, Office of Science, under Award No. DE-FG02-95ER40934.

H.C.: Supported by the U.S. Department of Energy, Office of Science, Office of Nuclear Physics under Contract No. DE-AC02-05CH11231 (LBNL).

P.D.: Supported by the U.S. Department of Energy Office of Science Grant No. DE-SC0019209.

C.D.: Supported by the U.S. Department of Energy, Office of Science, Office of Nuclear Physics, under the FRIB Theory Alliance award DE-SC0013617 and under the STREAMLINE collaboration award DE-SC0024233, and by the National Science Foundation under PHY 2339043.

J.E.: Work performed under the auspices of the U.S. Department of Energy by Lawrence Livermore National Laboratory under Contract DE-AC52-07NA27344, with support from LDRD projects 21-ERD-006 and 24-ERD-023.

K.F.: Supported by the U.S. NSF (PHY-2238752) and the U.S. DOE, Office of Science, Office of Nuclear Physics, under the FRIB Theory Alliance, award DE-SC0013617.

Pablo Giuliani: Supported by the National Science Foundation CSSI program under award number 2004601 (BAND collaboration)

C.H.: Supported by the U.S. Department of Energy under Award No. DE-AC02-06CH11357 (Argonne) through the Office of Science, Office of Nuclear Physics,

R.F.G.R.: Supported by by the U.S. Department of Energy under Awards No.DE-SC0021176 and DE-SC0021179.

K.G.: Supported by the department of Energy under Award Numbers DOE-DE-NA0004074 (NNSA, the Stewardship Science Academic Alliances program), DE-SC0023175 (Office of Science, NUCLEI SciDAC-5 collaboration), and DE-SC0023688; by the National Science Foundation CSSI program under award number 2004601 (BAND collaboration).

R.G.: Supported in part by the Office of Nuclear Physics, U.S. Department of Energy under award No. DE-FG02-96ER40983, and by the National Nuclear Security Administration under the Stewardship Science Academic Alliances program through DOE Awards No. DE-NA0004068.

L.H.: Supported by the U.S. Department of Energy, Office of Science, Office of Nuclear Physics, under Work Proposal No. SCW0498 and LLNL LDRD project No. 22-LW-003, and U.S. Department of Energy, Office of Science, Office of Nuclear Physics, under the FRIB Theory Alliance award DE-SC0013617.

J.H.: Supported by the U.S. NSF under Grant PHY-2209318.

D.L.: Supported by DOE Grants DE-SC0013365, DE-SC0023175, and DE-SC0024586.

A.O.M.: Support from the Laboratory Directed Research and Development Program of Oak Ridge National Laboratory, managed by UT-Battelle, LLC, for the U. S. Department of Energy.

G.M.-P.: Supported by the European Research Council (ERC) under the European Union's Horizon 2020 research and innovation programme (ERC Advanced Grant KILONOVA No. 885281) and the Deutsche Forschungsgemeinschaft (DFG, German Research Foundation)—Project-ID 279384907—SFB 1245, and MA 4248/3-1.

A.M.: Supported by the U.S. Department of Energy, Office of Science, under Award Numbers DE-SC0021027 and DE-SC0013617 (FRIB Theory Alliance).

K.M.: Support from NSF Grant PHY-2111185.

A.M.: Supported by the U.S. NSF Grant PHY-2327385.

B.M.: Supported by the National Science Foundation under Grant No. PHY-2209138 and Grant No. G0002815

P.N.: Support from NSERC Grant SAPIN-2022-00019. TRIUMF receives federal funding via a contribution agreement with the National Research Council of Canada. Computing

support is acknowledged from an INCITE Award on the Summit and Frontier supercomputer of the OLCF at ORNL.

W.N.: Supported by Grants DE-SC0013365 and DE-SC0023688 (MSU) through the Office of Science, Office of Nuclear Physics, and DE-NA0004074 (NNSA, the Stewardship Science Academic Alliances program).

R.R.: Support from NSF Grant PHY-2111185.

G.S.: Supported by the U.S. Department of Energy, Office of Science, Office of Nuclear Physics, under the FRIB Theory Alliance award DE-SC0013617.

H.S.: Supported by NSF award PHY-2209429. The work also benefited from interdisciplinary discussions facilitated by CeNAM DOE award DE-SC0023128 and IReNA NSF award OISE-1927130.

C.-Y.S.: Supported in part by the U.S. DOE, Office of Science, Office of Nuclear Physics, under the FRIB Theory Alliance award DE-SC0013617, and by the DOE Grant DE-FG02-97ER41014.

A.S.: Support by the U.S. Department of Energy, Office of Science, Office of Nuclear Physics, under Grant No. DE-FG02-00ER41132.

M.-C.S.: Supported by U.S. National Science Foundation (NSF) under Grant No. PHY-2012522, (WoU-MMA: Studies of Nuclear Structure and Nuclear Astrophysics).

N.V.: Supported by the Natural Sciences and Engineering Research Council of Canada (NSERC).

A.V.: Supported by the U.S. Department of Energy Office of Science, Office of Nuclear Physics under Award No. DE-SC0009883.

R.Z. and H.S.: Supported by US National Science Foundation No. PHY-2209429, Windows on the Universe: Nuclear Astrophysics at FRIB.

X.Z.: Supported by the U.S. Department of Energy, Office of Science, Office of Nuclear Physics, under the FRIB Theory Alliance Award No. DE-SC0013617 and under the STREAMLINE Collaboration Award No. DE-SC0024586.

Data availability statement

This is a review article that contains no new data. The data that support the findings of this study are available upon reasonable request from the authors.

Appendix A Orbitals and magic numbers

The nuclear shell model starts with the association of nuclear structure properties with those expected from the motion of a single neutron or proton in the average potential of all other nucleons. The gaps in the spacings of the single-particle energies give rise to 'magic numbers' for the number of protons Z and the number of neutrons N. The magic numbers are associated with those nuclei that have a relatively high energy for the 2_1^+ state. Experimental results shown in figure 18.

An example for the neutron single-particle energies (SPE) for ^{208}Pb is shown in figure 19. These are eigenstates in a spherical potential with a Woods–Saxon shape. The Woods–Saxon parameters were adjusted to qualitatively reproduce observed structure properties. Similar SPE spacings are obtained for protons. The neutron number for the energy gaps in the SPE shown in figure 19 are the shell-model magic numbers; 2, 8, 20, 28, 50, 82 and 126. The SPE

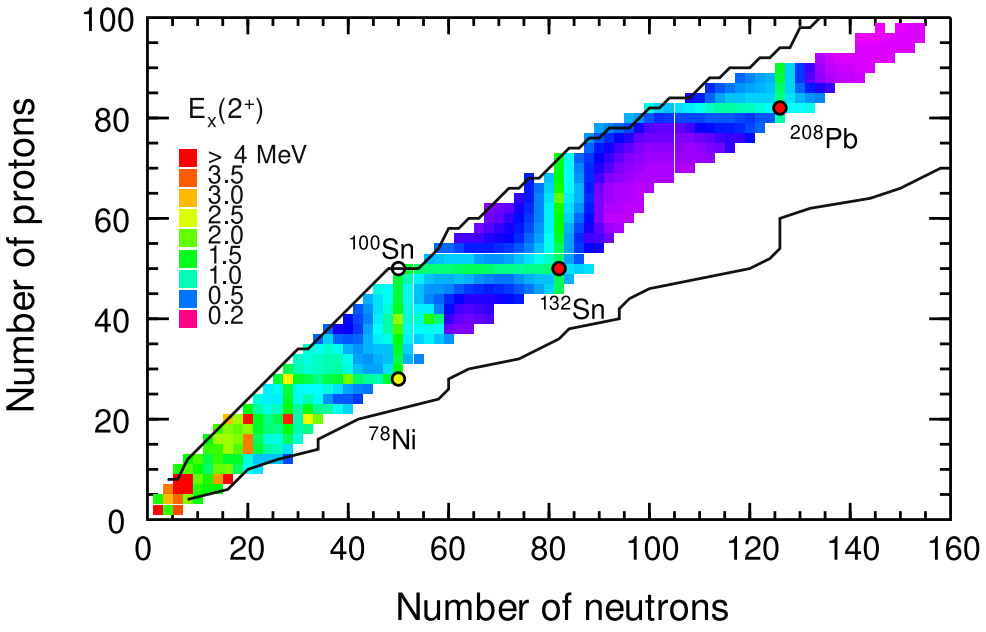

Figure 18. The nuclear chart showing the observed excitation energies of the 2_1^+ states. The black lines show where the two-proton (upper) and two-neutron (lower) separation energies obtained with the UNEDF1 energy-density functional (EDF) [10] cross one MeV. Reproduced from [195]. CC BY 4.0.

evolve with the number of protons and neutrons. The detailed ordering and the associated magic numbers can change.

The magic numbers 28, 50, 82 and 126, referred to as *jj* magic numbers, are associated with the gaps formed from the lowering of the $j = \ell + 1/2$ orbitals due to the spin–orbit single-particle potential. The nuclei associated with *jj* magic numbers are shown in nuclei figure 20. Doubly-magic nuclei are those with magic numbers for both protons and neutrons. The *jj* doubly-magic nuclei are shown in figure 20. The proton–neutron tensor interaction contained in the Hamiltonians used in CI calculations modifies the effective spin–orbit splittings for protons/neutrons depending on the filling of the neutron/proton spin–orbit doublets [197], [193].

For light nuclei, the magic numbers 2, 8 and 20 are observed. These are referred to as *ls* magic numbers, and are associated with the filling of a major harmonic-oscillator shell with $N_o = (2n + \ell)$ where both members of the spin–orbit pair $j = \ell \pm s$ ($s = 1/2$) are filled (except for $N_o = 0$ that contains only the $0s_{1/2}$ orbital). The nuclei associated with *ls* magic numbers are shown in figure 21. These include three nuclei with *ls* doubly-magic numbers, ^{4}He, ^{16}O and ^{40}Ca. There are many doubly-magic nuclei (shown with green circles) associated with nuclei where one kind of nucleon (proton or neutron) has an *ls* magic number and the other kind of nucleon fills the *j* levels in the order shown at the bottom right-hand side of figure 19. (Except that for light nuclei, the 1s1 orbital comes below the 0d3 orbital providing the filling number 16.)

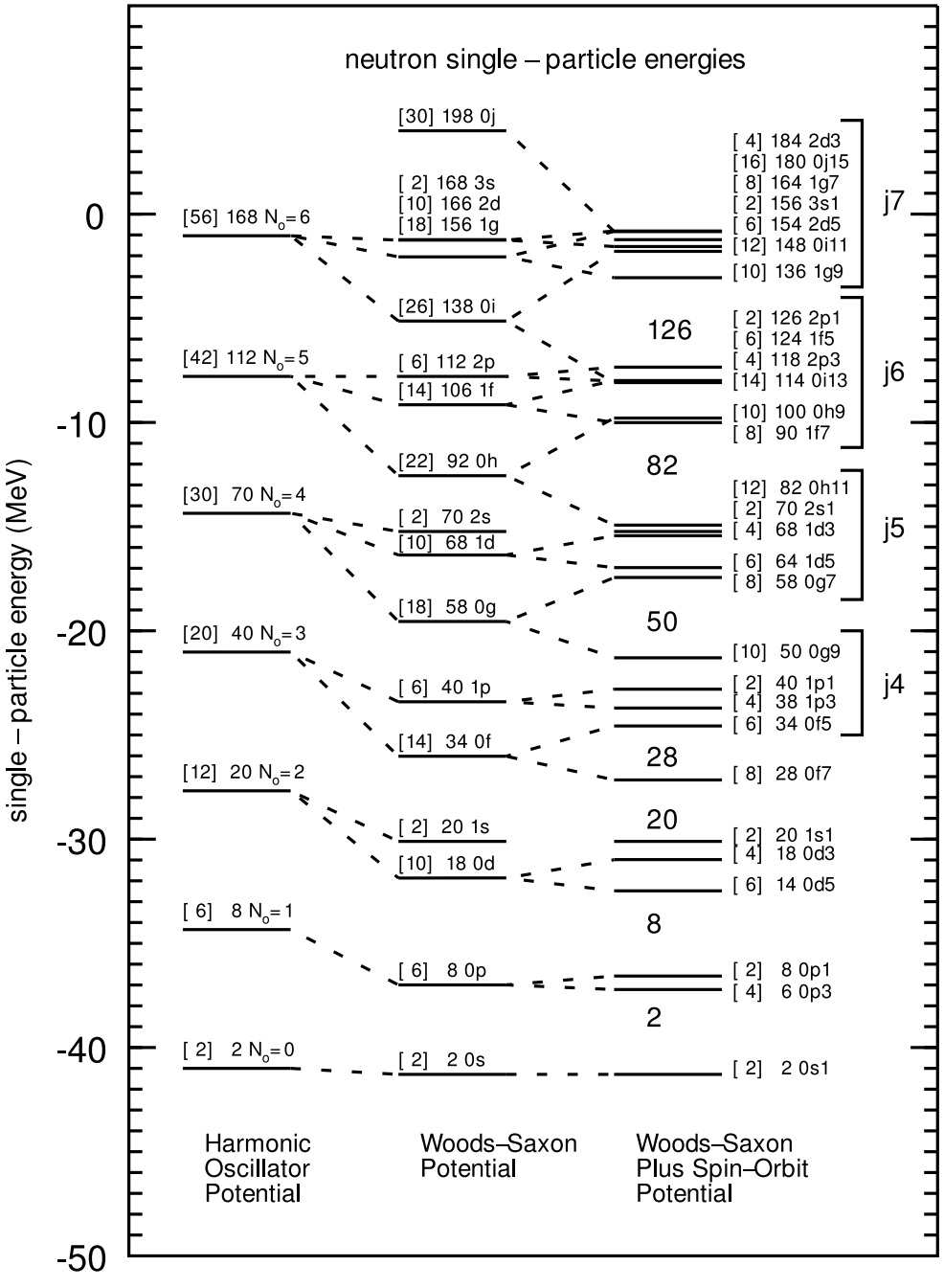

Figure 19. Neutron single-particle states in ^{208}Pb with three potential models, harmonic oscillator (left), Woods–Saxon without spin–orbit (middle) and Woods–Saxon with spin orbit (right). The numbers in square brackets are the maximum number of neutrons in that each level can contain, the following number is a running sum of the total. In addition the harmonic oscillator is labeled by the major quantum number $N = 2n + \ell$, the Woods–Saxon is labeled by (n, ℓ) and the Woods–Saxon with spin–orbit is labeled by $(n, \ell, 2j)$.

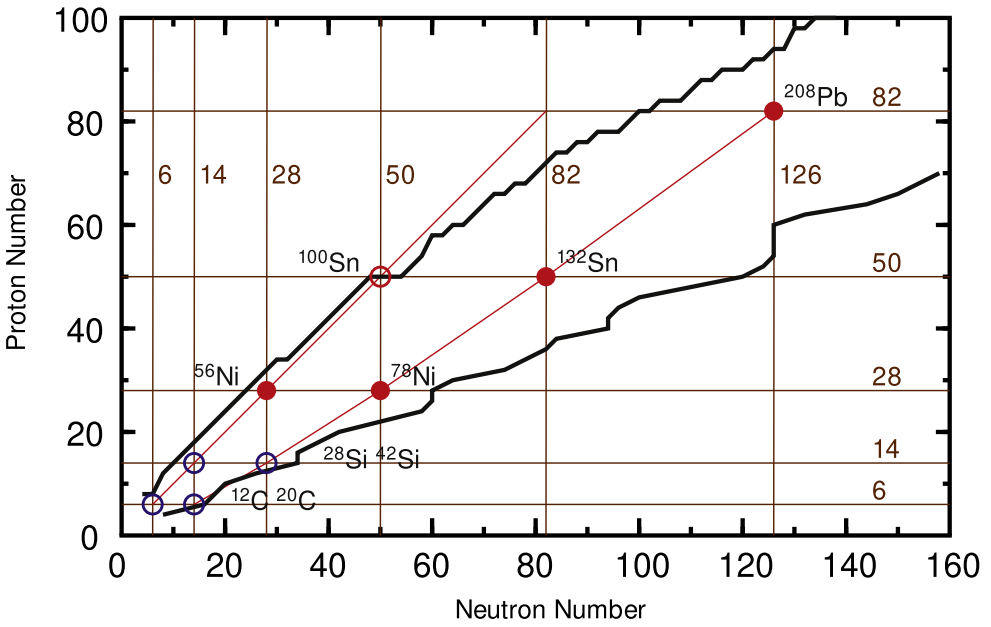

Figure 20. The nuclear chart showing *jj* magic numbers. The black lines show where the two-proton (upper) and two-neutron (lower) separation energies obtained with the UNEDF1 EDF [10] cross one MeV. The filled red circles shows the locations of doubly-*jj* magic nuclei established from experiment. The open red circle for ^{100}Sn indicates it is probably doubly-magic, but that the 2_1^+ energy is not yet measured. The blue circles in the bottom left-hand side are nuclei in the *jj* doubly-magic number sequence that are oblate deformed.

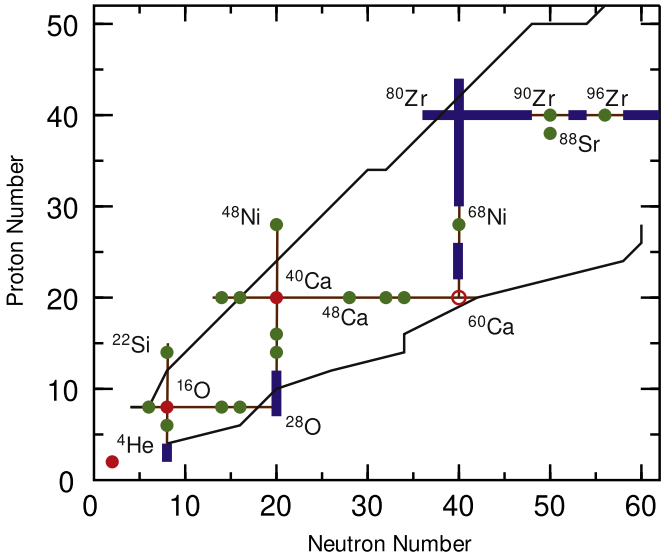

Figure 21. Lower mass region of the nuclear chart showing *ls* magic numbers, 8, 20 and 40. The black lines show where the two-proton (upper) and two-neutron (lower) separation energies obtained with the UNEDF1 EDF [10] functional cross one MeV. The filled red circles show the doubly-magic nuclei ^{4}He ^{16}O and ^{40}Ca. The open red circle for ^{60}Ca indicates a possible doubly-magic nucleus, but the 2_1^+ energy is not yet measured. The green circles are doubly-magic nuclei associated with the *j*-orbital fillings. The blue lines indicate isotopes or isotones where the *ls* magic number is observed to be broken. Reproduced from [195]. CC BY 4.0.

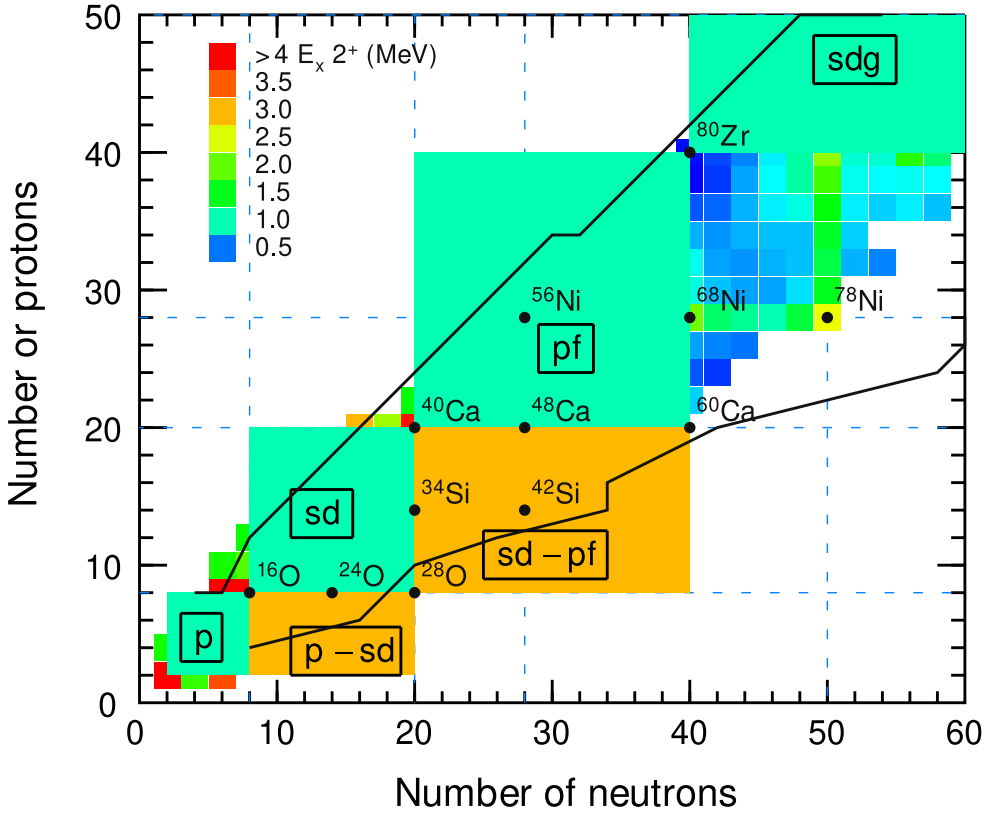

Figure 22. The nuclear chart showing the regions of nuclei associated with the harmonic-oscillator *ls* model spaces.

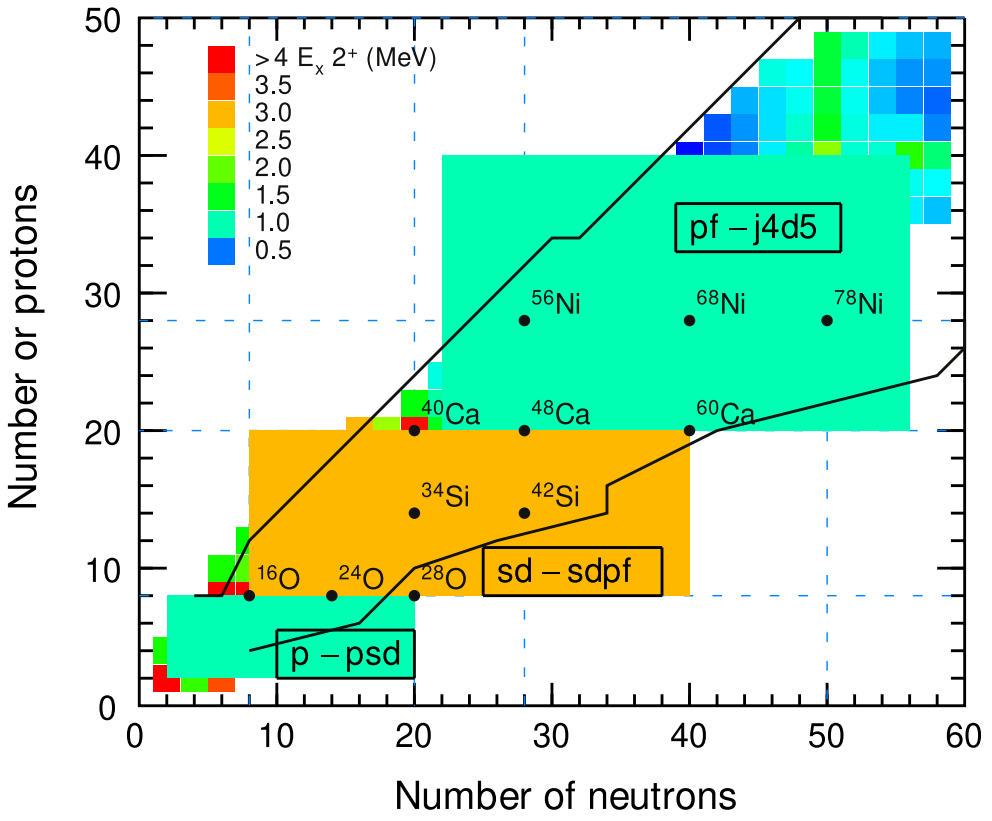

Figure 23. The nuclear chart showing the regions of nuclei associated with some larger model spaces.

Appendix B Model spaces

In this appendix we describe various model spaces relevant for shell model calculations. The magic numbers described in appendix A serve to define model spaces that are used to truncate the number of configurations that are used. The traditional names for model spaces based on the *ls* magic numbers for light nuclei are shown in figure 22. For example, *sd* stands for the model space with active nucleons in the ($0d_{5/2}$, $0d_{3/2}$, $1s_{1/2}$) set of orbitals. The model spaces *s*, *p*, *sd*, and *pf* are those for the major oscillator quantum numbers with $N_o = 0$, 1, 2, and 3, respectively, in figure 19. Near $N = Z$, protons and neutrons occupy the same major (oscillator) shell. Configurations for neutron-rich can involve protons and neutrons in two different major shells. For example, in the $sd - pf$ region of nuclei, protons occupy the *sd* major shell and neutrons occupy the *fp* major shell.

In the harmonic-oscillator basis, all of these *ls* model spaces involve nucleons in the lowest possible oscillator-energy configuration, often called the $0\hbar\omega$ configurations. Model spaces can involve more complex configuations. In the oscillator-basis, excited states involve $n\hbar\omega$ configurations. For example, starting with the *sd* model space, a $1\hbar\omega$ basis involves one nucleon excited from *p* to *sd* or one nucleon excited from *sd* to *pf*. In the $N = 8$, 20 and 40 neutron-rich islands of inversion, the model space for neutrons must involve two major shells. For example, for the $N = 20$ island of inversion, the model space for neutrons must contain both *sd* and *pf* major shells as shown in figure 23.

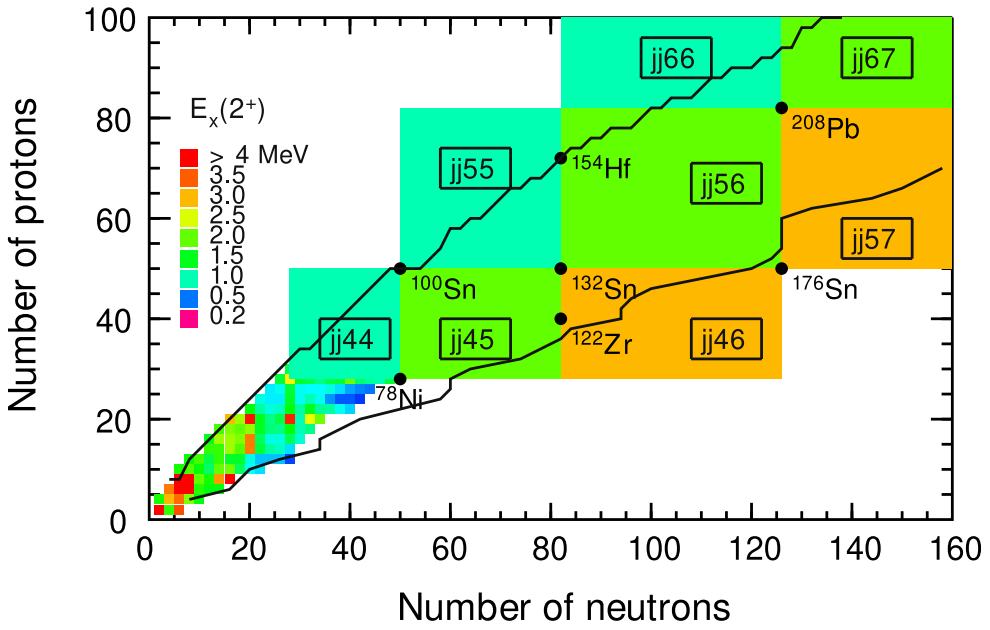

Figure 24. The nuclear chart showing the regions of nuclei associated with the *jj* model spaces.

Model spaces for heavy nuclei are shown in figure 24, labeled with the naming convention used in the NuShellX code [989]. Groups of orbitals are labeled by *jn* as shown by the labels on the right-hand side of figure 19. The notation *jjnm* indicates that protons occupy the *jn* set of orbitals and neutrons occupy the *jm* set of orbitals.

For a given calculation, the choice of model space is based on several interrelated factors.

1. One considers the limitation on the basis dimension connected to the computational methods and capabilities, as well as the practical consideration how many different nuclei and states need to be considered for a given experimental situation.
2. One considers to what extent the desired spectroscopic properties are contained within the model space. For example, an $\ell = 3$ transfer reaction cannot be described within the *sd* model space. Quadrupole deformation is connected to the mixing of orbitals with $\Delta\ell = 2$ and $\Delta j = 2$, and so it is preferable to have both type of orbitals contained in the model space if one is interested in collective properties [36], [194].

Ab initio no-core calculations for light nuclei are discussed in Sec. 5.4. A method for truncation is to use a restricted set of $\hbar\omega$ or particle-hole excitations [211,990].

In 'full-space' calculations for heavier nuclei, all possible configurations within a given model space are included. This is currently possible for matrix dimensions up to about 10^{12} . In many cases, low-lying states obtained from large-basis calculations can be related to a selective set of group theoretical based configurations or to those related to the Bohr–Mottelson collective model for even–even nuclei and the Nillson model for odd–even nuclei. For light nuclei the SU(3)-adapted basis has been used since the 1950s (see [991] and references therein). The symmetry-adapted bases provides a method of truncation for *Ab initio* calculations in light nuclei [53, 54]. For heavier nuclei, one can utilize methods like the generator-coordinate method [193, 992–994] or density matrix renormalization group [995] to obtain a truncated basis within the model space that reflects the collective properties.

Appendix C Abberviations

Table 1. Abbreviations.

ADWA	Adiabatic distorted wave approximation
ANC	Asymptotic normalization coefficient
AT-TPC	Active target time projection chamber
BAND	Bayesian analysis of nuclei dynamics
BBN	Big Bang Nucleosynthesis
BCS	Bardeen–Cooper–Schrieffer theory of superconductivity
BEC	Bose–Einstein condensation
BECOLA	BEam COoling and LAser spectroscopy
BMIS	Batch mode ion source
BSM	Beyond the Standard Model
CAESAR	CAESium-iodide scintillator ARray
CC	Coupled channels
CKM	Cabibbo–Kobayashi–Maskawa
CI	Configuration-interaction
CDCC	Continuum-discretized coupled channels
CLS	Collinear laser spectroscopy
CN	Compound nucleus
CREX	^{48}Ca Radius experiment (JLAB)
DFT	Density functional theory
DT	deuteron-tritium
DWBA	Distorted-wave born approximation
EDF	Energy-density functional
EDM	Electric dipole moments
EFT	Effective field theory
EOS	Equation of state
ESPE	Effective single-particle energy
FDSi	FRIB decay station initiator
FSNN	Fundamental symmetries, neutrons, and neutrinos
FRIB	Facility for rare isotopes
FRIB400	FRIB 400 MeV/u energy upgrade
FRIB-TA	FRIB theory alliance
G-DMRG	Gamow density matrix renormalization group
γSF	Gamma-ray strength function
GRETA	Gamma-ray energy tracking array
GRETINA	Gamma-ray energy tracking in-beam nuclear array
HF	Hauser–Feshbach
HFB	Hartree–Fock Boguliubov
HIC	Heavy-Ion Collision
HPGe	High purity germaniun (detector)
HRS	High resolution spectrometer
ISB	Isospin symmetry breaking
IMME	Isobaric multiplet mass equation
ISOL	Isotope separator on line

Table 1. (Continued.)

ITER	International thermonuclear experimental reactor
LEBIT	Low-energy beam ion trap
LEC	Low-energy coupling constant
LENDA	Low-energy neutron detector array
LD	Level density
LISA	Large multi-institutional scintillator array
JENSA	Jet experiments in nuclear structure and astrophysics
JLAB	Jefferson laboratory
MED	Mirror energy difference
MONA	Modular neutron array
MTAS	Modular total absorption spectrometer
MUSIC	Multi-sampling ionization chamber detector
NCSM	No-Core–Shell Model
NEXTi	Neutron (Xn) tracking initiator
NIF	National ignition facility
NCGSM	No-Core Gamow shell model
NNDC	National nuclear data center
NUCLEI	Nuclear computational low-energy initiative
NSAC	Nuclear science advisory committee
NSCL	National superconducting cyclotron laboratory
OMP	Optical model potential
PDR	Pygmy-dipole resonance
PREX	^{208}Pb Radius experiment (JLAB)
QCD	Quantum chromodynamics
QRPA	Quasiparticle random-phase approximation
RGM	Resonating group method
RIB	Radioactive ion beam
RIBF	Radioactive ion beam factory
RIKEN	Institute of Physical and Chemical Research (Japan)
S800	FRIB's high-resolution spectrometer
SA	Symmetry adapted (basis)
SA-NCSM	Symmetry adapted no-core–shell model
SAMURAI	Superconducting Analyzer for Multi-particles from Radioisotope beams
SECAR	Separator for capture reactions
SeGA	Segmented germanium array
SM	Standard Model
SπRIT	SAMURAI pion-reconstruction and ion-tracker
SOLARIS	SOLenoid spectrometer apparatus for reaction studies
SuN	Summing NaI(Tl) (gamma-ray detector)
TED	Triple energy difference
TOF	Time of flight
TPC	Time projection chamber
VANDLE	Versatile array of neutron detectors at low energy
WIMP	Weakly interacting massive particle

ORCID iDs

B Alex Brown https://orcid.org/0000-0002-6111-1906
Alexandra Gade https://orcid.org/0000-0001-8825-0976
S Ragnar Stroberg https://orcid.org/0000-0002-0635-776X
Jutta E Escher https://orcid.org/0000-0002-0829-9153
Kevin Fossez https://orcid.org/0000-0002-5823-4446
Pablo Giuliani https://orcid.org/0000-0002-8145-0745
Calem R Hoffman https://orcid.org/0000-0001-7141-9827
Witold Nazarewicz https://orcid.org/0000-0002-8084-7425
Chien-Yeah Seng https://orcid.org/0000-0002-3062-0118
Agnieszka Sorensen https://orcid.org/0000-0002-1984-8023
Nicole Vassh https://orcid.org/0000-0002-3305-4326
Daniel Bazin https://orcid.org/0000-0002-5663-9693
Kyle W Brown https://orcid.org/0000-0003-1923-3595
Mark A Caprio https://orcid.org/0000-0001-5138-3740
Heather Crawford https://orcid.org/0000-0002-7765-4235
Pawel Danielewicz https://orcid.org/0000-0002-1989-5241
Christian Drischler https://orcid.org/0000-0003-1534-6285
Ronald F Garcia Ruiz https://orcid.org/0000-0002-2926-5569
Kyle Godbey https://orcid.org/0000-0003-0622-3646
Robert Grzywacz https://orcid.org/0000-0002-0920-2587
Linda Hlophe https://orcid.org/0000-0001-6675-6132
Jeremy W Holt https://orcid.org/0000-0003-4373-3856
Hiro Iwasaki https://orcid.org/0000-0003-0750-380X
Dean Lee https://orcid.org/0000-0002-3630-567X
Silvia M Lenzi https://orcid.org/0000-0002-4666-8431
Sean Liddick https://orcid.org/0000-0003-1589-891X
Rebeka Lubna https://orcid.org/0000-0003-4976-3976
Augusto O Macchiavelli https://orcid.org/0000-0002-3144-1285
Gabriel Martínez-Pinedo https://orcid.org/0000-0002-3825-0131
Anna McCoy https://orcid.org/0000-0002-1033-1474
Alexis Mercenne https://orcid.org/0000-0002-2624-3911
Kei Minamisono https://orcid.org/0000-0003-2315-5032
Petr Navratil https://orcid.org/0000-0002-6535-2141
Ryan Ringle https://orcid.org/0000-0002-7478-259X
Grigor H Sargsyan https://orcid.org/0000-0002-3589-2315
Hendrik Schatz https://orcid.org/0000-0003-1674-4859
Mark-Christoph Spieker https://orcid.org/0000-0002-7214-7656
Alexander Volya https://orcid.org/0000-0002-1765-6466
Remco G T Zegers https://orcid.org/0000-0001-6076-5898
Vladimir Zelevinsky https://orcid.org/0000-0002-1705-5660
Xilin Zhang https://orcid.org/0000-0001-9278-5359

References

[1] Glasmacher T, Gade A, Bollen G and Wei J 2024 The facility for rare isotope beams: providing new opportunities for science *Nucl. Phys. News* **34** 5–12
[2] Tarasov O B *et al* 2024 Observation of new isotopes in the fragmentation of ^{198}Pt at frib *Phys. Rev. Lett.* **132** 072501
[3] Crawford H L *et al* 2022 Crossing $N = 28$ toward the neutron drip line: first measurement of half-lives at FRIB *Phys. Rev. Lett.* **129** 212501
[4] Gray T J *et al* 2023 Microsecond isomer at the $N = 20$ island of shape inversion observed at FRIB *Phys. Rev. Lett.* **130** 242501
[5] Cox I *et al* 2024 Proton shell gaps in $N = 28$ nuclei from the first complete spectroscopy study with FRIB decay station initiator *Phys. Rev. Lett.* **132** 152503
[6] Gade A *et al* 2025 In-beam spectroscopy reveals competing nuclear shapes in the rare isotope ^{62}Cr *Nat. Phys.* **21** 37–42
[7] Campbell S E *et al* 2024 Precision mass measurement of the proton dripline halo candidate ^{22}Al *Phys. Rev. Lett.* **132** 152501
[8] Thoennessen M 2004 Reaching the limits of nuclear stability *Rep. Prog. Phys.* **67** 1187
[9] Sherrill B M 2018 Future opportunities at the facility for rare isotope beams *EPJ Web Conf.* **178** 01001
[10] Bogner S *et al* 2013 Computational nuclear quantum many-body problem: the UNEDF project *Comput. Phys. Comm.* **184** 2235–50
[11] Aprahamian A *et al* 2015 Reaching for the Horizon: The 2015 long range plan for nuclear science, https://api.semanticscholar.org/CorpusID:120838987
[12] Nazarewicz W 2016 Challenges in nuclear structure theory *J. Phys.* G **43** 044002
[13] Nunes F M 2021 Why are theorists excited about exotic nuclei? *Phys. Today* **74** 34–40
[14] Carlson J *et al* 2016 *Nuclear Physics Exascale Requirements Review: An Office of Science Review sponsored jointly by Advanced Scientific Computing Research and Nuclear Physics* (Lawrence Berkeley National Laboratory (LBNL)) (https://doi.org/10.2172/1369223)
[15] Savage M J 2016 *Nucl. Phys.* arXiv:1611.02078 [hep-lat]
[16] Drischler C, Haxton W, McElvain K, Mereghetti E, Nicholson A, Vranas P and Walker-Loud A 2021 Toward grounding nuclear physics in QCD *Prog. Part. Nucl. Phys.* **121** 103888
[17] Cirigliano V *et al* 2022 Toward precise and accurate calculations of neutrinoless double-beta decay *J. Phys.* G **49** 120502
[18] Amarasinghe S, Baghdadi R, Davoudi Z, Detmold W, Illa M, Parreño A, Pochinsky A V, Shanahan P E and Wagman M L 2023 Variational study of two-nucleon systems with lattice QCD *Phys. Rev.* D **107** 094508
[19] Rodriguez Entem D, Machleidt R and Nosyk Y 2020 Nucleon–nucleon scattering up to N^{5}LO in chiral effective field theory *Front. Phys.* **8** 57
[20] Epelbaum E, Krebs H and Reinert P 2020 High-precision nuclear forces from chiral EFT: state-of-the-art, challenges, and outlook *Front. Phys.* **8** 98
[21] Piarulli M and Tews I 2020 Local nucleon–nucleon and three-nucleon interactions within chiral effective field theory *Front. Phys.* **7** 245
[22] Jiang W G, Ekström A, Forssén C, Hagen G, Jansen G R and Papenbrock T 2020 Accurate bulk properties of nuclei from $A = 2$ to ∞ from potentials with Δ isobars *Phys. Rev.* C **102** 054301
[23] Tews I, Davoudi Z, Ekström A, Holt J D and Lynn J E 2020 New ideas in constraining nuclear forces *J. Phys.* G **47** 103001
[24] Ekström A 2020 Analyzing the nuclear interaction: challenges and new ideas *Front. Phys.* **8** 29
[25] McIlroy C, Barbieri C, Inoue T, Doi T and Hatsuda T 2018 Doubly magic nuclei from lattice QCD forces *Phys. Rev.* C **97** 021303
[26] Ekström A, Forssén C, Hagen G, Jansen G R, Jiang W and Papenbrock T 2023 What is *ab initio* in nuclear theory? *Front. Phys.* **11** 1–10
[27] Hergert H 2020 A guided tour of *ab initio* nuclear many-body theory *Front. Phys.* **8** 379
[28] Hu B S, Padua-Arguelles J, Leutheusser S, Miyagi T, Stroberg S R and Holt J D 2022 *Ab initio* structure factors for spin-dependent dark matter direct detection *Phys. Rev. Lett.* **128** 072502
[29] Barrett B R, Navrátil P and Vary J P 2013 *Ab initio* no core–shell model *Prog. Part. Nucl. Phys.* **69** 131–81
[30] Carlson J, Gandolfi S, Pederiva F, Pieper S C, Schiavilla R, Schmidt K E and Wiringa R B 2015 Quantum Monte Carlo methods for nuclear physics *Rev. Mod. Phys.* **87** 1067–118
[31] Lee D 2020 Recent progress in nuclear lattice simulations *Front. Phys.* **8** 174

[32] Hagen G, Papenbrock T, Hjorth-Jensen M and Dean D J 2014 Coupled-cluster computations of atomic nuclei *Rep. Prog. Phys.* **77** 096302
[33] Soma V 2020 Self-consistent green's function theory for atomic nuclei *Front. Phys.* **8** 340
[34] Hergert H, Bogner S, Morris T, Schwenk A and Tsukiyama K 2016 The in-medium similarity renormalization group: a novel *ab initio* method for nuclei *Phys. Rep.* **621** 165–222
[35] Tichai A, Roth R and Duguet T 2020 Many-body perturbation theories for finite nuclei *Front. Phys.* **8** 164
[36] Caurier E, Martìnez-Pinedo G, Nowacki F, Poves A and Zuker A P 2005 The shell model as a unified view of nuclear structure *Rev. Mod. Phys.* **77** 427–88
[37] Shimizu N and Mizusaki T 2018 Variational Monte Carlo method for shell-model calculations in odd-mass nuclei and restoration of symmetry *Phys. Rev.* C **98** 054309
[38] Magilligan A and Brown B A 2020 New isospin-breaking 'USD' hamiltonians for the sd shell *Phys. Rev.* C **101** 064312
[39] Michel N, Nazarewicz W, Płoszajczak M and Vertse T 2008 Shell model in the complex energy plane *J. Phys.* G **36** 013101
[40] Johnson C W *et al* 2020 White paper: from bound states to the continuum *J. Phys.* G **47** 123001
[41] Bender M, Heenen P H and Reinhard P G 2003 Self-consistent mean-field models for nuclear structure *Rev. Mod. Phys.* **75** 121–80
[42] Drut J, Furnstahl R and Platter L 2010 Toward *ab initio* density functional theory for nuclei *Prog. Part. Nucl. Phys.* **64** 120–68
[43] Neufcourt L, Cao Y, Giuliani S A, Nazarewicz W, Olsen E and Tarasov O B 2020 Quantified limits of the nuclear landscape *Phys. Rev.* C **101** 044307
[44] Nakatsukasa T, Matsuyanagi K, Matsuo M and Yabana K 2016 Time-dependent density-functional description of nuclear dynamics *Rev. Mod. Phys.* **88** 045004
[45] Sheikh J A, Dobaczewski J, Ring P, Robledo L M and Yannouleas C 2021 Symmetry restoration in mean-field approaches *J. Phys.* G **48** 123001
[46] Garrett P E *et al* 2019 Multiple shape coexistence in ^{110,112}Cd *Phys. Rev. Lett.* **123** 142502
[47] Bender M *et al* 2020 Future of nuclear fission theory *J. Phys.* G (https://doi.org/10.1088/1361-6471/abab4f)
[48] Godbey K, Simenel C and Umar A S 2020 Microscopic predictions for the production of neutron-rich nuclei in the reaction ^{176}Yb + ^{176}Yb *Phys. Rev.* C **101** 034602
[49] Navrátil P, Quaglioni S, Hupin G, Romero-Redondo C and Calci A 2016 Unified *ab initio* approaches to nuclear structure *Phys. Scr.* **91** 053002
[50] Quaglioni S and Navrátil P 2020 Nuclear resonances, scattering, and reactions from first principles: progress and prospects *Nucl. Phys. News* **30** 12–6
[51] Hupin G, Quaglioni S and Navrátil P 2019 *Ab initio* predictions for polarized deuterium-tritium thermonuclear fusion *Nat. Commun.* **10** 351
[52] Hebborn C, Hupin G, Kravvaris K, Quaglioni S, Navrátil P and Gysbers P 2022 *Ab initio* prediction of the ^{4}He(d, γ)^{6}Li big bang radiative capture *Phys. Rev. Lett.* **129** 042503
[53] Launey K D, Mercenne A and Dytrych T 2021 Nuclear dynamics and reactions in the *ab initio* symmetry-adapted framework *Ann. Rev. Nucl. Part. Sci.* **71** 253–77
[54] Mercenne A, Launey K, Dytrych T, Escher J, Quaglioni S, Sargsyan G, Langr D and Draayer J 2022 Efficacy of the symmetry-adapted basis for *ab initio* nucleon–nucleus interactions for light- and intermediate-mass nuclei *Comput. Phys. Commun.* **280** 108476
[55] Zhang X 2020 Extracting free-space observables from trapped interacting clusters *Phys. Rev.* C **101** 051602
[56] Zhang X, Stroberg S R, Navrátil P, Gwak C, Melendez J A, Furnstahl R J and Holt J D 2020 *Ab initio* calculations of low-energy nuclear scattering using confining potential traps *Phys. Rev. Lett.* **125** 112503
[57] Bagnarol M, Schäfer M, Bazak B and Barnea N 2023 Five-body calculation of s-wave n-^{4}He scattering at next-to-leading order pionless effective field theory *Phys. Lett.* B **844** 138078
[58] Zhang X 2023 Recent developments on projection-based emulators for quantum continuum states *The Workshop on Progress in Ab Initio Nuclear Theory, February 2023, TRIUMF, Vancouver, BC, Canada*
[59] Zhang X 2024 A non-Hermitian quantum mechanics approach for extracting and emulating continuum physics based on bound-state-like calculations arXiv: 2408.03309
[60] Thompson I J and Nunes F 2009 *Nuclear Reactions for Astrophysics: Principles, Calculation and Applications of Low-energy Reactions* (Cambridge University Press)

[61] Brida I, Pieper S C and Wiringa R B 2011 Quantum Monte Carlo calculations of spectroscopic overlaps in $A \leqslant 7$ nuclei *Phys. Rev.* C **84** 024319
[62] Grinyer G F *et al* 2012 Systematic study of *p*-shell nuclei via single-nucleon knockout reactions *Phys. Rev.* C **86** 024315
[63] Nobre G P A, Dietrich F S, Escher J E, Thompson I J, Dupuis M, Terasaki J and Engel J 2010 Coupled-channel calculation of nonelastic cross sections using a density-functional structure model *Phys. Rev. Lett.* **105** 202502
[64] Nobre G P A, Dietrich F S, Escher J E, Thompson I J, Dupuis M, Terasaki J and Engel J 2011 Toward a microscopic reaction description based on energy-density-functional structure models *Phys. Rev.* C **84** 064609
[65] Dupuis M, Haouat G, Delaroche J P, Bauge E and Lachkar J 2019 Challenging microscopic structure and reaction models for nucleon scattering off nuclei in the $A = 208$ mass region *Phys. Rev.* C **100** 044607
[66] Potel G *et al* 2017 Toward a complete theory for predicting inclusive deuteron breakup away from stability *Eur. Phys. J.* A **53** 178
[67] Hebborn C and Potel G 2023 Green's function knockout formalism *Phys. Rev.* C **107** 014607
[68] Hagino K, Ogata K and Moro A 2022 Coupled-channels calculations for nuclear reactions: from exotic nuclei to superheavy elements *Prog. Part. Nucl. Phys.* **125** 103951
[69] Alt E, Grassberger P and Sandhas W 1967 Reduction of the three-particle collision problem to multi-channel two-particle Lippmann–Schwinger equations *Nucl. Phys.* B **2** 167–80
[70] Deltuva A 2019 Core-excitation effects in three-body breakup reactions studied using the Faddeev formalism *Phys. Rev.* C **99** 024613
[71] Moro A M and Crespo R 2012 Core excitation effects in the breakup of the one-neutron halo nucleus ^{11}Be on a proton target *Phys. Rev.* C **85** 054613
[72] Crespo R, Deltuva A and Moro A M 2011 Core excitation contributions to the breakup of the one-neutron halo nucleus ^{11}Be on a proton *Phys. Rev.* C **83** 044622
[73] Summers N C, Nunes F M and Thompson I J 2006 Core transitions in the breakup of exotic nuclei *Phys. Rev.* C **73** 031603
[74] Summers N C, Nunes F M and Thompson I J 2006 Extended continuum discretized coupled channels method: core excitation in the breakup of exotic nuclei *Phys. Rev.* C **74** 014606
[75] de Diego R, Arias J M, Lay J A and Moro A M 2014 Continuum-discretized coupled-channels calculations with core excitation *Phys. Rev.* C **89** 064609
[76] Timofeyuk N and Johnson R 2020 Theory of deuteron stripping and pick-up reactions for nuclear structure studies *Prog. Part. Nucl. Phys.* **111** 103738
[77] Descouvemont P 2018 Four-body extension of the continuum-discretized coupled-channels method *Phys. Rev.* C **97** 064607
[78] Watanabe S, Ogata K and Matsumoto T 2021 Practical method for decomposing discretized breakup cross sections into components of each channel *Phys. Rev.* C **103** L031601
[79] Descouvemont P and Baye D 2010 The *R*-matrix theory *Rep. Prog. Phys.* **73** 036301
[80] Capote R *et al* 2009 Ripl—reference input parameter library for calculation of nuclear reactions and nuclear data evaluations *Nucl. Data Sheets* **110** 3107–214
[81] Koning A, Hilaire S and Goriely S 2023 Talys: modeling of nuclear reactions *Eur. Phys. J.* A **59** 131
[82] Hebborn C *et al* 2023 Optical potentials for the rare-isotope beam era *J. Phys. G: Nucl. Part. Phys.* **50** 060501
[83] Boehnlein A *et al* 2022 Colloquium: machine learning in nuclear physics *Rev. Mod. Phys.* **94** 031003
[84] (FRIB Science Community) 2019 FRIB400: the Scientific Case for the 400 MeV/u Energy Upgrade of FRIB. https://frib.msu.edu/_files/pdfs/frib400_final.pdf, updated February 2023. accessed: 2023-07-16.
[85] Sorensen A *et al* 2024 Dense nuclear matter equation of state from heavy-ion collisions *Prog. Part. Nucl. Phys.* **134** 104080
[86] Huth S *et al* 2022 Constraining neutron-star matter with microscopic and macroscopic collisions *Nature* **606** 276–80
[87] Lovato A *et al* 2022 Long range plan: dense matter theory for heavy-ion collisions and neutron stars arXiv: 2211.02224
[88] Danielewicz P, Lacey R and Lynch W G 2002 Determination of the equation of state of dense matter *Science* **298** 1592–6

[89] Fuchs C 2004 Strangeness production in heavy ion reactions at intermediate-energies *Prog. Part. Nucl. Phys.* **53** 113–24
[90] Lynch W G, Tsang M B, Zhang Y, Danielewicz P, Famiano M, Li Z and Steiner A W 2009 Probing the symmetry energy with heavy ions *Prog. Part. Nucl. Phys.* **62** 427
[91] Le Fèvre A, Leifels Y, Reisdorf W, Aichelin J and Hartnack C 2016 Constraining the nuclear matter equation of state around twice saturation density *Nucl. Phys.* A **945** 112–33
[92] Oliinychenko D, Sorensen A, Koch V and McLerran L 2023 Sensitivity of Au+Au collisions to the symmetric nuclear matter equation of state at 2–5 nuclear saturation densities *Phys. Rev.* C **108** 034908
[93] Lynch W G and Tsang M B 2022 Decoding the density dependence of the nuclear symmetry energy *Phys. Lett.* B **830** 137098
[94] Drischler C, Furnstahl R J, Melendez J A and Phillips D R 2020 How well do we know the neutron-matter equation of state at the densities inside neutron stars? a bayesian approach with correlated uncertainties *Phys. Rev. Lett.* **125** 202702
[95] Kruse H, Jacak B V and Stoecker H 1985 Microscopic theory of pion production and sidewards flow in heavy ion collisions *Phys. Rev. Lett.* **54** 289–92
[96] Aichelin J and Ko C M 1985 Subthreshold kaon production as a probe of the nuclear equation of state *Phys. Rev. Lett.* **55** 2661–3
[97] Li B A 2002 Probing the high density behavior of nuclear symmetry energy with high-energy heavy ion collisions *Phys. Rev. Lett.* **88** 192701
[98] Li B A 2000 Neutron proton differential flow as a probe of isospin dependence of nuclear equation of state *Phys. Rev. Lett.* **85** 4221–4
[99] Li B A, Ramos A, Verde G and Vidana I 2014 Topical issue on nuclear symmetry energy *Eur. Phys. J.* A **50** 9
[100] Danielewicz P and Kurata-Nishimura M 2022 Deblurring for nuclei: 3D characteristics of heavy-ion collisions *Phys. Rev.* C **105** 034608
[101] Berkowitz R 2022 Bringing into focus the debris of heavy-ion collisions *APS Phys.* **15** s26
[102] Wolter H *et al* (TMEP) 2022 Transport model comparison studies of intermediate-energy heavy-ion collisions *Prog. Part. Nucl. Phys.* **125** 103962
[103] Morfouace P *et al* 2019 Constraining the symmetry energy with heavy-ion collisions and Bayesian analyses *Phys. Lett.* B **799** 135045
[104] Liyanage D, Ji Y, Everett D, Heffernan M, Heinz U, Mak S and Paquet J F 2022 Efficient emulation of relativistic heavy ion collisions with transfer learning *Phys. Rev.* C **105** 034910
[105] Phillips D R *et al* 2021 Get on the BAND wagon: a bayesian framework for quantifying model uncertainties in nuclear dynamics *J. Phys.* G **48** 072001
[106] Sherrill B M 2008 Designer atomic nuclei *Science* **320** 751–2
[107] Jones K L and Nazarewicz W 2010 Designer nuclei—making atoms that barely exist *Phys. Teach.* **48** 381–5
[108] Abel E P *et al* 2019 Isotope harvesting at FRIB: additional opportunities for scientific discovery *J. Phys.* G **46** 100501
[109] Lunney D, Pearson J M and Thibault C 2003 Recent trends in the determination of nuclear masses *Rev. Mod. Phys.* **75** 1021–82
[110] Matoš M *et al* 2012 Time-of-flight mass measurements of exotic nuclei *Nucl. Instrum. Meth. Phys. Res.* A **696** 171–9
[111] Meisel Z and George S 2013 Time-of-flight mass spectrometry of very exotic systems *Int. J. Mass Spectrom.* **349** 145–50
[112] Ringle R, Schwarz S and Bollen G 2013 Penning trap mass spectrometry of rare isotopes produced via projectile fragmentation at the LEBIT facility *Int. J. Mass Spectrom.* **349** 87–93
[113] Otten E W 1989 Nuclear radii and moments of unstable isotopes *Treatise Heavy-ion Sci.* **8** 517
[114] Billowes J and Campbell P 1995 High-resolution laser spectroscopy for the study of nuclear sizes and shapes *J. Phys.* G **21** 707
[115] Kluge H J and Nörtershäuser 2003 Lasers for nuclear physics *Spectrochim. Acta* B **58** 1031
[116] Cheal B *et al* 2010 Nuclear spins and moments of ga isotopes reveal sudden structural changes between $N = 40$ and $N = 50$ *Phys. Rev. Lett.* **104** 252502
[117] Blaum K, Dilling J and Nörtershäuser W 2013 Precision atomic physics techniques for nuclear physics with radioactive beams *Phys. Scr.* **2013** 014017
[118] Campbell P, Moore I and Pearson M 2016 Laser spectroscopy for nuclear structure physics *Prog. Part. Nucl. Phys.* **86** 127

[119] Neugart R, Billowes J, Bissell M, Blaum K, Cheal B, Flanagan K, Neyens G, Nörtershäuser W and Yordanov D 2017 Collinear laser spectroscopy at ISOLDE: new methods and highlights *J. Phys. G: Nucl. Part. Phys.* **44** 064002
[120] Yang X F, Wang S J, Wilkins S G and Garcia Ruiz R F 2023 Laser spectroscopy for the study of exotic nuclei *Prog. Part. Nucl. Phys.* **129** 104005
[121] Kaufman S L 1976 High-resolution laser spectroscopy in fast beams *Optic. Comm.* **17** 309
[122] Nieminen A *et al* 2002 On-line ion cooling and bunching for collinear laser spectroscopy *Phys. Rev. Lett.* **88** 094801
[123] Campbell P *et al* 2002 Laser spectroscopy of cooled zirconium fission fragments *Phys. Rev. Lett.* **89** 082501
[124] Barquest B, Bollen G, Mantica P, Minamisono K, Ringle R, Schwarz S and Sumithrarachchi C 2017 RFQ beam cooler and buncher for collinear laser spectroscopy of rare isotopes *Nucl. Instrum. Meth. Phys. Res.* A **866** 18
[125] Flanagan K T *et al* 2013 Collinear resonance ionization spectroscopy of neutron-deficient francium isotopes *Phys. Rev. Lett.* **111** 212501
[126] Minamisono K, Mantica P, Klose A, Vinnikova S, Schneider A, Johnson B and Barquest B 2013 Commissioning of the collinear laser spectroscopy system in the BECOLA facility at NSCL *Nucl. Instrum. Meth. Phys. Res.* A **709** 8
[127] Rossi D M *et al* 2014 A field programmable gate array-based time-resolved scaler for collinear laser spectroscopy with bunched radioactive potassium beams *Rev. Sci. Instrum.* **85** 093503
[128] Sumithrarachchi C, Morrissey D J, Schwarz S, Lund K, Bollen G, Ringle R, Savard G and Villari A C C 2020 Beam thermalization in a large gas catcher *Nucl. Instrum. Meth. Phys. Res.* B **463** 305
[129] Lund K, Bollen G, Lawton D, Morrissey D, Ottarson J, Ringle R, Schwarz S, Sumithrarachchi C, Villari A and Yurkon J 2020 Online tests of the advanced cryogenic gas stopper at NSCL *Nucl. Instrum. Meth. Phys. Res.* B **463** 378
[130] Sumithrarachchi C *et al* 2023 The new batch mode ion source for stand-alone operation at the facility for rare isotope beams (FRIB) *Nucl. Instrum. Meth. Phys. Res.* B **541** 301
[131] Ryder C, Minamisono K, Asberry H B, Isherwood B, Mantica P F, Miller A, Rossi D M and Strum R 2015 Population distribution subsequent to charge exchange of 29.85 keV Ni^{+} on sodium vapor *Spectrochim. Acta* B **113** 16
[132] Miller A J *et al* 2019 Proton superfluidity and charge radii in proton-rich calcium isotopes *Nat. Phys.* **15** 432
[133] Pineda S V *et al* 2021 Charge radius of neutron-deficient ^{54}Ni and symmetry energy constraints using the difference in mirror pair charge radii *Phys. Rev. Lett.* **127** 182503
[134] Rossi D M *et al* 2015 Charge radii of neutron-deficient K-36 and K-37 *Phys. Rev.* C **92** 014305
[135] Minamisono K *et al* 2016 Charge radii of neutron deficient ^{52,53}Fe produced by projectile fragmentation *Phys. Rev. Lett.* **117** 252501
[136] Sommer F *et al* 2022 Charge radii of ^{55,56}Ni reveal a surprisingly similar behavior at $N = 28$ in Ca and Ni isotopes *Phys. Rev. Lett.* **129** 132501
[137] König K *et al* 2023 Surprising charge-radius kink in the Sc isotopes at $N = 20$ *Phys. Rev. Lett* **131** 102501
[138] Miller A J *et al* 2017 First determination of ground state electromagnetic moments of ^{53}Fe *Phys. Rev.* C **96** 054314
[139] Klose A *et al* 2019 Ground-state electromagnetic moments of ^{37}Ca *Phys. Rev.* C **99** 061301
[140] Powel R, Brown B A, Holt J D, Klose A, Konig K, Lantis J, Minamisono K, Miyagi T and Pineda S 2022 Ground state magnetic dipole moment of ^{40}Sc *Phys. Rev.* C **105** 034310
[141] Maaß B *et al* 2019 Nuclear charge radii of ^{10,11}B *Phys. Rev. Lett.* **122** 182501
[142] King W H 1984 *Isotope Shifts in Atomic Spectra* (Springer Science+ Business Media)
[143] Osterfeld F 1992 Nuclear spin and isospin excitations *Rev. Mod. Phys.* **64** 491–557
[144] Ichimura M, Sakai H and Wakasa T 2006 Spin-isospin responses via (p, n) and (n, p) reactions *Prog. Part. Nucl. Phys.* **56** 446–531
[145] Fujita Y, Rubio B and Gelletly W 2011 Spin-isospin excitations probed by strong, weak and electro-magnetic interactions *Prog. Part. Nucl. Phys.* **66** 549–606
[146] Langanke K and Martínez-Pinedo G 2003 Nuclear weak-interaction processes in stars *Rev. Mod. Phys.* **75** 819–62
[147] Frekers D and Alanssari M 2018 Charge-exchange reactions and the quest for resolution *Eur. Phys. J.* A **54** 177

[148] Harakeh M N and van der Woude A 2001 *Giant Resonances: Fundamental High-Frequency Modes of Nuclear Excitations* (Oxford University Press)
[149] Langanke K, Martínez-Pinedo G and Zegers R G T 2021 Electron capture in stars *Rep. Prog. Phys.* **84** 066301
[150] Zegers R G T 2020 *Excitation of Isovector Giant Resonances Through Charge-Exchange Reactions* (Springer Nature) pp 1–35
[151] Bazin D, Caggiano J A, Sherrill B M, Yurkon J and Zeller A 2003 The S800 Spectrograph *Nucl. Inst. Meth. Phys. Res.* B **204** 629
[152] Simon A *et al* 2013 Summing NaI(Tl) gamma-ray detector for capture reaction measurements *Nucl. Instrum. Meth. Phys. Res.* A **703** 16–21
[153] Spyrou A *et al* 2014 Novel technique for constraining *r*-process (n, γ) reaction rates *Phys. Rev. Lett* **113** 232502
[154] Larsen A, Spyrou A, Liddick S and Guttormsen M 2019 Novel techniques for constraining neutron-capture rates relevant for *r*-process heavy-element nucleosynthesis *Prog. Part. Nucl. Phys.* **107** 69–108
[155] Bonin B *et al* 1984 Response functions of ^{58}Ni, ^{116}Sn and ^{208}Pb to the excitation of intermediate-energy α particles *Nucl. Phys.* A **430** 349–96
[156] Moinester M *et al* 1989 A study of spin isovector giant resonances with the ^{208}Pb(n, p)^{208}Tl reaction *Phys. Lett.* B **230** 41–5
[157] Wakasa T *et al* 1997 Gamow-teller strength of ^{90}Nb in the continuum studied via multipole decomposition analysis of the ^{90}Zr(p, n) reaction at 295 MeV *Phys. Rev.* C **55** 2909–22
[158] Taddeucci T, Goulding C, Carey T, Byrd R, Goodman C, Gaarde C, Larsen J, Horen D, Rapaport J and Sugarbaker E 1987 The (p, n) reaction as a probe of beta decay strength *Nucl. Phys.* A **469** 125–72
[159] Perdikakis G *et al* 2011 Gamow–Teller unit cross sections for (t, ^{3}He) and (^{3}He, t) reactions *Phys. Rev.* C **83** 054614
[160] Zegers R G T *et al* 2007 Extraction of weak transition strengths via the (^{3}He, t) reaction at 420 MeV *Phys. Rev. Lett* **99** 202501
[161] Sasano M *et al* 2009 Gamow-teller unit cross sections of the (p, n) reaction at 198 and 297 MeV on medium-heavy nuclei *Phys. Rev.* C **79** 024602
[162] Giraud S *et al* 2023 β^+ Gamow–Teller strengths from unstable ^{14}O via the (d, ^{2}He) reaction in inverse kinematics *Phys. Rev. Lett.* **130** 232301
[163] Ayyad Y *et al* 2020 Next-generation experiments with the active target time projection chamber (AT-TPC) *Nucl. Instrum. Meth. Phys. Res.* A **954** 161341
[164] Sasano M *et al* 2011 Gamow-teller transition strengths from ^{56}Ni *Phys. Rev. Lett.* **107** 202501
[165] Schmitt J *et al* 2022 Probing spin-isospin excitations in proton-rich nuclei via the ^{11}C(p, n) ^{11}N reaction *Phys. Rev.* C **106** 054323
[166] Weisshaar D *et al* 2017 The performance of the γ-ray tracking array GRETINA for γ-ray spectroscopy with fast beams of rare isotopes *Nucl. Instrum. and Meth. Phys. Res.* A **847** 187–98
[167] Yasuda J *et al* 2018 Extraction of the landau-migdal parameter from the gamow-teller giant resonance in ^{132}Sn *Phys. Rev. Lett.* **121** 132501
[168] Scott M *et al* 2017 Observation of the isovector giant monopole resonance via the ^{28}Si (^{10}Be, ^{10}B*[1.74 MeV]) reaction at 100 *A* MeV *Phys. Rev. Lett.* **118** 172501
[169] Sasamoto Y *et al* 2012 The super-allowed Fermi type charge exchange reaction for studies of isovector non-spin-flip monopole resonance *Proc. French-Japanese Symp.* p 148
[170] Sasamoto Y 2012 *Study of the Isovector Non-spin-flip Monopole Resonance via the Super-allowed Fermi Type Charge Exchange (^{10}C,^{10}Bγ) Reaction,* (University of Tokyo), https://ci.nii.ac.jp/naid/500002472579
[171] Noji S *et al* 2023 Design of the high rigidity spectrometer at FRIB *Nucl. Instrum. Meth. Phys. Res.* A **1045** 167548
[172] Mueller W, Church J, Glasmacher T, Gutknecht D, Hackman G, Hansen P, Hu Z, Miller K and Quirin P 2001 Thirty-two-fold segmented germanium detectors to identify gamma-rays from intermediate-energy exotic beams *Nucl. Instrum. Meth. Phys. Res.* A **466** 492–8
[173] Weisshaar D *et al* 2010 CAESAR—a high-efficiency CsI(Na) scintillator array for in-beam γ-ray spectroscopy with fast rare-isotope beams *Nucl. Instrum. Meth. Phys. Res.* A **624** 615–23
[174] 2023 Gamma-Ray Energy Tracking Array (GRETA), https://greta.lbl.gov/
[175] 2024 FRIB Decay Station (FDS), https://FDS.ornl.gov

[176] Yokoyama R *et al* 2019 Segmented YSO scintillation detectors as a new β-implant detection tool for decay spectroscopy in fragmentation facilities *Nucl. Instrum. Meth. Phys. Res.* A **937** 93–7
[177] Peters W *et al* 2016 Performance of the versatile array of neutron detectors at low energy (VANDLE) *Nucl. Instrum. Meth. Phys. Res.* A **836** 122–33
[178] Ong W J *et al* 2020 β decay of ^{61}V and its role in cooling accreted neutron star crusts *Phys. Rev. Lett.* **125** 262701
[179] Baumann T *et al* 2005 Construction of a modular large-area neutron detector for the NSCL *Nucl. Instrum. Meth. Phys. Res.* A **543** 517–27
[180] Wallace M *et al* 2007 The high resolution array (HiRA) for rare isotope beam experiments *Nucl. Instrum. Meth. Phys. Res.* A **583** 302–12
[181] Zecher P *et al* 1997 A large-area, position-sensitive neutron detector with neutron/gamma-ray discrimination capabilities *Nucl. Instrum. Meth. Phys. Res.* A **401** 329–44
[182] Estee J *et al* 2021 Probing the symmetry energy with the spectral pion ratio *Phys. Rev. Lett.* **126** 162701
[183] Jhang G *et al* 2021 Symmetry energy investigation with pion production from Sn+Sn systems *Phys. Lett.* B **813** 136016
[184] Gade A and Iwasaki H 2016 *Whitepaper on ReA Energy Upgrade*, https://fribusers.org/documents/2016/ReAEnergyUpgradeWP.pdf
[185] Kay B *et al* 2018 *SOLARIS: a Solenoidal Apparatus for Reaction Studies*, https://www.anl.gov/sites/www/files/2018-11/solaris_white_paper_final.pdf
[186] 2023 SOLARIS, https://www.anl.gov/phy/solaris
[187] Chen J *et al* 2024 Evolution of the nuclear spin–orbit splitting explored via the ^{32}Si(d, p)^{33}Si reaction using SOLARIS *Phys. Lett.* B **853** 138678
[188] Berg G *et al* 2018 Design of SECAR a recoil mass separator for astrophysical capture reactions with radioactive beams *Nucl. Instrum. Meth. Phys. Res.* A **877** 87–103
[189] Lunderberg E *et al* 2018 JANUS—a setup for low-energy Coulomb excitation at ReA3 *Nucl. Instrum. Meth. Phys. Res.* A **885** 30–7
[190] Lighthall J *et al* 2010 Commissioning of the HELIOS spectrometer *Nucl. Instrum. Meth. Phys. Res.* A **622** 97–106
[191] Sharp D 2022 *ISOLDE's Solenoidal Spectrometer (ISS): A New Tool for Studying Exotic Nuclei*, https://ep-news.web.cern.ch/content/isoldes-solenoidal-spectrometer-iss-new-tool-studying-exotic-nuclei
[192] MacGregor P T *et al* 2021 Evolution of single-particle structure near the $N = 20$ island of inversion *Phys. Rev.* C **104** L051301
[193] Otsuka T, Gade A, Sorlin O, Suzuki T and Utsuno Y 2020 Evolution of shell structure in exotic nuclei *Rev. Mod. Phys.* **92** 015002
[194] Nowacki F, Obertelli A and Poves A 2021 The neutron-rich edge of the nuclear landscape: experiment and theory *Prog. Part. Nucl. Phys.* **120** 103866
[195] Brown B A 2022 The nuclear shell model toward the drip lines *Physics* **4** 525–47
[196] Buskirk L, Godbey K, Nazarewicz W and Satuła W 2024 Nucleonic shells and nuclear masses *Phys. Rev.* C **109** 044311
[197] Otsuka T, Suzuki T, Fujimoto R, Grawe H and Akaishi Y 2005 Evolution of nuclear shells due to the tensor force *Phys. Rev. Lett.* **95** 232502
[198] Dobaczewski J, Michel N, Nazarewicz W, Ploszajczak M and Rotureau J 2007 Shell structure of exotic nuclei *Prog. Part. Nucl. Phys.* **59** 432–45 International Workshop on Nuclear Physics 28th Course
[199] Michel N, Nazarewicz W, Okolowicz J and Ploszajczak M 2010 Open problems in the theory of nuclear open quantum systems *J. Phys. G: Nucl. Part. Phys.* **37** 064042
[200] Baranger M 1970 A definition of the single-nucleon potential *Nucl. Phys.* A **149** 225–40
[201] Signoracci A and Brown B A 2007 Comment on 'reduction of the spin–orbit splittings at the $n = 28$ shell closure' *Phys. Rev. Lett.* **99** 099201
[202] Warburton E K, Becker J A and Brown B A 1990 Mass systematics for $A = 29$–44 nuclei—the deformed $a \sim 32$ region *Phys. Rev.* C **41** 1147–66
[203] Brown B A 2010 Islands of insight in the nuclear chart *Physics* **3** 104
[204] Nowacki F, Poves A, Caurier E and Bounthong B 2016 Shape coexistence in ^{78}Ni as the portal to the fifth island of inversion *Phys. Rev. Lett.* **117**
[205] Poves A 2018 Shape coexistence and islands of inversion monopole versus multipole *Proc. Ito Int. Research Center Symp., Perspectives of the Physics of Nuclear Structure, JPS Conf. Proc.* p 012015, https://doi.org/10.7566/JPSCP.23.012015

[206] Bonatsos D, Martinou A, Peroulis S K, Mertzimekis T J and Minkov N 2023 Signatures for shape coexistence and shape/phase transitions in even-even nuclei *J. Phys. G: Nucl. Part. Phys.* **50** 075105
[207] Brown B A and Minamisono K 2022 β_2 corrections to spherical energy-density functional calculations for root-mean-square charge radii *Phys. Rev.* C **106** L011304
[208] Reinhard P G and Nazarewicz W 2017 Toward a global description of nuclear charge radii: exploring the fayans energy density functional *Phys. Rev.* C **95**
[209] Caurier E, Nowacki F and Poves A 2001 Shell model studies of neutron-rich nuclei *Nucl. Phys.* A **693** 374–82
[210] Lubna R S, Kravvaris K, Tabor S L, Tripathi V, Volya A, Rubino E, Allmond J M, Abromeit B, Baby L T and Hensley T C 2019 Structure of ^{38}Cl and the quest for a comprehensive shell model interaction *Phys. Rev.* C **100** 034308
[211] Lubna R S, Kravvaris K, Tabor S L, Tripathi V, Rubino E and Volya A 2020 Evolution of the $n = 20$ and 28 shell gaps and two-particle-two-hole states in the FSU interaction *Phys. Rev. Res.* **2** 043342
[212] Lisetskiy A F, Brown B A, Horoi M and Grawe H 2004 New $t = 1$ effective interactions for the $f(5/2)$ $p(3/2)$ $p(1/2)$ $g(9/2)$ model space: implications for valence-mirror symmetry and seniority isomers *Phys. Rev.* C **70** 044314
[213] Brown B A 1998 New skyrme interaction for normal and exotic nuclei *Phys. Rev.* C **58** 220–31
[214] Lenzi S M, Nowacki F, Poves A and Sieja K 2010 Island of inversion around ^{64}Cr *Phys. Rev.* C **82** 054301
[215] Hansen P G and Tostevin J A 2003 Direct reactions with exotic nuclei *Ann. Rev. Nucl. Part. Sci.* **53** 219–61
[216] Wimmer K 2018 Nucleon transfer reactions with radioactive beams *J. Phys. G: Nucl. Part. Phys.* **45** 033002
[217] Kondo Y *et al* 2023 First observation of ^{28}O *Nature* **620** 965
[218] Lapoux V, Somà V, Barbieri C, Hergert H, Holt J D and Stroberg S R 2016 Radii and binding energies in oxygen isotopes: a challenge for nuclear forces *Phys. Rev. Lett.* **117** 052501
[219] Shukla A, Åberg S and Patra S K 2011 Nuclear structure and reaction properties of even-even oxygen isotopes toward drip line *J. Phys.* G **38** 095103
[220] Tsunoda N, Otsuka T, Takayanagi K, Shimizu N, Suzuki T, Utsuno Y, Yoshida S and Ueno H 2020 The impact of nuclear shape on the emergence of the neutron dripline *Nature* **587** 66
[221] Utsuno Y, Otsuka T, Brown B A, Honma M, Mizusaki T and Shimizu N 2012 Shell evolution around and beyond $n = 28$ studied with large-scale shell-model calculations *Prog. Theor. Phys. Supp.* **196** 304–9
[222] Nowacki F and Poves A 2009 New effective interaction for 0 $\hbar\omega$ shell-model calculations in the *sd–pf* valence space *Phys. Rev.* C **79** 014310
[223] Tostevin J A, Brown B A and Simpson E C 2013 Two-proton removal from ^{44}S and the structure of ^{42}Si *Phys. Rev.* C **87** 027601
[224] Gade A *et al* 2019 Is the structure of ^{42}Si understood? *Phys. Rev. Lett.* **122** 222501
[225] Singh J, Casal J, Horiuchi W, Walet N and Satuła W 2024 Prediction of two-neutron halos in the $N = 28$ isotones ^{40}Mg and ^{39}Na *Phys. Lett.* B **853** 138694
[226] Yoshida S, Utsuno Y, Shimizu N and Otsuka T 2018 Systematic shell-model study of beta-decay properties and Gamow–Teller strength distributions in a approximate to 40 neutron-rich nuclei *Phys. Rev.* C **97** 054321
[227] Tarasov O B *et al* 2018 Discovery of ^{Ca}60 and implications for the stability of ^{70}Ca *Phys. Rev. Lett.* **121** 022501
[228] Erler J, Birge N, Kortelainen M, Nazarewicz W, Olsen E, Perhac A M and Stoitsov M 2012 The limits of the nuclear landscape *Nature* **486** 509
[229] Ravlić A, Yüksel E, Nikšić T and Paar N 2023 Influence of the symmetry energy on the nuclear binding energies and the neutron drip line position *Phys. Rev.* C **108** 054305
[230] Neufcourt L, Cao Y, Nazarewicz W, Olsen E and Viens F 2019 Neutron drip line in the Ca region from Bayesian model averaging *Phys. Rev. Lett.* **122** 062502
[231] Stroberg S R, Holt J D, Schwenk A and Simonis J 2021 *Ab initio* limits of atomic nuclei *Phys. Rev. Lett.* **126** 022501
[232] Hagen G, Hjorth-Jensen M, Jansen G R, Machleidt R and Papenbrock T 2012 Evolution of shell structure in neutron-rich calcium isotopes *Phys. Rev. Lett.* **109** 032502
[233] Hagen G, Hagen P, Hammer H W and Platter L 2013 Efimov physics around the neutron-rich ^{60}Ca isotope *Phys. Rev. Lett.* **111** 132501

[234] Hergert H, Bogner S K, Morris T D, Binder S, Calci A, Langhammer J and Roth R 2014 *Ab initio* multireference in-medium similarity renormalization group calculations of even calcium and nickel isotopes *Phys. Rev.* C **90** 041302
[235] Hagen G *et al* 2016 Neutron and weak-charge distributions of the ^{48}Ca nucleus *Nat. Phys.* **12** 186
[236] Holt J D, Menéndez J, Simonis J and Schwenk A 2014 Three-nucleon forces and spectroscopy of neutron-rich calcium isotopes *Phys. Rev.* C **90** 024312
[237] Magilligan A, Brown B A and Stroberg S R 2021 Data-driven configuration-interaction Hamiltonian extrapolation to ^{60}Ca *Phys. Rev.* C **104** L051302
[238] Chen S *et al* 2023 Level structures of ^{56,58}Ca cast doubt on a doubly magic ^{60}Ca *Phys. Lett.* B **843** 138025
[239] Li J 2023 Merging of the island of inversion at $n = 40$ and =50 *Phys. Lett.* B **840** 137893
[240] Wimmer K *et al* 2019 First spectroscopy of ^{61}Ti and the transition to the island of inversion at $n = 40$ *Phys. Lett.* B **792** 16–20
[241] Taniuchi R *et al* 2019 ^{78}Ni revealed as a doubly magic stronghold against nuclear deformation *Nature* **569** 52+
[242] Olivier L *et al* 2017 Persistence of the $z = 28$ shell gap around ^{78}Ni: first spectroscopy of ^{79}Cu *Phys. Rev. Lett.* **119** 192501
[243] de Groote R P *et al* 2017 Dipole and quadrupole moments of $^{73-78}$Cu as a test of the robustness of the $z = 28$ shell closure near ^{78}Ni *Phys. Rev.* C **96** 041302
[244] De Groote R *et al* 2020 Measurement and microscopic description of odd–even staggering of charge radii of exotic copper isotopes *Nat. Phys.* **16** 620–4
[245] Hamaker A *et al* 2021 Precision mass measurement of lightweight self-conjugate nucleus ^{80}Zr *Nat. Phys.* **17** 1408–12
[246] Cheifetz E, Jared R C, Thompson S G and Wilhelmy J B 1970 Experimental information concerning deformation of neutron rich nuclei in the $a \sim 100$ region *Phys. Rev. Lett.* **25** 38
[247] de Roubin A *et al* 2017 Nuclear deformation in the a 100 region: comparison between new masses and mean-field predictions *Phys. Rev.* C **96** 014310
[248] Vernon A *et al* 2022 Nuclear moments of indium isotopes reveal abrupt change at magic number 82 *Nature* **607** 260
[249] Karthein J *et al* 2024 Electromagnetic properties of indium isotopes illuminate the doubly magic character of ^{100}Sn *Nat. Phys.* **20** 1719–25
[250] Heyde K and Wood J L 2011 Shape coexistence in atomic nuclei *Rev. Mod. Phys.* **83** 1467
[251] Freer M, Horiuchi H, Lee D and Meißner U G 2018 Microscopic clustering in light nuclei *Rev. Mod. Phys.* **90** 035004
[252] Rowe D J 1985 Microscopic theory of the nuclear collective model *Rep. Prog. Phys.* **48** 1419
[253] Dytrych T, Sviratcheva K D, Bahri C, Draayer J P and Vary J P 2007 Evidence for symplectic symmetry in *ab initio* no-core shell model results for light nuclei *Phys. Rev. Lett.* **98** 162503
[254] McCoy A E, Caprio M A, Dytrych T and Fasano P J 2020 Emergent Sp(3, R) dynamical symmetry in the nuclear many-body system from an *ab initio* description *Phys. Rev. Lett.* **125** 102505
[255] Dytrych T, Launey K, Draayer J, Rowe D, Wood J, Rosensteel G, Bahri C, Langr D and Baker R 2020 Physics of nuclei: key role of an emergent symmetry *Phys. Rev. Lett.* **124** 042501
[256] Harvey M 1968 The nuclear SU_3 model *Advances in Nuclear Physics* vol 1 ed M Baranger and E Vogt (Plenum) p 67
[257] Dytrych T, Launey K D, Draayer J P, Maris P, Vary J P, Saule E, Catalyurek U, Sosonkina M, Langr D and Caprio M A 2013 Collective modes in light nuclei from first principles *Phys. Rev. Lett.* **111** 252501
[258] Wigner E 1937 On the consequences of the symmetry of the nuclear hamiltonian on the spectroscopy of nuclei *Phys. Rev.* **51** 106
[259] Caprio M A, Maris P and Vary J P 2013 Emergence of rotational bands in *ab initio* no-core configuration interaction calculations of light nuclei *Phys. Lett.* B **719** 179
[260] Stroberg S R, Hergert H, Holt J D, Bogner S K and Schwenk A 2016 Ground and excited states of doubly open-shell nuclei from *ab initio* valence-space Hamiltonians *Phys. Rev.* C **93** 051301
[261] Jansen G R, Schuster M D, Signoracci A, Hagen G and Navrátil P 2016 Open *sd*-shell nuclei from first principles *Phys. Rev.* C **94** 011301
[262] Caprio M A, Fasano P J, Maris P, McCoy A E and Vary J P 2020 Probing *ab initio* emergence of nuclear rotation *Eur. Phys. J.* A **56** 120

[263] Yao J M, Bally B, Engel J, Wirth R, Rodrìguez T R and Hergert H 2020 *Ab initio* treatment of collective correlations and the neutrinoless double beta decay of ^{48}Ca *Phys. Rev. Lett.* **124** 232501
[264] Hagen G, Novario S J, Sun Z H, Papenbrock T, Jansen G R, Lietz J G, Duguet T and Tichai A 2022 Angular-momentum projection in coupled-cluster theory: structure of ^{34}Mg *Phys. Rev.* C **105** 064311
[265] Hu B S, Sun Z H, Hagen G and Papenbrock T 2024 *Ab initio* computations of strongly deformed nuclei near ^{80}Zr *Phys. Rev.* C **110** L011302
[266] Pieper S C, Wiringa R B and Carlson J 2004 Quantum Monte Carlo calculations of excited states in $A = 6$–8 nuclei *Phys. Rev.* C **70** 054325
[267] Neff T and Feldmeier H 2004 Cluster structures within fermionic molecular dynamics *Nucl. Phys.* A **738** 357
[268] Maris P 2012 *Ab initio* nuclear structure calculations of light nuclei *J. Phys. Conf. Ser.* **402** 012031
[269] Yoshida T, Shimizu N, Abe T and Otsuka T 2013 Intrinsic structure of light nuclei in Monte Carlo shell model calculation *Few-Body Syst.* **54** 1465
[270] Romero-Redondo C, Quaglioni S, Navrátil P and Hupin G 2016 How many-body correlations and α clustering shape ^{6}He *Phys. Rev. Lett.* **117** 222501
[271] Dreyfuss A C, Launey K D, Escher J E, Sargsyan G H, Baker R B, Dytrych T and Draayer J P 2020 Clustering and α -capture reaction rate from *ab initio* symmetry-adapted descriptions of ^{20}Ne *Phys. Rev.* C **102** 044608
[272] Shen S, Elhatisari S, Lähde T A, Lee D, Lu B-N and Meißner U-G 2023 Emergent geometry and duality in the carbon nucleus *Nature Commun.* **14** 2777
[273] Ono A, Horiuchi H, Maruyama T and Ohnishi A 1992 Fragment formation studied with antisymmetrized version of molecular dynamics with two-nucleon collisions *Phys. Rev. Lett.* **68** 2898–900
[274] Kanada-En'yo Y, Kimura M and Horiuchi H 2003 Antisymmetrized molecular dynamics: a new insight into the structure of nuclei *C.R. Phys.* **4** 497–520
[275] Pastore S, Pieper S C, Schiavilla R and Wiringa R B 2013 Quantum Monte Carlo calculations of electromagnetic moments and transitions in $A \leqslant 9$ nuclei with meson-exchange currents derived from chiral effective field theory *Phys. Rev.* C **87** 035503
[276] Gysbers P *et al* 2019 Discrepancy between experimental and theoretical β-decay rates resolved from first principles *Nat. Phys.* **15** 428
[277] Casten R F 2000 *Nuclear Structure from a Simple Perspective* vol 23 2nd edn (Oxford University Press)
[278] Garcia Ruiz R F *et al* 2016 Unexpectedly large charge radii of neutron-rich calcium isotopes *Nat. Phys.* **12** 594–8
[279] Kanada-En'yo Y and Horiuchi H 1997 Opposite deformations between protons and neutrons in proton-rich C isotopes *Phys. Rev.* C **55** 2860
[280] Caprio M A, McCoy A E, Fasano P J and Dytrych T 2022 Symmetry and shape coexistence in ^{10}Be *Bulg. J. Phys.* **49** 57
[281] Calci A and Roth R 2016 Sensitivities and correlations of nuclear structure observables emerging from chiral interactions *Phys. Rev.* C **94** 014322
[282] Sargsyan G H *et al* 2022 Impact of clustering on the ^{8}Li β decay and recoil form factors *Phys. Rev. Lett.* **128** 202503
[283] Caprio M A, Fasano P J, Maris P and McCoy A E 2021 Quadrupole moments and proton–neutron structure in *p*-shell mirror nuclei *Phys. Rev.* C **104** 034319
[284] Caprio M A and Fasano P J 2022 *Ab initio* estimation of E2 strengths in ^{8}Li and its neighbors by normalization to the measured quadrupole moment *Phys. Rev.* C **106** 034320
[285] Caprio M A, Fasano P J and Maris P 2022 Robust *ab initio* prediction of nuclear electric quadrupole observables by scaling to the charge radius *Phys. Rev.* C **105** L061302
[286] Bernstein A, Brown V and Madsen V 1983 Neutron and proton matrix elements for low-lying 2^{+} transitions and the probe dependence of the nuclear deformation parameter *Comments Nucl. Part. Phys.* **11** 203
[287] Furuno T *et al* 2019 Neutron quadrupole transition strength in ^{10}C deduced from the ^{10}C(α, α') measurement with the maiko active target *Phys. Rev.* C **100** 054322
[288] Garcia Ruiz R F *et al* 2020 Spectroscopy of short-lived radioactive molecules *Nature* **581** 396–400

[289] Udrescu S M *et al* 2021 Isotope shifts of radium monofluoride molecules *Phys. Rev. Lett.* **127** 033001
[290] Arrowsmith-Kron G *et al* 2024 Opportunities for fundamental physics research with radioactive molecules *Rep. Prog. Phys.* **87** 084301
[291] Kibedi T and Spear R H 2002 Reduced electric-octupole transition probabilities, B($E3;0_1^+ \rightarrow 3_1^-$)—an update *At. Data Nucl. Data Tables* **80** 35–82
[292] Butler P A and Nazarewicz W 1996 Intrinsic reflection asymmetry in atomic nuclei *Rev. Mod. Phys.* **68** 349–421
[293] Butler P A 2016 Octupole collectivity in nuclei *J. Phys. G: Nucl. Part. Phys.* **43** 073002
[294] Butler P 2021 Pear-shaped atomic nuclei *Proc. R. Soc.* A **476** 20200202
[295] Spieker M *et al* 2022 Investigation of octupole collectivity near the $A = 72$ shape-transitional point *Phys. Rev.* C **106** 054305
[296] Iskra L *et al* 2019 Revised B($E3$) transition rate and structure of the 3-level in ^{96}Zr *Phys. Lett.* B **788** 396–400
[297] Agbemava S E and Afanasjev A V 2017 Octupole deformation in the ground states of even–even $z \sim 96$, $n \sim 196$ actinides and superheavy nuclei *Phys. Rev.* C **96** 024301
[298] Cao Y, Agbemava S E, Afanasjev A V, Nazarewicz W and Olsen E 2020 Landscape of pear-shaped even-even nuclei *Phys. Rev.* C **102** 024311
[299] Chen M, Li T, Dobaczewski J and Nazarewicz W 2021 Microscopic origin of reflection-asymmetric nuclear shapes *Phys. Rev.* C **103** 034303
[300] Lanza E, Pellegri L, Vitturi A and Andres M 2023 Theoretical studies of pygmy resonances *Prog. Part. Nucl. Phys.* **129** 104006
[301] Roca-Maza X, Pozzi G, Brenna M, Mizuyama K and Colò G 2012 Low-lying dipole response: isospin character and collectivity in ^{68}Ni, ^{132}Sn, and ^{208}Pb *Phys. Rev.* C **85** 024601
[302] Savran D, Aumann T and Zilges A 2013 Experimental studies of the pygmy dipole resonance *Prog. Part. Nucl. Phys.* **70** 210–45
[303] Vretenar D, Niu Y F, Paar N and Meng J 2012 Low-energy isovector and isoscalar dipole response in neutron-rich nuclei *Phys. Rev.* C **85** 044317
[304] Bracco A, Lanza E and Tamii A 2019 Isoscalar and isovector dipole excitations: nuclear properties from low-lying states and from the isovector giant dipole resonance *Prog. Part. Nucl. Phys.* **106** 360–433
[305] Litvinova E, Loens H, Langanke K, Martinez-Pinedo G, Rauscher T, Ring P, Thielemann F K and Tselyaev V 2009 Low-lying dipole response in the relativistic quasiparticle time blocking approximation and its influence on neutron capture cross sections *Nucl. Phys.* A **823** 26–37
[306] Tsoneva N, Goriely S, Lenske H and Schwengner R 2015 Pygmy resonances and radiative nucleon captures for stellar nucleosynthesis *Phys. Rev.* C **91** 044318
[307] Tonchev A *et al* 2017 Pygmy and core polarization dipole modes in ^{206}Pb: connecting nuclear structure to stellar nucleosynthesis *Phys. Lett.* B **773** 20–5
[308] Angell C T, Hammond S L, Karwowski H J, Kelley J H, Krtička M, Kwan E, Makinaga A and Rusev G 2012 Evidence for radiative coupling of the pygmy dipole resonance to excited states *Phys. Rev.* C **86** 051302
[309] Martin D *et al* 2017 Test of the brink-axel hypothesis for the pygmy dipole resonance *Phys. Rev. Lett.* **119** 182503
[310] Isaak J *et al* 2019 The concept of nuclear photon strength functions: a model-independent approach via (γ, $\gamma'\gamma'$) reactions *Phys. Lett.* B **788** 225
[311] Markova M *et al* 2021 Comprehensive test of the brink-axel hypothesis in the energy region of the pygmy dipole resonance *Phys. Rev. Lett.* **127** 182501
[312] Ratkiewicz A *et al* 2019 Toward neutron capture on exotic nuclei: demonstrating (d, $p\gamma$) as a surrogate reaction for (n, γ) *Phys. Rev. Lett.* **122** 052502
[313] Spieker M *et al* 2020 Accessing the single-particle structure of the pygmy dipole resonance in ^{208}Pb *Phys. Rev. Lett.* **125** 102503
[314] Weinert M, Spieker M, Potel G, Tsoneva N, Müscher M, Wilhelmy J and Zilges A 2021 Microscopic structure of the low-energy electric dipole response of ^{120}Sn *Phys. Rev. Lett.* **127** 242501
[315] Spieker M, Baby L T, Conley A L, Kelly B, Müscher M, Renom R, Schüttler T and Zilges A 2023 Experimental study of excited states of ^{62}Ni via one-neutron (d, p) transfer up to the neutron-separation threshold and characteristics of the pygmy dipole resonance states *Phys. Rev.* C **108** 014311

[316] 2018 SOLARIS White Paper, https://www.anl.gov/sites/www/files/2018-11/solaris_white_paper_final.pdf
[317] Savran D *et al* 2011 Fragmentation and systematics of the pygmy dipole resonance in the stable $n = 82$ isotones *Phys. Rev.* C **84** 024326
[318] Avigo R *et al* 2020 Low-lying electric dipole γ-continuum for the unstable ^{62,64}Fe nuclei: strength evolution with neutron number *Phys. Lett.* B **811** 135951
[319] van Kolck U 1998 Nucleon–nucleon interaction and isospin violation *Chiral Dynamics: Theory and Experiment* ed A M Bernstein, D Drechsel and T Walcher (Springer) pp 62–77
[320] Miller G A, Opper A K and Stephenson E J 2006 Charge symmetry breaking and QCD *Annu. Rev. Nucl. Part. Sci.* **56** 253–92
[321] MacCormick M and Audi G 2014 Evaluated experimental isobaric analogue states from $T = 1/2$ to $T = 3$ and associated IMME coefficients *Nucl. Phys.* A **925** 61 95
[322] Ormand W E and Brown B A 1989 Empirical isospin-nonconserving hamiltonians for shell-model calculations *Nucl. Phys.* A **491** 1 23
[323] Ormand W E and Brown B A 1995 Isospin-mixing corrections for *fp*-shell Fermi transitions *Phys. Rev.* C **52** 2455
[324] Lam Y H, Blank B, Smirnova N A, Bueb J B and Antony M S 2013 The isobaric multiplet mass equation for $A < 71$ revisited *At. Data Nucl. Data Tables* **99** 680–703
[325] Lam Y H, Smirnova N A and Caurier E 2013 Isospin nonconservation in sd-shell nuclei *Phys. Rev.* C **87** 054304
[326] Martin M S, Stroberg S, Holt J and Leach K 2021 Testing isospin symmetry breaking in *ab initio* nuclear theory *Phys. Rev.* C **104** 014324
[327] Zuker A, Lenzi S, Martinez-Pinedo G and Poves A 2002 Isobaric multiplet yrast energies and isospin nonconserving forces *Phys. Rev. Lett.* **89** 142502
[328] Bentley M and Lenzi S 2007 Coulomb energy differences between high-spin states in isobaric multiplets *Prog. Part. Nucl. Phys.* **59** 497–561
[329] Ekman J *et al* 2004 Unusual isospin-breaking and isospin-mixing effects in the $a = 35$ mirror nuclei *Phys. Rev. Lett.* **92**
[330] Lalanne L *et al* 2022 Structure of ^{36}Ca under the Coulomb magnifying glass *Phys. Rev. Lett.* **129** 122501
[331] Lenzi S *et al* 2001 Coulomb energy differences in $t = 1$ mirror rotational bands in ^{50}Fe and ^{50}Cr *Phys. Rev. Lett.* **87** 132502
[332] Bonnard J, Lenzi S M and Zuker A P 2016 Neutron skins and halo orbits in the *sd* and *pf* shells *Phys. Rev. Lett.* **116** 212501
[333] Bonnard J and Zuker A P 2018 Radii in the *sd* shell and the $1s_{1/2}$ 'halo' orbit: a game changer *J. Phys.: Conf. Ser.* **1023** 012016
[334] Fernandez A *et al* 2021 Mirror energy differences above the $0f_{7/2}$ shell: first γ-ray spectroscopy of the $T_z = -2$ nucleus ^{56}Zn *Phys. Lett.* B **823** 136784
[335] Enciu M *et al* 2022 Extended $p_{3/2}$ neutron orbital and the $N = 32$ shell closure in ^{52}Ca *Phys. Rev. Lett.* **129** 262501
[336] Xu Z Y *et al* 2023 ^{133}In: a rosetta stone for decays of *r*-process nuclei *Phys. Rev. Lett* **131** 022501
[337] Okołowicz J, Płoszajczak M and Rotter I 2003 Dynamics of quantum systems embedded in a continuum *Phys. Rep.* **374** 271–383
[338] Spyrou A *et al* 2016 Strong neutron-gamma competition above the neutron threshold in the decay of ^{70}Co *Phys. Rev. Lett.* **117** 142701
[339] Ohm H, Rudolph W and Kratz K L 1976 Beta-delayed neutron emission following the decay of ^{17}N *Nucl. Phys.* A **274** 45–52
[340] Azuma R E *et al* 1979 First observation of beta-delayed two-neutron radioactivity: ^{11}Li *Phys. Rev. Lett.* **43** 1652–4
[341] Caballero-Folch R *et al* 2018 First determination of β-delayed multiple neutron emission beyond $A = 100$ through direct neutron measurement: the P_{2n} value of ^{136}Sb *Phys. Rev.* C **98** 034310
[342] Sarriguren P and Pereira J 2010 β-decay properties of neutron-rich Zr and mo isotopes *Phys. Rev.* C **81** 064314
[343] Miyagi T, Cao X, Seutin R, Bacca S, Ruiz R F G, Hebeler K, Holt J D and Schwenk A 2024 Impact of two-body currents on magnetic dipole moments of nuclei *Phys. Rev. Lett.* **132** 232503
[344] Garg U and Colò G 2018 The compression-mode giant resonances and nuclear incompressibility *Prog. Part. Nucl. Phys.* **101** 55–95

[345] Colò G, Nagarajan M A, Van Isacker P and Vitturi A 1995 Isospin mixing in proton-rich $n \simeq z$ nuclei *Phys. Rev.* C **52** R1175–8
[346] Cole A L *et al* 2006 Measurement of the Gamow–Teller strength distribution in ^{58}Co via the ^{58}Ni $(t, {}^3\mathrm{He})$ reaction at 115 Mev/nucleon *Phys. Rev.* C **74** 034333
[347] Fracasso S and Colò G 2005 Fully self-consistent charge-exchange quasiparticle random-phase approximation and its application to isobaric analog resonances *Phys. Rev.* C **72** 064310
[348] Robin C and Litvinova E 2018 Coupling charge-exchange vibrations to nucleons in a relativistic framework: effect on gamow-teller transitions and β -decay half-lives *Phys. Rev.* C **98** 051301
[349] Bohr A, Mottelson B R and Pines D 1958 Possible analogy between the excitation spectra of nuclei and those of the superconducting metallic state *Phys. Rev.* **110** 936–8
[350] Bardeen J, Cooper L N and Schrieffer J R 1957 Microscopic theory of superconductivity *Phys. Rev.* **106** 162–4
[351] Brink D M and Broglia R A 2005 Frontmatter *Nuclear Superfluidity: Pairing in Finite Systems* (Cambridge University Press) p i–vi
[352] Broglia R and Zelevinsky V 2013 *Fifty Years Nuclear BCS: Pairing in Finite Systems* (World Scientific) vol 01, pp 1–670
[353] Dean D J and Hjorth-Jensen M 2003 Pairing in nuclear systems: from neutron stars to finite nuclei *Rev. Mod. Phys.* **75** 607–56
[354] Matsuo M 2006 Spatial structure of neutron cooper pair in low density uniform matter *Phys. Rev.* C **73** 044309
[355] Yoshida S 1962 Note on the two-nucleon stripping reaction *Nucl. Phys.* **33** 685–92
[356] Bayman B F and Hintz N M 1968 Analysis of two-neutron ($l = 0$) transfer cross sections for calcium and nickel *Phys. Rev.* **172** 1113–23
[357] Broglia R A, Hansen O and Riedel C 1973 Two-neutron transfer reactions and the pairing model *Advances in Nuclear Physics* vol 6 ed M Baranger and E Vogt (Springer) pp 287–457
[358] Broglia R, Terasaki J and Giovanardi N 2000 The Anderson–Goldstone–Nambu mode in finite and in infinite systems *Phys. Rep.* **335** 1–18
[359] Shimoyama H and Matsuo M 2011 *Phys. Rev.* C **84** 044317
[360] Shimoyama H and Matsuo M 2013 *Phys. Rev.* C **88** 054308
[361] Frauendorf S and Macchiavelli A O 2014 Overview of neutron–proton pairing *Prog. Part. Nucl. Phys.* **78** 24–90
[362] Yoshida K 2014 Proton–neutron pairing vibrations in $N = Z$ nuclei: precursory soft mode of isoscalar pairing condensation *Phys. Rev.* C **90** 031303(R)
[363] Isacker P V, Warner D D and Brenner D S 1995 Test of Wigner's spin-isospin symmetry from double binding energy differences *Phys. Rev. Lett.* **74** 4607–10
[364] Chartier M *et al* 1996 Mass measurement of ^{100}Sn *Phys. Rev. Lett.* **77** 2400–3
[365] Barker F C 1964 A model for nuclear threshold levels *Proc. Phys. Soc.* **84** 681
[366] Baz I A 1958 The energy dependence of a scattering cross section near the threshold of a reaction *JETP* **6** 709
[367] Baz A I 1959 Resonance effects in the scattering of particles near a reaction threshold *JETP* **9** 1256
[368] Baz A I 1961 Energy dependence of cross sections near the 'threshold' for unstable particle production *JETP* **13** 1058
[369] Breit G 1957 Energy dependence of reactions at thresholds *Phys. Rev.* **107** 1612–5
[370] Inglis D R 1962 Nuclear models, threshold states and rearrangement energy *Nucl. Phys.* **30** 1–29
[371] Wigner E P 1948 On the behavior of cross sections near thresholds *Phys. Rev.* **73** 1002–9
[372] Volya A and Zelevinsky V 2006 Continuum shell model *Phys. Rev.* C **74** 064314
[373] Volya A and Zelevinsky V 2003 Non-hermitian effective hamiltonian and continuum shell model *Phys. Rev.* C **67** 054322
[374] Kay B P, Hoffman C R and Macchiavelli A O 2017 Effect of weak binding on the apparent spin–orbit splitting in nuclei *Phys. Rev. Lett.* **119** 182502
[375] Hoffman C R, Kay B P and Schiffer J P 2014 Neutron *s* states in loosely bound nuclei *Phys. Rev.* C **89** 061305
[376] Sorlin O, de Oliveira Santos F and Ebran J P 2020 Reduced spin–orbit splitting in ^{35}Si: weak binding or density-depletion effect? *Phys. Lett.* B **809** 135740
[377] Michel N and Płoszajczak M 2021 *Gamow Shell Model, The Unified Theory of Nuclear Structure and Reactions, Lecture Notes in Physics* vol 983 (Springer)

[378] Calci A, Navrátil P, Roth R, Dohet-Eraly J, Quaglioni S and Hupin G 2016 Can *ab initio* theory explain the phenomenon of parity inversion in ^{11}Be? *Phys. Rev. Lett.* **117** 242501
[379] Auerbach N and Zelevinsky V 2011 Super-radiant dynamics, doorways and resonances in nuclei and other open mesoscopic systems *Rep. Prog. Phys.* **74** 106301
[380] Wang S M, Nazarewicz W, Volya A and Ma Y G 2023 Probing the nonexponential decay regime in open quantum systems *Phys. Rev. Res.* **5** 023183
[381] Ikeda K, Takigawa N and Horiuchi H 1968 The systematic structure-change into the molecule-like structures in the self-conjugate 4*n* nuclei *Prog. Theo. Phys. Suppl* **E68** 464–75
[382] Volya A, Barbui M, Goldberg V Z and Rogachev G V 2022 Superradiance in Alpha Clustered Mirror Nuclei *Communications Physics* **5** 322
[383] Bazin D *et al* 2023 Perspectives on few-body cluster structures in exotic nuclei *Few-Body Syst.* **64** 25
[384] Baye D and Tursunov E 2011 β delayed emission of a proton by a one-neutron halo nucleus *Phys. Lett.* B **696** 464–7
[385] Ayyad Y *et al* 2019 Direct observation of proton emission in ^{11}Be *Phys. Rev. Lett.* **123** 082501
[386] Volya A 2020 Assessment of the beta-delayed proton decay rate of ^{11}Be *EPL* **130** 12001
[387] Pfützner M and Riisager K 2018 Examining the possibility to observe neutron dark decay in nuclei *Phys. Rev.* C **97** 042501
[388] Ayyad Y *et al* 2022 Evidence of a near-threshold resonance in ^{11}B relevant to the β-delayed proton emission of ^{11}Be *Phys. Rev. Lett.* **129** 012501
[389] Lopez-Saavedra E *et al* 2022 Observation of a near-threshold proton resonance in ^{11}B *Phys. Rev. Lett.* **129** 012502
[390] Okołowicz J, Płoszajczak M and Nazarewicz W 2020 Convenient location of a near-threshold proton-emitting resonance in ^{11}B *Phys. Rev. Lett.* **124** 042502
[391] Atkinson M C, Navrátil P, Hupin G, Kravvaris K and Quaglioni S 2022 *Ab initio* calculation of the β decay from ^{11}Be to a^{10}Be+p resonance *Phys. Rev.* C **105** 054316
[392] Volya A 2009 Time-dependent approach to the continuum shell model *Phys. Rev.* C **79** 044308
[393] Wang S M and Nazarewicz W 2021 Fermion pair dynamics in open quantum systems *Phys. Rev. Lett.* **126** 142501
[394] Pfützner M, Karny M, Grigorenko L V and Riisager K 2012 Radioactive decays at limits of nuclear stability *Rev. Mod. Phys.* **84** 567–619
[395] Pfützner M, Mukha I and Wang S 2023 Two-proton emission and related phenomena *Prog. Part. Nucl. Phys.* **132** 104050
[396] Bochkarev O V, Chulkov L V, Korsheninniicov A A, Kuz'min E A, Mukha I G and Yankov G B 1989 Democratic decay of ^{6}Be states *Nucl. Phys.* A **505** 215
[397] Kryger R *et al* 1995 Two-proton emission from the ground state of ^{12}O *Phys. Rev. Lett.* **74** 860
[398] Jager M F *et al* 2012 Two-proton decay of ^{12}O and its isobaric analog state in ^{12}N *Phys. Rev.* C **86** 011304(R)
[399] Webb T B *et al* 2019 First observation of unbound ^{11}O, the mirror of the halo nucleus ^{11}Li *Phys. Rev. Lett.* **122** 122501
[400] Wang S M, Nazarewicz W, Charity R J and Sobotka L G 2019 Structure and decay of the extremely proton-rich nuclei ^{11,12}O *Phys. Rev.* C **99** 054302
[401] Neufcourt L, Cao Y, Giuliani S, Nazarewicz W, Olsen E and Tarasov O B 2020 Beyond the proton drip line: Bayesian analysis of proton-emitting nuclei *Phys. Rev.* C **101** 014319
[402] Wang S M, Nazarewicz W, Charity R J and Sobotka L G 2022 Nucleon–nucleon correlations in the extreme oxygen isotopes *J. Phys.* G **49** 10LT02
[403] Hamamoto I 2019 Shape and shell structure of lighter ($N \lesssim 90$) neutron-rich nuclei based on a phenomenological Woods–Saxon potential *Phys. Rev.* C **99** 024319
[404] Macchiavelli A O, Crawford H L, Fallon P, Clark R M and Poves A 2022 Weak binding effects on the structure of ^{40}Mg *Eur. Phys. J.* A **58** 66
[405] Warner D and Van Isacker P 1997 The scissors mode in the presence of a neutron skin *Phys. Lett.* B **395** 145–50
[406] Misu T, Nazarewicz W and Åberg S 1997 Deformed nuclear halos *Nucl. Phys.* A **614** 44–70
[407] Bagchi S *et al* 2020 Two-neutron halo is unveiled in ^{29}F *Phys. Rev. Lett.* **124** 222504
[408] Kobayashi N *et al* 2016 One-neutron removal from ^{29}Ne: defining the lower limits of the island of inversion *Phys. Rev.* C **93** 014613
[409] Nakamura T *et al* 2014 Deformation-driven *p*-wave halos at the drip line: ^{31}Ne *Phys. Rev. Lett.* **112** 142501

[410] Kobayashi N *et al* 2014 Observation of a *p*-wave one-neutron halo configuration in ^{37}Mg *Phys. Rev. Lett.* **112** 242501
[411] Loelius C *et al* 2018 Enhanced electric dipole strength for the weakly bound states in ^{27}Ne *Phys. Rev. Lett.* **121** 262501
[412] Typel S and Baur G 2004 Effective-range approach and scaling laws for electromagnetic strength in neutron-halo nuclei *Phys. Rev. Lett.* **93** 142502
[413] Typel S and Baur G 2005 Electromagnetic strength of neutron and proton single-particle halo nuclei *Nucl. Phys.* A **759** 247
[414] Fossez K, Nazarewicz W, Jaganathen Y, Michel N and Płoszajczak M 2016 Nuclear rotation in the continuum *Phys. Rev.* C **93** 011305
[415] Fossez K and Rotureau J 2022 Density matrix renormalization group description of the island of inversion isotopes $^{28-33}$F *Phys. Rev.* C **106** 034312
[416] Luo Y X, Fossez K, Liu Q and Guo J Y 2021 Role of quadrupole deformation and continuum effects in the 'island of inversion' nuclei ^{28,29,31}F *Phys. Rev.* C **104** 014307
[417] Crawford H L *et al* 2014 Shell and shape evolution at $N = 28$: the ^{40}Mg ground state *Phys. Rev.* C **89** 041303
[418] Crawford H L *et al* 2019 First spectroscopy of the near drip-line nucleus ^{40}Mg *Phys. Rev. Lett.* **122** 052501
[419] Caurier E, Nowacki F and Poves A 2014 Merging of the islands of inversion at $N = 20$ and $N = 28$ *Phys. Rev.* C **90** 014302
[420] Hamamoto I 2007 Nilsson diagrams for light neutron-rich nuclei with weakly-bound neutrons *Phys. Rev.* C **76** 054319
[421] Nakada H and Takayama K 2018 Intertwined effects of pairing and deformation on neutron halos in magnesium isotopes *Phys. Rev.* C **98** 011301
[422] Fossez K, Rotureau J, Michel N, Liu Q and Nazarewicz W 2016 Single-particle and collective motion in unbound deformed ^{39}Mg *Phys. Rev.* C **94** 054302
[423] Riisager K 2020 *Beta Decay of Halo Nuclei* (Springer Nature Singapore) 1–24
[424] Lazauskas R 2018 Description of five-nucleon systems using Faddeev–Yakubovsky equations *Few-Body Syst.* **59** 13
[425] Baroni S, Navrátil P and Quaglioni S 2013 *Ab initio* description of the exotic unbound ^{7}He nucleus *Phys. Rev. Lett.* **110** 022505
[426] Vorabbi M, Calci A, Navrátil P, Kruse M K G, Quaglioni S and Hupin G 2018 Structure of the exotic ^{9}He nucleus from the no-core–shell model with continuum *Phys. Rev.* C **97** 034314
[427] Papadimitriou G, Rotureau J, Michel N, Płoszajczak M and Barrett B R 2013 *Ab initio* no-core Gamow shell model calculations with realistic interactions *Phys. Rev.* C **88** 044318
[428] Fossez K, Rotureau J, Michel N and Płoszajczak M 2017 Can tetraneutron be a narrow resonance? *Phys. Rev. Lett.* **119** 032501
[429] Li J G, Michel N, Zuo W and Xu F R 2021 Resonances of $A = 4T = 1$ isospin triplet states within the *ab initio* no-core Gamow shell model *Phys. Rev.* C **104** 024319
[430] Berggren T 1968 On the use of resonant states in eigenfunction expansions of scattering and reaction amplitudes *Nucl. Phys.* A **109** 265
[431] Berggren T and Lind P 1993 Resonant state expansion of the resolvent *Phys. Rev.* C **47** 768
[432] Serpico P D, Esposito S, Iocco F, Mangano G, Miele G and Pisanti O 2004 Nuclear reaction network for primordial nucleosynthesis: a detailed analysis of rates, uncertainties and light nuclei yields *J. Cosmol. Astropart. Phys.* JCAP12(2004)010
[433] Navrátil P and Quaglioni S 2012 *Ab initio* many-body calculations of the ^{3}H$(d, n)^{4}$ He and ^{3}He$(d, p)^{4}$ He fusion reactions *Phys. Rev. Lett.* **108** 042503
[434] Smith M S, Kawano L H and Malaney R A 1993 Experimental, computational, and observational analysis of primordial nucleosynthesis *Astrophys. J.* **85** 219–47
[435] Chadwick M B, Paris M W and Haines B M 2023 Dt fusion through the ^{5}He $3/2+$ 'bretscher state' accounts for $\geqslant$25% of our existence via nucleosynthesis and for the possibility of fusion energy arXiv:2305.00647
[436] Dohet-Eraly J, Navrátil P, Quaglioni S, Horiuchi W, Hupin G and Raimondi F 2016 3 He(α, γ) ^{7}Be and ^{3}H(α, γ) ^{7}Li astrophysical s factors from the no-core–shell model with continuum *Phys. Lett.* B **757** 430–6
[437] Vorabbi M, Navrátil P, Quaglioni S and Hupin G 2019 ^{7}Be and ^{7}Li nuclei within the no-core–shell model with continuum *Phys. Rev.* C **100** 024304

[438] Dronchi N *et al* 2023 Search for an *s*-wave resonance in ^{7}Li just above the proton-decay threshold *Phys. Rev.* C **107** L061303
[439] Yang J and Capel P 2018 Systematic analysis of the peripherality of the ^{10}Be(*d*, *p*) ^{11}Be transfer reaction and extraction of the asymptotic normalization coefficient of ^{11}Be bound states *Phys. Rev.* C **98** 054602
[440] Capel P, Philips D R and Hammer H W 2022 Dissecting reaction calculations using halo effective field theory and *ab initio* input *Phys. Rev.* C **98** 034610
[441] Moschini L, Yang J and Capel P 2019 ^{15}C: from halo effective field theory structure to the study of transfer, breakup, and radiative-capture reactions *Phys. Rev.* C **100** 044615
[442] Kravvaris K, Quaglioni S, Hupin G and Navrátil P 2024 *Ab initio* framework for nuclear scattering and reactions induced by light projectiles *Phys. Lett.* B **856** 138930
[443] Launey K D, Dytrych T and Draayer J P 2016 Symmetry-guided large-scale shell-model theory *Prog. Part. Nucl. Phys.* **89** 101
[444] Ruotsalainen P *et al* 2019 Isospin symmetry in *B*(*E*2) values: coulomb excitation study of ^{21}Mg *Phys. Rev.* C **99** 051301
[445] Henderson J *et al* 2018 Testing microscopically derived descriptions of nuclear collectivity: coulomb excitation of ^{22}Mg *Phys. Lett.* B **782** 468
[446] Williams J *et al* 2019 Structure of ^{28}Mg and influence of the neutron *pf* shell *Phys. Rev.* C **100** 014322
[447] Launey K D, Mercenne A, Sargsyan G H, Shows H, Baker R B, Miora M E, Dytrych T and Draayer J P 2018 Emergent clustering phenomena in the framework of the *ab initio* symmetry-adapted no-core–shell model *AIP Conf. Proc.* **2038** 020004
[448] Sargsyan G H, Launey K D, Shaffer R M, Marley S T, Dudeck N, Mercenne A, Dytrych T and Draayer J P 2023 *Ab initio* single-neutron spectroscopic overlaps in lithium isotopes *Phys. Rev.* C **108** 054303
[449] Holl M *et al* 2021 Proton inelastic scattering reveals deformation in ^{8}He *Phys. Lett.* B **822** 136710
[450] Kanungo R 2020 *Radii and Momentum Distribution of Unstable Nuclei* (Springer Nature) pp 1–44
[451] Chen J *et al* 2022 Probing the quadrupole transition strength of ^{1}5C via deuteron inelastic scattering *Phys. Rev.* C **106** 064312
[452] Navrátil P and Quaglioni S 2022 *Ab initio* nuclear reaction theory with applications to astrophysics *Handbook of Nuclear Physics* (Springer) pp 1–46
[453] Elhatisari S, Lee D, Rupak G, Epelbaum E, Krebs H, Lähde T A, Luu T and Meißner U-G 2015 *Ab initio* alpha–alpha scattering *Nature* **528** 111
[454] Elhatisari S *et al* 2024 Wavefunction matching for solving quantum many-body problems *Nature* **630** 59–63
[455] Elhatisari S, Epelbaum E, Krebs H, Lähde T A, Lee D, Li N, Lu B-n, Meißner U G and Rupak G 2017 *Ab initio* calculations of the isotopic dependence of nuclear clustering *Phys. Rev. Lett.* **119** 222505
[456] Kisamori K *et al* 2016 Candidate resonant tetraneutron state populated by the ^{4}He(^{8}He, ^{8}Be) reaction *Phys. Rev. Lett.* **116** 052501
[457] Duer M *et al* 2022 Observation of a correlated free four-neutron system *Nature* **606** 678–82
[458] Lazauskas R, Hiyama E and Carbonell J 2023 Low energy structures in nuclear reactions with 4*n* in the final state *Phys. Rev. Lett.* **130** 102501
[459] Faddeev L 1961 Scattering theory for a three-particle system *Sov. Phys. JETP* **1014** 014601
[460] Deltuva A and Fonseca A C 2007 Four-nucleon scattering: *ab initio* calculations in momentum space *Phys. Rev.* C **75** 014005
[461] Lazauskas R, Carbonell J, Fonseca A C, Viviani M, Kievsky A and Rosati S 2005 Low energy n-^{3}H scattering: a novel testground for nuclear interactions *Phys. Rev.* C **71** 034004
[462] Chimanski E V, In E J, Escher J E, Péru S and Younes W 2023 Addressing nuclear structure challenges in the Zr isotopes with self-consistent gogny-force HFB and QRPA predictions arXiv:2308.13374 [nucl-th]
[463] Lei J and Moro A M 2015 Reexamining closed-form formulae for inclusive breakup: application to deuteron- and ^{6}Li-induced reactions *Phys. Rev.* C **92** 044616
[464] Lei J and Moro A M 2015 Numerical assessment of post-prior equivalence for inclusive breakup reactions *Phys. Rev.* C **92** 061602
[465] Potel G, Nunes F M and Thompson I J 2015 Establishing a theory for deuteron-induced surrogate reactions *Phys. Rev.* C **92** 034611

[466] Carlson B V, Capote R and Sin M 2016 Inclusive proton emission spectra from deuteron breakup reactions *Few-Body Syst.* **57** 307–14
[467] Lei J and Moro A M 2019 Puzzle of complete fusion suppression in weakly bound nuclei: a trojan horse effect? *Phys. Rev. Lett.* **122** 042503
[468] Lei J and Moro A M 2019 Unraveling the reaction mechanisms leading to partial fusion of weakly bound nuclei *Phys. Rev. Lett.* **123** 232501
[469] Nunes F, Potel G, Poxon-Pearson T and Cizewski J 2020 Nuclear reactions in astrophysics: a review of useful probes for extracting reaction rates *Ann. Rev. Nucl. Part. Sci.* **70** 147–70
[470] Gómez-Ramos M, Gómez-Camacho J and Moro A 2022 Binding-energy asymmetry in absorption explored through CDCC extended for complex potentials *Phys. Lett.* B **832** 137252
[471] Lei J and Moro A M 2023 Advancing the Ichimura–Austern–Vincent model with continuum-discretized coupled-channels wave functions for realistic descriptions of two-body projectile breakup *Phys. Rev.* C **108** 034612
[472] Torabi F and Carlson B V 2023 A systematic analysis of deuteron breakup *J. Phys. G: Nucl. Part. Phys.* **50** 045107
[473] Capel P, Hussein M and Baye D 2010 Influence of the halo upon angular distributions for elastic scattering and breakup *Phys. Lett.* B **693** 448–51
[474] Capel P, Johnson R and Nunes F 2011 One-neutron halo structure by the ratio method *Phys. Lett.* B **705** 112–5
[475] Capel P, Johnson R C and Nunes F M 2013 The ratio method: a new tool to study one-neutron halo nuclei *Phys. Rev.* C **88** 044602
[476] Capel P, Johnson R C and Nunes F M 2020 Study of cluster structures in nuclei through the ratio method *Eur. Phys. J.* A **56** 300
[477] Aumann T *et al* 2021 Quenching of single-particle strength from direct reactions with stable and rare-isotope beams *Prog. Part. Nucl. Phys.* **118** 103847
[478] Kay B P *et al* 2022 Quenching of single-particle strength in $A = 15$ nuclei *Phys. Rev. Lett.* **129** 152501
[479] Hebborn C, Whitehead T R, Lovell A E and Nunes F M 2023 Quantifying uncertainties due to optical potentials in one-neutron knockout reactions *Phys. Rev.* C **108** 014601
[480] Tostevin J A and Gade A 2021 Updated systematics of intermediate-energy single-nucleon removal cross sections *Phys. Rev.* C **103** 054610
[481] Gade A *et al* 2008 Reduction of spectroscopic strength: weakly-bound and strongly-bound single-particle states studied using one-nucleon knockout reactions *Phys. Rev.* C **77** 044306
[482] Arcones A *et al* 2017 White paper on nuclear astrophysics and low energy nuclear physics: I. Nuclear astrophysics *Prog. Part. Nucl. Phys.* **94** 1
[483] Arnould M and Goriely S 2020 Astronuclear physics: a tale of the atomic nuclei in the skies *Prog. Part. Nucl. Phys.* **112** 103766
[484] Hayes A C 2017 Applications of nuclear physics *Rep. Prog. Phys.* **80** 026301
[485] Brown D *et al* 2018 ENDF/B-VIII.0: the 8th major release of the nuclear reaction data library with cielo-project cross sections, new standards and thermal scattering data *Nucl. Data Sheets* **148** 1
[486] Koning A, Rochman D, Sublet J C, Dzysiuk N, Fleming M and van der Marck S 2019 Tendl: complete nuclear data library for innovative nuclear science and technology *Nucl. Data Sheets* **155** 1–55
[487] Azuma R E *et al* 2010 Azure: an *r*-matrix code for nuclear astrophysics *Phys. Rev.* C **81** 045805
[488] Carlson B V, Escher J E and Hussein M S 2014 Theoretical descriptions of compound-nuclear reactions: open problems and challenges *J. Phys.,* G **41** 094003
[489] Koning A, Hilaire S and Goriely S 2008 Global and local level density models *Nucl. Phys.* A **810** 13–76
[490] Goriely S, Hilaire S and Koning A J 2008 Improved microscopic nuclear level densities within the hartree-fock-bogoliubov plus combinatorial method *Phys. Rev.* C **78** 064307
[491] Hilaire S, Girod M, Goriely S and Koning A J 2012 Temperature-dependent combinatorial level densities with the d1m gogny force *Phys. Rev.* C **86** 064317
[492] Alhassid Y 2015 The shell model monte carlo approach to level densities: recent developments and perspectives *Eur. Phys. J.* A **51** 1–9
[493] Shimizu N, Utsuno Y, Futamura Y, Sakurai T, Mizusaki T and Otsuka T 2016 Stochastic estimation of nuclear level density in the nuclear shell model: an application to parity-dependent level density in ^{58}Ni *Phys. Lett.* B **753** 13–7

[494] S K and V Z 2020 Nuclear shell model and level density *Int. J. Mod. Phys.* E **29** 2030005
[495] Ormand W E and Brown B A 2020 Microscopic calculations of nuclear level densities with the lanczos method *Phys. Rev.* C **102** 014315
[496] Goriely S, Larsen A C and Mücher D 2022 Comprehensive test of nuclear level density models *Phys. Rev.* C **106** 044315
[497] Døssing T and ÃĚberg S 2019 Collective enhancements in nuclear level densities *Eur. Phys. J.* A **55** 249
[498] Hilaire S, Goriely S, Péru S and Gosselin G 2023 A new approach to nuclear level densities: the QRPA plus boson expansion *Phys. Lett.* B **843** 137989
[499] Alhassid Y 2017 *Emergent Phenomena in Atomic Nuclei from Large-Scale Modeling: a Symmetry-Guided Perspective* (World Scientific) pp 267–298
[500] Alhassid Y, Fang L and Nakada H 2008 Heavy deformed nuclei in the shell model monte carlo method *Phys. Rev. Lett.* **101** 082501
[501] Gilbreth C N and Alhassid Y 2015 *Comput. Phys. Commun.* **188** 1
[502] Alhassid Y, Bonett-Matiz M, Liu S and Nakada H 2015 Direct microscopic calculation of nuclear level densities in the shell model monte carlo approach *Phys. Rev.* C **92** 024307
[503] Alhassid Y, Liu S and Nakada H 2007 Spin projection in the shell model monte carlo method and the spin distribution of nuclear level densities *Phys. Rev. Lett.* **99** 162504
[504] Fanto P and Alhassid Y 2024 Low-energy enhancement in the magnetic dipole γ-ray strength functions of heavy nuclei *Phys. Rev.* C **109** L031302
[505] Johnson C W and Gorton O C 2023 Proton–neutron entanglement in the nuclear shell model *J. Phys. G: Nucl. Part. Phys.* **50** 045110
[506] Goriely S *et al* 2019 Reference database for photon strength functions *Eur. Phys. J.* A **55** 172
[507] Goriely S and Plujko V 2019 Simple empirical $e1$ and $m1$ strength functions for practical applications *Phys. Rev.* C **99** 014303
[508] Goriely S, Hilaire S, Péru S and Sieja K 2018 Gogny-HFB+QRPA dipole strength function and its application to radiative nucleon capture cross section *Phys. Rev.* C **98** 014327
[509] Tsoneva N and Lenske H 2016 Energy-density functional plus quasiparticle-phonon model theory as a powerful tool for nuclear structure and astrophysics *Phys. Atom. Nucl.* **79** 885–903
[510] Tsoneva N 2018 Pygmy and giant resonances: connecting the nuclear structure to stellar astrophysics *EPJ Web Conf.* **194** 04001
[511] Péru S 2023 Private communication
[512] Brown B A and Larsen A C 2014 Large low-energy $m1$ strength for ^{56,57}Fe within the nuclear shell model *Phys. Rev. Lett.* **113** 252502
[513] Raman S, Fogelberg B, Harvey J A, Macklin R L, Stelson P H, Schröder A and Kratz K L 1983 Overlapping β decay and resonance neutron spectroscopy of levels in ^{87}Kr *Phys. Rev.* C **28** 602–22
[514] Raman S, Fogelberg B, Harvey J A, Macklin R L, Stelson P H, Schröder A and Kratz K L 1984 Erratum: overlapping β decay and resonance neutron spectroscopy of levels in ^{87}Kr *Phys. Rev.* C **29** 344–344
[515] Tain J L *et al* 2015 Enhanced γ-ray emission from neutron unbound states populated in β decay *Phys. Rev. Lett.* **115** 062502
[516] Madurga M *et al* 2016 Evidence for gamow-teller decay of ^{78}Ni core from beta-delayed neutron emission studies *Phys. Rev. Lett.* **117** 092502
[517] Spyrou A *et al* 2016 Strong neutron-γ competition above the neutron threshold in the decay of ^{70}Co *Phys. Rev. Lett.* **117** 142701
[518] Gottardo A *et al* 2017 Unexpected high-energy γ emission from decaying exotic nuclei *Phys. Lett.* B **772** 359–62
[519] Heideman J *et al* 2023 Evidence of nonstatistical neutron emission following β decay near doubly magic ^{132}Sn *Phys. Rev.* C **108** 024311
[520] Xu Z Y *et al* 2024 Compound-nucleus and doorway-state decays of β-delayed neutron emitters ^{51,52,53}K *Phys. Rev. Lett.* **133** 042501
[521] Kawano T, Möller P and Wilson W B 2008 Calculation of delayed-neutron energy spectra in a quasiparticle random-phase approximation-Hauser–Feshbach model *Phys. Rev.* C **78** 054601
[522] Slaughter D, Nuh F, Shihab-Eldin A and Prussin S 1972 Gamma-ray emission in competition with neutron emission in the beta decay of ^{87}Br *Phys. Lett.* B **38** 22–4
[523] Piersa M *et al* 2019 β decay of ^{133}In: γ emission from neutron-unbound states in ^{133}Sn *Phys. Rev.* C **99** 024304

[524] Escher J E, Burke J T, Dietrich F S, Scielzo N D, Thompson I J and Younes W 2012 Compound-nuclear reaction cross sections from surrogate measurements *Rev. Mod. Phys.* **84** 353–97
[525] Löher B *et al* 2013 The high-efficiency γ-ray spectroscopy setup γ^3 at HI γs *Nucl. Instrum. Methods Phys.* A **723** 136–42
[526] Escher J E *et al* 2016 Compound-nuclear reactions with unstable nuclei: constraining theory through innovative experimental approaches *EPJ Web Conf.* **122** 12001
[527] Rochman D, Goriely S, Koning A and Ferroukhi H 2017 Radiative neutron capture: Hauser Feshbach versus statistical resonances *Phys. Lett.* B **764** 109–13
[528] Rochman D, Koning A and Sublet J C 2020 A statistical analysis of evaluated neutron resonances with tares for JEFF-3.3, JENDL-4.0, ENDF/B-VIII.0 and TENDL-2019 *Nucl. Data Sheets* **163** 163–90
[529] Rauscher T, Bieber R, Oberhummer H, Kratz K L, Dobaczewski J, Möller P and Sharma M M 1998 Dependence of direct neutron capture on nuclear-structure models *Phys. Rev.* C **57** 2031–9
[530] Xu Y and Goriely S 2012 Systematic study of direct neutron capture *Phys. Rev.* C **86** 045801
[531] Xu Y, Goriely S, Koning A J and Hilaire S 2014 Systematic study of neutron capture including the compound, pre-equilibrium, and direct mechanisms *Phys. Rev.* C **90** 024604
[532] Thompson I, Escher J and Arbanas G 2014 Coupled-channel models of direct-semidirect capture via giant-dipole resonances *Nucl. Data Sheets* **118** 292–4
[533] Sieja K and Goriely S 2021 Shell-model based study of the direct capture in neutron-rich nuclei *Eur. Phys. J.* A **57** 110
[534] Saito T and Matsuo M 2023 Continuum random-phase approximation for (n, γ) reactions on neutron-rich nuclei: collective effects and resonances *Phys. Rev.* C **107** 064607
[535] Wang B, Xu Y and Goriely S 2024 Systematic study of the radiative proton capture including the compound, pre-equilibrium, and direct mechanisms *Phys. Rev.* C **109** 014611
[536] Escher J E, Burke J T, Hughes R O, Scielzo N D, Casperson R J, Ota S, Park H I, Saastamoinen A and Ross T J 2018 Constraining neutron capture cross sections for unstable nuclei with surrogate reaction data and theory *Phys. Rev. Lett.* **121** 052501
[537] Pérez Sánchez R *et al* 2020 Simultaneous determination of neutron-induced fission and radiative capture cross sections from decay probabilities obtained with a surrogate reaction *Phys. Rev. Lett.* **125** 122502
[538] Gorton O C and Escher J E 2023 Cross sections for neutron-induced reactions from surrogate data: reexamining the weisskopf-ewing approximation for (n, n') and (n, 2n) reactions *Phys. Rev.* C **107** 044612
[539] Escher J E 2023 Surrogate reaction theory for obtaining (n, n') and (n, 2n) cross sections from charged-particle scattering data *Bull. Am. Phys. Soc*
[540] Sharma A, Gandhi A and Kumar A 2022 Investigation of weisskopf-ewing approximation for the determination of (n, p) cross sections using the surrogate reaction technique *Phys. Rev.* C **105** 014624
[541] Casperson R J *et al* 2014 Measurement of the ^{240}Am(n, f) cross section using the surrogate-ratio method *Phys. Rev.* C **90** 034601
[542] Hughes R O *et al* 2014 ^{236}Pu(n, f), ^{237}Pu(n, f), and ^{238}Pu(n, f) cross sections deduced from (p, t), (p, d), and (p, p') surrogate reactions *Phys. Rev.* C **90** 014304
[543] Bennett S A *et al* 2023 Direct determination of Fission–Barrier heights using light-ion transfer in inverse kinematics *Phys. Rev. Lett.* **130** 202501
[544] Bouland O 2019 Reexamining fission-probability data using $\mathcal{R}$-matrix monte carlo simulations: beyond the surrogate-reaction method *Phys. Rev.* C **100** 064611
[545] Bouland O and Noguère G 2020 Reconciling surrogate-reaction probabilities and neutron-induced cross sections *Phys. Rev.* C **102** 054608
[546] Escher J *et al* 2023 Improving nuclear data evaluations with predictive reaction theory and indirect measurements *EPJ Web of Conf.* **284** 03012
[547] Koning A J and Delaroche J P 2003 Local and global nucleon optical models from 1 keV to 200 MeV *Nucl. Phys.* A **713** 231
[548] Varner R, Thompson W, McAbee T, Ludwig E and Clegg T 1991 A global nucleon optical model potential *Phys. Rep.* **201** 57–119
[549] Pruitt C D, Escher J E and Rahman R 2023 Uncertainty-quantified phenomenological optical potentials for single-nucleon scattering *Phys. Rev.* C **107** 014602

[550] Dickhoff W and Charity R 2019 Recent developments for the optical model of nuclei *Prog. Part. Nucl. Phys.* **105** 252–99
[551] Mahaux C, Ngo H and Satchler G R 1986 Causality and the threshold anomaly of the nucleus-nucleus potential *Nucl. Phys.* A **449** 354
[552] Mahaux C and Sartor R 1991 Single-particle motion in nuclei *Advances in Nuclear Physics* ed J W Negele and E Vogt (Springer) pp 1–223
[553] Dickhoff W H and Neck D V 2008 *Many-Body Theory Exposed!* (World Scientific)
[554] Watson K M 1953 Multiple scattering and the many-body problem—applications to photomeson production in complex nuclei *Phys. Rev.* **89** 575
[555] Kerman A K, McManus H and Thaler R M 1959 The scattering of fast nucleons from nuclei *Ann. Phys.* **8** 551
[556] Siciliano E R and Thaler R M 1977 Spectator expansion in multiple scattering theory *Phys. Rev.* C **16** 1322
[557] Rotureau J, Danielewicz P, Hagen G, Nunes F M and Papenbrock T 2017 Optical potential from first principles *Phys. Rev.* C **95** 024315
[558] Rotureau J, Danielewicz P, Hagen G, Jansen G R and Nunes F M 2018 Microscopic optical potentials for calcium isotopes *Phys. Rev.* C **98** 044625
[559] Burrows M, Launey K D, Mercenne A, Baker R B, Sargsyan G H, Dytrych T and Langr D 2024 *Ab initio* translationally invariant nucleon–nucleus optical potentials *Phys. Rev.* C **109** 014616
[560] Idini A, Barbieri C and Navraátil P 2019 *Ab initio* optical potentials and nucleon scattering on medium mass nuclei *Phys. Rev. Lett.* **123** 092501
[561] Burrows M, Baker R B, Elster C, Weppner S P, Launey K D, Maris P and Popa G 2020 *Ab initio* leading order effective potentials for elastic nucleon–nucleus scattering *Phys. Rev.* C **102** 033606
[562] Vorabbi M, Gennari M, Finelli P, Giusti C, Navraátil P and Machleidt R 2022 Elastic proton scattering off nonzero spin nuclei *Phys. Rev.* C **105** 014621
[563] Whitehead T R, Lim Y and Holt J W 2019 Proton elastic scattering on calcium isotopes from chiral nuclear optical potentials *Phys. Rev.* C **100** 014601
[564] Rotureau J, Potel G, Li W and Nunes F M 2020 Merging *ab initio* theory and few-body approach for (*d*, *p*) reactions *J. Phys. G: Nucl. Part. Phys.* **47** 065103
[565] Haesner B, Heeringa W, Klages H O, Dobiasch H, Schmalz G, Schwarz P, Wilczynski J, Zeitnitz B and Käppeler F 1983 Measurement of the ^{3}He and ^{4}He total neutron cross sections up to 40 Mev *Phys. Rev.* C **28** 995–9
[566] Coon J 1959 Total neutron cross sections of the hydrogen and helium isotopes *Nucl. Phys.* **12** 291–97
[567] Bashkin S, Mooring F P and Petree B 1951 Total cross section of helium for fast neutrons *Phys. Rev.* **82** 378–80
[568] Thomson D B, Cranberg L and Levin J S 1962 Scattering of fast neutrons by magnesium *Phys. Rev.* **125** 2049–53
[569] Sargsyan G H, Potel G, Kravvaris K and Escher J E 2023 *Microscopic structure-based optical potential for predictive calculations* submitted
[570] Feshbach H 1958 Unified theory of nuclear reactions *Ann. Phys.* **5** 357–90
[571] Arellano H F and Blanchon G 2018 Irreducible nonlocality of optical model potentials based on realistic nn interactions *Phys. Rev.* C **98** 054616
[572] Horowitz C J *et al* 2019 R-process nucleosynthesis: connecting rare-isotope beam facilities with the cosmos *J. Phys.* G **46** 083001
[573] Giuliani S A, Martìnez-Pinedo G, Wu M R and Robledo L M 2020 Fission and the *r*-process nucleosynthesis of translead nuclei in neutron star mergers *Phys. Rev.* C **102** 045804
[574] Giuliani S A, Matheson Z, Nazarewicz W, Olsen E, Reinhard P G, Sadhukhan J, Schuetrumpf B, Schunck N and Schwerdtfeger P 2019 Colloquium: superheavy elements: oganesson and beyond *Rev. Mod. Phys.* **91** 011001
[575] Smits O R, Düllmann C E, Indelicato P, Nazarewicz W and Schwerdtfeger P 2023 The quest for superheavy elements and the limit of the periodic table *Nat. Rev. Phys.* (https://doi.org/10.1038/s42254-023-00668-y)
[576] Schunck N and Robledo L M 2016 Microscopic theory of nuclear fission: a review *Rep. Prog. Phys.* **79** 116301
[577] Bender M *et al* 2020 Future of nuclear fission theory *J. Phys.* G **47** 113002

[578] Bulgac A, Jin S and Stetcu I 2020 Nuclear fission dynamics: past, present, needs, and future *Front. Phys.* **8**
[579] Flynn E, Lay D, Agbemava S, Giuliani P, Godbey K, Nazarewicz W and Sadhukhan J 2022 Nudged elastic band approach to nuclear fission pathways *Phys. Rev.* C **105** 054302
[580] Sadhukhan J, Giuliani S A and Nazarewicz W 2022 Theoretical description of fission yields: toward a fast and efficient global model *Phys. Rev.* C **105**
[581] Lovell A E, Mohan A T and Talou P 2020 Quantifying uncertainties on fission fragment mass yields with mixture density networks *J. Phys. G: Nucl. Part. Phys.* **47** 114001
[582] Lay D, Flynn E, Giuliani S A, Nazarewicz W and Neufcourt L 2024 Neural network emulation of spontaneous fission *Phys. Rev.* C **109** 044305
[583] Bertsch G F, Loveland W, Nazarewicz W and Talou P 2015 Benchmarking nuclear fission theory *J. Phys.* G **42** 077001
[584] Godbey K, Umar A S and Simenel C 2022 Theoretical uncertainty quantification for heavy-ion fusion *Phys. Rev.* C **106** L051602
[585] deSouza R T, Godbey K, Hudan S and Nazarewicz W 2024 Search for beyond-mean-field signatures in heavy-ion fusion reactions *Phys. Rev.* C **109** L041601
[586] Andreyev A N *et al* 2010 New type of asymmetric fission in proton-rich nuclei *Phys. Rev. Lett.* **105** 252502
[587] Warda M, Staszczak A and Nazarewicz W 2012 Fission modes of mercury isotopes *Phys. Rev.* C **86** 024601
[588] Tsekhanovich I *et al* 2019 Observation of the competing fission modes in ^{178}Pt *Phys. Lett.* B **790** 583–8
[589] Jhingan A *et al* 2022 ^{178}Hg and asymmetric fission of neutron-deficient pre-actinides *Phys. Rev.* C **106** 044607
[590] Godbey K, Umar A S and Simenel C 2019 Deformed shell effects in ^{48}Ca + ^{249}Bk quasifission fragments *Phys. Rev.* C **100** 024610
[591] McGlynn P and Simenel C 2023 Time-dependent hartree-fock study of quasifission trajectories in reactions forming ^{294}Og *Phys. Rev.* C **107** 054614
[592] Godbey K, Umar A S and Simenel C 2017 Dependence of fusion on isospin dynamics *Phys. Rev.* C **95** 011601
[593] Simenel C, Godbey K and Umar A S 2020 Timescales of quantum equilibration, dissipation and fluctuation in nuclear collisions *Phys. Rev. Lett.* **124** 212504
[594] Sekizawa K 2019 TDHF theory and its extensions for the multinucleon transfer reaction: a mini review *Front. Phys.* **7** 20
[595] Godbey K and Umar A S 2020 Quasifission dynamics in microscopic theories *Front. Phys.* **8** 40
[596] Zhang Y X, Danielewicz P, Famiano M, Li Z, Lynch W G, Tsang M B and Li Z 2008 The influence of cluster emission and the symmetry energy on neutron–proton spectral double ratios *Phys. Lett.* B **664** 145–8
[597] Zhang Z and Chen L W 2023 Bayesian inference of the symmetry energy and the neutron skin in ^{48}Ca and ^{208}Pb from CREX and PREX-2 *Phys. Rev.* C **108** 024317
[598] Tsang C Y, Tsang M B, Lynch W G, Kumar R and Horowitz C J 2024 Determination of the equation of state from nuclear experiments and neutron star observations *Nat. Astron.* **8** 328 336
[599] Thiel M, Sfienti C, Piekarewicz J, Horowitz C J and Vanderhaeghen M 2019 Neutron skins of atomic nuclei: per aspera ad astra *J. Phys.* G **46** 093003
[600] Hebeler K, Holt J D, Menendez J and Schwenk A 2015 Nuclear forces and their impact on neutron-rich nuclei and neutron-rich matter *Ann. Rev. Nucl. Part. Sci.* **65** 457–84
[601] Lynn J E, Tews I, Gandolfi S and Lovato A 2019 Quantum monte carlo methods in nuclear physics: recent advances *Ann. Rev. Nucl. Part. Sci.* **69** 279–305
[602] Drischler C and Bogner S K 2021 A brief account of steven weinberg's legacy in *ab initio* many-body theory: special issue in few-body systems: celebrating 30 years of steven weinberg's papers on nuclear forces from chiral lagrangians *Few Body Syst.* **62** 109
[603] Drischler C, Holt J W and Wellenhofer C 2021 Chiral effective field theory and the high-density nuclear equation of state *Ann. Rev. Nucl. Part. Sci.* **71** 403–32
[604] Gale C, Bertsch G and Das Gupta S 1987 Heavy-ion collision theory with momentum-dependent interactions *Phys. Rev.* C **35** 1666–71
[605] Sammarruca F and Millerson R 2021 Overview of symmetric nuclear matter properties from chiral interactions up to fourth order of the chiral expansion *Phys. Rev.* C **104** 064312

[606] Li B A, Cai B J, Chen L W and Xu J 2018 Nucleon effective masses in neutron-rich matter *Prog. Part. Nucl. Phys.* **99** 29–119
[607] Most E R, Papenfort L J, Dexheimer V, Hanauske M, Schramm S, Stöcker H and Rezzolla L 2019 Signatures of quark-hadron phase transitions in general-relativistic neutron-star mergers *Phys. Rev. Lett.* **122** 061101
[608] Radice D, Bernuzzi S and Perego A 2020 The dynamics of binary neutron star mergers and GW170817 *Ann. Rev. Nucl. Part. Sci.* **70** 95–119
[609] Adamczewski-Musch J *et al* 2019 Probing dense baryon-rich matter with virtual photons *Nat. Phys.* **15** 1040–5
[610] Wen P and Holt J W 2021 Constraining the nonanalytic terms in the isospin-asymmetry expansion of the nuclear equation of state *Phys. Rev.* C **103** 064002
[611] Bethe H A 1971 Theory of nuclear matter *Ann. Rev. Nucl. Part. Sci.* **21** 93–244
[612] Dutra M, Lourenco O, Sa Martins J S, Delfino A, Stone J R and Stevenson P D 2012 Skyrme interaction and nuclear matter constraints *Phys. Rev.* C **85** 035201
[613] Drischler C, Han S and Reddy S 2022 Large and massive neutron stars: implications for the sound speed within QCD of dense matter *Phys. Rev.* C **105** 035808
[614] Kumar R *et al* 2024 Theoretical and experimental constraints for the equation of state of dense and hot matter *Living Rev. Relativ.* **27**
[615] Essick R, Tews I, Landry P, Reddy S and Holz D E 2020 Direct astrophysical tests of chiral effective field theory at supranuclear densities *Phys. Rev.* C **102** 055803
[616] Rose H, Kunert N, Dietrich T, Pang P T H, Smith R, Van Den Broeck C, Gandolfi S and Tews I 2023 Revealing the strength of three-nucleon interactions with the proposed Einstein Telescope *Phys. Rev.* C **108** 025811
[617] Ekström A, Jansen G R, Wendt K A, Hagen G, Papenbrock T, Carlsson B D, Forssén C, Hjorth-Jensen M, Navrátil P and Nazarewicz W 2015 Accurate nuclear radii and binding energies from a chiral interaction *Phys. Rev.* C **91** 051301
[618] Drischler C, Hebeler K and Schwenk A 2019 Chiral interactions up to next-to-next-to-next-to-leading order and nuclear saturation *Phys. Rev. Lett.* **122** 042501
[619] Dyhdalo A, Furnstahl R J, Hebeler K and Tews I 2016 Regulator artifacts in uniform matter for chiral interactions *Phys. Rev.* C **94** 034001
[620] Furnstahl R J, Hammer H W and Schwenk A 2021 Nuclear structure at the crossroads *Few Body Syst.* **62** 72
[621] Wesolowski S, Svensson I, Ekström A, Forssén C, Furnstahl R J, Melendez J A and Phillips D R 2021 Rigorous constraints on three-nucleon forces in chiral effective field theory from fast and accurate calculations of few-body observables *Phys. Rev.* C **104** 064001
[622] Hu B *et al* 2022 *Ab initio* predictions link the neutron skin of ^{208}Pb to nuclear forces *Nat. Phys.* **18** 1196–200
[623] Yang J and Piekarewicz J 2018 Difference in proton radii of mirror nuclei as a possible surrogate for the neutron skin *Phys. Rev.* C **97** 014314
[624] Reinhard P G and Nazarewicz W 2022 Information content of the differences in the charge radii of mirror nuclei *Phys. Rev.* C **105** L021301
[625] Somasundaram R, Drischler C, Tews I and Margueron J 2021 Constraints on the nuclear symmetry energy from asymmetric-matter calculations with chiral *NN* and 3*N* interactions *Phys. Rev.* C **103** 045803
[626] Piekarewicz J and Centelles M 2009 Incompressibility of neutron-rich matter *Phys. Rev.* C **79** 054311
[627] Howard K B 2020 Structure effects on the giant monopole resonance and determinations of the nuclear incompressibility *PhD thesis* Notre Dame U
[628] Drischler C, Han S, Lattimer J M, Prakash M, Reddy S and Zhao T 2021 Limiting masses and radii of neutron stars and their implications *Phys. Rev.* C **103** 045808
[629] Adhikari D *et al* (PREX) 2021 Accurate determination of the neutron skin thickness of ^{208}Pb through parity-violation in electron scattering *Phys. Rev. Lett.* **126** 172502
[630] Adhikari D *et al* (CREX) 2022 Precision Determination of the Neutral Weak Form Factor of Ca48 *Phys. Rev. Lett.* **129** 042501
[631] Hebeler K and Schwenk A 2010 Chiral three-nucleon forces and neutron matter *Phys. Rev.* C **82** 014314
[632] Hammer H W, Nogga A and Schwenk A 2013 Three-body forces: from cold atoms to nuclei *Rev. Mod. Phys.* **85** 197

[633] Brown B A 2017 Mirror charge radii and the neutron equation of state *Phys. Rev. Lett.* **119** 122502
[634] Yang X F *et al* 2018 Investigating the large deformation of the $5/2(+)$ isomeric state in ^{73}Zn: an indicator for triaxiality *Phys. Rev.* C **97** 014314
[635] Brown B A *et al* 2020 Implications of the ^{36}Ca–^{36} and ^{38}Ca–^{38}Ar difference in mirror charge radii on the neutron matter equation of state *Phys. Rev. Res.* **2** 022035(R)
[636] König K *et al* 2024 Nuclear charge radii of silicon isotopes *Phys. Rev. Lett.* **132** 162502
[637] Raithel C A and Özel F 2019 Measurement of the nuclear symmetry energy parameters from gravitational-wave events *Astrophys. J.* **885** 121
[638] Stoecker H, Maruhn J A and Greiner W 1980 Collective sideward flow of nuclear matter in violent high-energy heavy ion collisions *Phys. Rev. Lett.* **44** 725
[639] Hartnack C, Aichelin J, Stoecker H and Greiner W 1994 Out of plane squeeze of clusters in relativistic heavy ion collisions *Phys. Lett.* B **336** 131–5
[640] Nara Y and Ohnishi A 2022 Mean-field update in the JAM microscopic transport model: mean-field effects on collective flow in high-energy heavy-ion collisions at sNN = 2–20 GeV energies *Phys. Rev.* C **105** 014911
[641] Russotto P *et al* 2011 Symmetry energy from elliptic flow in ^{197}Au + ^{197}Au *Phys. Lett.* B **697** 471–6
[642] Zhang Y and Li Z 2006 Elliptic flow and system size dependence of transition energies at intermediate energies *Phys. Rev.* C **74** 014602
[643] Zhang Y, Tsang M B, Li Z and Liu H 2014 Constraints on nucleon effective mass splitting with heavy ion collisions *Phys. Lett.* B **732** 186–90
[644] Russotto P *et al* 2016 Results of the ASY-EOS experiment at GSI: the symmetry energy at suprasaturation density *Phys. Rev.* C **94** 034608
[645] Danielewicz P 2000 Determination of the mean field momentum dependence using elliptic flow *Nucl. Phys.* A **673** 375–410
[646] Pan Q and Danielewicz P 1993 From sideward flow to nuclear compressibility *Phys. Rev. Lett.* **70** 2062–5
Pan Q and Danielewicz P 1993 From sideward flow to nuclear compressibility *Phys. Rev. Lett.* **70** 3523 (erratum)
[647] Cozma M D and Tsang M B 2021 In-medium $\Delta(1232)$ potential, pion production in heavy-ion collisions and the symmetry energy *Eur. Phys. J.* A **57** 309
[648] Wellenhofer C, Holt J W, Kaiser N and Weise W 2014 Nuclear thermodynamics from chiral low-momentum interactions *Phys. Rev.* C **89** 064009
[649] Keller J, Hebeler K and Schwenk A 2023 Nuclear equation of state for arbitrary proton fraction and temperature based on chiral effective field theory and a gaussian process emulator *Phys. Rev. Lett.* **130** 072701
[650] Botermans W and Malfliet R 1990 Quantum transport theory of nuclear matter *Phys. Rept.* **198** 115–94
[651] Xu J *et al* 2024 Comparing pion production in transport simulations of heavy-ion collisions at 270*A* MeV under controlled conditions *Phys. Rev.* C **109** 044609
[652] Persram D and Gale C 2002 Elliptic flow in intermediate-energy heavy ion collisions and in-medium effects *Phys. Rev.* C **65** 064611
[653] Zhang Y, Li Z and Danielewicz P 2007 In-medium *NN* cross-sections determined from stopping and collective flow in intermediate-energy heavy-ion collisions *Phys. Rev.* C **75** 034615
[654] Muther H and Polls A 2000 Two-body correlations in nuclear systems *Prog. Part. Nucl. Phys.* **45** 243–334
[655] Pandharipande V R and Pieper S C 1992 Nuclear transparency to intermediate-energy nucleons from (e, e'p) reactions *Phys. Rev.* C **45** 791–8
[656] Li B A and Chen L W 2005 Nucleon–nucleon cross sections in neutron-rich matter and isospin transport in heavy-ion reactions at intermediate energies *Phys. Rev.* C **72** 064611
[657] Chen B, Sammarruca F and Bertulani C A 2013 Microscopic in-medium nucleon–nucleon cross sections with improved Pauli blocking effects *Phys. Rev.* C **87** 054616
[658] Sammarruca F and Krastev P 2006 Effective nucleon–nucleon cross sections in symmetric and asymmetric nuclear matter *Phys. Rev.* C **73** 014001
[659] Westfall G D *et al* 1993 Mass dependence of the disappearance of flow in nuclear collisions *Phys. Rev. Lett.* **71** 1986–9

[660] Li P, Wang Y, Li Q and Zhang H 2022 Accessing the in-medium effects on nucleon–nucleon elastic cross section with collective flows and nuclear stopping *Phys. Lett.* B **828** 137019
[661] Barker B and Danielewicz P 2019 Shear viscosity from nuclear stopping *Phys. Rev.* C **99** 034607
[662] Lee J W *et al* (SpiRIT) 2022 Isoscaling in central Sn+Sn collisions at 270 MeV/*u* *Eur. Phys. J.* A **58** 201
[663] Reisdorf W *et al* (FOPI) 2010 Systematics of central heavy ion collisions in the 1*A* GeV regime *Nucl. Phys.* A **848** 366–427
[664] Andronic A *et al* (FOPI) 2003 Directed flow in Au + Au, Xe + CsI and Ni + Ni collisions and the nuclear equation of state *Phys. Rev.* C **67** 034907
[665] Ono A 2020 Impacts of cluster correlations on heavy-ion collision dynamics *JPS Conf. Proc.* **32** 010076
[666] Zhang Y, Danielewicz P, Li Z, Liu H, Lu F, Lynch W G and Tsang M B 2012 The Influence of in-medium *NN* cross-sections, symmetry potential and impact parameter on the isospin observables *Phys. Rev.* C **85** 024602
[667] Liu J Y, Guo W J, Wang S J, Zuo W, Zhao Q and Yang Y F 2001 Nuclear stopping as a probe for in-medium nucleon–nucleon cross sections in intermediate energy heavy ion collisions *Phys. Rev. Lett.* **86** 975–8
[668] Tsang M B *et al* (SpiRIT) 2017 Pion production in rare isotope collisions *Phys. Rev.* C **95** 044614
[669] Danielewicz P 1990 Multiparticle interactions in backward proton production, subthreshold antiproton production, and inclusive electron scattering from nuclei *Phys. Rev.* C **42** 1564–76
[670] Effenberger M and Mosel U 1999 Off-shell effects on particle production *Phys. Rev.* C **60** 051901
[671] Bertsch G F and Danielewicz P 1996 Off-shell effects in heavy particle production *Phys. Lett.* B **367** 55–9
[672] Cassing W and Juchem S 2000 Semiclassical transport of hadrons with dynamical spectral functions in A+A collisions at SIS/AGS energies *Nucl. Phys.* A **672** 417–45
[673] Buss O, Gaitanos T, Gallmeister K, van Hees H, Kaskulov M, Lalakulich O, Larionov A B, Leitner T, Weil J and Mosel U 2012 Transport-theoretical description of nuclear reactions *Phys. Rept.* **512** 1–124
[674] Linnyk O, Bratkovskaya E L and Cassing W 2016 Effective QCD and transport description of dilepton and photon production in heavy-ion collisions and elementary processes *Prog. Part. Nucl. Phys.* **87** 50–115
[675] Moreau P, Soloveva O, Oliva L, Song T, Cassing W and Bratkovskaya E 2019 Exploring the partonic phase at finite chemical potential within an extended off-shell transport approach *Phys. Rev.* C **100** 014911
[676] Aichelin J, Bratkovskaya E, Le Fèvre A, Kireyeu V, Kolesnikov V, Leifels Y, Voronyuk V and Coci G 2020 Parton-hadron-quantum-molecular dynamics: a novel microscopic *n*-body transport approach for heavy-ion collisions, dynamical cluster formation, and hypernuclei production *Phys. Rev.* C **101** 044905
[677] Sobotka L G, Dempsey J F, Charity R J and Danielewicz P 1997 Clustered and neutron-rich low density 'neck' region produced in heavy-ion collisions *Phys. Rev.* C **55** 2109–11
[678] Bastian N U, Batyuk P, Blaschke D, Danielewicz P, Ivanov Y B, Karpenko I, Röpke G, Rogachevsky O and Wolter H H 2016 Light cluster production at NICA *Eur. Phys. J.* A **52** 244
[679] Tanaka J *et al* 2021 Formation of alphs clusters in dilute neutron-rich matter *Science* **371** 260–4
[680] Dorso C and Aichelin J 1995 When and how are fragments formed in heavy ion collisions? *Phys. Lett.* B **345** 197–202
[681] Puri R K, Hartnack C and Aichelin J 1996 Early fragment formation in heavy-ion collisions *Phys. Rev.* C **54** R28–31
[682] Kaneko M *et al* (SpiRIT) 2021 Rapidity distributions of $Z = 1$ isotopes and the nuclear symmetry energy from Sn+Sn collisions with radioactive beams at 270 MeV/nucleon *Phys. Lett.* B **822** 136681
[683] Danielewicz P 1995 Effects of compression and collective expansion on particle emission from central heavy-ion reactions *Phys. Rev.* C **51** 716–50
[684] Ono A 2019 Dynamics of clusters and fragments in heavy-ion collisions *Prog. Part. Nucl. Phys.* **105** 139–79
[685] Fèvre L, Aichelin A, Hartnack C and Leifels Y 2019 FRIGA: a new approach to identify isotopes and hypernuclei in *n*-body transport models *Phys. Rev.* C **100** 034904

[686] Danielewicz P and Bertsch G F 1991 Production of deuterons and pions in a transport model of energetic heavy ion reactions *Nucl. Phys.* A **533** 712–48
[687] Oliinychenko D, Pang L G, Elfner H and Koch V 2019 Microscopic study of deuteron production in PbPb collisions at $\sqrt{s} = 2.76TeV$ via hydrodynamics and a hadronic afterburner *Phys. Rev.* C **99** 044907
[688] Arrington J, Higinbotham D W, Rosner G and Sargsian M 2012 Hard probes of short-range nucleon–nucleon correlations *Prog. Part. Nucl. Phys.* **67** 898–938
[689] Hen O *et al* 2014 Momentum sharing in imbalanced Fermi systems *Science* **346** 614–7
[690] Hen O, Miller G A, Piasetzky E and Weinstein L B 2017 Nucleon–nucleon correlations, short-lived excitations, and the quarks within *Rev. Mod. Phys.* **89** 045002
[691] Arrington J, Fomin N and Schmidt A 2022 Progress in understanding short-range structure in nuclei: an experimental perspective *Ann. Rev. Nucl. Part. Sci.* **72** 307–37
[692] Li B A, Guo W J and Shi Z 2015 Effects of the kinetic symmetry energy reduced by short-range correlations in heavy-ion collisions at intermediate energies *Phys. Rev.* C **91** 044601
[693] Wang Z, Xu C, Ren Z and Gao C 2017 Probing the high-momentum component in the nucleon momentum distribution by nucleon emission from intermediate-energy nucleus-nucleus collisions *Phys. Rev.* C **96** 054603
[694] Bonasera A and Gulminelli F 1992 Mean free path simulation of three body collisions in the Boltzmann–Nordheim–Vlasov equation *Phys. Lett.* B **275** 24–8
[695] Xu C, Li A and Li B A 2013 Delineating effects of tensor force on the density dependence of nuclear symmetry energy *J. Phys. Conf. Ser.* **420** 012090
[696] Rios A, Polls A and Dickhoff W H 2014 Density and isospin asymmetry dependence of high-momentum components *Phys. Rev.* C **89** 044303
[697] Rios A, Polls A and Dickhoff W H 2009 Depletion of the nuclear Fermi sea *Phys. Rev.* C **79** 064308
[698] Bell J S and Squires E J 1959 A formal optical model *Phys. Rev. Lett.* **3** 96–7
[699] Lane A M 1962 Isobaric spin dependence of the optical potential and quasi-elastic (p, n) reactions *Nucl. Phys.* **35** 676
[700] Danielewicz P, Singh P and Lee J 2017 Symmetry energy: III. Isovector skins *Nucl. Phys.* A **958** 147–86
[701] Charity R J *et al* 2007 Particle decay of ^{12}Be excited states *Phys. Rev.* C **76** 064313
[702] Pruitt C D *et al* 2020 Isotopically resolved neutron total cross sections at intermediate energies *Phys. Rev.* C **102** 034601
[703] Reed B T, Fattoyev F J, Horowitz C J and Piekarewicz J 2021 Implications of PREX-2 on the equation of state of neutron-rich matter *Phys. Rev. Lett.* **126** 172503
[704] Hugenholtz N and van Hove L 1958 A theorem on the single particle energy in a fermi gas with interaction *Physica* **24** 363–76
[705] Xu C, Li B A and Chen L W 2010 Symmetry energy, its density slope, and neutron–proton effective mass splitting at normal density extracted from global nucleon optical potentials *Phys. Rev.* C **82** 054607
[706] Galitskii V M and Migdal A B 1958 Application of quantum field theory methods to the many body problem *Soviet Phys. JETP* **7** 96
[707] Koltun D S 1974 Theory of mean removal energies for single particles in nuclei *Phys. Rev.* C **9** 484–97
[708] Carbone D *et al* 2018 Microscopic cluster model for the description of (^{18}O, ^{16}O) two-neutron transfer reactions *Acta Phys. Pol.* B **49** 373–80
[709] Rios A 2020 Green's function techniques for infinite nuclear systems *Front. Phys.* **8** 387
[710] Holt J W and Kaiser N 2017 Equation of state of nuclear and neutron matter at third-order in perturbation theory from chiral effective field theory *Phys. Rev.* C **95** 034326
[711] Whitehead T R, Lim Y and Holt J W 2021 Global microscopic description of nucleon–nucleus scattering with quantified uncertainties *Phys. Rev. Lett.* **127** 182502
[712] Xu X *et al* 2019 Masses of neutron-rich $^{52-54}$Sc and ^{54}Ti, ^{56}Ti nuclides: the $n = 32$ subshell closure in scandium *Phys. Rev.* C **99** 064303
[713] Zhang Y H *et al* 2018 Isochronous mass measurements of $T_z = -1$ *fp*-shell nuclei from projectile fragmentation of ^{58}Ni *Phys. Rev.* C **98** 014319
[714] Wang Y, Li Q, Leifels Y and Le Fèvre A 2020 Study of the nuclear symmetry energy from the rapidity-dependent elliptic flow in heavy-ion collisions around 1 Gev/nucleon regime *Phys. Lett.* B **802** 135249

[715] Li B A and Han X 2013 Constraining the neutron–proton effective mass splitting using empirical constraints on the density dependence of nuclear symmetry energy around normal density *Phys. Lett.* B **727** 276–81
[716] Hong J and Danielewicz P 2014 Subthreshold pion production within a transport description of central Au + Au collisions *Phys. Rev.* C **90** 024605
[717] Burbidge E M, Burbidge G R, Fowler W A and Hoyle F 1957 Synthesis of the elements in stars *Rev. Mod. Phys.* **29** 547–650
[718] Cameron A G W 1957 Nuclear reactions in stars and nucleogenesis *Publ. Astron. Soc. Pac.* **69** 201
[719] Abbott B P *et al* (LIGO Scientific Collaboration and Virgo Collaboration) 2017 GW170817: Observation of gravitational waves from a binary neutron star inspiral *Phys. Rev. Lett.* **119** 161101
[720] Cowperthwaite P S *et al* 2017 The electromagnetic counterpart of the binary neutron star merger LIGO/VIRGO GW170817: II. UV, optical, and near-infrared light curves and comparison to kilonova models *ApJL* **848** L17
[721] Villar V A *et al* 2017 The combined ultraviolet, optical, and near-infrared light curves of the kilonova associated with the binary neutron star merger GW170817: unified data set, analytic models, and physical implications *Astrophys. J. Lett.* **851** L21
[722] Hall E D *et al* 2021 Gravitational-wave physics with cosmic explorer: limits to low-frequency sensitivity *Phys. Rev.* D **103** 122004
[723] Evans M *et al* 2023 Cosmic explorer: a submission to the NSF MPSAC ngGW subcommittee arXiv:2306.13745
[724] Maggiore M *et al* 2020 Science case for the Einstein telescope *J. Cosmol. Astropart. Phys.* JCAP03(2020)050
[725] Farouqi K, Thielemann F K, Rosswog S and Kratz K L 2022 Correlations of r-process elements in very metal-poor stars as clues to their nucleosynthesis sites *Astronomy and Astrophysics* **663** A70
[726] 2024 The *R*-Process Alliance, https://sites.google.com/view/rprocessalliance/home
[727] Côté B *et al* 2018 The origin of *r*-process elements in the Milky Way *Astrophys. J.* **855** 99
[728] Holmbeck E M, Sprouse T M, Mumpower M R, Vassh N, Surman R, Beers T C and Kawano T 2019 Actinide production in the neutron-rich ejecta of a neutron star merger *Astrophys. J.* **870** 23
[729] Côté B *et al* 2021 ^{129}I and ^{247}Cm in meteorites constrain the last astrophysical source of solar *r*-process elements *Science* **371** 945–8
[730] Wang X, Clark A M, Ellis J, Ertel A F, Fields B D, Fry B J, Liu Z, Miller J A and Surman R 2021 *r*-process radioisotopes from near-earth supernovae and kilonovae *Astrophys. J.* **923** 219
[731] Barnes J, Kasen D, Wu M R and Martìnez-Pinedo G 2016 Radioactivity and thermalization in the ejecta of compact object mergers and their impact on kilonova light curves *Astrophys. J.* **829** 110
[732] Kasen D, Metzger B, Barnes J, Quataert E and Ramirez-Ruiz E 2017 Origin of the heavy elements in binary neutron-star mergers from a gravitational-wave event *Nature* **551** 80–4
[733] Zhu Y L, Lund K A, Barnes J, Sprouse T M, Vassh N, McLaughlin G C, Mumpower M R and Surman R 2021 Modeling kilonova light curves: dependence on nuclear inputs *Astrophys. J.* **906** 94
[734] Barnes J, Zhu Y L, Lund K A, Sprouse T M, Vassh N, McLaughlin G C, Mumpower M R and Surman R 2021 Kilonovae across the nuclear physics landscape: the impact of nuclear physics uncertainties on *r*-process-powered emission *Astrophys. J.* **918** 44
[735] Wang X, Vassh N, Sprouse T, Mumpower M, Vogt R, Randrup J, Surman R and (N3AS Collaboration)(FIRE Collaboration) 2020 MeV gamma rays from fission: a distinct signature of actinide production in neutron star mergers *Astrophys. J. Lett.* **903** L3
[736] Cowan J J, Sneden C, Lawler J E, Aprahamian A, Wiescher M, Langanke K, Martínez-Pinedo G and Thielemann F K 2021 Origin of the heaviest elements: the rapid neutron-capture process *Rev. Mod. Phys.* **93** 015002
[737] Zhu Y *et al* 2018 Californium-254 and kilonova light curves *Astrophys. J. Lett.* **863** L23
[738] Wu M R, Barnes J, Martìnez-Pinedo G and Metzger B D 2019 Fingerprints of heavy-element nucleosynthesis in the late-time lightcurves of kilonovae *Phys. Rev. Lett.* **122** 062701
[739] Vassh N *et al* 2019 Using excitation-energy dependent fission yields to identify key fissioning nuclei in *r*-process nucleosynthesis *J. Phys. G: Nucl. Phys.* **46** 065202

[740] Just O, Vijayan V, Xiong Z, Goriely S, Soultanis T, Bauswein A, Guilet J, Janka H T and Martìnez-Pinedo G 2023 End-to-end kilonova models of neutron star mergers with delayed black hole formation *Astrophys. J. Lett.* **951** L12
[741] Shingles L J, Collins C E, Vijayan V, Flörs A, Just O, Leck G, Xiong Z, Bauswein A, Martìnez-Pinedo G and Sim S A 2023 Self-consistent 3D radiative transfer for kilonovae: directional spectra from merger simulations *Astrophys. J. Lett.* **954** L41
[742] Cowan J J, Sneden C, Lawler J E, Aprahamian A, Wiescher M, Langanke K, Martìnez-Pinedo G and Thielemann F K 2021 Origin of the heaviest elements: the rapid neutron-capture process *Rev. Mod. Phys.* **93** 015002
[743] Meyer B S 1994 The *r*-, *s*-, and *p*-processes in nucleosynthesis *Annu. Rev. Astron. Astrophys.* **32** 153–90
[744] Lippuner J and Roberts L F 2017 SkyNet: a modular nuclear reaction network library *Astrophys. J. Suppl.* **233** 18
[745] Flörs A *et al* 2023 Opacities of singly and doubly ionized neodymium and uranium for kilonova emission modeling *Mon. Not. Roy. Astron. Soc.* **524** 3083–101
[746] Pognan Q, Grumer J, Jerkstrand A and Wanajo S 2023 NLTE spectra of kilonovae *Mon. Not. Roy. Astron. Soc.* **526** 5220–48
[747] Fujimoto S-i and Hashimoto M-a 2020 The impact of isomers on a kilonova associated with neutron star mergers *Mon. Not. Roy. Astron. Soc.* **493** L103–7
[748] Misch G W, Sprouse T M and Mumpower M R 2021 Astromers in the radioactive decay of *r*-process Nuclei *ApJL* **913** L2
[749] Misch G W *et al* 2023 Executive summary of the topical program: nuclear isomers in the era of FRIB arXiv:2304.10608
[750] Nikas S, Perdikakis G, Beard M, Surman R, Mumpower M R and Tsintari P 2020 Propagation of Hauser–Feshbach uncertainty estimates to r-process nucleosynthesis: benchmark of statistical property models for neutron rich nuclei far from stability arXiv:2010.01698
[751] Marketin T, Huther L and Martínez-Pinedo G 2016 Large-scale evaluation of β-decay rates of *r*-process nuclei with the inclusion of first-forbidden transitions *Phys. Rev.* C **93** 025805
[752] Ney E M, Engel J, Li T and Schunck N 2020 Global description of β^- decay with the axially deformed Skyrme finite-amplitude method: extension to odd-mass and odd–odd nuclei *Phys. Rev.* C **102** 034326
[753] Famiano M, Balantekin A B, Kajino T, Kusakabe M, Mori K and Luo Y 2020 Nuclear reaction screening, weak interactions, and *r*-process nucleosynthesis in high magnetic fields *Astrophys. J.* **898** 163
[754] Lund K A, Engel J, McLaughlin G C, Mumpower M R, Ney E M and Surman R 2023 The influence of β -decay rates on *r*-process observables *Astrophys. J.* **944** 144
[755] Kullmann I, Goriely S, Just O, Bauswein A and Janka H T 2023 Impact of systematic nuclear uncertainties on composition and decay heat of dynamical and disc ejecta in compact binary mergers *Mon. Not. Roy. Astron. Soc.* **523** 2551–76
[756] Minato F, Marketin T and Paar N 2021 β-delayed neutron-emission and fission calculations within relativistic quasiparticle random-phase approximation and a statistical model *Phys. Rev.* C **104** 044321
[757] Giuliani S A, Martínez-Pinedo G and Robledo L M 2018 Fission properties of superheavy nuclei for *r*-process calculations *Phys. Rev.* C **97** 034323
[758] Eichler M *et al* 2015 The Role of fission in neutron star mergers and its impact on the *r*-process peaks *Astrophys. J.* **808** 30
[759] Vassh N, Mumpower M R, McLaughlin G C, Sprouse T M and Surman R 2020 Coproduction of light and heavy *r*-process elements via fission deposition *Astrophys. J.* **896** 28
[760] Goriely S, Sida J L, Lemaître J F, Panebianco S, Dubray N, Hilaire S, Bauswein A and Janka H T 2013 New fission fragment distributions and *r*-process origin of the rare-earth elements *Phys. Rev. Lett.* **111** 242502
[761] Petermann I, Langanke K, Martínez-Pinedo G, Panov I V, Reinhard P G and Thielemann F K 2012 Have superheavy elements been produced in nature? *Eur. Phys. J.* A **48** 122
[762] Goriely S and Martínez-Pinedo G 2015 The production of transuranium elements by the *r*-process nucleosynthesis *Nucl. Phys.* A **944** 158–76
[763] Mumpower M R, Kawano T, Sprouse T M, Vassh N, Holmbeck E M, Surman R and Möller P 2018 β-delayed fission in *r*-process nucleosynthesis *Astrophys. J.* **869** 14

[764] Sneden C, Cowan J J and Gallino R 2008 Neutron-capture elements in the early galaxy *Annu. Rev. Astron. Astrophys.* **46** 241–88
[765] Shibagaki S, Kajino T, Mathews G J, Chiba S, Nishimura S and Lorusso G 2016 Relative contributions of the weak, main, and fission-recycling *r*-process *Astrophys. J.* **816** 79
[766] Mumpower M R, Jaffke P, Verriere M and Randrup J 2020 Primary fission fragment mass yields across the chart of nuclides *Phys. Rev.* C **101** 054607
[767] Sadhukhan J, Giuliani S A and Nazarewicz W 2022 Theoretical description of fission yields: toward a fast and efficient global model *Phys. Rev.* C **105** 014619
[768] Orford R *et al* 2018 Precision mass measurements of neutron-rich neodymium and samarium isotopes and their role in understanding rare-earth peak formation *Phys. Rev. Lett.* **120** 262702
[769] Vilen M *et al* 2018 Precision mass measurements on neutron-rich rare-earth isotopes at JYFLTRAP: reduced neutron pairing and implications for *r*-process calculations *Phys. Rev. Lett.* **120** 262701
[770] Kiss G G *et al* 2022 Measuring the β-decay properties of neutron-rich exotic Pm, Sm, Eu, and Gd isotopes to constrain the nucleosynthesis yields in the rare-earth region *Astrophys. J.* **936** 107
[771] Mumpower M R, McLaughlin G C and Surman R 2012 Formation of the rare-earth peak: gaining insight into late-time *r*-process dynamics *Phys. Rev.* C **85** 045801
[772] Vassh N, McLaughlin G C, Mumpower M R and Surman R 2021 Markov chain monte carlo predictions of neutron-rich lanthanide properties as a probe of *r*-process dynamics *Astrophys. J.* **907** 98
[773] Korobkin O, Rosswog S, Arcones A and Winteler C 2012 On the astrophysical robustness of the neutron star merger *r*-process *Mon. Not. R. Astron. Soc.* **426** 1940–9
[774] Cowan J J and Rose W K 1977 Production of ^{14}C and neutrons in red giants *Astrophys. J.* **212** 149–58
[775] Côté B, Denissenkov P, Herwig F, Ruiter A J, Ritter C, Pignatari M and Belczynski K 2018 *i*-process contribution of rapidly accreting white dwarfs to the solar composition of first-peak neutron-capture elements *Astrophys. J.* **854** 105
[776] Hampel M, Karakas A I, Stancliffe R J, Meyer B S and Lugaro M 2019 Learning about the intermediate neutron-capture process from lead abundances *Astrophys. J.* **887** 11
[777] Denissenkov P A, Herwig F, Woodward P, Andrassy R, Pignatari M and Jones S 2019 The *i*-process yields of rapidly accreting white dwarfs from multicycle He-shell flash stellar evolution models with mixing parametrizations from 3D hydrodynamics simulations *Mon. Not. R. Astron. Soc.* **488** 4258–70
[778] Choplin A, Siess L and Goriely S 2022 The intermediate neutron capture process: I. Development of the *i*-process in low-metallicity low-mass AGB stars (Corrigendum) *Astron. Astrophys.* **662**
[779] Denissenkov P A, Herwig F, Perdikakis G and Schatz H 2021 *Mon. Not. R. Astron. Soc.* **503** 3913–25
[780] Abohalima A and Frebel A 2018 JINAbase—a database for chemical abundances of metal-poor stars *Astrophys. J. Suppl.* **238** 36
[781] Sneppen A, Watson D, Damgaard R, Heintz K E, Vieira N, Väisänen P and Mahoro A 2024 Emergence hour-by-hour of *r*-process features in the kilonova AT2017gfo *Astronomy and Astrophysics* **690** A398
[782] Collins C E *et al* 2024 Toward inferring the geometry of kilonovae *Mon. Not. Roy. Astron. Soc.* **529** 1333–46
[783] Sneppen A, Watson D, Bauswein A, Just O, Kotak R, Nakar E, Poznanski D and Sim S 2023 Spherical symmetry in the kilonova AT2017gfo/GW170817 *Nature* **614** 436–9
[784] Sneppen A, Watson D, Poznanski D, Just O, Bauswein A and Wojtak R 2023 Measuring the Hubble constant with kilonovae using the expanding photosphere method *Astron. Astrophys.* **678** A14
[785] Mendoza-Temis J J, Wu M R, Langanke K, Martínez-Pinedo G, Bauswein A and Janka H T 2015 Nuclear robustness of the *r* process in neutron-star mergers. *Phys. Rev.* C **92** 055805
[786] Eichler M, Sayar W, Arcones A and Rauscher T 2019 Probing the production of actinides under different *r*-process conditions *Astrophys. J.* **879** 47
[787] Martin D, Arcones A, Nazarewicz W and Olsen E 2016 Impact of nuclear mass uncertainties on the r process *Phys. Rev. Lett.* **116** 121101

[788] Sprouse T M, Navarro Perez R, Surman R, Mumpower M R, McLaughlin G C and Schunck N 2020 Propagation of statistical uncertainties of Skyrme mass models to simulations of *r*-process nucleosynthesis *Phys. Rev.* C **101** 055803
[789] Caballero O L, Arcones A, Borzov I N, Langanke K and Martinez-Pinedo G 2014 Local and global effects of beta decays on r-process arXiv:1405.0210
[790] Metzger B D, Bauswein A, Goriely S and Kasen D 2015 Neutron-powered precursors of kilonovae *Mon. Not. R. Astron. Soc.* **446** 1115–20
[791] Mendoza-Temis J, Wu M R, Langanke K, Martìnez-Pinedo G, Bauswein A and Janka H T 2015 Nuclear robustness of the *r* process in neutron-star mergers *Phys. Rev.* C **92** 055805
[792] Just O, Bauswein A, Ardevol Pulpillo R, Goriely S and Janka H T 2015 Comprehensive nucleosynthesis analysis for ejecta of compact binary mergers *Mon. Not. R. Astron. Soc.* **448** 541–67
[793] Wang X, N3AS Collaboration, Fields B D, Mumpower M, Sprouse T, Surman R and Vassh N 2020 Sandblasting the *r*-process: spallation of ejecta from neutron star mergers *Astrophys. J.* **893** 92
[794] Placco V M *et al* 2020 The *r*-process alliance: the peculiar chemical abundance pattern of RAVE J183013.5-455510 *Astrophys. J.* **897** 78
[795] Holmbeck E M, Barnes J, Lund K A, Sprouse T M, McLaughlin G C and Mumpower M R 2023 Superheavy elements in kilonovae *Astrophys. J. Lett.* **951** L13
[796] Vassh N, Wang X, Larivière M, Sprouse T, Mumpower M R, Surman R, Liu Z, McLaughlin G C, Denissenkov P and Herwig F 2024 Thallium-208: a beacon of in situ neutron capture nucleosynthesis *Phys. Rev. Lett.* **132** 052701
[797] Hotokezaka K, Wanajo S, Tanaka M, Bamba A, Terada Y and Piran T 2016 Radioactive decay products in neutron star merger ejecta: heating efficiency and γ-ray emission *Mon. Not. R. Astron. Soc.* **459** 35–43
[798] Korobkin O *et al* 2020 Gamma rays from kilonova: a potential probe of *r*-process nucleosynthesis *Astrophys. J.* **889** 168
[799] Wu M R, Banerjee P, Metzger B D, Martìnez-Pinedo G, Aramaki T, Burns E, Hailey C J, Barnes J and Karagiorgi G 2019 Finding the remnants of the milky way's last neutron star mergers *Astrophys. J.* **880** 23
[800] Hotokezaka K and Nakar E 2020 Radioactive heating rate of *r*-process elements and macronova light curve *Astrophys. J.* **891** 152
[801] Kvassheim M, Gyland Mikalsen L T and Stokke C 2022 ^{208}Tl 2.6 Mev emission is the major contributor to the energy spectra when imaging ^{224}Ra and ^{212}Pb *J. Nucl. Med.* **63** 3280–3280
[802] Hawkins R H, Overman R F and Corey J C 1971 ^{208}Tl and ^{24}Na gamma sources for identifying soil water tagged with deuterium *Soil Sci. Soc. Am. J.* **35** 199–201
[803] Endrestole G O 1980 Principle and method for measurement of snow water equivalent by detection of natural gamma radiation/principe et méthode pour la mesure de l'hauteur d'eau équivalente par détection du rayonnement gamma naturel *Hydrol. Sci. Bull.* **25** 77–83
[804] Oberer R B *et al* 2009 The use of Tl-208 gamma rays for safeguards, nondestructive-assay (NDA) measurements (https://doi.org/10.2172/1009245)
[805] Boger J, Hahn R and Rowley eJ K 2000 The sudbury neutrino observatory *Nucl. Instrum. Methods Phys. Res.* A **449** 172–207
[806] Aalseth C E *et al* (Majorana Collaboration) 2018 Search for neutrinoless double-β decay in ^{76}Ge with the majorana demonstrator *Phys. Rev. Lett.* **120** 132502
[807] Siegel D M, Barnes J and Metzger B D 2019 Collapsars as a major source of *r*-process elements *Nature* **569** 241–4
[808] Radice D, Perego A, Hotokezaka K, Fromm S A, Bernuzzi S and Roberts L F 2018 Binary neutron star mergers: mass ejection, electromagnetic counterparts, and nucleosynthesis *Astrophys. J.* **869** 130
[809] Miller J M, Ryan B R, Dolence J C, Burrows A, Fontes C J, Fryer C L, Korobkin O, Lippuner J, Mumpower M R and Wollaeger R T 2019 Full transport model of GW170817-like disk produces a blue kilonova *Phys. Rev.* D **100** 023008
[810] Fahlman S, Fernández R and Morsink S 2023 Secular outflows from 3D MHD hypermassive neutron star accretion disc systems *Mon. Not. R. Astron. Soc.* **526** 952–65
[811] Fernández R, Just O, Xiong Z and Martìnez-Pinedo G 2023 Viscous hydrodynamic evolution of neutron star merger accretion disks: a code comparison arXiv:2307.02554

[812] Sprouse T M, Lund K A, Miller J M, McLaughlin G C and Mumpower M R 2024 Emergent nucleosynthesis from a 1.2 s long simulation of a black hole accretion disk *Astrophys. J.* **962** 79
[813] Wanajo S, Sekiguchi Y, Nishimura N, Kiuchi K, Kyutoku K and Shibata M 2014 Production of all the *r*-process nuclides in the dynamical ejecta of neutron star mergers *Astrophys. J. Lett.* **789** L39
[814] Foucart F, Duez M D, Hebert F, Kidder L E, Pfeiffer H P and Scheel M A 2020 Monte-carlo neutrino transport in neutron star merger simulations *Astrophys. J. Lett.* **902** L27
[815] Bliss J, Arcones A, Montes F and Pereira J 2017 Impact of (α, n) reactions on weak *r*-process in neutrino-driven winds *J. Physi. G: Nucl. Phys.* **44** 054003
[816] Watson D *et al* 2019 Identification of strontium in the merger of two neutron stars *Natur* **574** 497–500
[817] Denissenkov P, Perdikakis G, Herwig F, Schatz H, Ritter C, Pignatari M, Jones S, Nikas S and Spyrou A 2018 The impact of (n, γ) reaction rate uncertainties of unstable isotopes near $N = 50$ on the *i*-process nucleosynthesis in He-shell flash white dwarfs *J. Phys. G: Nucl. Phys.* **45** 055203
[818] Nishimura N, Sawai H, Takiwaki T, Yamada S and Thielemann F K 2017 The intermediate *r*-process in core-collapse supernovae driven by the magneto-rotational instability *Astrophys. J. Lett.* **836** L21
[819] Mösta P, Roberts L F, Halevi G, Ott C D, Lippuner J, Haas R and Schnetter E 2018 *r*-process nucleosynthesis from three-dimensional magnetorotational core-collapse supernovae *Astrophys. J.* **864** 171
[820] Reichert M, Obergaulinger M, Eichler M, Aloy M Á and Arcones A 2021 Nucleosynthesis in magneto-rotational supernovae *Mon. Not. R. Astron. Soc.* **501** 5733–45
[821] Roederer I U *et al* 2023 Element abundance patterns in stars indicate fission of nuclei heavier than uranium *Science* **382** 1177–80
[822] Xiong Z, Martìnez-Pinedo G, Just O and Sieverding A 2024 Production of *p* nuclei from *r*-process seeds: The νr process *Phys. Rev. Lett.* **132** 192701
[823] Woosley S E, Heger A and Weaver T A 2002 The evolution and explosion of massive stars *Rev. Mod. Phys.* **74** 1015–71
[824] Andrews S, Fryer C, Even W, Jones S and Pignatari M 2020 The nucleosynthetic yields of core-collapse supernovae: prospects for the next generation of gamma-ray astronomy *Astrophys. J.* **890** 35
[825] Hermansen K, Couch S M, Roberts L F, Schatz H and Warren M L 2020 Reaction rate sensitivity of the production of γ -ray emitting isotopes in core-collapse supernovae *Astrophys. J.* **901** 77
[826] Timmes F *et al* 2019 Catching element formation in the act; the case for a new mev gamma-ray mission: radionuclide astronomy in the 2020s *Bull. Am. Astron. Soc.* **51** 2
[827] The L S, Clayton D D, Jin L and Meyer B S 1998 Nuclear reactions governing the nucleosynthesis of ^{44} Ti *Astrophys. J.* **504** 500515
[828] Magkotsios G, Timmes F X, Hungerford A L, Fryer C L, Young P A and Wiescher M 2010 Trends in ^{44}Ti and ^{56}Ni from core-collapse supernovae *Astrophys. J. Suppl. Ser.* **191** 66
[829] Subedi S K, Meisel Z and Merz G 2020 Sensitivity of ^{44}Ti and ^{56}Ni production in core-collapse supernova shock-driven nucleosynthesis to nuclear reaction rate variations *Astrophys. J.* **898** 5
[830] Pignatari M, Göbel K, Reifarth R and Travaglio C 2016 The production of proton-rich isotopes beyond iron: the γ-process in stars *Int. J. Mod. Phys.* E **25** 1630003–232
[831] Rapp W, Görres J, Wiescher M, Schatz H and Käppeler F 2006 Sensitivity of *p*-process nucleosynthesis to nuclear reaction rates in a 25 $M_{\odot}$ supernova model *Astrophys. J.* **653** 474–89
[832] Rauscher T, Nishimura N, Hirschi R, Cescutti G, Murphy A S J and Heger A 2016 Uncertainties in the production of *p* nuclei in massive stars obtained from monte carlo variations *Mon. Not. R. Astron. Soc.* **463** 4153–66
[833] Nishimura N, Rauscher T, Hirschi R, Murphy A S J, Cescutti G and Travaglio C 2018 Uncertainties in the production of *p* nuclides in thermonuclear supernovae determined by Monte Carlo variations *Mon. Not. R. Astron. Soc.* **474** 3133–9
[834] Williams M *et al* 2023 Cross sections of the ^{83}Rb(p, γ)^{84}Sr and ^{84}Kr(p, γ)^{85}Rb reactions at energies characteristic of the astrophysical γ process *Phys. Rev.* C **107** 035803
[835] Tsantiri A *et al* 2023 *Phys. Rev.* C **107** 035808
[836] Nishimura N, Rauscher T, Hirschi R, Cescutti G, Murphy A S J and Fröhlich C 2019 Uncertainties in νp-process nucleosynthesis from monte carlo variation of reaction rates *Mon. Not. R. Astron. Soc.* **489** 1379–96

[837] Schatz H and Rehm K E 2006 X-ray binaries *Nucl. Phys.* A **777** 601–22
[838] Fisker J L, Schatz H and Thielemann F K 2008 Explosive hydrogen burning during type I x-ray bursts *Astrophys. J. Suppl. Ser.* **174** 261–76
[839] Parikh A, José J, Sala G and Iliadis C 2013 Nucleosynthesis in type I x-ray bursts *Prog. Part. Nucl. Phys.* **69** 225–53
[840] Weinberg N N, Bildsten L and Schatz H 2006 Exposing the nuclear burning ashes of radius expansion type I x-ray bursts *Astrophys. J.* **639** 1018–32
[841] Herrera Y, Sala G and José J 2023 Mass-loss and composition of wind ejecta in type I x-ray bursts *Astron. Astrophys.* **678** A156
[842] Meisel Z, Deibel A, Keek L, Shternin P and Elfritz J 2018 Nuclear physics of the outer layers of accreting neutron stars *J. Phys. G: Nucl. Part. Phys.* **45** 093001
[843] Meisel Z, Merz G and Medvid S 2019 Influence of nuclear reaction rate uncertainties on neutron star properties extracted from x-ray burst model-observation comparisons *Astrophys. J.* **872** 84
[844] Cyburt R H, Amthor A M, Heger A, Johnson E, Keek L, Meisel Z, Schatz H and Smith K 2016 Dependence of x-ray burst models on nuclear reaction rates *Astrophys. J.* **830** 55
[845] Browne J *et al* (JENSA Collaboration) 2023 *Phys. Rev. Lett.* **130** 212701
[846] Randhawa J S *et al* 2020 First direct measurement of ^{22}Mg(α, p) ^{25}Al and implications for x-ray burst model-observation comparisons *Phys. Rev. Lett.* **125** 202701
[847] Jayatissa H *et al* 2023 *Phys. Rev. Lett.* **131** 112701
[848] Budner T *et al* 2022 Constraining the ^{30}P(p, γ)^{31}S reaction rate in one novae via the weak, low-energy, β-delayed proton decay of ^{31}Cl *Phys. Rev. Lett.* **128** 182701
[849] Wolf C *et al* 2019 Constraining the neutron star compactness: extraction of the ^{23}Al(p, γ) reaction rate for the *rp* process *Phys. Rev. Lett.* **122** 232701
[850] Hutchins T J and Jones D I 2023 Gravitational radiation from thermal mountains on accreting neutron stars: sources of temperature non-axisymmetry *Mon. Not. R. Astron. Soc.* **522** 226–51
[851] Saito Y, Dillmann I, Kruecken R, Mumpower M R and Surman R 2023 Uncertainty quantification of mass models using ensemble bayesian model averaging
[852] Acharya B *et al* 2023 Fundamental symmetries, neutrons, and neutrinos (FSNN): whitepaper for the 2023 NSAC long range plan arXiv:2304.03451
[853] Cabibbo N 1963 Unitary symmetry and leptonic decays *Phys. Rev. Lett.* **10** 531
[854] Kobayashi M and Maskawa T 1973 Cp-violation in the renormalizable theory of weak interaction *Prog. Theor. Phys.* **49** 652–7
[855] Cirigliano V, Crivellin A, Hoferichter M and Moulson M 2023 Scrutinizing ckm unitarity with a new measurement of the $k_{\mu3}/k_{\mu2}$ branching fraction *Phys. Lett.* B **838** 137748
[856] MacDonald W M 1958 Coulomb corrections to the fermi nuclear matrix element *Phys. Rev.* **110** 1420
[857] Towner I and Hardy J C 2010 Comparative tests of isospin-symmetry-breaking corrections to superallowed $0^+ \rightarrow 0^+$ nuclear β decay *Phys. Rev.* C **82** 065501
[858] Hardy J C and Towner I 2005 Superallowed $0^+ \rightarrow 0^+$ nuclear β decays: a critical survey with tests of the conserved vector current hypothesis and the standard model *Phys. Rev.* C **71** 055501
[859] Seng C Y 2023 Model-independent determination of nuclear weak form factors and implications for standard model precision tests *Phys. Rev. Lett.* **130** 152501
[860] Seng C Y and Gorchtein M 2023 Electroweak nuclear radii constrain the isospin breaking correction to vud *Phys. Lett.* B **838** 137654
[861] Seng C Y and Gorchtein M 2024 Toward *ab initio* nuclear theory calculations of δ_C *Phys. Rev.* C **109** 044302
[862] Baroni S, Navrátil P and Quaglioni S 2013 Unified *ab initio* approach to bound and unbound states: no-core shell model with continuum and its application to ^{7}he *Phys. Rev.* C **87** 034326
[863] Caurier E, Navrátil P, Ormand W E and Vary J P 2002 *Ab initio* shell model for $A = 10$ nuclei *Phys. Rev.* C **66** 024314
[864] Seng C Y and Gorchtein M 2023 Dispersive formalism for the nuclear structure correction $\delta_{\rm ns}$ to the β decay rate *Phys. Rev.* C **107** 035503
[865] Haydock R 1974 The inverse of a linear operator *J. Phys. A: Math. Nucl. Gen.* **7** 2120–4
[866] Marchisio M A, Barnea N, Leidemann W and Orlandini G 2003 Efficient method for lorentz integral transforms of reaction cross sections *Few-Body Syst.* **33** 259–76
[867] Hao Y, Navrátil P, Norrgard E B, Iliaš M, Eliav E, Timmermans R G E, Flambaum V V and Borschevsky A 2020 Nuclear spin-dependent parity-violating effects in light polyatomic molecules *Phys. Rev.* A **102** 052828

[868] Froese P and Navratil P 2021 *Ab initio* calculations of electric dipole moments of light nuclei *Phys. Rev.* C **104** 025502
[869] Gennari M, Drissi M, Gorchtein M, Navratil P and Seng C Y 2025 *Ab initio* strategy for taming the nuclear-structure dependence of V_{ud} extractions: the ^{10}C $\rightarrow$ ^{10}B Superallowed Transition *Phys. Rev. Lett.* **134** 012501
[870] Hardy J and Towner I 2020 *Phys. Rev.* C **102** 045501
[871] Sternberg M *et al* 2015 Limit on tensor currents from ^{8}Li β decay *Phys. Rev. Lett.* **115** 182501
[872] Burkey M *et al* 2022 Improved limit on tensor currents in the weak interaction from ^{8}Li β decay *Phys. Rev. Lett.* **128** 202502
[873] Gallant A *et al* 2023 Angular correlations in the β decay of ^{8}B: first tensor-current limits from a mirror-nucleus pair *Phys. Rev. Lett.* **130** 192502
[874] Longfellow B *et al* 2023 Determination of the ^{8}B neutrino energy spectrum using trapped ions *Phys. Rev.* C **107** L032801
[875] Longfellow B *et al* 2024 Improved tensor current limit from ^{8}B β decay including new recoil-order calculations *Phys. Rev. Lett.* **132** 142502
[876] Müller P *et al* 2022 β-nuclear-recoil correlation from ^{6}He decay in a laser trap *Phys. Rev. Lett.* **129** 182502
[877] Fenker B *et al* 2016 Precision measurement of the nuclear polarization in laser-cooled, optically pumped ^{37}k *New J. Phys.* **18** 073028
[878] Fenker B *et al* 2018 Precision measurement of the β asymmetry in spin-polarized ^{37}K decay *Phys. Rev. Lett.* **120** 062502
[879] King G B, Baroni A, Cirigliano V, Gandolfi S, Hayen L, Mereghetti E, Pastore S and Piarulli M 2023 *Ab initio* calculation of the β-decay spectrum of ^{6}He *Phys. Rev.* C **107** 015503
[880] Glick-Magid A, Forssén C, Gazda D, Gazit D, Gysbers P and Navrátil P 2022 Nuclear *ab initio* calculations of ^{6}He β-decay for beyond the Standard Model studies *Phys. Lett.* B **832** 137259
[881] BROWN B and WILDENTHAL B 1985 Experimental and theoretical gamow-teller beta-decay observables for the *sd*-shell nuclei *At. Data Nucl. Data Tables* **33** 347–404
[882] MartinezPinedo G, Poves A, Robledo L, Caurier E, Nowacki F, Retamosa J and Zuker A 1996 Backbending in ^{50}Cr *Phys. Rev.* C **54** R2150–4
[883] Engel J and Menéndez J 2017 Status and future of nuclear matrix elements for neutrinoless double-beta decay: a review *Rep. Prog. Phys.* **80** 046301
[884] Engel J, Pittel S and Vogel P 1992 Nuclear physics of dark matter detection *Int. J. Mod. Phys.* E **1** 137
[885] Menendez J, Gazit D and Schwenk A 2012 Spin-dependent wimp scattering off nuclei *Phys. Rev.* D **86** 103511
[886] Towner I and Hardy J C 2002 Calculated corrections to superallowed fermi β decay: new evaluation of the nuclear-structure-dependent terms *Phys. Rev.* C **66** 035501
[887] Gazit D, Quaglioni S and Navrátil P 2009 Three-nucleon low-energy constants from the consistency of interactions and currents in chiral effective field theory *Phys. Rev. Lett.* **103** 102502
[888] Gazit D, Quaglioni S and Navrátil P 2019 Erratum: three-nucleon low-energy constants from the consistency of interactions and currents in chiral effective field theory [Phys. Rev. Lett. 103, 102502 (2009)] *Phys. Rev. Lett.* **122** 029901
[889] Lubos D *et al* 2019 Improved value for the Gamow–Teller strength of the ^{100}Sn beta decay *Phys. Rev. Lett.* **122**
[890] Engel J, Ramsey-Musolf M J and van Kolck U 2013 Electric dipole moments of nucleons, nuclei, and atoms: the standard model and beyond *Prog. Part. Nucl. Phys.* **71** 21–74
[891] Auerbach N, Flambaum V V and Spevak V 1996 Collective *t*- and *p*-odd electromagnetic moments in nuclei with octupole deformations *Phys. Rev. Lett.* **76** 4316–9
[892] Spevak V, Auerbach N and Flambaum V V 1997 Enhanced *t*-odd, *p*-odd electromagnetic moments in reflection asymmetric nuclei *Phys. Rev.* C **56** 1357–69
[893] Flambaum V V 2008 Electric dipole moments of actinide atoms and rao molecule *Phys. Rev.* A **77** 024501
[894] Bishof M *et al* 2016 Improved limit on the ^{225}Ra electric dipole moment *Phys. Rev.* C **94** 025501
[895] Chupp T E, Fierlinger P, Ramsey-Musolf M J and Singh J T 2019 Electric dipole moments of atoms, molecules, nuclei, and particles *Rev. Mod. Phys.* **91** 015001
[896] Singh J 2019 A new concept for searching for time-reversal symmetry violation using ^{229}Pa ions trapped in optical crystals *Hyperfine Interact.* **240** 29

[897] Flambaum V V and Feldmeier H 2020 Enhanced nuclear schiff moment in stable and metastable nuclei *Phys. Rev.* C **101** 015502
[898] Udrescu S M *et al* 2024 Precision spectroscopy and laser-cooling scheme of a radium-containing molecule *Nat. Phys.* **20** 202–7
[899] Gaffney L P *et al* 2013 Studies of pear-shaped nuclei using accelerated radioactive beams *Nature* **497** 199
[900] Butler P A *et al* 2019 The observation of vibrating pear-shapes in radon nuclei *Nat. Commun.* **10** 2473
[901] Butler P A *et al* 2020 Evolution of octupole deformation in radium nuclei from coulomb excitation of radioactive ^{222}Ra and ^{228}Ra beams *Phys. Rev. Lett.* **124** 042503
[902] Dobaczewski J, Engel J, Kortelainen M and Becker P 2018 Correlating schiff moments in the light actinides with octupole moments *Phys. Rev. Lett.* **121** 232501
[903] 2023 FRIB Estimated Rates Version 2.10, https://groups.nscl.msu.edu/frib/rates/fribrates.html
[904] Ahmad I, Gindler J E, Betts R R, Chasman R R and Friedman A M 1982 Possible ground-state octupole deformation in ^{229}Pa *Phys. Rev. Lett.* **49** 1758–61
[905] Ahmad I, Chasman R R, Greene J P, Kondev F G and Zhu S 2015 Electron capture decay of 58 min $^{229}_{92}$U and levels in $^{229}_{91}$Pa *Phys. Rev.* C **92** 024313
[906] Robledo L M and Bertsch G F 2012 Electromagnetic transition strengths in soft deformed nuclei *Phys. Rev.* C **86** 054306
[907] 2020 Gamma-ray energy tracking array (GRETA) final design report, lawrence berkeley national laboratory, https://greta.lbl.gov/
[908] Wu C, Cline D, Hayes A, Flight R, Melchionna A, Zhou C, Lee I, Swan D, Fox R and Anderson J 2016 CHICO2, a two-dimensional pixelated parallel-plate avalanche counter *Nucl. Instrum. Methods Phys. Res.* A **814** 6–11
[909] E. Düllmann C, Herzberg R D, Nazarewicz W and Oganessian Y 2015 Special issue on superheavy elements *Nucl. Phys.* A **944** 1
[910] Nazarewicz W 2018 The limits of nuclear mass and charge *Nat. Phys* **14** 537
[911] Altuntaş E, Ammon J, Cahn S B and DeMille D 2018 Demonstration of a sensitive method to measure nuclear-spin-dependent parity violation *Phys. Rev. Lett.* **120** 142501
[912] Karthein J *et al* 2024 Electroweak nuclear properties from single molecular ions in a penning trap *Phys. Rev. Lett.* **133** 033003
[913] Piekarewicz J, Linero A R, Giuliani P and Chicken E 2016 Power of two: assessing the impact of a second measurement of the weak-charge form factor of ^{208}Pb *Phys. Rev.* C **94** 034316
[914] Giuliani P G and Piekarewicz J 2021 From noise to information: the transfer function formalism for uncertainty quantification in reconstructing the nuclear density *Phys. Rev.* C **104** 024301
[915] Melendez J, Furnstahl R, Grießhammer H, McGovern J, Phillips D and Pratola M 2021 Designing optimal experiments: an application to proton compton scattering *Eur. Phys. J.* A **57** 1–24
[916] Farr J N, Meisel Z and Steiner A W 2021 Decision theory for the mass measurements at the facility for rare isotope beams arXiv:2111.11536
[917] Gelman A, Carlin J B, Stern H S and Rubin D B 1995 *Bayesian Data Analysis* (Chapman and Hall/CRC)
[918] McDonnell J D, Schunck N, Higdon D, Sarich J, Wild S M and Nazarewicz W 2015 Uncertainty quantification for nuclear density functional theory and information content of new measurements *Phys. Rev. Lett.* **114** 122501
[919] Utama R, Chen W C and Piekarewicz J 2016 Nuclear charge radii: density functional theory meets Bayesian neural networks *J. Phys. G: Nucl. Part. Phys.* **43** 114002
[920] Neufcourt L, Cao Y, Nazarewicz W and Viens F 2018 Bayesian approach to model-based extrapolation of nuclear observables *Phys. Rev.* C **98** 034318
[921] Brunton S L and Kutz J N 2022 *Data-driven Science and Engineering: Machine Learning, Dynamical Systems, and Control* (Cambridge University Press)
[922] Giuliani P, Godbey K, Bonilla E, Viens F and Piekarewicz J 2023 Bayes goes fast: uncertainty quantification for a covariant energy density functional emulated by the reduced basis method *Front. Phys.* **10** 1–23
[923] Beyer K *et al* 2023 BANDFramework: an open-source framework for Bayesian analysis of nuclear dynamics *Technical Report Version 0.3.0*
[924] Yamauchi Y, Buskirk L, Giuliani P and Godbey K 2023 Normalizing flows for Bayesian posteriors: reproducibility and deployment arXiv:2310.04635

[925] Join A 2011 Uncertainty estimates *Phys. Rev.* A **83** 040001
[926] Dobaczewski J, Nazarewicz W and Reinhard P 2014 Error estimates of theoretical models: a guide *J. Phys. G: Nucl. Part. Phys.* **41** 074001
[927] Ekström A, Ireland D and Phillips D R 2024 Information and Statistics in Nuclear Experiment and Theory (ISNET) *Nuclear Physics News* **34** 9–14
[928] 2019 TALENT School on Learning from Data: Bayesian Methods and Machine Learning, https://fribtheoryalliance.org/TALENT/courses/course_11.php
[929] Bonilla E, Giuliani P, Godbey K, Hjorth-Jensen M, Jain R, Montes F, Semposki A and Viens F 2023 FRIB-TA Summer School, https://github.com/ascsn/2023-FRIB-TA-Summer-School
[930] 2024 Bayesian Analysis of Nuclear Dynamics, https://bandframework.github.io/
[931] 2024 Bayesian Uncertainty Quantification: Errors in Your EFT, https://buqeye.github.io/
[932] 2024 Nuclear Computational Low-Energy Initiative, https://nuclei.mps.ohio-state.edu/
[933] Aidala C *et al* 2023 *A New Era of Discovery: The 2023 Long Range Plan for Nuclear Science (V. 1.2)* (Lawrence Livermore National Laboratory (LLNL))
[934] Duguet T, Ekström A, Furnstahl R J, König S and Lee D 2024 Colloquium: eigenvector continuation and projection-based emulators *Rev. Mod. Phys.* **96** 031002
[935] Frame D, He R, Ipsen I, Lee D, Lee D and Rrapaj E 2018 Eigenvector continuation with subspace learning *Phys. Rev. Lett.* **121** 032501
[936] Furnstahl R, Garcia A, Millican P and Zhang X 2020 Efficient emulators for scattering using eigenvector continuation *Phys. Lett.* B **809** 135719
[937] Melendez J, Drischler C, Garcia A, Furnstahl R and Zhang X 2021 Fast and accurate emulation of two-body scattering observables without wave functions *Phys. Lett.* B **821** 136608
[938] Drischler C, Quinonez M, Giuliani P, Lovell A and Nunes F 2021 Toward emulating nuclear reactions using eigenvector continuation *Phys. Lett.* B **823** 136777
[939] König S, Ekström A, Hebeler K, Lee D and Schwenk A 2020 Eigenvector continuation as an efficient and accurate emulator for uncertainty quantification *Phys. Lett.* B **810** 135814
[940] Zhang X and Furnstahl R 2022 Fast emulation of quantum three-body scattering *Phys. Rev.* C **105** 064004
[941] Melendez J A, Drischler C, Furnstahl R J, Garcia A J and Zhang X 2022 Model reduction methods for nuclear emulators *J. Phys. G: Nucl. Part. Phys.* **49** 102001
[942] Drischler C, Melendez J A, Furnstahl R J, Garcia A J and Zhang X 2023 Buqeye guide to projection-based emulators in nuclear physics *Front. Phys.* **10** 1–19
[943] Garcia A J, Drischler C, Furnstahl R J, Melendez J A and Zhang X 2023 Wave-function-based emulation for nucleon–nucleon scattering in momentum space *Phys. Rev.* C **107** 054001
[944] Sarkar A and Lee D 2021 Convergence of eigenvector continuation *Phys. Rev. Lett.* **126** 032501
[945] Sarkar A and Lee D 2022 Self-learning emulators and eigenvector continuation *Phys. Rev. Res.* **4** 023214
[946] Demol P, Duguet T, Ekström A, Frosini M, Hebeler K, König S, Lee D, Schwenk A, Somà V and Tichai A 2020 Improved many-body expansions from eigenvector continuation *Phys. Rev.* C **101** 041302
[947] Djärv T, Ekström A, Forssén C and Johansson T H 2022 Bayesian predictions for $A = 6$ nuclei using eigenvector continuation emulators *Phys. Rev.* C **105** 014005
[948] Yapa N and König S 2022 Volume extrapolation via eigenvector continuation *Phys. Rev.* C **106** 014309
[949] Companys Franzke M, Tichai A, Hebeler K and Schwenk A 2022 Excited states from eigenvector continuation: the anharmonic oscillator *Phys. Lett.* B **830** 137101
[950] Bonilla E, Giuliani P, Godbey K and Lee D 2022 Training and projecting: a reduced basis method emulator for many-body physics *Phys. Rev.* C **106** 054322
[951] Anderson A L, O'Donnell G L and Piekarewicz J 2022 Applications of reduced-basis methods to the nuclear single-particle spectrum *Phys. Rev.* C **106** L031302
[952] Bai D and Ren Z 2021 Generalizing the calculable *r*-matrix theory and eigenvector continuation to the incoming-wave boundary condition *Phys. Rev.* C **103** 014612
[953] Ekström A and Hagen G 2019 Global sensitivity analysis of bulk properties of an atomic nucleus *Phys. Rev. Lett.* **123** 252501
[954] Sürer Ö., Plumlee M and Wild S M 2023 Sequential Bayesian experimental design for calibration of expensive simulation models arXiv:2305.16506
[955] Liyanage D, Sürer Ö., Plumlee M, Wild S M and Heinz U 2023 Bayesian calibration of viscous anisotropic hydrodynamic simulations of heavy-ion collisions arXiv:2302.14184

[956] Sürer O, Nunes F M, Plumlee M and Wild S M 2022 Uncertainty quantification in breakup reactions *Phys. Rev.* C **106** 024607
[957] Higdon D, McDonnell J D, Schunck N, Sarich J and Wild S M 2015 A bayesian approach for parameter estimation and prediction using a computationally intensive model *J. Phys. G: Nucl. Part. Phys.* **42** 034009
[958] Plumlee M, Sürer O, Wild S M and Chan M Y H 2023 Surmise 0.2.1 Users Manual *Technical Report Version 0.2.1, NAISE*
[959] Odell D, Giuliani P, Beyer K, Catacora-Rios M, Chan M Y H, Bonilla E, Furnstahl R J, Godbey K and Nunes F M 2024 Rose: a reduced-order scattering emulator for optical models *Phys. Rev.* C **109** 044612
[960] Godbey K, Giuliani P, Bonilla E, Flynn E, Odell D, Beyer K, Lay D, Figueroa D and Garg R 2022 Dimensionality reduction in nuclear physics, https://dr.ascsn.net/
[961] Bakurov I, Giuliani P, Godbey K, Haut N, Banzhaf W and Nazarewicz W 2024 Discovering reduced order model equations of many-body quantum systems using genetic programming: a technical report arXiv:2406.04279
[962] Cook P, Jammooa D, Hjorth-Jensen M, Lee D D and Lee D 2024 Parametric matrix models arXiv:2401.11694
[963] Somasundaram R, Armstrong C L, Giuliani P, Godbey K, Gandolfi S and Tews I 2024 Emulators for scarce and noisy data: application to auxiliary field diffusion Monte Carlo for the deuteron arXiv:2404.11566
[964] Reed B T, Somasundaram R, De S, Armstrong C L, Giuliani P, Capano C, Brown D A and Tews I 2024 toward accelerated nuclear-physics parameter estimation from binary neutron star mergers: emulators for the Tolman–Oppenheimer–Volkoff equations arXiv:2405.20558
[965] Anderson A L and Piekarewicz J 2024 A universal reduced basis for the calibration of covariant energy density functionals arXiv:2406.01747
[966] Lassila T, Manzoni A, Quarteroni A and Rozza G 2014 *Model Order Reduction in Fluid Dynamics: Challenges and Perspectives* (Springer International Publishing) pp 235–73
[967] Quarteroni A, Manzoni A and Negri F 2015 *Reduced Basis Methods for Partial Differential Equations: An Introduction* vol 92 (Springer)
[968] Hesthaven J S, Rozza G and Stamm B 2016 *Certified Reduced Basis Methods for Parametrized Partial Differential Equations* vol 590 (Springer)
[969] Pan S, Brunton S L and Kutz J N 2022 Neural implicit flow: a mesh-agnostic dimensionality reduction paradigm of spatio-temporal data arXiv:2204.03216
[970] Brunton S L, Proctor J L and Kutz J N 2016 Discovering governing equations from data by sparse identification of nonlinear dynamical systems *Proc. Natl Acad. Sci.* **113** 3932–7
[971] Scheinker A, Cropp F, Paiagua S and Filippetto D 2021 An adaptive approach to machine learning for compact particle accelerators *Sci. Rep.* **11** 1918709
[972] Miskovich S A *et al* 2022 Online bayesian optimization for a recoil mass separator *Phys. Rev. Accel. Beams* **25** 044601
[973] Figueroa D, Garg R and Giuliani P 2024 Efficient Emulation of Secar Beam, https://dr.ascsn.net/blackbox_galerkin/SECAR.html
[974] Hoeting J A, Madigan D, Raftery A E and Volinsky C T 1999 Bayesian model averaging: a tutorial (with comments by M. Clyde, David Draper and E. I. George, and a rejoinder by the authors) *Stat. Sci.* **14** 382–417
[975] Fernández C and Green P J 2002 Modelling spatially correlated data via mixtures: a Bayesian approach *J. R. Stat. Soc. Ser.* B **64** 805–26
[976] Lovell A E, Mohan A T, Sprouse T M and Mumpower M R 2022 Nuclear masses learned from a probabilistic neural network *Phys. Rev.* C **106** 014305
[977] Utama R and Piekarewicz J 2017 Refining mass formulas for astrophysical applications: a Bayesian neural network approach *Phys. Rev.* C **96** 044308
[978] Semposki A C, Furnstahl R J and Phillips D R 2022 Interpolating between small- and large-g expansions using bayesian model mixing *Phys. Rev.* C **106** 044002
[979] Kejzlar V, Neufcourt L, Nazarewicz W and Reinhard P G 2020 Statistical aspects of nuclear mass models *J. Phys. G: Nucl. Part. Phys.* **47** 094001
[980] Semposki A, Drischler C, Furnstahl R and Phillips D 2023 Mind the gaps: applying bayesian model mixing to the dense matter equation of state *Meeting Abstracts* D06-005
[981] Vojtech Kejzlar M S, Bhattacharya S and Maiti T 2023 Black box variational bayesian model averaging *Am. Stat.* **77** 85–96

[982] Kejzlar V, Neufcourt L and Nazarewicz W 2023 Local bayesian dirichlet mixing of imperfect models *Sci. Rep.* **13** 19600
[983] Giuliani P, Godbey K, Kejzlar V and Nazarewicz W 2024 Model orthogonalization and bayesian forecast mixing via principal component analysis arXiv:2405.10839
[984] Drischler C, Giuliani P, Bezoui S, Piekarewicz J and Viens F 2024 Bayesian mixture model approach to quantifying the empirical nuclear saturation point *Phys. Rev.* C **110** 044320
[985] Semposki A C, Furnstahl R J and Phillips D R 2023 SAMBA 1.0.1 Sandbox for mixing using Bayesian analysis *Technical Report Version 1.0.1,* https://github.com/asemposki/SAMBA
[986] Ingles K, Liyanage D, Semposki A C and Yannotty J C 2023 Taweret Documentation, https://taweretdocs.readthedocs.io/en/latest/
[987] 2022 BMEX—The Bayesian Mass Explorer, Zenodo, https://zenodo.org/records/8317327
[988] 2023 Advanced Scientific Computing and Statistics Network (ASCSN), https://ascsn.net/
[989] Brown B A and Rae W D M 2014 The shell-model code NuShellX@MSU *Nucl. Data Sheets* **120** 115–18
[990] Warburton E and Brown B 1992 Effective interactions for the 0*p*1*s*0*d* nuclear shell-model space *Phys. Rev.* C **46** 923–44
[991] Arima A 1999 Elliott's SU(3) model and its developments in nuclear physics *J. Phys. G: Nucl. Part. Phys.* **25** 581–8
[992] Shimizu N, Tsunoda Y, Utsuno Y and Otsuka T 2021 Variational approach with the superposition of the symmetry-restored quasiparticle vacua for nuclear shell-model calculations *Phys. Rev.* C **103** 104312
[993] Dao D D and Nowacki F 2022 Nuclear structure within a discrete nonorthogonal shell model approach: New frontiers *Phys. Rev.* C **105** 054314
[994] Lian Z J, Gao Z C and Chen Y S 2024 A novel algorithm to the shell model study of heavy deformed nuclei using the variation after projection approach *Phys. Lett.* B **853** 138674
[995] Tichai A, Kapás K, Miyagi T, Werner M, Legeza Ö., Schwenk A and Zarand G 2024 Spectroscopy of $n = 50$ isotones with the valence-space density matrix renormalization group *Phys. Lett.* B **855** 138841